Crystallography Reports, Vol. 49, No. 1, 2004, pp. 1–3. Translated from Kristallografiya, Vol. 49, No. 1, 2004, pp. 5–7.

JUBILEE

The 80th Birthday of Lev Aleksandrovich Shuvalov

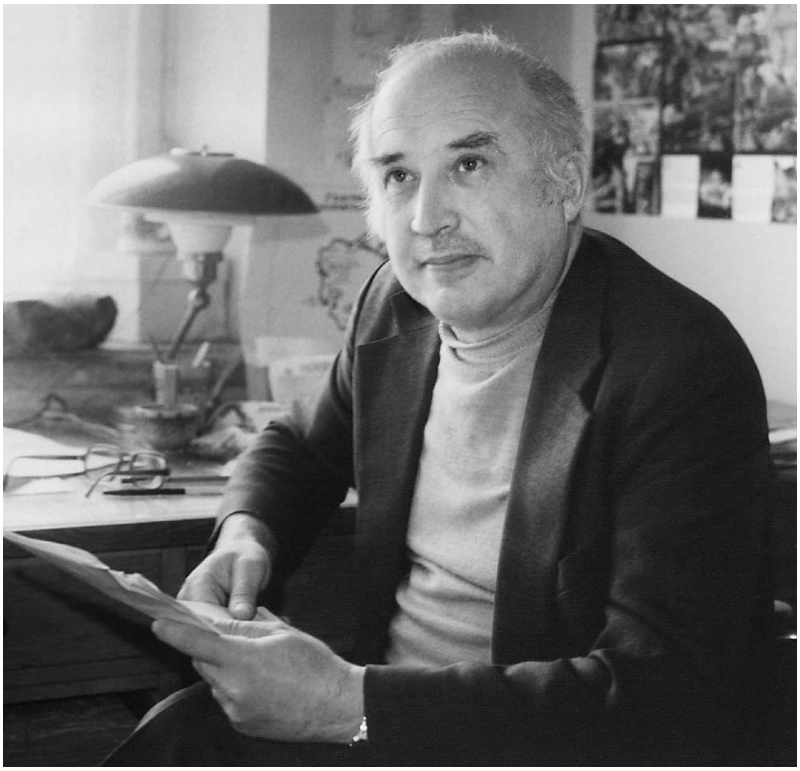

On November 15, 2003, an Honorary Scientist of the Russian Federation, Doctor in Physics and Mathematics Professor Lev Aleksandrovich Shuvalov, will celebrate his 80th birthday. One can hardly find a scientist engaged in crystal physics, physics of ferroelectrics, or structural phase transitions who would not know Professor Shuvalov and his numerous scientific publications. The recognized authority, he became a teacher of many generations of scientists working in crystal physics. The leading role of the Russian science in physics of condensed matter is associated, to a large degree, with the works performed by Shuvalov and his colleagues.

Shuvalov belongs to the generation whose youth was interrupted by the Great Patriotic War of 1941–1945. In 1941, almost immediately after graduation from school, Shuvalov entered the Red Army. From July 1942, Shuvalov took part in military operations as a pyrotechnician. In May 1942, these battalions received a new secret weapon—a heavy analogue of the famous Katyusha (the soldiers called it Andryusha). It was a breakthrough weapon and, therefore, its location and movements were top secret. It was fired by pyrotechnicians. Thus, within less than a year, Shuvalov fired more than 150 tons of missiles. He learned the hardship of war, the bitterness of losses and defeats, and the great joy of more and more frequent victories, and finally, witnessed the complete defeat of German fascism. A participant of the battles at Moscow, Stalingrad, and Kursk, Guards' master sergeant Shuvalov ended the war in Prague. He was awarded the order of the Red Star and several medals, including the Medal of Valour. His fate guarded him and he survived the war without any wounds.

Shuvalov tested through the first semester, and in March 1946, entered the Faculty of Physics of Moscow State University; he graduated from it with distinction in 1951. Then, Shuvalov worked for five years at the Hydroproject Institute and studied as a post-graduate student at the Institute of Crystallography under the guidance of A.V. Shubnikov, who greatly influenced the formation of Shuvalov's scientific views and interests.

1063-7745/04/4901-0001$26.00 © 2004 MAIK "Nauka/Interperiodica"

In 1956, Shuvalov started working at the Institute of Crystallography and still works there today. In 1961, he defended his Candidate thesis, and in 1971, his Doctoral thesis. For 20 years Shuvalov headed the Laboratory of Phase transitions founded in 1972. He has more than 700 scientific publications and is the creator of 20 inventions.

In the period from 1956 to 1974, Shuvalov performed the fundamental studies which have played the key role in the development of the symmetry approach in crystallography and crystal physics of ferroelectrics. At the same time, he also performed the first studies of pulsed switching in dielectrics, very important for use in various memory devices. Among the studies mentioned above, we should like to emphasize the formulation and elegant solution of the problems associated with the change of the symmetry during ferroelectric, ferroelastic, and ferromagnetic phase transitions. Shuvalov's works associated with the establishment of the general rules governing the domain structures of ferroelectrics and their effect on the macroscopic properties of crystals and the crystallophysical classification of ferroelectrics have become classical and are considered in numerous monographs and handbooks. For these works, Shuvalov was awarded the USSR State Prize in 1976.

We should like to indicate those results obtained by Shuvalov which formed the basis for new directions in physics of ferroelectrics and related materials. The pioneering complex studies of ferroelastics performed by Shuvalov and his coworkers played the most important role in the transformation of physics of ferroelastics into a new field of condensed matter physics at the junction of physics of ferroelastics and physics of structural phase transitions. Shuvalov is not only one of the founders of this field but is also its recognized leader in this country.

Shuvalov and his coworkers suggested and developed practically the first method of direct study of the statics and dynamics of domains in collinear (pure) ferroelectrics with the aid of nematic liquid crystals, now widely used everywhere. The authors of this method established the most important features of switching in ferroelectrics and also the specific features of the geometry of their domain and real structure, which is very important for the practical use of these crystals in pyrovidicons and other devices. Shuvalov's cycle of works on crystal physics (studies of ferroelastics, ferroelectric structural phase transitions, and domains) was awarded the Fedorov prize of the Russian Academy of Sciences.

Shuvalov and his coworkers discovered and studied in detail a new large family of ferro- and antiferroelectrics—alkali trihydroselenites possessing a number of unusual physical properties. They also discovered a number of new ferroelectrics, including those which are transformed into the ferroelectric phase at helium temperatures; they also established the most important characteristics of the physical properties of irreversible, improper, and quasi-one-dimensional ferroelectrics.

One of the most important results obtained in the two last decades is the discovery and thorough investigation of a new class of crystals with superionic conductivity (superprotonic conductors)—a number of families of alkali hydrosulfates and hydroselenates and compounds with quasi-two-dimensional protonic glassy state. It should be emphasized that these outstanding results on superprotonic compounds were obtained in such a short time because Shuvalov managed to create an informal team of Soviet scientists and scientists from other countries. This was one of the first examples of the creation and efficient work of informal research groups.

We should like to mention the studies performed by Shuvalov and his group on the theory of propagation of bulk and surface acoustic waves in crystals and layered systems of different symmetries, the development of various methods of studying the real structure of ferroelectrics and ferroelastics, the investigation and practical applications of the pyroelectric effect in specially designed devices, and the study of high-temperature phase transformations in protonic glassy compounds of the KADP type.

Shuvalov supervized more than 35 Candidate and 8 Doctoral theses. He organized large groups engaged in the research of ferroelectric and related phenomena at the University of Tver, Voronezh State Technical University, Volgograd Architectural and Civil Engineering Academy, Rostov State University, and others. Shuvalov managed to found a successfully developing scientific school.

Shuvalov is also engaged in the scientific-organizational activity. He is the vice-chairman of the section *Physics of ferroelectrics and dielectrics* of the Scientific council on Condensed Matter Physics of the Russian Academy of Sciences, the editor-in-chief of the journal *Kristallografiya*, one of the organizers of the National conferences on ferroelectricity, and the chairman of the organizing committees of all the National seminars on ferroelastics. He is the permanent chairman of the organizing committees of the meetings of students who graduated from the Faculty of Physics of Moscow State University in 1950.

Shuvalov is very active in establishing international cooperation with groups and individual scientists in Japan, the USA, Slovenia, Poland, Czech Republic, Lithuania, Ukraine, Germany, and other countries. He is an initiator and organizer of international conferences on physics of domains in ferroelectrics and related materials, bilateral Soviet (Russian)–Japanese and Soviet (Russian)–American symposia on ferroelectricity. He is (or was) a permanent member of the International and European consultative committees on ferroelectricity and a member of the editorial boards of international journals *Ferroelectrics*, *Ferroelectrics*

Letters, *Zeitschrift für Kristallographie*, *Crystallography Reviews*, and *Condensed Matter News*.

Shuvalov, together with V.A. Yurin, J. Stankovsky, and S. Waplyak, was awarded the Prize in Physics of the USSR and Polish Academies of Sciences. He is an honorary doctor of the Martin Luther University in Halle, Germany, an associated member of the Jozef Stefan Institute in Lublyana, Slovenia.

Shuvalov's colleagues, friends, and students highly estimate not only the scientific and organizational activity of Professor Shuvalov, they also appreciate his invariable optimism, interest in new ideas, openness, benevolence, and readiness to help everybody. He is always happy for scientific achievements of his colleagues, friends, and students. Great respect and affection of the scientific community was manifested during the time when Shuvalov was seriously ill. A special International Foundation was created to help Shuvalov to solve the most difficult problems and, in fact, to save his life. The activity of this Foundation was highly estimated by the 9th European Conference on Ferroelectricity in Prague in 1999. The support given to Shuvalov was considered to be a brilliant, although, unfortunately, rather rare example of the mutual international cooperation of scientists under critical conditions.

The Editorial Board, Shuvalov's colleagues, friends, and students wish him excellent health and many years of fruitful activity.

Translated by L. Man

Crystallography Reports, Vol. 49, No. 1, 2004, pp. 100–107. Translated from Kristallografiya, Vol. 49, No. 1, 2004, pp. 107–114.

LATTICE DYNAMICS AND PHASE TRANSITIONS

Dedicated to the 80th Birthday of L.A. Shuvalov

Ferroelastic Phase Transitions in Fluorides with Cryolite and Elpasolite Structures

I. N. Flerov*, M. V. Gorev*, K. S. Aleksandrov*, A. Tressaud, and V. D. Fokina***

** Kirensky Institute of Physics, Siberian Division, Russian Academy of Sciences, Akademgorodok, Krasnoyarsk, 660036 Russia*

e-mail: flerov@iph.krasn.ru

*** Institut de Chimie de la Matiére Condensée de Bordeaux, Pessac, F-33608 France*

Received June 3, 2003

Abstract—The ferroelastic phase transitions are investigated in several series of fluoride crystals belonging to the elpasolite and cryolite families (space group $Fm\bar{3}m$) with the general formula $A_2BB'F_6$. The influence of the size and shape of cations and anions on the entropy and the mechanism of structural distortions is discussed.

INTRODUCTION

Perovskite-like compounds have attracted the particular attention of researchers due to a large variety of physical properties and their possible use in different technical devices. The perovskite structure is characterized by a relatively simple crystal lattice, on the one hand, and the striking flexibility that makes it possible to change the composition of ions forming the lattice over a wide range and, thus, to achieve the desirable properties of the material, on the other hand. In this respect, perovskite compounds play an important role in solid-state physics and materials science. All unique (and practically useful) properties predominantly manifest themselves in compounds whose structure differs from an ideal cubic structure of the ABX_3 perovskite due to different-type distortions, such as polar and antipolar displacements of *A* and (or) *B* ions from their positions at the centers of octahedra and cubooctahedra, octahedron rotations, Jahn–Teller distortions, or magnetic ordering.

Investigations into the mechanisms responsible for phase transformations and changes in the sequences of structural distortions occurring in perovskite-like compounds as a result of variations in external (temperature, pressure) and internal (doping, composition) parameters are of considerable interest both from the point of view of elucidation of the composition–structure–property relations and from the practical standpoint of searching for the criteria for syntheses of crystals with controlled properties.

Among perovskite-like compounds, the elpasolite and cryolite families are most representative owing to the great diversity of possible substitutions for atoms in crystals of the general formula $A_2BB'X_6$. According to [1, 2], more than 350 compounds with a similar structure were known until recently and, as follows from the crystal chemical analysis, more than 1500 new elpasolites can be obtained only based on halides. In the initial phase, crystals of this family have cubic symmetry (space group $Fm\bar{3}m$ – O_h^6, $Z = 4$). Unlike the simple perovskites ABX_3, in which all the octahedra are equivalent, the elpasolites (also referred to as ordered perovskites) contain two types of ionic groups (BX_6, $B'X_6$) alternating along the three fourfold axes. Therefore, the elpasolite cubic cell can be treated as a perovskite cell with double the unit cell parameter. The crystal structure of the cryolite $A_3B'X_6$, in which the *A* and *B* atoms are chemically equivalent, is a special case of the elpasolite structure.

For compounds of these families, the group-theoretic analysis of the possible phase transitions from the initial phase was performed in [3, 4], the symmetry analysis of the lattice vibrations was carried out in [5, 6], and the phase transitions were phenomenologically described in [5]. In the majority of cases, the phase transformations were treated as displacive transitions. However, there are a large number of experimental facts indicating a crossover from the displacive-type mechanism to the order–disorder mechanism of phase transitions with a change in the type of *A*, *B*, and *B*' ions. The problem of possible disordering in perovskites, which was formulated by Comes *et al.* [7], is still debated in the literature [8, 9]. The order–disorder phase transitions most clearly manifest themselves in compounds with nonspherical cations *A* and *B* (for example, with tetrahedral ammonium ions). It seems

likely that ordering upon these phase transitions involves not only ammonium ions but also octahedral ions, which, upon other phase transitions, execute small rotations due to softening of the lattice rotational vibration modes. The role played by the ordering processes in the mechanisms of phase transformations in these compounds is still not clearly understood.

In this work, we analyzed the thermal and structural data obtained for several series of fluorides with elpasolite-like and cryolite-like structures in order to elucidate how the sizes and shape of cations affect the position and motion of fluorine ions and the entropy of phase transitions. It should be noted that, according to the results of investigations performed in polarized light, all the studied crystals undergoing displacive and (or) order–disorder phase transitions are ferroelastic materials.

ELPASOLITES WITH ATOMIC CATIONS

In $Rb_2KB^{3+}F_6$ crystals, a decrease in the size of the B^{3+} cation (Fig. 1) leads to the change in the sequence of structural distortions from $Fm\bar{3}m \longrightarrow P12_1/n1$ (B^{3+} = Er, Ho, Dy, Y, Tb) to $Fm\bar{3}m \longrightarrow I4/m \longrightarrow P12_1/n1$ (B^{3+} = Lu, In, Sc), a decrease in the stability temperature of the cubic phase, and an increase in the temperature range of the stability of the intermediate tetragonal phase from 3 (B^{3+} = Lu) to 30 K (B^{3+} = Sc) [10]. The triple point with the coordinates $R_{B^{3+}} \sim 0.88$ Å and $T_0 \sim 370$ K is observed in the $R_{B^{3+}}$–T phase diagram. The transition to the tetragonal phase is characterized by the small entropy ΔS, which is of the order of $0.2R$ [10]. This value of ΔS indicates that the above transformations can be attributed to displacive phase transitions. The structural distortions in the compounds under consideration are associated with the crystal lattice instability with respect to small rotations of fluorine octahedra (the rotational modes Γ_4^+, X_2^+) [5]. The tetragonal symmetry is caused by the (00φ) rotations of octahedra about one of the fourfold axes of the cubic cell [5] due to the condensation of the Γ_4^+ rotational mode at the center of the Brillouin zone. The monoclinic distortion $P12_1/n1$ is associated with the condensation of the X_2^+ rotational mode and can be treated as a superposition of the (ψφφ) rotations of octahedra about three principal cubic axes at once. The total entropy change upon transition from the cubic phase to the monoclinic phase depends on the size of the trivalent ion and decreases from $1.3R$ (Ho) to $0.7R$ (Sc) [10]. The maximum value ($1.3R$) is rather large for purely displacive transitions but does not allow us to assign these transformations to order–disorder transitions. In this case, an increase in the entropy with an increase in the size of the trivalent cation is associated with the increase in the anharmonicity and anisotropy of vibrations of fluorine ions, which is confirmed by the results of structural investigations [10, 11].

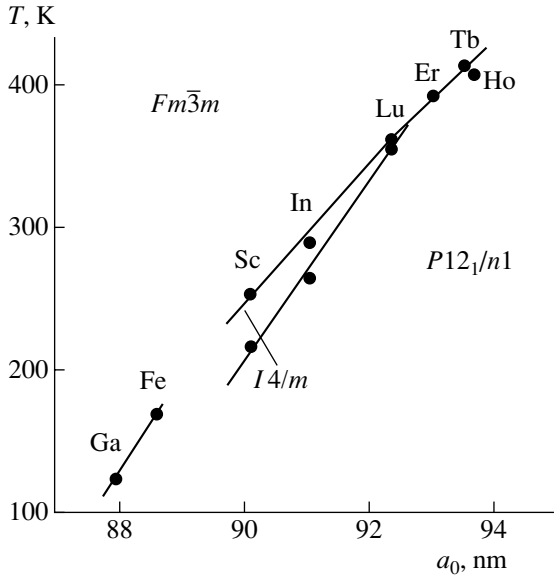

Fig. 1. Dependence of the phase transition temperature T_i on the parameter a_0 of the cubic unit cell for $Rb_2KB^{3+}F_6$ elpasolites.

A further decrease in the parameter of the cubic unit cell of $Rb_2KB^{3+}F_6$ crystals (B^{3+} = Fe, Cr, Ga) leads to only one ferroelastic first-order transition, which is accompanied by a considerable volume jump and, consequently, results in the failure of single-crystal samples [10, 12]. Symmetry of the distorted phase in these crystals is not established uniquely [13–15]. The experimental data cannot be described in the framework of the models successfully used for rotational phase transitions and suggest that the phase transitions in crystals with small-sized trivalent cations proceed through a mechanism different from the purely rotational mechanism. The $R_{B^{3+}}$–T phase diagram should be complex in the range between the sizes of the Sc^{3+} and Fe^{3+} ions. In this range, the competition between different mechanisms of phase transitions can be responsible for the appearance of new distorted phases and triple points (Table 1).

In order to elucidate the changes in the sequence and mechanism of structural distortions, $Rb_2KGa_xSc_{1-x}F_6$ solid solutions were studied in [13, 16–20]. Figure 2 depicts the composition–temperature phase diagram of these solid solutions. The temperature dependences of the heat capacity $C_p(T)$ and the interplanar distance d_{440} for compounds with $x \le 0.6$ exhibit two anomalies associated with the phase transitions from the cubic phase to the tetragonal phase $I4/m$ and then to the monoclinic phase $P12_1/n1$. The entropy change $\Delta S_2/R \sim 0.51$ upon second phase transition agrees well with that obtained for the $I4/m \longrightarrow P12_1/n1$ transition in pure

Table 1. Thermodynamic characteristics of the phase transitions in haloid elpasolites with atomic cations

$A_2B^+B^{3+}X_6$	Type of distorted structure	System of octahedron rotations	T_i, K	$T^{-1}dT/dp$, GPa^{-1}	$\Delta S/R$
Rb_2KFeF_6	?	?	170	0.78	1.88
Rb_2KGaF_6	?	?	123	0.90	1.73
$Rb_2KGa_{0.95}Sc_{0.05}F_6$	$I4/m$?	00φ	130		
	?	?	123.5		
$Rb_2KGa_{0.9}Sc_{0.1}F_6$					
	?	?	117		
$Rb_2KGa_{0.6}Sc_{0.4}F_6$	$I4/m$	00φ	?		
	$P2_1/n$	ψφφ	102.5		
$Rb_2KGa_{0.2}Sc_{0.8}F_6$	$I4/m$	00φ	218		
	$P2_1/n$	ψφφ	189		
Rb_2KScF_6	$I4/m$	00φ	252	0.07	0.20
	$P2_1/n$	ψφφ	223	0.01	0.51
Rb_2KInF_6	$I4/m$	00φ	283	0.07	0.18
	$P2_1/n$	ψφφ	264	0.03	0.59
Rb_2KLuF_6	$I4/m$	00φ	370	0.06	
	$P2_1/n$	ψφφ	366	0.05	1.05
Rb_2KErF_6	$P2_1/n$	ψφφ	395	0.06	0.95
Rb_2KHoF_6	$P2_1/n$	ψφφ	400	0.05	1.13
Rb_2KTbF_6	$P2_1/n$	ψφφ	412	0.06	

Note: R is the gas constant.

Rb_2KScF_6. The phase transition from the cubic phase to the tetragonal phase in compounds with $x > 0.4$ was not observed by the calorimetric methods due to the small entropy of this transition and a possible smearing of anomalies in the heat capacity. Therefore, in the solid solutions (at least, in the range $x = 0$–0.6), the sequence of the phase transitions $Fm\bar{3}m \longrightarrow I4/m \longrightarrow P12_1/n1$ remains unchanged and corresponds to a sequential increase in the rotational distortions induced by the lattice vibrational and X_2^+ modes.

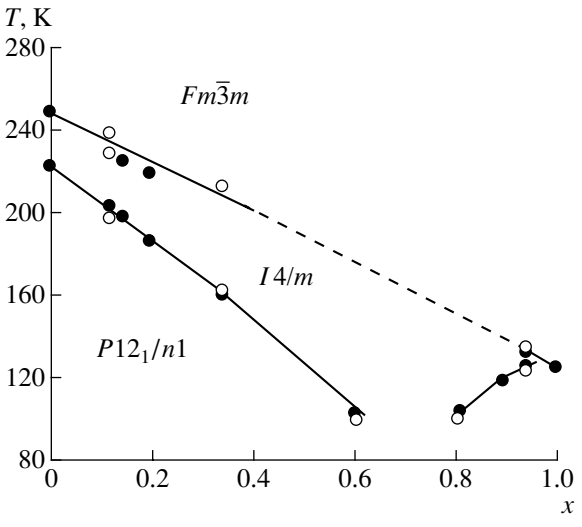

Fig. 2. x–T phase diagram of $Rb_2KGa_xSc_{1-x}F_6$ elpasolites according to the calorimetric (closed circles) and X-ray diffraction (open circles) data.

For compounds with $x \geq 0.8$, the temperatures of two phase transitions become close to each other and the intermediate phase disappears at a gallium content close to $x = 1$. The entropy and the quantity dT/dp considerably exceed the values characteristic of rotational transitions and are in good agreement with the results obtained for the Rb_2KFeF_6 compound [12]. The difference in the sequences of structural transformations in compounds with $x < 0.6$ and $x > 0.8$ is confirmed by the X-ray diffraction and elastic neutron scattering data [18, 20].

An analysis of the structural and Raman scattering data for compounds with $x = 0.8$–1.0 [15, 21] demonstrates that, among all possible space groups, the groups $I4/m$, $P2/m$, and $P112_1/n$ are most probable and consistent with the experimental data. The arising instability of the cubic cell in these compounds can be associated not only with the two purely rotational

modes X_2^+ and Γ_4^+ but also with the low-lying X_2^+ mode [15, 21], which is due to the octahedron rotations and the displacements of Rb ions in holes between octahedra. The interaction of these modes can result in the triggered $Fm\bar{3}m \longrightarrow P112_1/n$ and successive $Fm\bar{3}m \longrightarrow I4/m \longrightarrow P112_1/n$ and $Fm\bar{3}m \longrightarrow I4/m \longrightarrow P2/m \longrightarrow P112_1/n$ phase transitions. These sequences involve the intermediate tetragonal phase $I4/m$, which is observed in other compounds of the solid solutions under consideration.

Therefore, investigations of a number of $Rb_2KB^{3+}F_6$ crystals made it possible to refine the phase diagram and elucidate the influence of the size of the trivalent ion on the sequences and mechanisms of phase transitions.

AMMONIUM CRYOLITES $(NH_4)_3B^{3+}F_6$

In structural investigations of halide compounds, authors often noted that the thermal parameter of halogen atoms in the cubic phase is rather large and, in this respect, proposed different variants of possible orientational disordering of octahedra [11, 22, 23]. However, the refinement of the structural data in the framework of these models did not lead to a substantial decrease in the R factor [11, 23]. Moreover, the thermodynamic data unambiguously indicate that the phase transformations in halide compounds with atomic cations are displacive phase transitions associated with the condensation of lattice modes. This allows us to assume that a considerable anharmonicity of vibrations rather than disordering over several positions is characteristic of fluorine atoms.

A different situation occurs in the case when atomic cations in the elpasolite structure are replaced by tetrahedral ammonium cations. These compounds with small-sized trivalent cations (Ga, Cr, Fe, V) undergo phase transitions from the cubic phase $Fm\bar{3}m$ to the triclinic phase $P\bar{1}$ with a large entropy change, which suggests that the transformations are associated with the ordering processes [24–27]. On the other hand, compounds with large-sized trivalent cations (Sc, In) are characterized by the successive $Fm\bar{3}m \longrightarrow P112_1/n \longrightarrow I12/m1 \longrightarrow P\bar{1}$ phase transitions [28]. The deuteration of ammonium cryolites does not lead to noticeable changes in the thermodynamic parameters, which indicates that hydrogen bonds do not play a significant role in the mechanism of phase transitions [29]. It is worth noting that the total entropy changes for all compounds are close to $R\ln(16)$ irrespective of whether a compound undergoes one phase transition or a sequence of transitions (Table 2). Consequently, these transformations proceed through the order–disorder mechanism.

In the structure under investigation, ionic groups of two types, namely, NH_4 tetrahedra and fluorine octahedra, are involved in ordering. The ammonium tetrahedra located in the holes between octahedra in the cubic phase (position 8*c*, CN = 12) are ordered, because their symmetry corresponds to symmetry of the occupied site. The tetrahedra situated at the center of the fluorine octahedra (position 4*b*, CN = 6) in the cubic phase can have two possible orientations. The fluorine ions in the cubic lattice with symmetry $Fm\bar{3}m$ in the general case can be distributed over twelve different crystallographic positions. Among them, only two positions, 24*e* and 192*l*, satisfy the conditions of a rigid regular octahedron [26]. If the fluorine ions are located at the cubic cell edges (positions 24*e*), the octahedra are ordered. When the fluorine ions are distributed over the 192*l* positions, each fluorine octahedron in the cubic phase can have eight equally probable orientations [26]. Complete ordering of the octahedra and tetrahedra should result in an entropy change of $R\ln(16)$, which is in good agreement with the experimental results.

In the case of single phase transitions, for example, in the gallium compound, the octahedra and tetrahedra are ordered simultaneously. This is confirmed by the nuclear magnetic resonance (NMR) data [33]. It was found that the spin–lattice relaxation times of both protons and fluorine ions exhibit jumps upon phase transition, which indicates a change in the character of their motion.

For successive phase transitions, for example, in the scandium cryolite, the first two transitions according to the calorimetric data [$\Delta S_1 = R\ln 8$, $\Delta S_2 = R\ln 2$] can be associated with the order–disorder processes. The third phase transition with a small change in the entropy is the transformation between two completely ordered distorted phases. We could assume that the first and second transitions are due to complete ordering of octahedra and tetrahedra, respectively. However, ordering of the octahedra should necessarily be accompanied by the change in symmetry of the position occupied by the tetrahedra and their forced ordering. Moreover, according to the NMR data [33], the spin–lattice relaxation time of fluorine ions exhibit jumps upon the first and second transitions. On the other hand, the spin–lattice relaxation time of protons considerably changes only upon the first phase transition. It was assumed that the phase transition from the cubic phase is due to complete ordering of the tetrahedra and partial ordering of the octahedra. In the distorted phase, the octahedra can have two equally probable orientations. The second phase transition results in complete ordering of the octahedra.

The analysis of the thermodynamic parameters and the phase diagrams allows us to construct the generalized pressure–temperature (or cell volume–temperature) phase diagram for the entire series of ammonium cryolites (Fig. 3). This diagram illustrates a gradual evolution of the sequences of phase transitions with a

Table 2. Thermodynamic characteristics of the phase transitions in $(NH_4)_3B^{3+}F_6$ ammonium cryolites

B^{3+}:		Al	V	Fe	Ga	$Ga_{0.6}Sc_{0.4}$	$Ga_{0.4}Sc_{0.6}$	Sc
$G_0 \longrightarrow G_1$	$\Delta S/R$							1.63
	dT/dp, K/GPa						–8.2	–16.4
$G_1 \longrightarrow G_2$	$\Delta S/R$							0.81
	dT/dp, K/GPa						46.4	57.5
$G_2 \longrightarrow G_3$	$\Delta S/R$							0.08
	dT/dp, K/GPa						65.2	59.9
$G_0 \longrightarrow G_2$	$\Delta S/R$							
	dT/dp, K/GPa							
$G_0 \longrightarrow G_3$	$\Delta S/R$		2.99	2.77	2.76	2.60		
	dT/dp, K/GPa				–12.1	–15.3	–8.1	
$G_0 \longrightarrow G_4$	$\Delta S/R$							
	dT/dp, K/GPa	50.4 ± 1.2			101.3			
$G_4 \longrightarrow G_5$	$\Delta S/R$							
	dT/dp, K/GPa	–670 ± 100			~0			
$G_5 \longrightarrow G_3$	$\Delta S/R$	0.5 ± 0.1						
	dT/dp, K/GPa	–700 ± 100			–22.5			
$G_0 \longrightarrow G_5$	$\Delta S/R$	2.22 ± 0.08						
	dT/dp, K/GPa	–11.8 ± 4			73.1	60.1		
References		[27, 30]	[25]	[26]	[31, 32]	[32]	[32]	[31, 32]

variation in the parameters. The scandium and gallium compounds have the following distorted phases with symmetries determined in [28, 34]: $G_1(P12_1/n1, Z = 2)$, $G_2(I12/m1, Z = 16)$, and $G_3(I\bar{1}, Z = 16)$. Symmetries of the high-pressure phases G_4 and G_5 in the gallium cryolite still remain unknown.

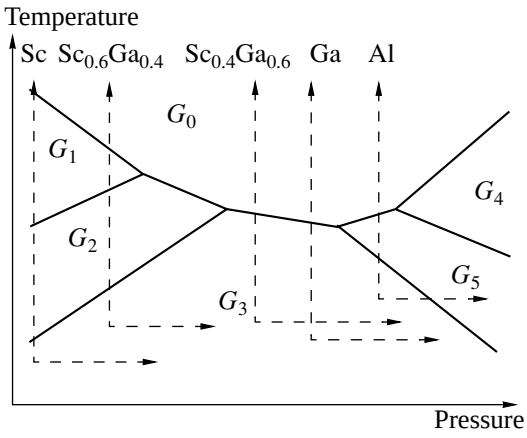

Fig. 3. Generalized phase diagram of $(NH_4)_3B^{3+}F_6$ ammonium cryolites.

AMMONIUM ELPASOLITES

In order to elucidate the role played by the ammonium ions occupying different crystallographic positions, two types of ammonium elpasolites were examined in our earlier works [35, 36]. In $Cs_2NH_4GaF_6$, the NH_4 ions are located at the cubic cell edges at the centers of fluorine octahedra. In the $(NH_4)_2KGaF_6$ compound, the ammonium ions occupy the holes between octahedra.

The $Cs_2NH_4GaF_6$ elpasolite undergoes one phase transition with the large entropy change $R\ln(8)$ [36]. No high-pressure phases or triple points were found in the p–T phase diagram [36]. We believe that, like the transitions in ammonium cryolites, this transition is accompanied by complete ordering of the NH_4 tetrahedra and partial ordering of the octahedra. The complete ordering of the octahedra can occur at temperatures below the liquid-nitrogen temperature. Thus, a comparison with the $(NH_4)_2NH_4GaF_6$ compound shows that the presence of the Cs^+ spherical cation in the hole between octahedra renders the crystal structure more rigid and stable. This can be judged from the lower temperature of the transition from the cubic phase (162 K) in $Cs_2NH_4GaF_6$ and the absence of splitting of the phase boundary under pressure.

The assumption regarding the occurrence of the second phase transition is supported by the data obtained for the $Cs_2NH_4ScF_6$ elpasolite. An increase in the size of the B^{3+} ion leads not only to an increase in the stability temperature of the cubic phase (T_1 = 285 K) but also to the second phase transition (T_2 = 195 K).

A quite different situation is observed for the $(NH_4)_2KGaF_6$ compound characterized by the sequence of two transformations [35]. The entropy change ($\Delta S = 0.12R$) upon phase transition from the cubic phase uniquely indicates that this is the displacive phase transition associated with the condensation of lattice modes. According to the structural data, the first distorted phase has symmetry $I4/m$. This symmetry is identical to symmetry of the distorted phase in compounds with atomic cations (see $Rb_2KB^{3+}F_6$). In this case, the fluorine octahedra are ordered in the cubic phase and the phase transition is due to the condensation of the Γ_4^+ mode.

The large entropy change ($\Delta S = 1.8R$) upon the second phase transition suggests that this transformation proceeds through the order–disorder mechanism. When considering the ammonium cryolites, we assumed that the NH_4 ions in the holes between octahedra are ordered completely. However, symmetry $Fm\bar{3}m$ is also retained if the hydrogen ion is shifted from the threefold axis and the nitrogen–hydrogen bonds are directed toward fluorine ions. In this situation, the tetrahedron in the cubic phase has three equally probable orientations. This disordering is most pronounced in the ammonium antifluorite with a similar structure [37]. For completely ordered tetrahedra, the entropy change should be equal to $2R\ln(3)$. This value agrees well with the experimentally determined entropy change ΔS. The above model of structural distortions is confirmed by the NMR data [38]. The spin–lattice relaxation time of fluorine ions remains unchanged upon both the first and second transitions. The spin–lattice relaxation time of protons substantially changes only upon the second phase transition.

The $(NH_4)_2KScF_6$ elpasolite is characterized by appreciably higher temperatures of the phase transitions and a considerably narrower temperature range of the stability of the tetragonal phase (T_1 = 367 K, T_2 = 361 K). However, as follows from the data on the entropy change, the structural transformations occur through the same mechanism.

Therefore, the analysis of the ammonium compounds allows us to make the inference that the replacement of the atomic cations at the center of the fluorine octahedra by the NH_4 tetrahedra results in orientational disordering of the octahedra and pronounced order–disorder phase transitions. The presence of the ammonium ions in the holes between octahedra does not affect the character of octahedron motion, and the phase transformations are the displacive transitions associated with the condensation of soft lattice modes. The ammonium tetrahedra are disordered and undergo ordering at lower temperatures.

Table 3. Strengths μ_A and μ_B of interatomic bonds and the temperatures T_1 of transitions from the cubic phase of fluoride compounds

	$B^{3+} = Ga^{3+}$			$B^{3+} = Sc^{3+}$		
	μ_A, %	μ_B, %	T_1, K	μ_A, %	μ_B, %	T_1, K
$Cs_2NH_4B^{3+}F_6$	4.7	10.3	162	2.4	10.4	285
$(NH_4)_2NH_4B^{3+}F_6$	0.4	11.5	250	–2.0	11.5	330
$(NH_4)_2KB^{3+}F_6$	2.0	12.4	280	–0.1	13.9	367
$Rb_2KB^{3+}F_6$	4.3	13	126	1.9	13.0	280
$Cs_2KB^{3+}F_6$	7.0	11.7	<77 ?	4.4	11.3	<77 ?

ON THE INTERATOMIC BOND STRENGTH

We studied four series of compounds with the elpasolite and cryolite structures and revealed that different sequences and mechanisms of phase transitions can be observed in these compounds depending on the unit cell volume and the cation shape. However, the "closed" elpasolite series $(NH_4)_2NH_4$–Cs_2NH_4–Cs_2K–Rb_2K–$(NH_4)_2K$–$(NH_4)_2NH_4$, which is formed by sequential replacements of cations at a constant size of the $B^{3+}F_6$ octahedron, involves compounds with a Cs_2K combination of cations that are absent among the objects under consideration. In the studied Cs_2KGaF_6 and Cs_2KScF_6 crystals, no phase transitions were found at temperatures down to 77 K. This circumstance and the stability of the cubic phase can be explained in terms of the hypothesis of interatomic bond strength [39].

According to this hypothesis, the stability of the initial cubic phase is determined by the ratio between the ion sizes and the lattice parameter a_0, i.e., by the ion bond strength in the A^+–F^- and B^{3+}–F^-–B^+–F^-–B^{3+} chains. The ratios $\mu_A = (a_p' - a_0)/a_p'$ and $\mu_B = (a_p - a_0)/a_p$, where $a_p = 2(R_{B^+} + 2R_F + R_{B^{3+}})$ and $a_p' = 2\sqrt{2}(R_{A^+} + R_F)$, can serve as the quantitative measures of the strength. An increase in the μ_B value is equivalent to an increase in the repulsion energy in the crystal potential and leads to an increase in the anisotropy of motion of F atoms and, hence, to a decrease in the stability of the initial phase. An increase in the μ_A value causes a hindrance to the octahedron rotation and results in an increase in the stability of the undistorted lattice.

The validity of this hypothesis for the closed series of crystals can be illustrated using the examples presented in Table 3. An increase in the size of the $B^{3+}F_6$ octahedron upon replacement of Ga by Sc in all the cases primarily leads to a substantial change in the μ_A value and, correspondingly, to an increase in the stability temperature of the cubic phase. From analyzing the structural data and the parameters of the phase transitions in compounds with rare-earth elements as the B^{3+} cation, we established that no phase transitions should occur in Ga and Sc compounds for the Cs_2K combination of cations. It can be seen from Table 3 that the predicted absence of phase transitions is associated with the considerable difference in the μ_A values for these crystals. An increase in the temperature T_1 is also observed in the series of the compounds formed upon replacement of the *A* cation: Cs_2K–Rb_2K–$(NH_4)_2K$.

Thus, the hypothesis of interatomic bond strength appeared to be fruitful for describing not only the displacive phase transitions but also the order–disorder transitions. In ammonium cryolites, an increase in the unit cell size is attended by a substantial decrease in the μ_A value and an increase in the μ_B value, which results in an increase in the phase transition temperatures [32]. Furthermore, these data demonstrate that, in ammonium cryolites with successive transformations, the transition from the cubic phase is predominantly associated with ordering of octahedral ionic groups. This ordering upon order–disorder phase transition can also be treated as octahedron rotation but through a considerably larger angle. However, when the structural distortions cannot be described by octahedron rotations, the hypothesis is invalid, which was shown earlier for cryolites with atomic cations [40].

ACKNOWLEDGMENTS

This work was supported by the Ministry of Science, Industry, and Technology of the Russian Federation (project no. NSh-939.2003.2) and the program of the Physical Science Division of the Russian Academy of Sciences (project no. 2.2.6.1).

REFERENCES

1. B. V. Beznosikov and K. S. Aleksandrov, Preprint No. IFSO-753F, IF SO RAN (Inst. of Physics, Siberian Division, Russian Academy of Sciences, Krasnoyarsk, 1994).
2. K. S. Aleksandrov and B. V. Beznosikov, *Perovskite-Like Crystals* (Nauka, Novosibirsk, 1997).
3. V. I. Zinenko and S. V. Misyul', *Possible Phase Transitions in Crystals with Space Group O_h^5*, Available from VINITI, No. 313-78 (Moscow, 1978).
4. G. P. O'Leary and R. G. Wheeler, Phys. Rev. B **1**, 4409 (1970).
5. K. S. Aleksandrov and S. V. Misyul', Kristallografiya **26** (5), 1074 (1981) [Sov. Phys. Crystallogr. **26**, 612 (1981)].
6. S. V. Misyul', Kristallografiya **29** (5), 941 (1984) [Sov. Phys. Crystallogr. **29**, 554 (1984)].
7. R. Comes, M. Lambert, and A. Guinier, Acta Crystallogr., Sect. A: Cryst. Phys., Diffr., Theor. Gen. Crystallogr. **26** (2), 244 (1970).
8. J.-M. Kiat, G. Baldinozzi, M. Dunlop, *et al.*, J. Phys.: Condens. Matter **12**, 8411 (2000).
9. Ch. Malibert, B. Dkhil, M. Dunlop, *et al.*, Ferroelectrics **235** (1), 97 (1999).
10. I. N. Flerov, M. V. Gorev, K. S. Aleksandrov, *et al.*, Mater. Sci. Eng. R **24** (3), 81 (1998).
11. H. Faget, J. Grannec, A. Tressaud, *et al.*, Eur. J. Solid State Inorg. Chem. **33** (9), 893 (1996).
12. M. V. Gorev, I. N. Flerov, V. N. Voronov, *et al.*, Fiz. Tverd. Tela (St. Petersburg) **36** (4), 1121 (1994) [Phys. Solid State **36**, 609 (1994)].
13. J. M. Dance, J. Grannec, A. Tressaud, *et al.*, Phys. Status Solidi B **173** (2), 579 (1992).
14. C. Marco de Lucas, F. Rodriguez, J. M. Dance, *et al.*, J. Lumin. **48/49** (2), 553 (1991).
15. A. Tressaud, S. Khairoun, J.-P. Chaminade, and M. Couzi, Phys. Status Solidi A **98** (2), 417 (1986).
16. M. V. Gorev, A. F. Bovina, G. V. Bondarenko, *et al.*, Fiz. Tverd. Tela (St. Petersburg) **37** (3), 819 (1995) [Phys. Solid State **37**, 444 (1995)].
17. M. V. Gorev, I. N. Flerov, A. Tressaud, and J. Grannec, Fiz. Tverd. Tela (St. Petersburg) **39** (10), 1844 (1997) [Phys. Solid State **39**, 1647 (1997)].
18. M. V. Gorev, I. N. Flerov, A. F. Bovina, *et al.*, Izv. Akad. Nauk, Ser. Fiz. **62** (4), 1532 (1998).
19. M. V. Gorev, I. N. Flerov, A. Tressaud, *et al.*, *BENSC Experimental Reports 1995* (Hahn-Meitner Inst., Berlin, 1996), p. 180.
20. M. V. Gorev, I. N. Flerov, A. Tressaud, *et al.*, Ferroelectr. Lett. Sect. **22** (5–6), 127 (1997).
21. M. Couzi, S. Khairoun, and A. Tressaud, Phys. Status Solidi B **98** (1), 423 (1986).
22. R. Haegele, W. Verscharen, and D. Babel, Z. Naturforsch. **30** (3), 462 (1975).
23. W. Massa, D. Babel, M. Epple, and W. Rudorff, Rev. Chim. Miner. **23** (4–5), 508 (1986).
24. A. Tressaud, S. Khairoun, L. Rabardel, *et al.*, Phys. Status Solidi A **96**, 407 (1986).
25. K. Kobayashi, T. Matsuo, and H. Suga, Solid State Commun. **53** (8), 719 (1985).
26. K. Moriya, T. Matsuo, H. Suga, and S. Seki, Bull. Chem. Soc. Jpn. **50** (8), 1920 (1977).
27. K. Moriya, T. Matsuo, H. Suga, and S. Seki, Bull. Chem. Soc. Jpn. **52** (11), 3152 (1979).
28. M. V. Gorev, I. N. Flerov, S. V. Mel'nikova, *et al.*, Izv. Akad. Nauk, Ser. Fiz. **64** (6), 1104 (2000).
29. I. N. Flerov, M. V. Gorev, M. L. Afanas'ev, and T. V. Ushakova, Fiz. Tverd. Tela (St. Petersburg) **44** (10), 1870 (2002) [Phys. Solid State **44**, 1961 (2002)].
30. M. V. Gorev, I. N. Flerov, A. Tressaud, and E. Durand, J. Phys.: Condens. Matter **14** (25), 6447 (2002).
31. M. V. Gorev, I. N. Flerov, and A. Tressaud, J. Phys.: Condens. Matter **11**, 7493 (1999).

32. I. N. Flerov, M. V. Gorev, and T. V. Ushakova, Fiz. Tverd. Tela (St. Petersburg) **41** (3), 523 (1999) [Phys. Solid State **41**, 468 (1999)].
33. A. Sasaki, Y. Furukawa, and D. Nakamura, Ber. Bunsenges. Phys. Chem. **93**, 1142 (1989).
34. S. V. Mel'nikova, S. V. Misyul', A. F. Bovina, and M. L. Afanas'ev, Fiz. Tverd. Tela (St. Petersburg) **43** (8), 1533 (2001) [Phys. Solid State **43**, 1594 (2001)].
35. I. N. Flerov, M. V. Gorev, M. L. Afanas'ev, and T. V. Ushakova, Fiz. Tverd. Tela (St. Petersburg) **43** (12), 2209 (2001) [Phys. Solid State **43**, 2301 (2001)].
36. M. V. Gorev, I. N. Flerov, A. Tressaud, *et al.*, Solid State Sci. **4** (1), 15 (2002).
37. E. O. Schlemper, W. C. Hamilton, and J. J. Rush, J. Chem. Phys. **44** (5), 2499 (1966).
38. K. Hirokawa and Y. Furukawa, J. Phys. Chem. Solids **49** (9), 1047 (1988).
39. K. S. Aleksandrov, A. T. Anistratov, B. V. Beznosikov, and N. V. Fedoseeva, *Phase Transitions in Crystals of ABX_3 Halide Compounds* (Nauka, Novosibirsk, 1981).
40. I. N. Flerov, M. V. Gorev, V. N. Voronov, and A. F. Bovina, Fiz. Tverd. Tela (St. Petersburg) **38**, 2203 (1996) [Phys. Solid State **38**, 1213 (1996)].

Translated by O. Borovik-Romanova

Crystallography Reports, Vol. 49, No. 1, 2004, pp. 108–113. Translated from Kristallografiya, Vol. 49, No. 1, 2004, pp. 115–120.

LATTICE DYNAMICS AND PHASE TRANSITIONS

Dedicated to the 80th Birthday of L.A. Shuvalov

On the Existence of the Relaxation Mode in Relaxor Ferroelectrics

S. N. Gvasaliya[1, 2], S. G. Lushnikov[2], and B. Roessli[1]

[1]*Laboratory for Neutron Scattering, ETHZ and Paul-Scherrer Institute, CH-5232 Villigen PSI, Switzerland*

[2]*Ioffe Physicotechnical Institute, Russian Academy of Sciences, Politekhnicheskaya ul. 26, St. Petersburg, 194021 Russia*

e-mail: sergey.lushnikov@mail.ioffe.ru

Received August 4, 2003

Abstract—The lattice dynamics of $PbMg_{1/3}Nb_{2/3}O_3$ and $PbMg_{1/3}Ta_{2/3}O_3$ relaxor ferroelectrics is investigated by inelastic neutron scattering. The relaxation mode in these crystals is revealed from an analysis of the low-frequency part of the vibrational spectrum. The possible reasons for the appearance of this mode are discussed, and different approaches to the description of the low-frequency spectrum of ferroelectrics are compared. © *2004 MAIK "Nauka/Interperiodica".*

INTRODUCTION

Perovskite-like relaxor ferroelectrics (relaxors) of the general formula $AB'_xB''_{1-x}O_3$ have attracted the particular attention of researchers for many years [1]. These compounds differ from classical perovskites of the formula ABO_3 by the presence of heterovalent ions B' and B'' in the crystallographically equivalent positions of the B sublattice. A distinguishing feature of the relaxor ferroelectrics is that their permittivity exhibits a broad frequency-dependent peak, which is not associated with the structural phase transition [2].

Crystals of $PbMg_{1/3}Nb_{2/3}O_3$ (PMN) are well-known model relaxor ferroelectrics [1]. The real part ε' of the permittivity of the PMN crystal at the frequency ν = 10 kHz exhibits a maximum at $T \sim 270$ K. In the absence of an external electric field, the PMN crystal in the range from approximately 1000 K to the liquid-helium temperature has macroscopic cubic symmetry $Pm3m$ [3]. At high temperatures, ions in the PMN crystal are displaced from equilibrium, highly symmetric positions of the perovskite cell [4]. Investigations into the optical properties of the PMN compound (and a number of other relaxors) in the vicinity of the smeared phase transition have revealed that the PMN structure involves regions with local polarization [5, 6], which also suggests ion displacements from the symmetric positions. In the PMN crystal, the electric field ($E > 2.2$ kV/cm^2) induces a structural transition to a phase with rhombohedral symmetry at $T_C \sim 210$ K [7, 8]. Thus, the PMN crystal is characterized by both the lattice instability associated with relaxor behavior over a wide range of temperatures and the instability at $T \sim 210$ K due to the phase transition suppressed in the absence of an external electric field.

The $PbMg_{1/3}Ta_{2/3}O_3$ (PMT) crystal is a relaxor ferroelectric whose properties are very similar to those of the PMN compound [1]. The real part ε' of the permittivity of the PMT crystal at the frequency ν = 10 kHz exhibits a maximum at $T \sim 190$ K. In this case, the permittivity ε' at the maximum for the PMT crystal at comparable frequencies is approximately half the permittivity at the maximum for the PMN crystal. The PMT crystal, like the PMN crystal, has symmetry $Pm3m$. However, the tendency toward ordering of ions in the B sublattice in the PMT crystal is more pronounced than that in the PMN crystal [9]. The fundamental difference between these two materials lies in the fact that no structural phase transition is induced in the PMT crystal in external electric fields [10, 11]. Consequently, the PMT crystal can be treated as a model material for use in studies of the relaxor behavior without additional structural instabilities.

The nontrivial ferroelectric state formed in relaxors at low temperatures has been investigated for a long time. One of the established facts is the nonergodicity of the ferroelectric phase. To date, there has been no agreement among the researchers regarding the mechanism of formation of this nonergodic state. With due regard for the intimate connection between relaxors of the $AB'_xB''_{1-x}O_3$ family and classical oxygen-containing perovskites, it could be expected that the soft mode is responsible for the ferroelectric state in relaxors. However, attempts to reveal the soft mode in PMN [12–14] (extensive literature on light scattering in the PMN materials is reviewed in [14]) and PMT [15] crystals

with the use of optical methods have not been successful.[1] It has been found that the light scattering spectra contain a broad quasi-elastic component, which strongly depends on the temperature [16, 17] and can be described by a Lorentzian function centered at zero frequency [17]. An analysis of the temperature dependence of the quasi-elastic component in the light scattering spectra of the PMN crystal has demonstrated that there is a correlation between the behavior of the width of this component and the dielectric anomalies observed in the PMN crystal [17]. Quasi-elastic scattering with similar properties has also been observed in relaxor ferroelectrics $PbSc_{1/2}Ta_{1/2}O_3$ [18] and $Na_{1/2}Bi_{1/2}O_3$ [19]. One of the main features of quasi-elastic light scattering in relaxors is an anomalously large width of this component. For example, the full width at half-maximum of the Lorentzian corresponding to quasi-elastic light scattering in the PMN crystal is as large as 25 cm^{-1} at T = 440 K [17], whereas the characteristic width for NBT relaxors is approximately equal to 150 cm^{-1} at T = 443 K [19]. The use of different models developed for describing the behavior of the central peaks observed upon structural phase transitions [20] makes describing the quasi-elastic scattering with the above properties impossible. The experimental data on light scattering in the PMN crystal can be compared with those for $BaTiO_3$ and $KNbO_3$ crystals. The latter crystals belong to a small class of ferroelectric compounds for which the full widths at half-maximum of the quasi-elastic component are as large as 10 cm^{-1} [21]; i.e., they are comparable to those observed for relaxors. An analysis of the lattice dynamics in the $BaTiO_3$ and $KNbO_3$ crystals in the framework of the eight-position model made it possible to assign quasi-elastic scattering to the relaxation mode and to elucidate the origin of the broad central peak. It turned out that this peak is governed by the ionic displacements in the *B* sublattice from ideal positions of the perovskite structure [21]. Attempts to apply the modified eight-position model [21] to the description of the temperature behavior of the parameters of the relaxation mode in the PMN crystal have led to nonphysical parameters [17].

All the foregoing demonstrates that the nature of quasi-elastic light scattering in relaxors remains unclear; i.e., the low-frequency lattice dynamics in the crystals under consideration is not understood. In this situation, complementary information can be obtained using inelastic neutron scattering, which is an efficient method for investigating the lattice dynamics in objects at different magnitudes of the wave vector **k** of the Brillouin zone.

In recent years, many works have been concerned with the inelastic neutron scattering investigation into the lattice dynamics of the PMN crystal [22–28]. At temperatures of the order of the Burns temperature, a narrow central peak whose width is determined by the spectrometer resolution has been revealed in the vicinity of the (0 0 2) Bragg position [22]. This result was unexpected, because the spectrometer resolution used in [22, 23] provided a means for determining the intrinsic excitation width of the order of 25 cm^{-1} (as can be judged from the data on light scattering in the PMN compound).

In our earlier work [29], we studied diffuse neutron scattering in the PMT crystal in the vicinity of the temperature corresponding to a maximum in the dielectric anomaly. It was revealed that the diffuse scattering component has a finite width of 0.65 meV (1 meV = 8.04 cm^{-1}) at room temperature. This value is slightly smaller than that expected for quasi-elastic scattering in the PMT crystal at room temperature [30]. In the present work, we thoroughly investigated the low-frequency range of the vibrational spectrum of the PMN and PMT crystals with the use of inelastic neutron scattering and attempted to solve the problem regarding the existence of the relaxation mode in relaxors.

EXPERIMENTAL TECHNIQUE AND DATA PROCESSING

The neutron scattering experiments were performed on a TASP three-axis spectrometer (ETHZ and Paul-Scherrer Institute, Villigen, Switzerland). Pyrolytic graphite with the (0 0 2) reflection was used as a monochromator and analyzer of neutron beams. The vertical focusing of the monochromator provided an increase in the signal intensity. A pyrolytic graphite filter served for suppressing higher harmonics in a scattered neutron beam. The spectrum intensity was normalized to the intensity measured by a monitor placed in a neutron beam incident on a sample. The measurements were carried out at the fixed wave vector k_F = 1.97 $Å^{-1}$ with the following collimation: neutron guide–80'–80'–80'. The spectrometer resolution measured with a reference cylindrical vanadium sample was equal to 0.4 meV (the full width at half-maximum of the Gaussian function) for the elastic line. A number of experiments were carried out with wave vector k_F = 1.64 $Å^{-1}$. In this case, the resolution with allowance made for the collimation (neutron guide–80'–80'–80') was equal to 0.2 meV.

High-quality PMN (volume, ~8 cm^3) and PMT (volume, ~0.05 cm^3) single crystals served as the samples. Both samples were mounted with aluminum holders in such a way as to ensure the possibility of measuring in the vicinity of the (*hh*0), (00*l*), and (*hhl*) Bragg positions. The temperature measurements of neutron scattering for the PMN crystal were performed in a closed-cycle refrigerator equipped with a small-sized heater. A standard closed-cycle refrigerator was used for the PMT crystal. The temperature was controlled accurate to within 1 K. Prior to measurements, both samples

[1] Note that the origin of the active modes in the Raman spectra of the PMN compound and related $AB'_xB''_{1-x}O_3$ relaxors is the subject of considerable discussion (see, for example, [14]).

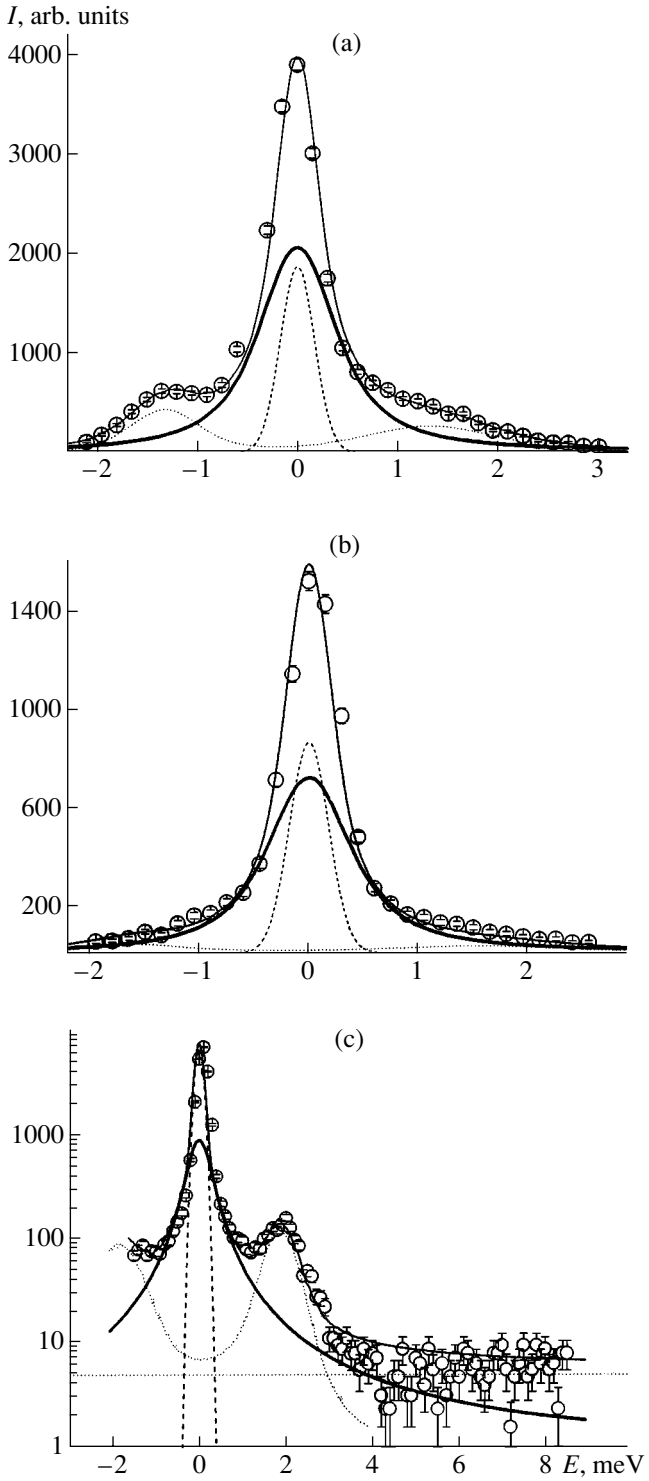

Fig. 1. Decomposition of the neutron scattering spectra of the PMN crystal: (a) T = 450 K, Q = (1 1 –0.05); (b) T = 450 K, Q = (0.05 0.05 1); and (c) T = 300 K, Q = (1 1 0.075). The thin solid line is the resultant spectrum, the thick solid line corresponds to the quasi-elastic scattering component, the dashed line indicates the narrow central peak, and the dotted line represents the damped-harmonic oscillator function [relationship (3)]. Details of the decomposition procedure are given in the text.

were annealed at a temperature of 450 K for 4 h. In this work, we will not analyze the measured temperature dependences and instead focus our attention on the description of the obtained data within a proposed model in which the possible existence of the relaxation mode in the studied crystals is taken into account. The unit cell parameters at room temperature are as follows: a = 4.04 Å for the PMN crystal and a = 4.03 Å for the PMT crystal. Therefore, for both crystals, we have 1 rlu = 1.55 Å^{-1}.

Figure 1a shows the inelastic neutron scattering spectrum of the PMN crystal at T = 450 K. The peaks corresponding to acoustic phonons are observed in the spectrum at energies of the order of 1.5 meV. At negative energies, the phonon peak is more intense and relatively narrow, which is explained by the focusing effect (see, for example, [31]). Attempts to approximate the experimental spectrum only with the use of the phonon components failed. It is clearly seen from Fig. 1a that the scattering spectrum contains an additional intense component at zero imparted energy. Consequently, the model describing the experimental spectrum should allow for the additional excitation at zero imparted energy. This is supported by the fact that an intense broad central peak is observed in the light scattering spectra at 450 K. The experimental data were processed under the assumption that the central peak in the spectrum consists of narrow (intense) and broad components. The narrow intense central peak was described by the Gaussian function

$$G = \sqrt{\frac{\ln 2}{\pi}}\frac{A}{0.5\Gamma}\exp\left[-\ln 2\left(\frac{\omega}{0.5\Gamma}\right)^2\right]. \quad (1)$$

Quasi-elastic scattering was approximated by the Lorentzian function

$$L = \frac{1}{\pi}\frac{A}{0.5\Gamma}\frac{1}{1+\left(\frac{\omega-\Omega_0}{0.5\Gamma}\right)^2}. \quad (2)$$

The phonon peaks were modeled by the damped-harmonic oscillator function

$$DHO = \frac{\omega}{1-\exp(-\omega/T)}\frac{1}{\pi}\frac{A}{0.5\Gamma}\frac{\Gamma^2\Omega_0^2}{(\omega^2-\Omega_0^2)^2+\omega^2\Gamma^2}. \quad (3)$$

The calculations included the four-dimensional convolution of the *DHO* and *L* functions with the spectrometer resolution function. The last function was calculated according to the Mfit program [32]. Since the measurements were carried out at $q < 0.1$ rlu, the linear approximation for the dispersion of *TA* phonons was used in the convolution with the resolution function. In all three functions, the parameters are as follows: Γ is the full width at half-maximum, Ω_0 is the position of the function, A is the area of the function, and ω is the frequency in energy units. The data were processed with allowance made for the incoherent scattering

background at zero imparted energy. This background approximated by the Gaussian function (1) is not shown in Fig. 1, because the peak intensity of the background is less than 100 counts. Note that an attempt to describe the experimental data according to the approach proposed in [33] without regard for the Gaussian function for the central peak also has not met with success.

RESULTS AND DISCUSSION

As can be seen from Fig. 1a, the experimental data are adequately described in the framework of the proposed model ($\chi^2 \sim 1.6$). The Lorentzian function approximating the quasi-elastic component (depicted by the thick solid line in Fig. 1) is characterized by the width $\Gamma = 0.75$ meV. This value is in good agreement with the width $\Gamma = 0.65$ meV obtained in our previous work [29] for the PMT crystal at room temperature. The intense narrow central peak (the dashed line in Fig. 1) has no intrinsic width; i.e., the energy width (0.4 meV) of this peak is completely determined by the spectrometer resolution. This is consistent with the narrow central peaks observed earlier for the PMN crystal [22, 23] and the related compound $Pb(Zn_{1/3}Nb_{2/3})O_3$ + 8% $PbTiO_3$ [34].

In recent works [22, 27, 28], as in the well-known works [35] ($BaTiO_3$) and [36] ($KNbO_3$), the phonon response of the PMN crystal was interpreted in terms of the coupled-oscillator function. According to [27], the response function in the form of coupled oscillators [35] can lead to a considerable intensity in the vicinity of zero imparted energy, because transverse optical phonons with an energy of the order of 10 meV are strongly damped. In order to elucidate the possible relation between transverse optical phonons and the relaxation mode in the PMN crystal, we investigated quasi-elastic neutron scattering in the vicinity of the (0 0 1) and (1 1 0) Bragg positions at $T = 450$ and 300 K, respectively. These experimental conditions make it possible to reduce the contribution of acoustic phonons to the neutron scattering spectrum and, thus, to reveal the relation between the relaxation mode and the phonon subsystem. On the one hand, as follows from the Bose–Einstein statistics [see Eq. (3)], a decrease in the temperature leads to a decrease in the intensity of the acoustic phonon mode. In this case, according to [17], changes in the intensity of the relaxation mode should not be very large. On the other hand, the intensity of the acoustic phonon mode is proportional to the structure factor of the Bragg peak. Therefore, the intensity of the acoustic phonon mode at the (0 0 1) Bragg position should be approximately ten times lower than that at the (1 1 0) Bragg position. Moreover, the intensity of neutron scattering by the phonons is proportional to the scattering vector squared. This results in an additional twofold decrease in the intensity. Consequently, when changing over from the (1 1 0) Bragg position to the (0 0 1) Bragg position, the intensity of the acoustic phonon mode should decrease by a factor of approximately 20.

The neutron scattering spectrum of the PMN crystal in the vicinity of the (0 0 1) Bragg position at a temperature of 450 K is depicted in Fig. 1b. It is clearly seen that, in the vicinity of the (0 0 1) Bragg position, the intensity of the transverse phonon mode at a relatively high temperature ($T = 450$ K) is negligible compared to the intensity of the quasi-elastic component. The experimental data processing with the aforementioned procedure leads to the width of the quasi-elastic component $\Gamma = 0.75$ meV [as is the case with the (1 1 0) Bragg position]. Note that $Q = (1\ 1\ -0.05)$ corresponds to $q = 0.078$ Å^{-1}, whereas $Q = (0.05\ 0.05\ 1)$ corresponds to $q = 0.11$ Å^{-1}. Consequently, the width of the quasi-elastic component only weakly depends on the wave vector, at least, at small values of q. The integrated intensity of the quasi-elastic component is approximately halved when changing over from $Q = (1\ 1\ -0.05)$ to $Q = (0.05\ 0.05\ 1)$. Now, it is hard to tell whether such a substantial decrease in the intensity is associated with the change in the wave vector q within the Brillouin zone, with the change in the structure factor of the relaxation mode when changing over from the (1 1 0) Bragg position to the (0 0 1) Bragg position, or with the contribution of both these factors.

The neutron scattering spectrum of the PMN crystal at the (1 1 0.075) Bragg position at a temperature of 300 K is shown in Fig. 1c (the horizontal dotted line indicates the background intensity). It should be noted that this spectrum was measured with a higher resolution (0.2 meV) in the energy range from –1.9 to 8.5 meV. As can be seen from Fig. 1c, the experimental spectrum is described very well in the framework of the proposed model. Note also that attempts to describe the neutron scattering spectrum within the coupled-oscillator model proposed in [35, 36] failed. The processing of the experimental data at $Q = (1\ 1\ 0.075)$ and a temperature of 300 K in terms of our model leads to the width of the quasi-elastic component $\Gamma = 0.46$ meV, which is somewhat less than that at $T = 450$ K. A decrease in the width of the relaxation mode with a decrease in the temperature indicates an increase in the relaxation time $\tau = 2/\Gamma$. This is consistent with the behavior of quasi-elastic scattering in the PMN [17], $BaTiO_3$, and $KNbO_3$ [21] crystals. Furthermore, when analyzing diffuse scattering in the PMT crystal [29], we found that the diffuse neutron scattering component characterized by a finite energy width at room temperature becomes elastic at $T = 40$ K to within the limits of experimental resolution. This also suggests an increase in the relaxation time with a decrease in the temperature.

A rather unexpected result was obtained in [29]: no narrow central peak was observed in the neutron scattering spectrum of the PMT crystal. With the aim of elucidating whether the narrow central peak is actually observed in the neutron scattering spectra of the PMT

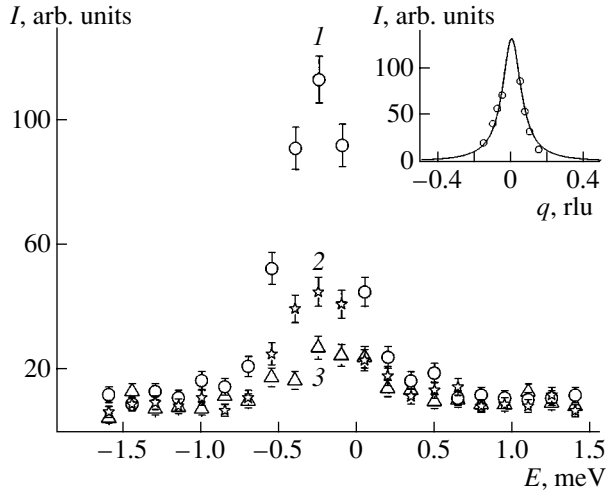

Fig. 2. Neutron scattering spectra of the PMT crystal at T = 300 K and Q = (*1*) (1 1 0.05), (*2*) (1 1 0.10), and (*3*) (1 1 0.15). The inset shows the dependence of the integrated intensity I of the resolution-limited central peak on the wave vector q. The approximation is performed by the Lorentzian function.

crystal and whether the narrow central peak is associated with the induced structural phase transition in the PMN crystal, we investigated the inelastic neutron scattering spectra of the PMT crystal at room temperature. The neutron scattering spectra of the PMT crystal at different wave vectors q are depicted in Fig. 2. As is clearly seen, the spectra consist of a narrow component (whose intensity considerably varies with an increase in the wave vector q) and a broad component (with nearly constant parameters). The narrow component is well described by the Gaussian function with a width of 0.4 meV. Therefore, the spectra of the PMT crystal involve a narrow central peak, as is the case with the PMN crystal. We failed to observe the narrow central peak in the neutron scattering spectra of the PMT crystal in our earlier work [29], because, directly at the (1 1 0) position, the narrow central peak overlaps with the intense Bragg reflection and, moreover, the quasi-elastic component has a high intensity. In view of the insufficient statistics, we cannot analyze the dependence of the broad quasi-elastic component on the wave vector q for the PMT crystal. The inset in Fig. 2 shows the dependence of the intensity of the central peak on the wave vector q for the PMT crystal. This dependence is well approximated by the Lorentzian function with the width Γ = 0.122 rlu, which corresponds to the correlation length ξ = 10.5 Å. It should be emphasized that, in [29], we investigated diffuse scattering in the PMT crystal preliminarily cooled to 20 K, whereas the sample studied in the present work was annealed before measurements. It is evident that the 2.5-fold difference between the values obtained in [29] and in the present work is associated with the nonergodicity of the PMT crystal.

It should be noted that the choice of the response function for describing the experimental data is a complicated problem which is not necessarily solved in a unique way (see, for example, [36, 37]). Without invoking the appropriate model concepts, we cannot argue that the Lorentzian function completely corresponds to the line shape of the relaxation mode. However, as was noted above, it became possible to adequately describe the experimental data with the use of only an additional excitation in the form of the Lorentzian centered at zero frequency. Analysis of the dependences of the parameters of the relaxation mode on the temperature and the wave vector q can help to elucidate its origin. At present, it seems likely that the relaxation mode can be associated with both the relaxation of ions displaced from equilibrium positions (by analogy with the model developed in [21]) and phonon density fluctuations [20]. In these cases, the relaxation mode can be described by the Lorentzian function and both processes are pronounced at high temperatures. We can also assume that the temperature dependence of the relaxation time exhibits a thermally activated behavior. It is of interest to ascertain whether there is a relation between the relaxation mode in the PMN crystal and the soft mode observed in [28], because both excitations are considered to be additional to the phonon spectrum predicted for crystals with a perovskite structure.

CONCLUSIONS

Thus, we investigated the vibrational spectra of the PMN and PMT relaxor ferroelectrics. The quasi-elastic component (relaxation mode) and the resolution-limited central peak were separated for both compounds with the use of different procedures of experimental data processing. The relaxation time of the quasi-elastic component increases with a decrease in the temperature. It was found that the correlation length associated with the elastic central peak in the neutron scattering spectrum of the PMT crystal strongly depends on the prehistory of the sample.

ACKNOWLEDGMENTS

This work was supported by the Russian Foundation for Basic Research (project no. 02-02-17678) and the Leading Scientific School (project no. NSh-15.14.2003.2).

The experiments were performed with the use of the SINQ neutron source (ETHZ & Paul-Scherrer Institute, Villigen, Switzerland).

REFERENCES

1. G. A. Smolenskiĭ, V. A. Bokov, V. A. Isupov, N. N. Kraĭnik, R. E. Pasynkov, A. I. Sokolov, and N. K. Yushin, *Physics of Ferroelectric Phenomena* (Nauka, Leningrad, 1985).

2. L. E. Cross, Ferroelectircs **76**, 241 (1987).
3. P. Bonneau, P. Garnier, G. Calvarin, *et al.*, J. Solid State Chem. **91**, 350 (1991).
4. S. B. Vakhrushev, S. Zhukov, G. Fetisov, *et al.*, J. Phys.: Condens. Matter **6**, 4021 (1994).
5. G. Burns and F. Facol, Solid State Commun. **48**, 853 (1983).
6. K. Fujishiro, Y. Uesu, Y. Yamada, *et al.*, J. Korean Phys. Soc. **32**, S964 (1998).
7. G. Schmidt, H. Arndt, J. Cieminski, *et al.*, Krist. Tech. **15**, 1415 (1980).
8. G. Calvarin, E. Husson, and Z. G. Ye, Ferroelectrics **165**, 349 (1995).
9. M. Akbas and P. Davies, Int. J. Inorg. Mater. **3**, 123 (2001).
10. Z. G. Lu, C. Flicoteaux, and G. Calvarin, Mater. Res. Bull. **31**, 445 (1996).
11. Z. G. Ye, Key Eng. Mater. **155–156**, 81 (1998).
12. G. Burns and B. A. Scott, Solid State Commun. **13**, 423 (1973).
13. A. A. Karamyan and N. N. Kraĭnik, Fiz. Tverd. Tela (Leningrad) **15**, 2534 (1973) [Sov. Phys. Solid State **15**, 1687 (1973)].
14. I. G. Siny, S. G. Lushnikov, R. S. Kariyar, and V. H. Schmidt, Ferroelectrics **226**, 191 (1999).
15. I. G. Siniĭ and T. A. Smirnova, Fiz. Tverd. Tela (Leningrad) **30**, 823 (1988) [Sov. Phys. Solid State **30**, 473 (1988)].
16. S. D. Prokhorova and S. G. Lushnikov, Ferroelectrics **90**, 190 (1989).
17. I. G. Siny, S. G. Lushnikov, R. S. Katiyar, and E. A. Rogacheva, Phys. Rev. B **56**, 7962 (1997).
18. S. G. Lushnikov, F. M. Jiang, and S. Kojima, Solid State Commun. **122**, 129 (2002).
19. I. G. Siny, E. Husson, J. M. Beny, *et al.*, Physica B (Amsterdam) **293**, 382 (2001).
20. A. D. Bruce and R. A. Cowley, Adv. Phys. **29**, 219 (1980).
21. J. P. Sokoloff, L. L. Chase, and D. Rytz, Phys. Rev. B **38**, 597 (1988).
22. A. A. Naberezhnov, S. B. Vakhrushev, B. Dorner, *et al.*, Eur. Phys. J. B **11**, 13 (1999).
23. Y. O. Chetverikov, A. A. Naberezhnov, S. B. Vakhrushev, *et al.*, Appl. Phys. A **74**, S989 (2002).
24. P. M. Gehring, S. Wakimoto, Z.-G. Ye, *et al.*, Phys. Rev. Lett. **87**, 277601 (2001).
25. K. Hirota, Z.-G. Ye, S. Wakimoto, *et al.*, Phys. Rev. B **65**, 104105 (2002).
26. S. Wakimoto, C. Stock, Z.-G. Ye, *et al.*, Phys. Rev. B **66**, 224102 (2002).
27. S. Wakimoto, C. Stock, R. J. Birgeneau, *et al.*, Phys. Rev. B **65**, 172105 (2002).
28. S. B. Vakhrushev and S. M. Shapiro, Phys. Rev. B **66**, 214101 (2002).
29. S. N. Gvasaliya, B. Roessli, and S. G. Lushnikov, Europhys. Lett. **63**, 303 (2003).
30. S. G. Lushnikov, G. A. Siniĭ, T. A. Smirnova, *et al.*, Kristallografiya **49** (2004) (in press).
31. M. J. Cooper and R. Nathans, Acta Crystallogr. **23**, 357 (1967).
32. D. A. Tennant and D. McMorrow, *Rescal v.5.1, a Matlab Tool for 3-Axis Neutron-Scattering-Resolution Calculation* (1996).
33. S. M. Shapiro, J. D. Axe, G. Shirane, and T. Riste, Phys. Rev. B **6**, 4332 (1972).
34. J. Hlinkal, S. Kamba, J. Petzelt, *et al.*, J. Phys.: Condens. Matter **15**, 4249 (2003).
35. J. Harada, J. Axe, and G. Shirane, Phys. Rev. B **4**, 155 (1971).
36. R. Currat, H. Buhay, C. H. Perry, *et al.*, Phys. Rev. B **40**, 10741 (1989).
37. B. D. Silverman, Phys. Rev. B **9**, 203 (1974).

Translated by O. Borovik-Romanova

Crystallography Reports, Vol. 49, No. 1, 2004, pp. 114–118. Translated from Kristallografiya, Vol. 49, No. 1, 2004, pp. 121–125.

LATTICE DYNAMICS AND PHASE TRANSITIONS

Dedicated to the 80th Birthday of L.A. Shuvalov

Soft Mode in $CsHSO_4$-Type Crystals

N. M. Plakida and V. S. Shakhmatov

Joint Institute for Nuclear Research, Dubna, Moscow oblast, 141980 Russia

e-mail: shakh@thsun1.jinr.ru

Received August 27, 2003

Abstract—A superionic phase transition is investigated in $CsHSO_4$-type crystals. It is demonstrated that the soft mode of this transition is associated with both an orientational ordering of SO_4 tetrahedra and an ordering of hydrogen ions in the crystal lattice. The phase transition is accompanied by distortions of SO_4 tetrahedra and small rotations of the tetrahedra as a whole. The specific orientational basis of the superionic phase transition is determined. The experimental verification of the theoretical predictions is proposed. © *2004 MAIK "Nauka/Interperiodica".*

INTRODUCTION

Crystals of the *Me*H*A*O_4 type (*Me* = Cs, Rb, NH_4; *A* = S, Se) and their deuterated analogues at temperatures $T \geq T_C$ possess high electrical conductivity due to translational motion of hydrogen (deuterium) ions [1]. The phase transition temperature T_C for different compounds falls in the range from ~400 to ~450 K. The conductivity at the phase transition point abruptly changes by three or four orders of magnitude and reaches a value of $\sim 10^{-2}\ \Omega^{-1}\ cm^{-1}$ in the high-temperature phase. In the $CsHSO_4$ compound, the high electrical conductivity is observed in superionic phases **I**, **VI**, and **VII** (see Fig. 1).

In order to explain the high conductivity provided by hydrogen ions, it is necessary to investigate the hydrogen subsystem. Important information on the physical properties of the hydrogen subsystem can be obtained by scattering of slow neutrons [9]. In [10], the hydrogen subsystem of $CsHSO_4$ crystals was analyzed in the framework of the Slater model and the symmetry approach was applied to the description of the superionic phase transition. In our earlier works [11, 12], we developed the phenomenological theory of phase transitions in the $CsHSO_4$ compound. A model of hydrogen bonds in all high-pressure phases of this material was proposed on the basis of the symmetry analysis in [13].

However, the experimental data on the conductivity [14], nuclear magnetic resonance [15], neutron scattering [16], and mechanical properties of the superionic phase [17] indicate that the rotation of SO_4 tetrahedra through large angles should also be taken into account. In order to correctly describe the superionic phase transition in the $CsHSO_4$ crystal, it is necessary to analyze not only the hydrogen subsystem but also the subsystem of SO_4 tetrahedra and the possible interactions between these subsystems. This raises the question as to the physical nature of the soft mode of the superionic phase transition in the $CsHSO_4$ crystal. It is clear that the soft mode should be associated with the changes observed in the hydrogen subsystem [12, 13], the subsystem of SO_4 tetrahedra (rotations through large angles) [16], and the phonon subsystem. The changes in the phonon subsystem are considered to mean small atomic displacements, librations of the SO_4 tetrahedra

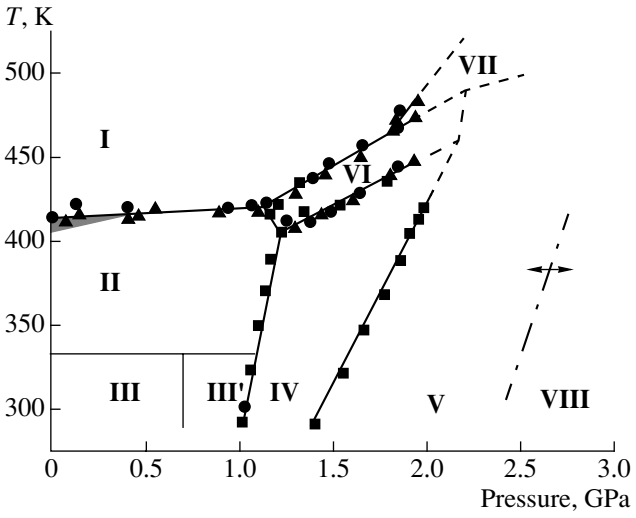

Fig. 1. Phase diagram of the $CsHSO_4$ crystal in the pressure–temperature coordinates. Roman numerals **I**, …, **VIII** denote different phases. Solid lines show the experimentally determined phase boundaries [2–4]. Dashed lines represent the possible extrapolation of the phase boundaries. The dot-dashed line indicates the boundary of possible new phase **VIII** [5]. The hatched region corresponds to low pressures and temperatures close to $T \sim 410$ K at which a new superionic phase can be formed in $CsHSO_4$ [6–8].

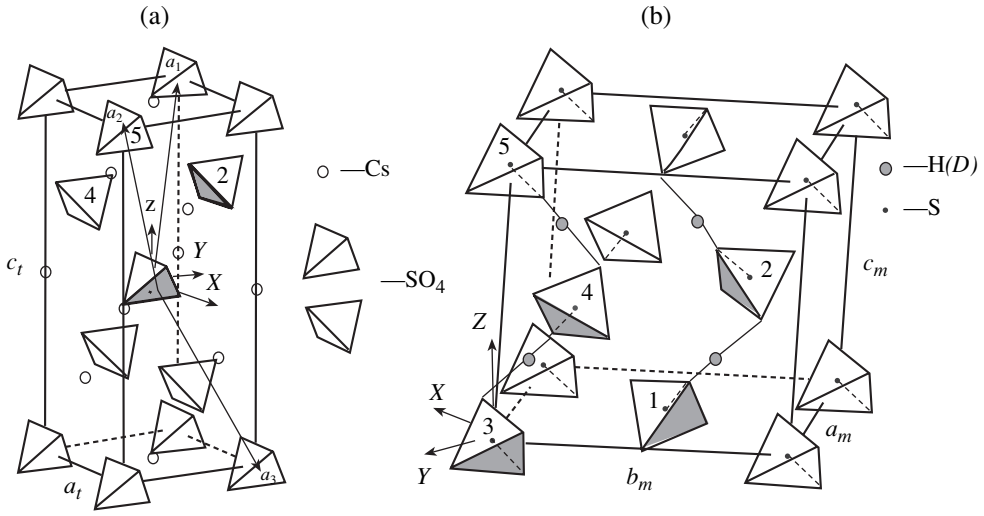

Fig. 2. Crystal structure of the $CsHSO_4$ compound [16]. (a) Phase **I** [symmetry $I4_1/amd(D_{4h}^{19})$, a_t = 5.74147(9) Å, c_t = 14.31513(3) Å]. Tetrahedra SO_4 are shown in the most symmetric position. The primitive cell constructed along the fundamental translation vectors $\mathbf{a}_i$ contains two $CsHSO_4$ formula units. Two translationally nonequivalent SO_4 tetrahedra are marked. (b) Phase **II** [symmetry $P2_1/c(C_{2h}^5)$, a_m = 7.78013(9) Å, b_m = 8.13916(2) Å, c_m = 7.72187(9) Å, β = 110.8720(4)°]. The primitive cell contains four $CsHSO_4$ formula units. Nonequivalent SO_4 tetrahedra are marked and denoted by numerals 1–4. Dashed lines indicate the long S–O bonds. Cesium atoms are not shown.

as a whole [18], and distortions of SO_4 tetrahedra upon superionic phase transitions.

In this work, the soft mode of the superionic phase transition **I** ⟶ **II** (with the symmetry change $I4_1/amd \longrightarrow P2_1/c$) in the $CsHSO_4$ crystal was investigated using the symmetry analysis.

SOFT MODE OF THE SUPERIONIC PHASE TRANSITION $I4_1/amd \longrightarrow P2_1/c$

The crystal structure of $CsHSO_4$ in phases **I** and **II** is shown in Fig. 2. (Note that the structures of $CsHSO_4$ and $CsDSO_4$ crystals in phases **I** and **II** are identical.) The structural symmetry was determined for superionic phase **I** in [16, 19, 20] and for phase **II** in [16, 18, 19, 21, 22].

The phase transition $I4_1/amd \longrightarrow P2_1/c$ can be described by the expansion of the free energy in the following form [11]:

$$F_1 = F_\varphi + F_{\varphi;\psi;\theta} + F_{\psi;\theta}, \tag{1}$$

where

$$F_\varphi = \frac{1}{2}r(\varphi_1^2 + \varphi_2^2 + \varphi_3^2 + \varphi_4^2) + \frac{1}{4}u_1(\varphi_1^2 + \varphi_2^2 + \varphi_3^2 + \varphi_4^2)^2 + \frac{1}{6}u_2(\varphi_1^2 + \varphi_2^2 + \varphi_3^2 + \varphi_4^2)^3 + \frac{1}{4}\nu_1(\varphi_1^2\varphi_2^2 + \varphi_3^2\varphi_4^2) + \frac{1}{4}\nu_2(\varphi_1^2\varphi_3^2 + \varphi_2^2\varphi_4^2) + \frac{1}{4}\nu_3(\varphi_1^2\varphi_4^2 + \varphi_2^2\varphi_3^2) + \ldots,$$

$$F_{\varphi;\psi;\theta} = \alpha(\varphi_1^2 + \varphi_2^2 - \varphi_3^2 - \varphi_4^2)\psi + \beta(\varphi_1\varphi_2\theta_1 + \varphi_3\varphi_4\theta_2),$$

$$F_{\psi;\theta} = \frac{1}{2}r_1\psi^2 + \frac{1}{2}r_2(\theta_1^2 + \theta_2^2). \tag{2}$$

Here, $r = a(T - T_C)$; a, u_1, u_2, ν_1, ν_2, ν_3, α, β, r_1, and r_2 are the temperature-independent constants; $\{\varphi_i\}$ (i = 1–4) is the four-component order parameter; and ψ and $\{\theta_i\}$ (i = 1, 2) are the secondary order parameters. The phase transition from phase **I** to one of the four single-domain states of phase **II** is described by the following nonzero order parameter components: $\varphi_1 = \varphi_2 \neq 0$, $\psi \neq 0$, and $\theta_1 \neq 0$. The nonzero order parameter components $\varphi_3 = \varphi_4 \neq 0$, $\psi \neq 0$, and $\theta_2 \neq 0$ describe the phase transition to another domain. The monoclinic axes of these two domains lie in the (001) plane (see Fig. 2a) and are perpendicular to each other.

The order parameters $\{\varphi_i\}$ (i = 1–4), ψ, and $\{\theta_i\}$ (i = 1, 2) describe the orientational ordering of SO_4 tetrahedra. The orientational states of the SO_4 tetrahedron with different symmetries are shown in Fig. 3. Four orientational bases with different symmetries are possible in space group $I4_1/amd$. These are three special bases with

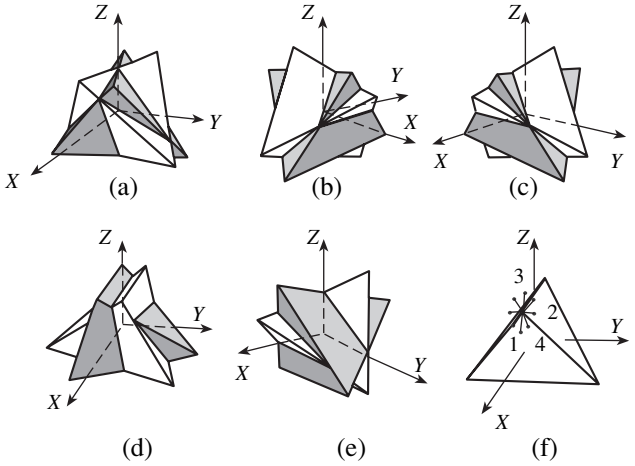

Fig. 3. Orientational states of an SO_4 tetrahedron in phase **I**. (a) Twofold orientational basis. The orientational states correspond to rotations of the SO_4 tetrahedron about the *Z* axis. (b, c) The first fourfold orientational basis. Different orientational states of the SO_4 tetrahedron are obtained by rotations of the tetrahedron about the $[\bar{1}10]$ and [110] crystallographic directions. (d, e) The second fourfold orientational basis. Different orientational states of the SO_4 tetrahedron are obtained by rotations of the tetrahedron about the *X* and *Y* axes. (f) Position of one vertex of the SO_4 tetrahedron in the orientational states of two fourfold bases. Numerals denote four orientational states of the first fourfold basis.

internal symmetry and one common basis. The special bases are represented by one twofold orientational basis (Fig. 3a) and two fourfold orientational bases (Figs. 3b–3e). The orientational state of the common eightfold basis can be obtained from the orientational state of any special basis (Fig. 3c) by additional rotation through an arbitrary (small) angle about the axis orthogonal to the symmetry axes of the special basis.

The primitive cell of phase **I** (Fig. 2a) contains two nonequivalent SO_4 tetrahedra. Figure 3 presents the orientational states for only one SO_4 tetrahedron. Note that all the orientational states shown in this figure correspond to an angle of $\pi/12$. The real angle of rotation of the SO_4 tetrahedron in phase **II** is determined from the experimental data (see below).

All the orientational bases can be formally used for describing the symmetry change $I4_1/amd \longrightarrow P2_1/c$ upon the phase transition: phase **I** $\longrightarrow$ phase **II**. However, the sequence of phase transitions

$$I4_1/amd(\text{phase } \mathbf{I}) \longrightarrow Pnma(\text{phase } \mathbf{VI}) \Rightarrow \begin{cases} \longrightarrow P2_1/c \\ \longrightarrow P2_1/m \end{cases} \quad (\text{phases } \mathbf{III}, \mathbf{IV}) \tag{3}$$

cannot be represented in the twofold basis due to its internal symmetry (for more details, see [5, 23, 24]). The proper choice of the orientational basis can be made from experimental data. It can be seen from Fig. 2b that the orientations of tetrahedra 1 and 3 correspond to orientations 1 and 3 in Fig. 3f; in this case, the angle of rotation is approximately equal to 13°. The orientations of tetrahedra 2 and 4 in Fig. 2b correspond to orientations 2 and 4 in Fig. 3f with additional rotation through an angle of $\pi/2$ due to the translational nonequivalence of two tetrahedra in phase **I** (see Fig. 2a). In addition to the rotations through an angle of ~13° about the $[\bar{1}10]$ and [110] crystallographic directions, the precise orientation of tetrahedra 1–4 in Fig. 2b requires an additional rotation of these tetrahedra through an angle of ~6° about the *Z* axis. As was noted above, this additional rotation of the tetrahedron leads to the fact that the fourfold orientational basis (Figs. 3b, 3c) transforms into a common eightfold basis.

Thus, the analysis of the experimental data [16] demonstrates that the orientational ordering of SO_4 tetrahedra in phase **II** (Fig. 2b) is associated with the common eightfold basis. Specific numerical values of the angles of rotation (~13° about the $[\bar{1}10]$ and [110] crystallographic directions and ~6° about the *Z* axis) indicate that the dominant contribution to the orientation of SO_4 tetrahedra is made by the states of the fourfold orientational basis, which is shown in Figs. 3b and 3c.

The order parameters describing the ordering of hydrogen ions in the crystal lattice are identical in symmetry to the order parameters representing the orientational ordering of SO_4 tetrahedra. In our previous work [12], we proposed a scheme of hydrogen bonds in phase **II** (Fig. 2b). In phase **II**, there are two nonequivalent hydrogen bond chains related to each other by a monoclinic twofold screw axis. Both chains of hydrogen bonds (tetrahedra 1–5) are aligned along the c_m crystallographic axis. Note that tetrahedra 3–5 in Fig. 2a correspond to tetrahedra 3–5 in Fig. 2b and tetrahedra 2 are translationally equivalent.

The order parameters describing the ordering of hydrogen ions in the crystal lattice are denoted as follows: $\{\varphi_i'\}$ (i = 1–4), $\{\theta_i'\}$ (i = 1, 2), and ψ'. Both types of ordering can be represented by the expansion of the free energy in the following form:

$$F_2 = F_1 + F_{\varphi\varphi'} + F_{\varphi;\,\psi'\theta'} + F_{\varphi';\,\psi';\,\theta'}, \tag{4}$$

where

$$\begin{aligned} F_{\varphi\varphi'} &= \gamma(\varphi_1\varphi_1' + \varphi_2\varphi_2' + \varphi_3\varphi_3' + \varphi_4\varphi_4'), \\ F_{\varphi;\,\psi'\theta'} &= \alpha_1(\varphi_1^2 + \varphi_2^2 - \varphi_3^2 - \varphi_4^2)\psi' \\ &\quad + \beta_1(\varphi_1\varphi_2\theta_1' + \varphi_3\varphi_4\theta_2'), \\ F_{\varphi';\,\psi';\,\theta'} &= \frac{1}{2}r_3\varphi'^2 + \frac{1}{2}r_4\psi'^2 + \frac{1}{2}r_5(\theta_1'^2 + \theta_2'^2). \end{aligned} \tag{5}$$

Then, the terms with the order parameters describing the changes in the phonon subsystem (in particular,

rotations of the tetrahedra as a whole [18]) are added to relationship (4). As a result, we obtain

$$F_3 = F_2 + F_{\varphi\varphi''} + F_{\varphi;\,\psi''\theta''} + F_{\varphi'';\,\psi'';\,\theta''}, \quad (6)$$

where

$$\begin{aligned} F_{\varphi\varphi''} &= \gamma_1(\varphi_1\varphi_1'' + \varphi_2\varphi_2'' + \varphi_3\varphi_3'' + \varphi_4\varphi_4''), \\ F_{\varphi;\,\psi''\theta''} &= \alpha_2(\varphi_1^2 + \varphi_2^2 - \varphi_3^2 - \varphi_4^2)\psi'' \\ &\quad + \beta_2(\varphi_1\varphi_2\theta_1'' + \varphi_3\varphi_4\theta_2''), \\ F_{\varphi'';\,\psi'';\,\theta''} &= \frac{1}{2}r_6\varphi''^2 + \frac{1}{2}r_7\psi''^2 + \frac{1}{2}r_8(\theta_1''^2 + \theta_2''^2). \end{aligned} \quad (7)$$

All the phenomenological constants in formulas (5) and (7) do not depend on the temperature.

Expression (6) describes all changes in the $CsHSO_4$ crystal upon the superionic phase transition $I4_1/amd \longrightarrow P2_1/c$.

RESULTS, DISCUSSION, AND CONCLUSIONS

Let us summarize the results obtained. The superionic phase transition (phase **I** ⟶ phase **II**) in the $CsHSO_4$ crystal results in the symmetry change $I4_1/amd(D_{4h}^{19}) \longrightarrow P2_1/c(C_{2h}^5)$. This phase transition can be described by the expansion of the free energy in the form of relationships (1) and (2). The phase transition to a single-domain state can be represented by the following nonzero order parameter components: $\varphi_1 = \varphi_2 \neq 0$, $\psi \neq 0$, and $\theta_1 \neq 0$. Consequently, all the changes associated with the phase transition $I4_1/amd \longrightarrow P2_1/c$ should also be described by these order parameters. In the present work, these order parameters are used to describe the orientational ordering of SO_4 tetrahedra in phase **II** (Fig. 2b). In [12, 13], the ordering of hydrogen ions in the crystal lattice was described by analogous order parameters. In this work, these are primed order parameters. The changes observed in the phonon subsystem (small rotations of SO_4 tetrahedra and their distortions) are represented by the order parameters with two primes. Therefore, the use of expansion (6) of the free energy makes it possible to describe the fundamental changes in the $CsHSO_4$ crystal upon the superionic phase transition $I4_1/amd \longrightarrow P2_1/c$.

The symmetry analysis revealed that the orientational ordering of SO_4 tetrahedra, ordering of hydrogen ions in the crystal lattice, and small rotations of SO_4 tetrahedra [18] can equally play the role of a soft mode in the $CsHSO_4$ crystal. From analyzing the neutron diffraction data [16, 25], we can infer that the softness arises in the subsystem of SO_4 tetrahedra. The soft mode is taken to mean the fundamental changes in the crystal due to the phase transition. Therefore, making allowance for the linear interaction between orderings, the soft mode of the superionic phase transition should be associated with both the orientational ordering of SO_4 tetrahedra and the ordering of hydrogen ions in the crystal lattice, especially as the two subsystems are responsible for the ionic conductivity, which is the basic parameter of the superionic phase transition. Note that the phase transition $I4_1/amd \longrightarrow P2_1/c$ in the $CsHSO_4$ crystal is accompanied by substantial distortions of the crystal lattice, and the scheme of hydrogen bonds in phase **II** should be constructed with due regard for the strains e_{xz} and e_{yz} (interactions of the order parameter with the strain tensor components [11]).

The above analysis of the experimental data obtained in [16] (see Fig. 2b) demonstrated that the orientational ordering of SO_4 tetrahedra in phase **II** should be described in the eightfold orientational basis. The orientation of tetrahedron 3 in Fig. 2b can be obtained first by rotation of this tetrahedron through an angle of ~13° about the $[\bar{1}10]$ crystallographic direction (this is orientational state 3 in Fig. 3f) and then by clockwise rotation through an angle of ~6° about the *Z* axis. (The orientations of other nonequivalent tetrahedra, namely, 1, 2, and 4 in Fig. 2b, can be obtained from the orientation of tetrahedron 3 with the use of the rotation about a twofold axis, inversion, and reflection in the plane, respectively.) By assuming that the rotations of SO_4 tetrahedra through an angle of ~6° about the *Z* axis can be assigned to the phonon degrees of freedom and that these rotations are described by the order parameters with two primes [see relationship (6)], we obtain the fourfold orientational basis (Figs. 3b, 3c), which was found in [16]. However, this inference provokes the following objections. First, in the $CsHSeO_4$ compound [26], which also undergoes a superionic phase transition $I4_1/amd \longrightarrow P2_1/c$ [19], the change in the entropy upon the transition was determined to be $\Delta S = 16.1\ \mathrm{J\ mol^{-1}\ K^{-1}}$. This change in the entropy corresponds to an eightfold basis. Second, the angle of rotation of SO_4 tetrahedra in the fourfold orientational basis [16] is approximately equal to 22° rather than to ~13°, as follows from examination of the crystal structure of phase **II**. Therefore, despite the fact that the fourfold orientational basis exists in the $CsHSO_4$ crystal and that the change in the entropy upon the superionic phase transition is equal to $R \times 1.32$ (where *R* is the gas constant), the experimental data obtained in [16] for phase **I** should be revised. Note that a new superionic phase can be formed in the $CsHSO_4$ compound (see the hatched region in Fig. 1). Since the phase transition between superionic phases results in a change in the number of orientational states by a factor of at least two, the total change in the entropy upon two transitions (phase **I** ⟶ intermediate superionic phase ⟶ phase **II**) is as follows: $\Delta S = 16.1\ \mathrm{J\ mol^{-1}\ K^{-1}} \sim R\ln 2 + R \times 1.32$. This also indicates the eightfold orientational basis in the $CsHSO_4$ crystal. We can assume that, as was noted above, the diffraction data obtained in [16] for phase **I** should be fitted using the eightfold orientational basis

with rotations of tetrahedra through angles of ~13° and ~6°. Moreover, it can also be assumed that, in addition to the above orientational basis, superionic phase **I** at temperatures far from the phase transition point T_C can be characterized by other orientational bases, for example, the orientational basis relating the so-called 8*e* positions [16]. In this case, the phase transition in the $CsHSO_4$ crystal proceeds through the mechanism proposed for describing phase transitions in fullerenes [27].

In conclusion, we should note that the complete understanding of the physical phenomena associated with the superionic phase transition under consideration calls for further experimental investigation. The symmetry of the high-pressure phases (theoretically predicted in [5, 23]) was experimentally verified only for phases **IV** and **V** [24] (see Fig. 1). The schemes of hydrogen bonds in all high-pressure phases were theoretically analyzed in [13]. Unfortunately, experimental data on the crystal structure of $CsHSO_4$ in high-pressure phases are not available in the literature.

ACKNOWLEDGMENTS

This work was supported in part by the Russian Foundation for Basic Research (project no. 04-02-16817) and the State Program of Support for Leading Scientific Schools of the Russian Federation.

REFERENCES

1. A. I. Baranov, L. A. Shuvalov, and N. M. Shchagina, Pis'ma Zh. Éksp. Teor. Fiz. **36**, 381 (1982) [JETP Lett. **36**, 459 (1982)].
2. E. G. Ponyatovskiĭ, V. I. Rashchupkin, V. V. Sinitsyn, *et al.*, Pis'ma Zh. Éksp. Teor. Fiz. **41**, 114 (1985) [JETP Lett. **41**, 139 (1985)].
3. V. V. Sinitsyn, E. G. Ponyatovskiĭ, A. I. Baranov, *et al.*, Zh. Éksp. Teor. Fiz. **100**, 693 (1991) [Sov. Phys. JETP **73**, 386 (1991)].
4. A. Lunden, B. Baranowski, and M. Friesel, Ferroelectrics **167**, 33 (1995).
5. V. S. Shakhmatov, High Press. Res. **14**, 67 (1995).
6. A. I. Baranov, V. V. Sinitsyn, E. G. Ponyatovskiĭ, and L. A. Shuvalov, Pis'ma Zh. Éksp. Teor. Fiz. **44**, 186 (1986) [JETP Lett. **44**, 237 (1986)].
7. L. F. Kirpichnikova, M. Polomska, J. Wolak, and B. Hilczer, Pis'ma Zh. Éksp. Teor. Fiz. **63**, 871 (1996) [JETP Lett. **63**, 912 (1996)].
8. V. Sh. Shekhtman and R. A. Dilanyan, Ferroelectrics **167**, 115 (1995).
9. A. V. Belushkin, I. Natkaniec, N. M. Plakida, *et al.*, J. Phys. C: Solid State Phys. **20**, 671 (1987).
10. N. M. Plakida, Pis'ma Zh. Éksp. Teor. Fiz. **41**, 95 (1985) [JETP Lett. **41**, 114 (1985)].
11. N. M. Plakida and V. S. Shakhmatov, Izv. Akad. Nauk SSSR, Ser. Fiz. **51**, 2107 (1987).
12. N. M. Plakida and V. S. Shakhmatov, Ferroelectrics **167**, 73 (1995).
13. A. I. Beskrovnyi and V. S. Shakhmatov, Kristallografiya **47**, 101 (2002) [Crystallogr. Rep. **47**, 94 (2002)].
14. A. I. Baranov, Izv. Akad. Nauk SSSR, Ser. Fiz. **51**, 2146 (1987).
15. D. Arcon, R. Blinc, J. Dolinsek, and L. A. Shuvalov, Phys. Rev. B **55**, 8961 (1997).
16. A. V. Belushkin, W. I. F. David, R. M. Ibberson, and L. A. Shuvalov, Acta Crystallogr., Sect. B: Struct. Sci. **47**, 167 (1991).
17. L. F. Kirpichnikova, A. A. Urusovskaya, and V. I. Mozgovoĭ, Pis'ma Zh. Éksp. Teor. Fiz. **62**, 616 (1995) [JETP Lett. **62**, 638 (1995)].
18. Z. Jirak, M. Dlouha, S. Vratislav, *et al.*, Phys. Status Solidi B **100**, 117 (1987).
19. A. M. Balagurov, A. V. Belushkin, A. I. Beskrovnyĭ, *et al.*, Kratk. Soobshch. Ob. Inst. Yad. Issled. (Dubna), No. 13 (1985).
20. B. V. Merinov, A. I. Baranov, and L. A. Shuvalov, Kristallografiya **32** (1), 86 (1987) [Sov. Phys. Crystallogr. **32**, 47 (1987)].
21. S. Yokota, J. Phys. Soc. Jpn. **51**, 1884 (1982).
22. B. V. Merinov, A. I. Baranov, B. A. Maksimov, and L. A. Shuvalov, Kristallografiya **31**, 450 (1986) [Sov. Phys. Crystallogr. **31**, 264 (1986)].
23. V. S. Shakhmatov, Kristallografiya **38** (6), 176 (1993) [Crystallogr. Rep. **38**, 805 (1993)].
24. A. V. Belushkin, M. A. Adams, S. Hull, *et al.*, Physica B (Amsterdam) **213/214**, 1034 (1995).
25. A. V. Belushkin, C. J. Carlile, and L. A. Shuvalov, Ferroelectrics **167**, 21 (1995).
26. S. Yokota, N. Takanohashi, T. Osaka, and Y. Makita, J. Phys. Soc. Jpn. **51**, 199 (1982).
27. V. L. Aksenov, Yu. A. Osip'yan, and V. S. Shakhmatov, Zh. Éksp. Teor. Fiz. **113**, 1081 (1998) [JETP **86**, 591 (1998)].

Translated by O. Borovik-Romanova

Crystallography Reports, Vol. 49, No. 1, 2004, pp. 119–122. Translated from Kristallografiya, Vol. 49, No. 1, 2004, pp. 126–130.

LATTICE DYNAMICS AND PHASE TRANSITIONS

Dedicated to the 80th Birthday of L.A. Shuvalov

Central Peak in the Raman Spectra of $LiNbO_3$ Crystals Far below the Phase Transition

V. K. Malinovskiĭ*, A. M. Pugachev*, H. V. Surovtsev*, and A. P. Shebanin**

** Institute of Automatics and Electrometry, Siberian Division, Russian Academy of Sciences, Novosibirsk, 630090 Russia*

e-mail:mvk@iae.nsk.su

*** Joint Institute of Geology and Geophysics, Siberian Division, Russian Academy of Sciences, Novosibirsk, 630090 Russia*

Received June 19, 2003

Abstract—A central peak has been revealed in the Raman spectrum of ferroelectric crystals of lithium niobate $LiNbO_3$ in the temperature range 80–300 K. It is shown that the extrapolation of the central peak, which manifests itself in inelastic-light-scattering spectra near the ferroelectric transition (T_c ~ 1400 K), cannot account for the existence of the central peak so far from the phase transition. © *2004 MAIK "Nauka/Interperiodica".*

INTRODUCTION

The issues related to the central peak in the Raman spectra of ferroelectrics near the phase-transition point (phenomenology, origin, mechanisms of manifestation in spectra, relationship with the theoretical description of phase transitions) constitute one of the most interesting problems of solid-state physics [1]. The implied relationship between the central peak and the phase transition suggests that the central peak in experimental spectra should be most pronounced in the temperature range near the phase-transition temperature. For example, in the case of ferroelectric crystals of lithium niobate $LiNbO_3$, the central peak can be clearly seen at temperatures above 850 K (T_c ~ 1400 K) [2–4] and the intensity of the peak observed in the Raman spectrum decreases with decreasing temperature. A relatively short time ago, it was shown in [5] that the central peak can be detected in the spectra of $LiNbO_3$ at temperatures as high as ~470 K. The experiments carried out in [5] demonstrated that the central peak is well pronounced in the scattering geometry with allowed phonons of symmetry A_1 and is absent in the geometry corresponding to E phonons.

It is shown in this study that the central peak in the Raman spectrum of $LiNbO_3$ is retained even at very low temperatures (80 and 300 K) as compared with the ferroelectric-transition temperature. However, the experimentally observed features of the low-temperature central peak suggest a phenomenology different from that of the central peak near the phase-transition temperature.

EXPERIMENTAL

We measured the Raman spectra of optically polished crystals cut in the form of a parallelepiped with edges parallel to the crystallographic axes. Nominally pure congruent crystals [6] and $LiNbO_3$ crystals with a composition close to stoichiometric were studied.

The Raman spectra were measured on a U1000 double-grating spectrometer with excitation at the 458- and 514-nm lines of an argon laser and the 647-nm line of a krypton laser. A DFS-24 spectrometer was also used to measure the spectra with excitation at the 1064-nm line of a neodymium laser. The experiments did not show any noticeable effect of the excitation wavelength on the spectra obtained. The effect of the excitation wavelength on the low-frequency spectrum of lithium niobate was considered in more detail in [7]. Figure 2 in [7] is rather representative; it should only be noted that the spectral range investigated here was extended to lower frequencies up to ~2 cm^{-1}. Hereinafter, the presented results correspond to an excitation wavelength of 514 nm and a power of 150 mW. The right-angle scattering geometry was used. When measuring the low-frequency part of the spectrum (<50 cm^{-1}), we used slits with a spectral width of 0.5 cm^{-1}. The contribution of the elastic rescattering of light and the Mandelshtam–Brillouin lines was completely suppressed at a frequency of ~2 cm^{-1}. The suppression was controlled by measuring the dependence of the shape of the low-frequency spectrum on the spectral width of the slits [8].

In the scattering $x(zz)y$ geometry, the Raman spectra of congruent $LiNbO_3$ crystals were measured at room and liquid-nitrogen temperatures. In other cases, the

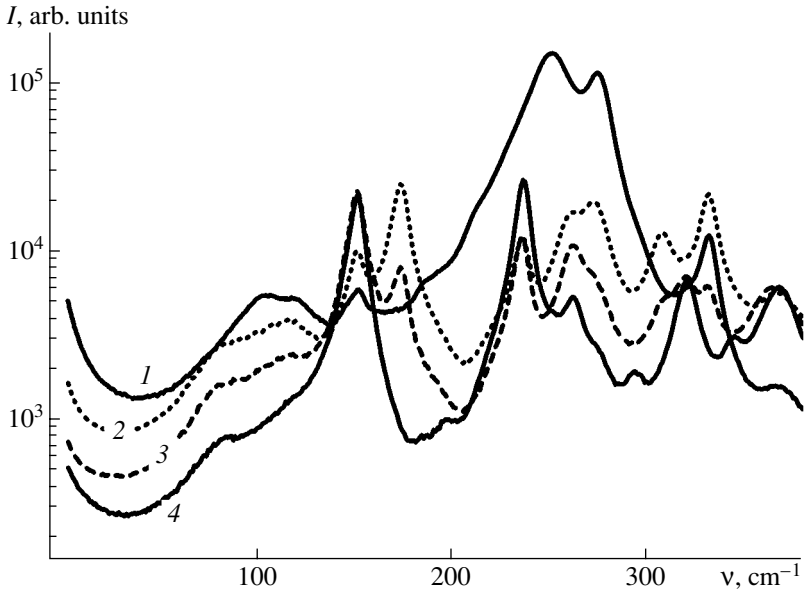

Fig. 1. Raman spectra of congruent $LiNbO_3$ at T = 300 K for four polarization geometries: (*1*) *x*(*zz*)*y*, (*2*) *z*(*xx*)*y*, (*3*) *z*(*yx*)*y*, and (*4*) *x*(*zx*)*y*.

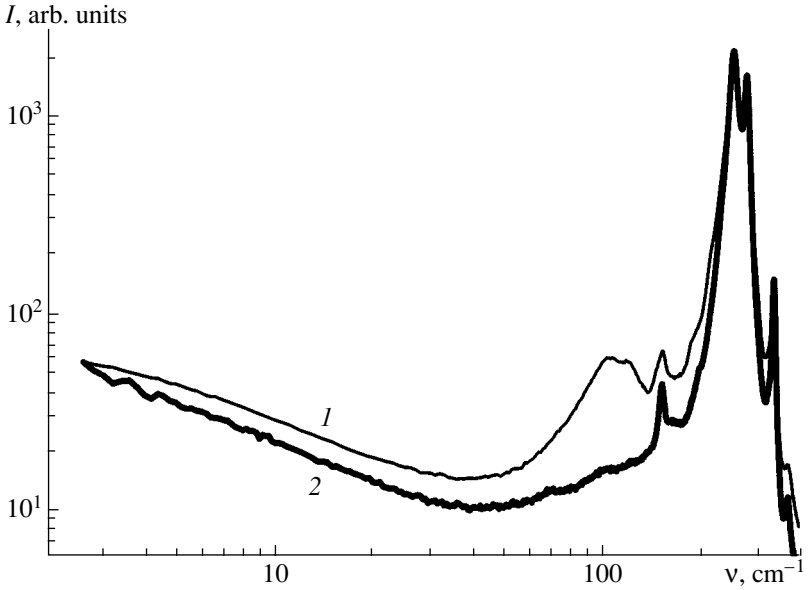

Fig. 2. Raman spectra of (*1*) congruent and (*2*) stoichiometric $LiNbO_3$ crystals at T = 300 K in the *x*(*zz*)*y* geometry.

measurements were performed only at room temperature.

RESULTS AND DISCUSSION

The Raman spectra of congruent $LiNbO_3$ crystals, recorded in different polarization geometries, are shown in Fig. 1. Logarithmic scale is used for the intensity to visualize weak spectral features. The central peak is pronounced in the low-frequency part of the spectrum, being the main spectral feature in the frequency range <40–50 cm^{-1}. It can be seen from Fig. 1 that, in contrast to the results of [5], the central peak is present in the spectra obtained in all the polarization geometries: in both those with allowed A_1 phonons and those with allowed phonons of E symmetry. It is worth noting that the intensity of the central peak in the Raman spectra measured in different geometries correlates with the integrated intensity of Raman lines, whereas the Raman signal in the *x*(*zz*)*y* geometry

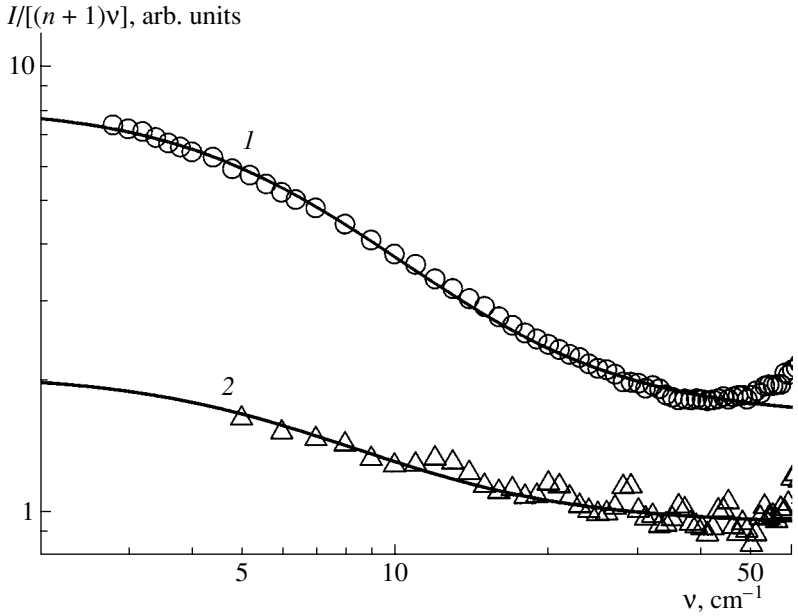

Fig. 3. Bose normalized Raman spectra $I/[\nu(n+1)]$ of congruent $LiNbO_3$ crystals at T = (*1*) 300 and (*2*) 80 K. The solid lines represent the results of fitting by the Lorentz profile.

exceeds Raman signals measured in other geometries by almost an order of magnitude.

Comparison of the central peak in the spectrum of a congruent $LiNbO_3$ crystal and in a $LiNbO_3$ crystal with a composition close to stoichiometric (Fig. 2) shows that the intensity and shape of the central peak do not change with increasing concentration of stoichiometric defects. The spectral intensities for the two samples in Fig. 2 are normalized to the integrated intensity of the modes at 250 and 270 cm^{-1}. Thus, we may suggest that the central peak, which manifests itself in the Raman spectra of $LiNbO_3$ crystals at low temperatures, is mainly of internal origin rather than being due to stoichiometric defects.

The main difference between the Raman spectra of the two crystals shown in Fig. 2 is in the absence of the defect line in the vicinity of 100 cm^{-1}, which is due to nonstoichiometric defects [7] (vice versa, the absence of this peak indicates that the degree of stoichiometry of a sample is rather high). Note that the multiphonon contribution, which manifests itself in the spectra in the form of a background weakly dependent on frequency [7], is also smaller for the stoichiometric sample (by approximately 40%). In this case, the central peaks in the spectra of the two samples coincide accurate to ~10%.

Figure 3 shows the low-frequency part of the Raman spectrum of a congruent $LiNbO_3$ crystal at T = 300 and 80 K. In order to exclude a trivial temperature dependence for the first-order Raman spectra, the spectra are presented in the Bose normalized form:

$$I_n(\nu, T) = \frac{I(\nu, T)}{(n+1)\nu}. \quad (1)$$

Here, $I(\nu, T)$ is the Stokes part of the spectrum and $n = [\exp(h\nu/kT) - 1]^{-1}$ is the Bose factor.

It is reasonable to suggest that the central peak accounts for the relaxation susceptibility of a material. When the relaxation behavior of a medium is described by a correlation function with a single relaxation time, the relaxation response of the medium leads to the appearance of the central peak, which is described by the Lorentz profile in the Bose normalized representation (1). Notably, the width of the central peak is inversely proportional to the characteristic relaxation time. The solid lines in Fig. 3 show the fitting of the central peak by the Lorentz profile and the frequency-independent contribution of the multiphonon spectrum:

$$\frac{A}{1 + (\nu/\gamma)^2} + \text{const}. \quad (2)$$

The central peak in the spectrum obtained at room temperature (Fig. 3) was fitted with γ = 7 cm^{-1}, which corresponds to the relaxation time $\tau \sim 0.75$ ps. It can be seen that the single-relaxation-time approximation describes the central peak fairly well. With a decrease in temperature to 80 K, the central-peak intensity decreases faster than the Bose factor but the characteristic peak width does not change noticeably: $\gamma = 10 \pm 4$ cm^{-1}. Figure 3 shows the fitting of the low-temperature spectrum with the use of the same profile width that was applied for the room-temperature spectrum. In

this case, the integrated intensity of the central peak is lower by a factor of 5.5–6.

It should be noted that the experimental characteristics of the central peak in the room-temperature and low-temperature spectra of $LiNbO_3$ differ noticeably from the behavior of the central peak in the Raman spectra measured at temperatures close to the ferroelectric-transition temperature. First, in contrast to the case of high temperatures, the low-temperature central peak manifests itself in all polarization geometries (Fig. 1) rather than only in the geometry with the allowed ferroelectric mode A_1 [5]. Second, in the case of high-temperature relaxation, the width of the central peak shows noticeable temperature dependence and, according to [5], is described by the expression

$$\gamma(T) = \gamma_0 \frac{T_0 - T}{T_0}. \quad (3)$$

Expression (3) with the parameters described in [5] predicts the values of the peak width $\gamma \sim 41$ and 50 cm^{-1} at $T = 300$ and 80 K, respectively. At low temperatures, the experimental widths of the central peak differ from those obtained by extrapolation of the high-temperature behavior by more than a factor of five.

As a possible alternative to the relaxation description of the low-temperature central peak in the Raman spectra, a description in terms of entropy fluctuations or second-order scattering could be used [1]. However, for the description in terms of entropy fluctuations, the observed width of the central peak is too large and does not change noticeably with changing wave vector (when the excitation wavelength changes from 458 to 1064 nm, the scattering wave vector changes by a factor of about two) [1]. It is also unlikely that the central peak is due to the second-order difference Raman spectrum recorded in the regime described in [9] (the collision-dominated regime), since one should expect in this case the width of the central peak with the characteristic value smaller than 1 cm^{-1} to be proportional to the squared wave vector. There is also another possibility, which consists in the classical variant of the second-order Raman scattering. In this case, the peak width is determined by the specific form of the dispersion curves for optical phonons and weakly depends on the scattering wave vector in the visible spectral range. For the second-order Raman scattering, a weak temperature dependence of the width of the central peak is expected. However, in this case, the intensity of the peak at zero frequency is related to the general second-order background, which depends weakly on frequency (the examples of such calculations for the second-order Raman scattering were reported in [10, 11]). As can be seen from Fig. 2, comparison of the cases of congruent and stoichiometric crystals shows that there is no correlation between the central-peak intensity with the frequency-independent multiphonon background. For stoichiometric crystals, the multiphonon contribution (which is mainly two-phonon at low temperatures) is noticeably smaller than for congruent crystals, whereas the central-peak intensity is of the same order of magnitude. Thus, it is unlikely that the observed low-temperature central peak is related to the two-phonon Raman scattering.

The main reason for the appearance of the low-temperature central peak in the Raman spectra of $LiNbO_3$ crystals is the manifestation of the relaxation susceptibility. By analogy with the central peak in spectra of glasses [12, 13], we may suggest that this is the same relaxation that manifests itself in the acoustic-wave damping.

ACKNOWLEDGMENTS

We are grateful to A.E. Batalov for measuring the Raman spectrum with excitation at 1.064 μm and to C.M. Kostritskiĭ for delivering a crystal of stoichiometric composition.

This study was supported by the Russian Foundation for Basic Research, project no. 02-02-16112.

REFERENCES

1. P. A. Fleury and K. B. Lyons, in *Light Scattering Near Phase Transitions*, Ed. by H. Z. Cummins and A. P. Levanyuk (North-Holland, Amsterdam, 1983; Nauka, Moscow, 1990).
2. V. S. Gorelik, S. V. Ivanova, I. P. Kucheruk, *et al.*, Fiz. Tverd. Tela (Leningrad) **18** (8), 2297 (1976) [Sov. Phys. Solid State **18**, 1340 (1976)].
3. Yu. K. Voron'ko, A. B. Kudryavtsev, V. V. Osiko, *et al.*, Fiz. Tverd. Tela (Leningrad) **29** (5), 1348 (1987) [Sov. Phys. Solid State **29**, 771 (1987)].
4. Y. Okamoto, P.-C. Wang, and J. F. Scott, Phys. Rev. B **32** (10), 6787 (1985).
5. A. Ridah, M. D. Fontana, and P. Bourson, Phys. Rev. B **56** (10), 5967 (1997).
6. S. C. Abrahams and P. Marsh, Acta Crystallogr., Sect. B: Struct. Sci. **42**, 61 (1986).
7. N. V. Surovtsev, V. K. Malinovskiĭ, A. M. Pugachev, and A. P. Shebanin, Fiz. Tverd. Tela (St. Petersburg) **45**, 505 (2003) [Phys. Solid State **45**, 534 (2003)].
8. N. V. Surovtsev, A. E. Batalov, V. I. Kulakov, *et al.*, Phys. Rev. B **66** (20), 205412 (2002).
9. K. B. Lyons and P. A. Fleury, Phys. Rev. Lett. **37** (3), 161 (1976).
10. A. Zwick and R. Carles, Phys. Rev. B **48** (9), 6024 (1993).
11. A. Chehaidar, A. Zwick, R. Carles, and J. Bandet, Phys. Rev. B **50** (8), 5345 (1994).
12. N. V. Surovtsev, J. Wiedersich, V. N. Novikov, *et al.*, Phys. Rev. B **58** (21), 14888 (1998).
13. J. Wiedersich, S. V. Adichtchev, and E. Rössler, Phys. Rev. Lett. **84** (12), 2718 (2000).

Translated by Yu. Sin'kov

Crystallography Reports, Vol. 49, No. 1, 2004, pp. 123–129. Translated from Kristallografiya, Vol. 49, No. 1, 2004, pp. 131–137.

PHYSICAL PROPERTIES OF CRYSTALS

Dedicated to the 80th Birthday of L.A. Shuvalov

Electrical and Nonlinear Optical Properties of $KTiOPO_4$ Single Crystals Doped with Niobium, Antimony, and Tantalum

V. I. Voronkova*, V. K. Yanovskiĭ*, T. Yu. Losevskaya*, S. Yu. Stefanovich*, S. A. Zver'kov, O. A. Alekseeva***, and N. I. Sorokina*****

** Moscow State University, Vorob'evy gory, Moscow, 119992 Russia*

e-mail: voronk@crysc24.phys.msu.ru

*** Institute of Solid-State Physics, Russian Academy of Sciences, Chernogolovka, Moscow oblast, 142432 Russia*

**** Shubnikov Institute of Crystallography, Russian Academy of Sciences, Leninskiĭ pr. 59, Moscow, 119333 Russia*

Received June 25, 2003

Abstract—Single crystals of $K_{1-x}Ti_{1-x}Nb_xOPO_4$ (KTP : Nb), $K_{1-x}Ti_{1-x}Sb_xOPO_4$ (KTP : Sb), and $K_{1-x}Ti_{1-x}Ta_xOPO_4$ (KTP : Ta) solid solutions are grown and their dielectric, conducting, and nonlinear optical properties are investigated. The maximum contents x of niobium, antimony, and tantalum impurities in the crystals are equal to 0.11, 0.23, and 0.25, respectively. The doping of the $KTiOPO_4$ crystals with niobium, antimony, and tantalum brings about the formation of additional potassium vacancies and additional potassium positions and, as a consequence, an increase in the ionic conductivity σ_{33}. An increase in the doping level leads to a smearing of the ferroelectric phase transitions and a decrease in the phase transition temperatures. The permittivity of the doped crystals exhibits a broad relaxation peak in the temperature range 200–600°C. © *2004 MAIK "Nauka/Interperiodica".*

INTRODUCTION

Single crystals of $KTiOPO_4$ (KTP) are well known as promising materials for use in nonlinear optics. Moreover, these crystals are of considerable interest due to their unique combination of ferroelectric properties and high ionic conductivity. In this respect, KTP single crystals can be referred to as ferroelectric superionic conductors [1]. The physical properties of KTP crystals can be modified over a wide range by doping with different elements. In recent years, a number of works have appeared dealing with the $K_{1-x}Ti_{1-x}Nb_xOPO_4$ crystals in which Ti^{4+} ions are replaced by Nb^{5+} ions [2–9]. It has been found that the aforementioned doping leads to an increase in the intensity of the second harmonic generation (SHG) signal under laser irradiation and to a shift in the second harmonic wavelength toward the short-wavelength range [2–7]. The doping is accompanied by an increase in the ionic conductivity [9]. X-ray diffraction investigations have revealed that the introduction of Nb^{5+} ions brings about the formation of both additional potassium vacancies in accordance with the composition $K_{1-x}Ti_{1-x}Nb_xOPO_4$ [2, 3] and additional potassium positions [10, 11]. It has been established that KTP : Nb solid solutions are limited solutions; however, the data on the maximum degree of substitution of niobium atoms for titanium atoms are contradictory. For example, the maximum niobium content was determined to be equal to 25% in [3], 12% in [6, 9], and only 7% in [8]. According to the X-ray diffraction data [2], niobium atoms occupy positions in $Ti(1)O_6$ octahedra. It has been demonstrated that the doping of KTP crystals with niobium substantially affects the crystal morphology and leads to the formation of a more developed {100} face and a platelike habit [4, 7, 8]. At high niobium contents, the quality of crystals deteriorates significantly [4–7].

Tantalum impurities are more readily incorporated into the crystal lattice, because the tantalum atoms can occupy both Ti(1) and Ti(2) positions [8]. As in the case of niobium ions, the doping with Ta^{5+} brings about a shift in the wavelength of second harmonic generation of laser radiation toward the short-wavelength range [3, 8].

The data available in the literature for $K_{1-x}Ti_{1-x}Sb_xOPO_4$ solid solutions in which antimony atoms substitute for titanium atoms are very scarce. In [12], titanium was replaced by antimony and phosphorus was replaced by silicon in order to retain the electroneutrality of the unit cell. The compounds prepared in that work were characterized by nonlinear concentra-

1063-7745/04/4901-0123$26.00 © 2004 MAIK "Nauka/Interperiodica"

Table 1. Melt compositions, temperature conditions of crystallization, niobium contents in $K_{1-x}Ti_{1-x}Nb_xOPO_4$ crystals, and structural types of crystalline phases

Experiment	Melt composition, mol %				Temperature conditions, °C	Niobium content in crystals, *x*	Crystalline phase
	K_2O	TiO_2	Nb_2O_5	P_2O_5			
1	40	32.8	0.2	27	1000–875	0.002	KTP
2	40	32.6	0.4	27	1020–880	0.004	KTP
3	40	32	1	27	1020–865	0.01	KTP
4	40	31	2	27	1060–860	0.02	KTP
5	40	30	3	27	1060–770	0.04	KTP
6	40	28	5	27	1100–800	0.05	KTP
7	40	26	7	27	1100–800	0.07	KTP
8	40	23	10	27	1030–800	0.11	KTP
9	40	16.5	16.5	27	1110–920	0.66	$K_2TiNb_2P_2O_{13}$
10	40	13	20	27	1100–960	0.71	$K_2TiNb_2P_2O_{13}$

Table 2. Melt compositions, temperature conditions of crystallization, antimony contents in $K_{1-x}Ti_{1-x}Sb_xOPO_4$ crystals, and structural types of crystalline phases

Experiment	Melt composition, mol %				Temperature conditions, °C	Antimony content in crystals, *x*	Crystalline phase
	K_2O	TiO_2	Sb_2O_3	P_2O_5			
1	42	24.8	0.2	33	1100–800	0.01	KTP
2	42	24.6	0.4	33	1000–800	0.015	KTP
3	42	24	1	33	1000–900	0.05	KTP
4	42	23	2	33	1000–880	0.07	KTP
5	42	22	3	33	1000–850	0.09	KTP
6	42	21	4	33	1000–880	0.10	KTP
7	42	20	5	33	1000–850	0.17	KTP
8	42	19	6	33	1080–880	0.21	KTP
9	42	15	10	33	1080–800	0.23	KTP
10	42	12.5	12.5	33	1030–800	1	$K_3Sb_3P_2O_{14}$

Table 3. Melt compositions, temperature conditions of crystallization, tantalum contents in $K_{1-x}Ti_{1-x}Ta_xOPO_4$ crystals, and structural types of crystalline phases

Experiment	Melt composition, mol %				Temperature conditions, °C	Tantalum content in crystals, *x*	Crystalline phase
	K_2O	TiO_2	Ta_2O_5	P_2O_5			
1	41	26.8	0.2	32	1130–930	0.02	KTP
2	41	26.6	0.4	32	1130–930	0.05	KTP
3	41	26	1	32	1150–950	0.10	KTP
4	41	25	2	32	1150–950	0.15	KTP
5	41	24	3	32	1145–950	0.19	KTP
6	41	23	4	32	1145–930	0.24	KTP
7	41	22	5	32	1145–930	0.25	KTP

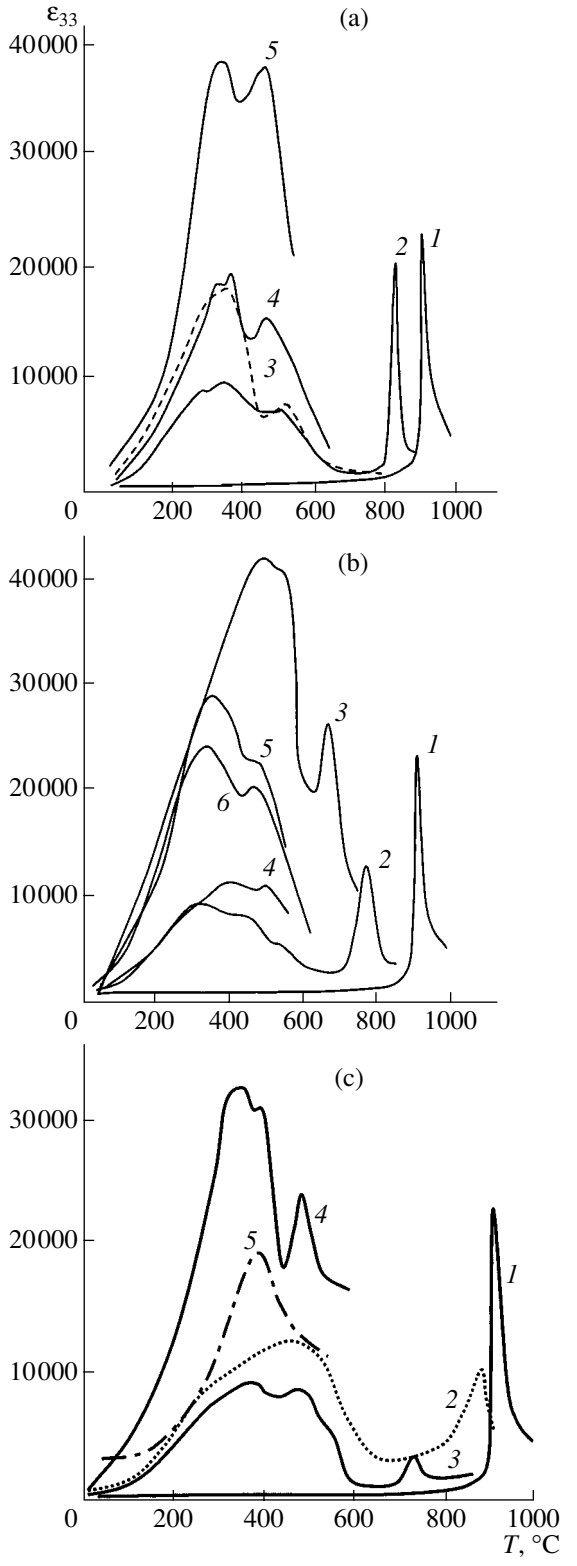

Fig. 1. Temperature dependences of the permittivity of the crystals (a) $K_{1-x}Ti_{1-x}Nb_xOPO_4$ at x = (*1*) 0.0, (*2*) 0.002, (*3*) 0.02, (*4*) 0.05, and (*5*) 0.11; (b) $K_{1-x}Ti_{1-x}Sb_xOPO_4$ at x = (*1*) 0.0, (*2*) 0.01, (*3*) 0.015, (*4*) 0.05, (*5*) 0.07, and (*6*) 0.17; and (c) $K_{1-x}Ti_{1-x}Ta_xOPO_4$ at x = (*1*) 0.0, (*2*) 0.02, (*3*) 0.05, (*4*) 0.10, and (*5*) 0.25.

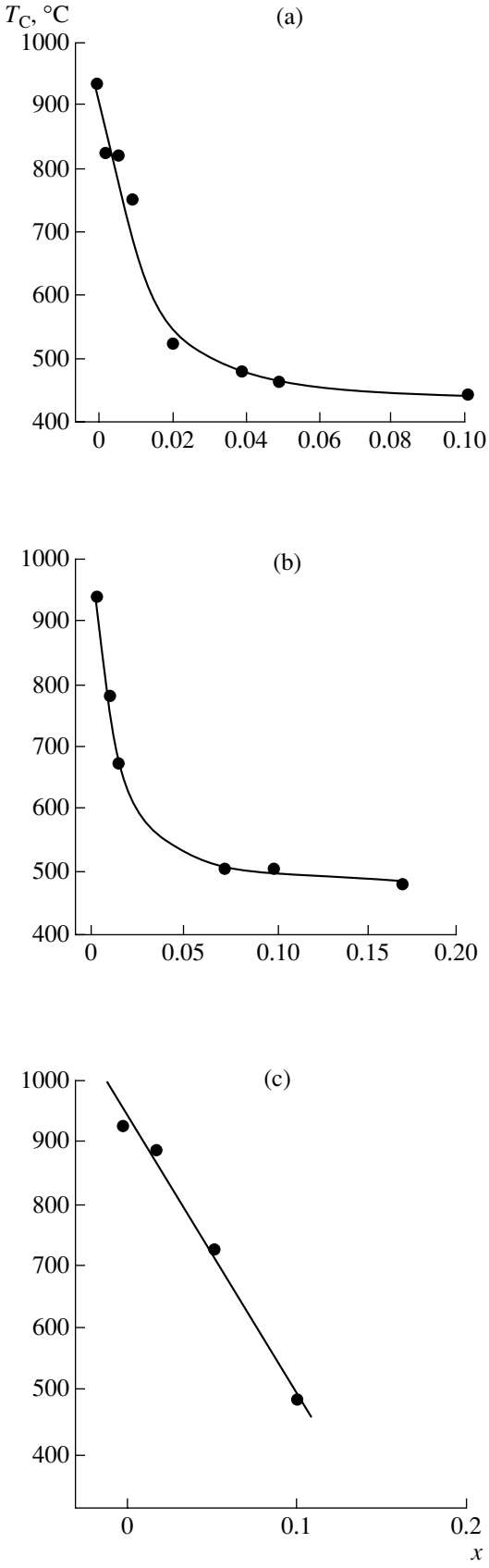

Fig. 2. Concentration dependences of the Curie temperature T_C for (a) KTP : Nb, (b) KTP : Sb, and (c) KTP : Ta crystals.

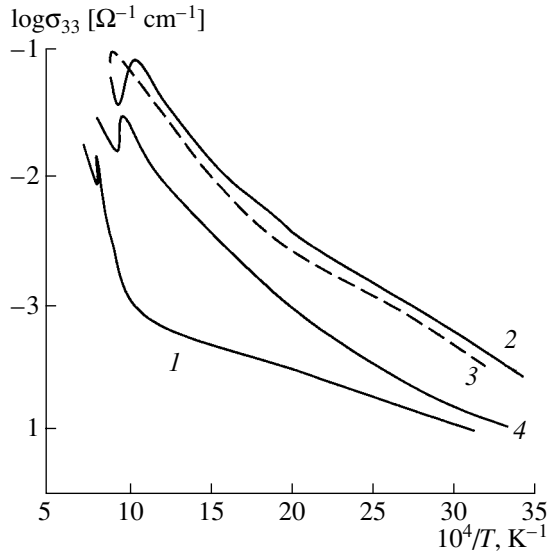

Fig. 3. Temperature dependences of the electrical conductivity for (*1*) KTP, (*2*) $K_{1-x}Ti_{1-x}Nb_xOPO_4$, (*3*) $K_{1-x}Ti_{1-x}Sb_xOPO_4$, and (*4*) $K_{1-x}Ti_{1-x}Ta_xOPO_4$ crystals.

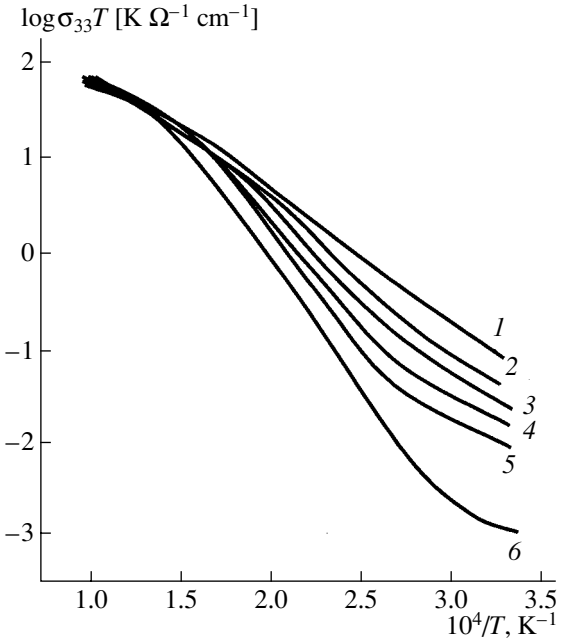

Fig. 4. Temperature dependences of the electrical conductivity of the $K_{1-x}Ti_{1-x}Sb_xOPO_4$ (x = 0.10) crystal at frequencies of (*1*) 1, (*2*) 10, (*3*) 20, (*4*) 50, (*5*) 100, and (*6*) 1000 kHz.

tion dependences of the Curie temperature and the SHG signal.

The purpose of the present work was to grow KTP : Nb, KTP : Sb, and KTP : Ta crystals and to investigate their properties.

SAMPLE PREPARATION AND EXPERIMENTAL TECHNIQUE

Doped KTP crystals were grown through spontaneous crystallization from a solution in the melt in the K_2O–TiO_2–P_2O_5–Nb_2O_5 (Sb_2O_3, Ta_2O_5) systems. Mixtures of the K_2CO_3, $NH_4H_2PO_4$, TiO_2, Nb_2O_5, Sb_2O_3, or Ta_2O_5 components (special-purity grade) were heated to a temperature of 600°C until the carbonate and ammonium salts decomposed. Then, the annealed reactants were mixed in an agate mill and melted in 50-ml platinum crucibles. The melts were allowed to stand at temperatures of 1000–1050°C for a day and then were cooled to 850–800°C at a rate of 1 K/h. Thereafter, the melt was poured out and the crystals grown were washed with water from the remaining solvent.

Tables 1–3 present the initial compositions of the melts used for growing the crystals; temperature conditions of crystallization; and the Nb, Ta, and Sb impurity contents. The phases that first crystallize in the aforementioned systems are also listed in these tables. Single crystals of compositions $K_{1-x}Ti_{1-x}Nb_xOPO_4$, $K_{1-x}Ti_{1-x}Sb_xOPO_4$, and $K_{1-x}Ti_{1-x}Ta_xOPO_4$ were grown using the method described above. In these crystals, the maximum contents x of Nb, Sb, and Ta dopants were equal to 0.11, 0.23, and 0.25, respectively. An increase in the niobium content in the melt resulted in the growth of $K_2TiNb_2P_2O_{13}$ monoclinic crystals [13, 14]. In the second system, the use of the initial melts containing more than 10 mol % Sb_2O_3 led to the formation of hexagonal platelike crystals, which, according to the X-ray powder diffraction data, corresponded to the $K_3Sb_3P_2O_{14}$ compound [15]. In the case of $K_{1-x}Ti_{1-x}Ta_xOPO_4$ crystals, an increase in the impurity content of higher than x = 0.25 brought about the formation of a phase differing from the KTP phase. The composition and structure of this phase were not investigated. The KTP : Nb, KTP : Sb, and KTP : Ta crystals were transparent and their sizes varied from 3 to 15 mm. The niobium and antimony impurities turned the doped crystals violet and yellow, respectively. The KTP : Ta single crystals were colorless. The coloration disappeared after annealing of the crystals at 600°C in air. As a rule, the quality of the crystals deteriorated at high impurity contents in the initial melts, and the crystals contained solvent inclusions and cracks. At high impurity contents in the crystal of all three systems, the {110} face disappeared, whereas the {100} face became most developed, which led to a platelike habit of the doped crystals.

The chemical composition of the crystals was determined on a CAMEBAX SX-50 microanalyzer. The temperature dependences of the permittivity and the electrical conductivity in the temperature range 20–900°C were measured with a Tesla BM 431E bridge at a frequency of 1 MHz and with a P5083 bridge in the frequency range 10–100 kHz. Electrodes were produced with the use of silver or platinum pastes. The

nonlinear optical properties were investigated using laser radiation (the Kurtz technique).

RESULTS AND DISCUSSION

The temperature dependences of the permittivity ε_{33} measured at a frequency of 1 MHz for the KTP : Nb, KTP : Sb, and KTP : Ta crystals with different impurity contents are depicted in Fig. 1. It can be seen that, with an increase in the impurity content, these dependences change in a similar way for all three types of crystals. As the impurity content increases, the anomalies associated with the ferroelectric phase transitions shift toward the low-temperature range by 300–400°C and become smeared at high contents of niobium, antimony, and tantalum. The broad anomalies observed in the temperature range 100–600°C are due to the relaxation processes [1, 16], and their magnitude at the maximum is as high as 40000 for the $K_{1-x}Ti_{1-x}Nb_xOPO_4$ crystals at $x = 0.11$, 42000 for the $K_{1-x}Ti_{1-x}Sb_xOPO_4$ crystals at $x = 0.015$, and 32000 for the $K_{1-x}Ti_{1-x}Ta_xOPO_4$ crystals at $x = 0.25$. As a rule, the relaxation anomalies involve two or three additional maxima, which was previously observed for the KTP : Nb crystals [17]. At high contents of niobium, antimony, and tantalum impurities, the peak corresponding to the ferroelectric phase transition lies in the range of these relaxation anomalies.

Figures 2a–2c show the concentration dependences of the ferroelectric phase transition temperature determined from the dielectric data. As can be seen from these figures, the concentration dependences exhibit a pronounced nonlinear behavior for the KTP : Nb and KTP : Sb crystals (Figs. 2a, 2b). The Curie temperature T_C linearly varies at low impurity contents ($x = 0.02$–0.05) and remains virtually constant at high contents.

The temperature dependences of the electrical conductivity of the KDP, $K_{1-x}Ti_{1-x}Nb_xOPO_4$ ($x = 0.002$), $K_{1-x}Ti_{1-x}Sb_xOPO_4$ ($x = 0.01$), and $K_{1-x}Ti_{1-x}Ta_xOPO_4$ ($x = 0.02$) crystals in the range 20–950°C at a frequency of 1 MHz are plotted in Fig. 3. Over the entire range of temperatures, the electrical conductivity σ_{33} of the doped crystals is one or two orders of magnitude higher than that of the pure KTP crystals and can be as high as 10^{-2} Ω^{-1} cm^{-1} at 300°C.

Figure 4 depicts the temperature dependences of the electrical conductivity σ_{33} of the $K_{1-x}Ti_{1-x}Sb_xOPO_4$ ($x = 0.1$) crystal at different frequencies in the range from 1 kHz to 1 MHz. These dependences are characterized by a considerable dispersion at low temperatures and frequencies. The temperature–frequency dependences of the electrical conductivity σ_{33} of this crystal are shown in Fig. 5. It can be seen that the electrical conductivity of the crystal at temperatures above 500–700°C becomes independent of the frequency. Note that the dielectric anomaly also disappears at these temperatures.

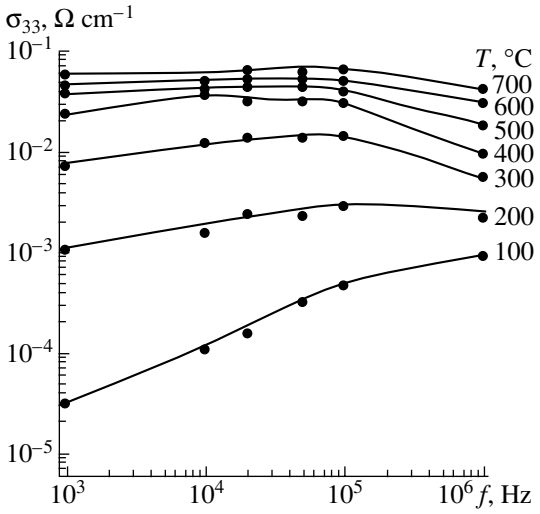

Fig. 5. Temperature–frequency dependences of the electrical conductivity of the $K_{1-x}Ti_{1-x}Sb_xOPO_4$ ($x = 0.10$) crystal.

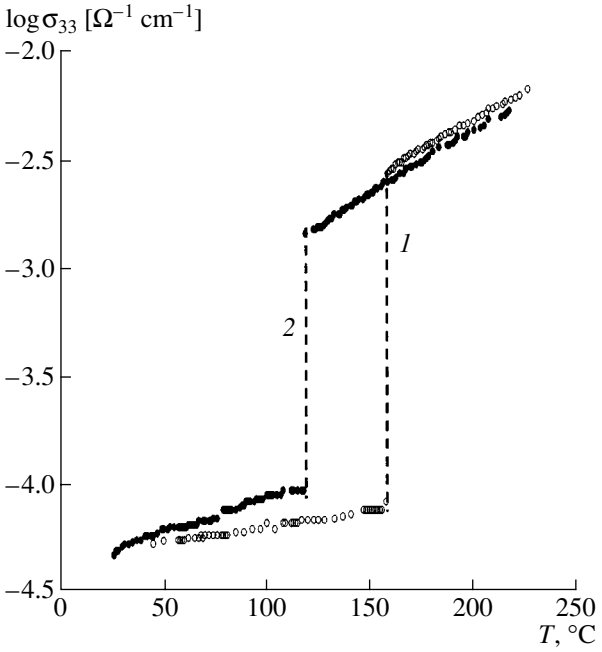

Fig. 6. Jumpwise changes in the electrical conductivity of KTP : Nb crystals in the course of (*1*) heating and (*2*) cooling.

The temperature dependences of the electrical conductivity of the $K_{1-x}Ti_{1-x}Nb_xOPO_4$ crystal at $x = 0.02$ in the range 100–400°C exhibit sharp jumps with a pronounced temperature hysteresis (Fig. 6). Similar conductivity jumps were revealed earlier for KTP crystals doped with tin [18].

Figure 7 shows the temperature dependences of the SHG signal intensity for the best-studied KTP : Nb and KTP : Sb crystals. An analysis of these dependences

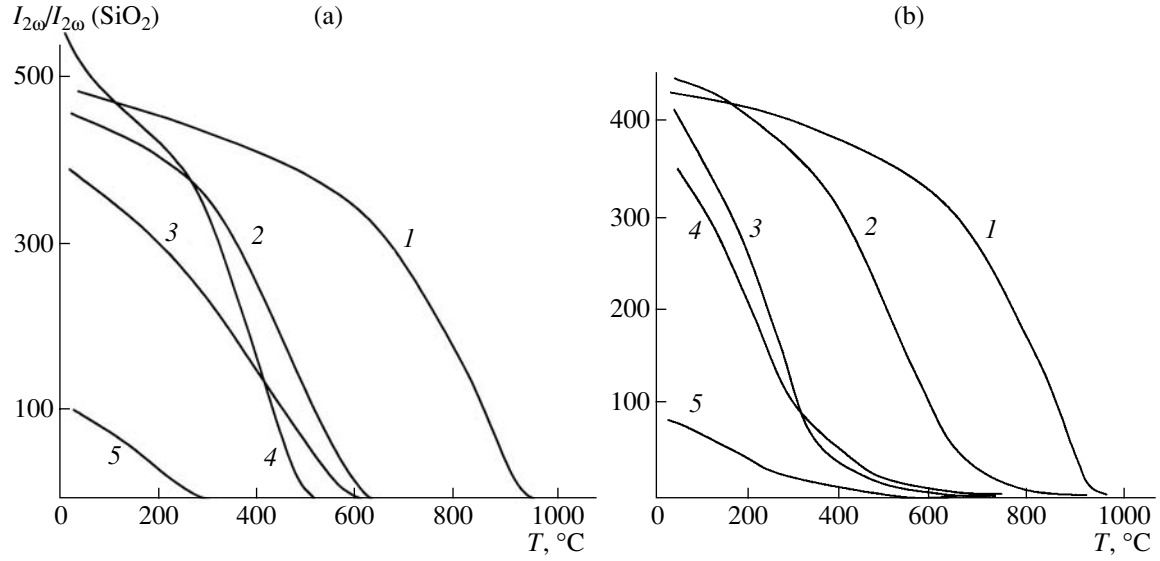

Fig. 7. Temperature dependences of the SHG signal intensity for crystals (a) $K_{1-x}Ti_{1-x}Nb_xOPO_4$ at x = (*1*) 0.0, (*2*) 0.02, (*3*) 0.03, (*4*) 0.05, and (*5*) 0.11 and (b) $K_{1-x}Ti_{1-x}Sb_xOPO_4$ at x = (*1*) 0.0, (*2*) 0.05, (*3*) 0.07, (*4*) 0.10, and (*5*) 0.17.

demonstrates that an increase in the Nb and Sb content in the doped crystals leads to the smearing of the ferroelectric phase transitions and a decrease in their temperatures. This is in complete agreement with the results of the dielectric measurements. It should be noted that the intensity of the SHG signal of laser radiation somewhat increases for the crystals with x close to 0.05.

Niobium, antimony, and tantalum belong to different subgroups of Group V in the periodic table and possess different chemical properties. However, the effect of these elements on the ferroelectric properties and the electrical conductivity of the KTP crystals is similar in character. Actually, the ferroelectric phase transition temperature T_C decreases, the electrical conductivity increases, the relaxation phenomena become more pronounced, and the intensity of the SHG signal usually decreases with an increase in the impurity content in the KTP : Nb, KTP : Sb, and KTP : Ta crystals. A slight increase in the intensity of the SHG signal at a certain impurity content (Fig. 7) was also observed in [2, 3]. Wang *et al.* [19] believe that a similar phenomenon is characteristic of solid solution crystals of the KTP family.

As is known, a number of potassium vacancies are formed in pure KTP crystals as a result of their growth at high temperatures [20]. The presence of potassium vacancies in these crystals accounts for their high ionic conductivity and the relaxation maxima in the temperature dependence of the permittivity ε_{33} in the range 100–600°C [21, 22].

Table 4. Occupancies of potassium positions in KTP : Nb structures

Composition	K(1)	K(2)	K(3)	K(4)
4 at. % Nb	0.899 (1)	0.858 (2)	0.108 (2)	
7 at. % Nb	0.702 (2)	0.773 (1)	0.148 (1)	0.168 (2)
11 at. % Nb	0.610 (1)	0.636 (1)	0.275 (1)	0.228 (2)

The results obtained in the present work are in complete agreement with the statement that the doping of the KTP crystals with Nb^{5+}, Sb^{5+}, and Ta^{5+} cations, i.e., the substitution of pentavalent atoms for tetravalent titanium atoms, leads to the formation of additional potassium vacancies according to the general scheme of heterovalent substitution in $K_{1-x}Ti_{1-x}Me_xOPO_4$ (*Me* = Nb, Sb, Ta). Furthermore, the precision X-ray diffraction analysis of KTP : Nb crystals revealed additional potassium positions [10, 11]. As can be seen from Table 4, the occupancy of all potassium positions substantially changes with a variation in the niobium content in the crystal. An increase in the niobium content is attended by a decrease in the occupancy of the K(1) and K(2) main positions and an increase in the occupancy of the K(3) and K(4) additional positions, i.e., by a more pronounced splitting of the potassium positions. The formation of the additional potassium positions can be responsible for the appearance of several maxima in the relaxation anomaly.

In the KTP : Nb, KTP : Sb, and KTP : Ta crystals, the potassium vacancies and additional potassium positions lead to disordering in the potassium sublattice, an increase in the mobility of K^+ cations and in the electrical conductivity, and an enhancement of relaxation phenomena due to the formation of additional relaxators in the form of "potassium cation–potassium vacancy" and "potassium cation–additional potassium position" pairs.

REFERENCES

1. V. K. Yanovskii and V. I. Voronkova, Phys. Status Solidi A **93**, 665 (1986).
2. P. A. Thomas and B. E. Watts, Solid State Commun. **73**, 97 (1990).
3. L. T. Cheng, L. K. Cheng, R. L. Harlow, and J. D. Bierlein, Appl. Phys. Lett. **64**, 155 (1994).
4. W. Y. Wei, J. Wang, Y. Liu, *et al.*, Chin. Phys. Lett. **13**, 203 (1996).
5. W. J. Liu, S. S. Jiang, X. R. Huang, *et al.*, J. Cryst. Growth **169**, 534 (1996).
6. W. J. Liu, S. S. Jiang, C. Z. Ge, *et al.*, Phys. Status Solidi A **161**, 329 (1997).
7. D. Y. Zhang, H. Y. Shen, W. Liu, *et al.*, J. Cryst. Growth **218**, 98 (2000).
8. K. B. Hutton, R. C. C. Ward, C. Rae, *et al.*, Proc. SPIE **3928**, 77 (2000).
9. T. Yu. Losevskaya, O. A. Alekseeva, V. K. Yanovskiĭ, *et al.*, Kristallografiya **45** (5), 809 (2000) [Crystallogr. Rep. **45**, 739 (2000)].
10. O. A. Alekseeva, M. K. Blomberg, V. N. Molchanov, *et al.*, Kristallografiya **46** (4), 710 (2001) [Crystallogr. Rep. **46**, 642 (2001)].
11. O. A. Alekseeva, N. I. Sorokina, I. A. Verin, *et al.*, Kristallografiya **48** (2), 238 (2003) [Crystallogr. Rep. **48**, 205 (2003)].
12. J. Ravez, A. Simon, and B. Boulanger, Ferroelectrics **214**, 379 (1991).
13. T. Yu. Losevskaya, V. I. Voronkova, V. K. Yanovskiĭ, and N. I. Sorokina, Neorg. Mater. **37** (9), 1136 (2001).
14. O. A. Alekseeva, N. I. Sorokina, I. A. Verin, *et al.*, Kristallografiya **46** (5), 816 (2001) [Crystallogr. Rep. **46**, 741 (2001)].
15. Y. Piffard, A. Lachgar, and M. Tournoux, Rev. Chim. Miner. **22**, 101 (1985).
16. S. G. Moorthy, F. J. Kumar, C. V. Kannan, *et al.*, Ferroelectrics **230**, 175 (1999).
17. S. Yu. Stefanovich and A. V. Mosunov, Izv. Akad. Nauk, Ser. Fiz. **64** (6), 1163 (2000).
18. Liu Wen, V. I. Voronkova, V. K. Yanovskiĭ, *et al.*, Neorg. Mater. **37** (3), 359 (2001).
19. J. Wang, J. Wei, Y. Liu, *et al.*, Prog. Cryst. Growth Charact. Mater. **40** (1–4), 3 (2000).
20. N. Angert, M. Tseitlin, E. Yashchin, and M. Roth, Appl. Phys. Lett. **67**, 1941 (1995).
21. V. K. Yanovskiĭ, V. I. Voronkova, A. P. Leonov, and S. Yu. Stefanovich, Fiz. Tverd. Tela (Leningrad) **27** (5), 2516 (1985) [Sov. Phys. Solid State **27**, 1508 (1985)].
22. J. D. Bierlein and C. W. Arweiler, Appl. Phys. Lett. **49**, 917 (1986).

Translated by O. Borovik-Romanova

Crystallography Reports, Vol. 49, No. 1, 2004, pp. 130–133. Translated from Kristallografiya, Vol. 49, No. 1, 2004, pp. 138–141.

PHYSICAL PROPERTIES OF CRYSTALS

Dedicated to the 80th Birthday of L.A. Shuvalov

Internal Bias Field in TGS Crystals Doped with Different Impurities

A. S. Sidorkin, S. D. Milovidova, O. V. Rogazinskaya, and A. A. Sidorkin

Voronezh State University, Universitetskaya pl. 1, Voronezh, 394006 Russia

e-mail: sidorkin@dom.vsu.ru

Received June 27, 2003

Abstract—The influence of an internal bias field formed by impurity ions of heavy metals and alpha-alanine molecules on the dielectric nonlinearity and emission properties of ferroelectric triglycine sulfate crystals has been studied. It is shown that a role of defects increases near the phase transition, which manifests itself in a decrease in the maximum values of the effective permittivity and an increase in the emission current with increasing impurity concentration. © *2004 MAIK "Nauka/Interperiodica".*

The introduction of defects into a ferroelectric crystal in one way or another significantly affects most of its electric properties. An oriented system of defects makes a ferroelectric material unipolar. Methods of defect introduction and, hence, formation of the unipolar state may differ. One of these methods is the introduction of impurities into a crystal during its growth. In particular, it is well known [1, 2] that the introduction of *L*, α-alanine molecules (substitutional impurity) or ions of heavy metals (interstitial impurity) into triglycine sulfate (TGS) crystals leads to the formation of the unipolar state, with the degree of unipolarity depending on the impurity concentration. A similar effect can be obtained by either irradiating a ferroelectric material or growing a crystal from unipolar seed [3].

In this study, we analyzed the influence of internal bias field on the dielectric nonlinearity and electron-emission characteristics of TGS crystals doped with either trivalent europium ions or *L*, α-alanine molecules and TGS crystals grown from X-ray-irradiated seeds. The samples were prepared by a conventional technique. A bar ~40 mm in length was cut from a grown TGS crystal doped with trivalent Eu ions. The long axis of the bar coincided with the polar *Y* axis perpendicular to the (010) face and the bar cross section (5×5 mm^2) was in the *XZ* plane. Then, the bar was separated in the cleavage planes into ~1-mm-thick samples. Electrodes on samples were prepared by depositing silver in vacuum. The amplitude and sign of the bias field were evaluated from the shift of the dielectric-hysteresis loops along the *E* axis.

The studies we performed showed that Eu-doped TGS crystals have a high degree of single-domain ordering: relatively large domains (3×7 mm^2 and larger) of unusual rectangular shape (instead of the lenticular shape typical of TGS) are observed visually on cleavage surfaces. Apparently, the formation of such a structure (as in the case of TGS crystals doped with *L*, α-alanine) may be related to high elastic stresses caused by the large radius of Eu ions during growth of Eu-doped TGS crystals.

As is well known, the dependence of the effective permittivity of a pure TGS crystal on the strength of an alternating electric field has a characteristic maximum in the case of fields comparable with coercive fields E_c. As the temperature approaches the Curie point, the maximum value of ε_{eff} increases and the peak in the field dependence of the effective permittivity shifts to weaker fields. The dependences $\varepsilon_{eff}(E_\sim)$ for TGS crystals with a high concentration of either *L*, α-alanine molecules or chromium ions exhibit minima, which may be caused by internal bias fields [4, 5]. The maxima in these dependences for Cr-doped TGS crystals are observed at fields approximately equal to E_b, whereas the corresponding dependences for pure TGS are peaked at E_c.

The dependences $\varepsilon_{eff}(E)$ for Cr-doped X-ray-irradiated TGS crystals with weak internal fields E_b (30–40 V/cm) were reported in [6]. These dependences are qualitatively similar to those obtained at high bias fields [3, 4]; however, at room temperature, the maxima in the curves $\varepsilon_{eff}(E)$ are observed at fields of 300–400 V/cm, i.e., one order of magnitude stronger as compared to E_b. The maximum values of ε_{eff} for Cr-doped crystals decrease as temperature approaches the Curie point. The maximum value of ε_{eff} for X-ray-irradiated TGS crystals first increases, like for pure TGS, and drops only at a temperature 2 K before the Curie point [6].

1063-7745/04/4901-0130$26.00 © 2004 MAIK "Nauka/Interperiodica"

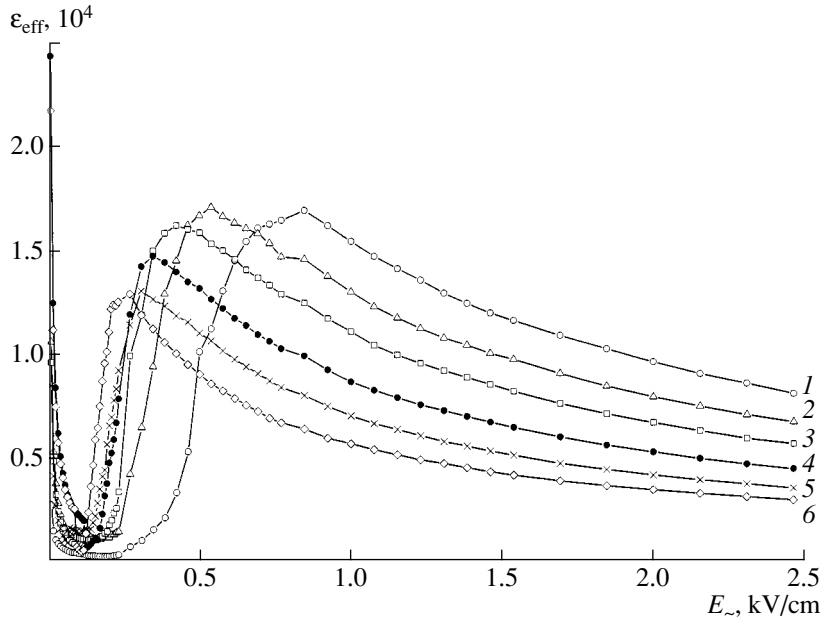

Fig. 1. Dependences of the effective permittivity on the ac electric field strength (f = 50 Hz) for a Eu-doped TGS crystal at (*1*) 19.2, (*2*) 34.8, (*3*) 41.2, (*4*) 45.0, (*5*) 47.5, and (*6*) 48.6°C.

The dependences of ε_{eff} on the external electric field E for TGS crystals doped with trivalent Eu ions (1 mol % in solution) are shown in Fig. 1. In contrast to pure TGS crystals, as well as to TGS crystals doped with all the impurities studied previously, minima are observed in the dependence $\varepsilon_{eff}(E)$ at fields comparable with the internal bias fields, which were determined by the shift of dielectric-hysteresis loops. Obviously, as long as the external field is weaker than the internal one, it does not lead to an increase in the polarization, and ε_{eff} decreases. As soon as the external field exceeds the internal bias field, ε_{eff} begins to increase in a conventional way with increasing E (which is typical of pure TGS crystals). As temperature approaches the value corresponding to the phase transition, the range of minimum values of ε_{eff} narrows and shifts to weaker fields. This phenomenon is in good agreement with the fact that internal bias fields decrease with increasing temperature. The maximum values of ε_{eff} in the curves under consideration decrease simultaneously (Fig. 2, curve *3*).

TGS crystals doped with L, α-alanine are characterized by a small variation in the maximum values of ε_{eff} with increasing temperature. These values decrease only in the vicinity of the phase transition (Fig. 2, curve *4*).

The experimental data we obtained show that the role of defects and the internal bias field increases in the vicinity of the phase transition. This is also confirmed by investigations of the behavior of dielectric-hysteresis loops for TGS crystals with a low defect concentration. Both Cr-doped samples and X-ray-irradiated ones show a normal unshifted hysteresis loop at room temperature. At a temperature of about 47°C, a waist arises in the loop. Then, the loop becomes double and remains the same until completely disappearing at the Curie point.

One of the properties of a ferroelectric crystal, which is most sensitive to introduction of impurities, is the electron emission induced in different ways. As is well known, the emission from pure TGS crystals grown from nonirradiated seeds is characterized by two maxima in the temperature dependence of the emission current. One of them is in the range of the domain restructuring, and the other one is near the phase transition (hereinafter, the first and second maxima, respec-

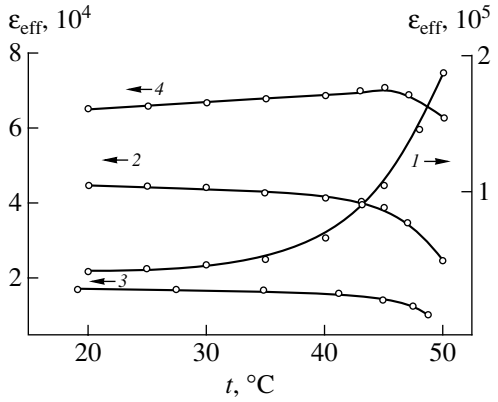

Fig. 2. Temperature dependences of the maximum values of the effective permittivity of TGS crystals: (*1*) pure and doped with (*2*) chromium ions; (*3*) europium ions; and (*4*) L,α-alanine molecules.

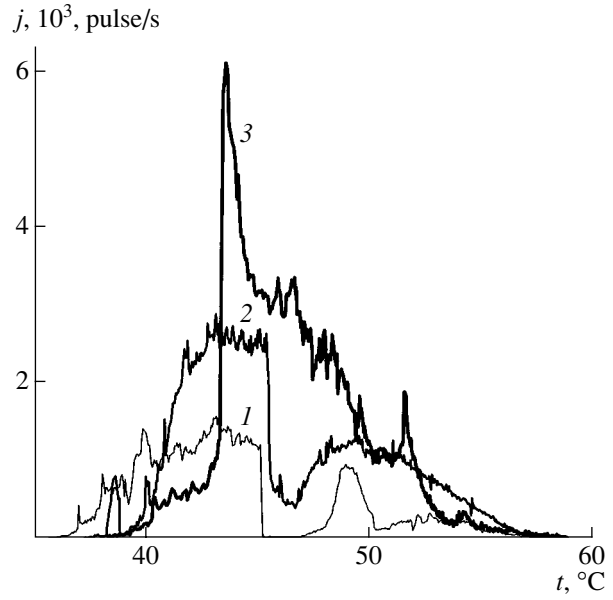

Fig. 3. Temperature dependences of the emission current from a pure TGS crystal grown from a unipolar seed irradiated by X rays in the direction antiparallel to the direction of macroscopic polarization for the samples from the regions spaced at (*1*) 1, (*2*) 6, and (*3*) 10 mm from the seed.

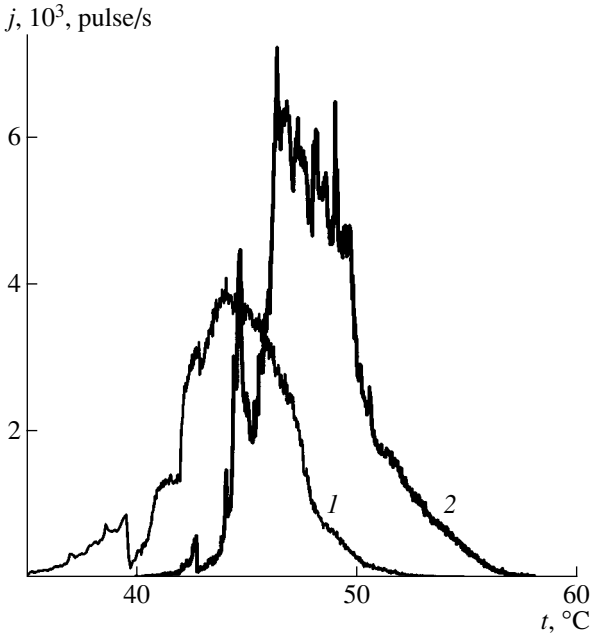

Fig. 4. Temperature dependences of the emission current from a TGS crystal doped with *L*,α-alanine molecules (1 mol % in solution) and grown from a unipolar seed irradiated by X rays parallel to the direction of macroscopic polarization for the samples from the regions spaced (*1*) 8 and (*2*) 16 mm from the seed.

tively) [7]. The emission current density j_{em} was measured by a conventional technique (using a secondary-emission multiplier) [7] in vacuum with a residual pressure of 6.5×10^{-3} Pa. The study of the influence of the seed irradiation on the temperature dependence of the emission current for the case when the direction of X rays coincides with the direction of the macroscopic (preferred) polarization P_M of a seed showed the following results. For the samples of pure TGS grown from a seed irradiated in the above way, which correspond to the regions adjacent to the seed, two maxima are also observed in the temperature dependence $j_{em}(T)$ (Fig. 3, curve *1*). In this case, the intensity of the thermionic electron emission in the first maximum exceeds the emission intensity in the vicinity of the phase transition.

As can be clearly seen from Fig. 3, a distinctive feature of these curves is that the current density in the first maximum almost smoothly increases and both maxima shift to each other with subsequent merging as the distance between the region corresponding to a sample and the seed increases.

The study of electron emission from *L*, α-alanine-doped TGS crystals grown from X-ray-irradiated seeds show different results. The samples corresponding to the regions close to the seed also show two maxima (although not clearly pronounced) in the dependence $j_{em}(T)$. With an increase in the distance between the region corresponding to a sample and the seed, the first maximum decreases and the second one (near the phase transition) increases. The sample corresponding to the region most remote from the seed has only one main maximum (Fig. 4, curve *2*).

The study of electron emission from pure and *L*, α-alanine-doped TGS crystals, as well as from TGS crystals grown from X-ray-irradiated seeds showed the following. The magnitudes and positions of the two characteristic maxima in the temperature dependence of the emission current (in the range of domain restructuring and near the Curie point) depend not only on the type of impurity introduced into a crystal and the seed irradiation but also on the distance between the region corresponding to a sample and the seed. A distinctive feature of a pure TGS crystal grown from a seed irradiated by X rays antiparallel to the direction of macroscopic polarization is that the current in the first maximum increases almost smoothly and both maxima shift to each other with subsequent merging as the distance between the region corresponding to a sample and the seed increases. Such behavior may be caused by the formation of a strong internal bias field (~75 V/cm) in a seed during its irradiation under the above conditions [8]. In this case, the degree of the single-domain ordering in the seed increases and, hence, the samples from the regions close to the seed have a higher degree of single-domain ordering. With an increase in the distance from the seed, the influence of the field E_b weakens. As a result, the degree of single-domain ordering in TGS

samples decreases with a corresponding increase in the emission current in the range of domain restructuring. The opposite result is obtained for an *L*, α-alanine-doped TGS crystal grown from a seed irradiated by X rays parallel to the direction of macroscopic polarization. As the distance between the region corresponding to a sample and the seed increases, the first maximum decreases, while the second one (near the phase transition) increases. Apparently, such behavior is related to a weaker bias field of the seed (~40 V/cm) and, in addition, to the increase in the concentration of impurity introduced during crystal growth.

ACKNOWLEDGMENTS

This study was supported by the joint project VZ-010 of the US Civilian Research and Development Foundation (CRDF) and the Ministry of Education of the Russian Federation.

REFERENCES

1. M. E. Lines and A. M. Glass, *Principles and Applications of Ferroelectrics and Related Materials* (Oxford Univ. Press, Oxford, 1977; Mir, Moscow, 1981).
2. A. P. Levanyuk, V. V. Osipov, A. S. Sigov, and A. A. Sobyanin, Zh. Éksp. Teor. Fiz. **76** (1), 345 (1979) [Sov. Phys. JETP **49**, 176 (1979)].
3. S. D. Milovidova, I. I. Evseev, I. V. Vavresyuk, and S. A. Aleshin, Kristallografiya **42**, 1137 (1997) [Crystallogr. Rep. **42**, 1060 (1997)].
4. L. N. Kamysheva, O. A. Godovannaya, S. D. Milovidova, *et al.*, Izv. Akad. Nauk SSSR, Ser. Fiz. **39** (4), 857 (1975).
5. L. N. Kamysheva, O. A. Godovannaya, S. D. Milovidova, *et al.*, Kristallografiya **19** (4), 824 (1974) [Sov. Phys. Crystallogr. **19**, 510 (1974)].
6. S. D. Milovidova, I. I. Evseev, I. V. Vavresyuk, *et al.*, *Ferroelectrics and Piezoelectrics* (Tver, 1991), p. 108.
7. A. M. Kostsov, A. S. Sidorkin, V. S. Zal'tsberg, and S. P. Gribkov, Fiz. Tverd. Tela (Leningrad) **24**, 3436 (1982) [Sov. Phys. Solid State **24**, 1952 (1982)].
8. A. S. Sidorkin, S. D. Milovidova, and O. V. Rogazinskaya, Ferroelectrics **265**, 189 (2001).

Translated by T. Dmitrieva

Crystallography Reports, Vol. 49, No. 1, 2004, pp. 134–136. Translated from Kristallografiya, Vol. 49, No. 1, 2004, pp. 142–144.

SURFACE, THIN FILMS

Dedicated to the 80th Birthday of L.A. Shuvalov

Specific Features of Dielectric Response in PZT Ferroelectric Films

A. I. Burkhanov*, A. S. Kudashev*, A. V. Shil'nikov*, I. N. Zakharchenko, S. G. Gakh**, and V. A. Aleshin****

** Volgograd State Architectural and Civil Engineering Academy, ul. Akademicheskaya 1, Volgograd, 400074 Russia*

e-mail: postmaster@vgasa.ru

*** Research Institute of Physics, Rostov State University, pr. Stachki 194, Rostov-on-Don, 344104 Russia*

Received June 5, 2003

Abstract—Reverse dependences of the permittivity $\varepsilon'(E_=)$ of $Pb(Ti_{0.45}Zr_{0.53}W_{0.01}Cd_{0.01})O_3$ ferroelectric films prepared by high-frequency magnetron sputtering on a stainless steel substrate have been studied. The $\varepsilon'(E_=)$ dependences and the polarization loops are compared. The mechanisms responsible for the specific features of the dielectric response in the films under study are discussed. © *2004 MAIK "Nauka/Interperiodica".*

INTRODUCTION

One of the pressing problems in studying ferroelectric films is the nature of internal fields. In some studies (see, for example, [1]), it is believed that the internal field arises due to the difference in the materials of the top electrode and the substrate electrode. At the same time, the experimental data of [2] show that the shift of the polarization loops (which indicates the presence of an internal field in a sample) is observed even for identical electrodes. In addition, noble-metal electrodes (e.g., made of platinum) are used in preparation of ferroelectric films to reduce the effect of near-electrode phenomena. The search for cheaper materials for this purpose is an urgent problem.

The method of reverse dependences $\varepsilon^*(E_=)$ is used in studying switching processes in ferroelectrics [3]. In this method, the response of a material is measured in a weak ac field when a bias dc field applied to a sample is varied. With the use of this method, the well-known antiparallel-domain-clamping effect (the Drougard–Young effect) was discovered [4]. In the study of relaxor lead lanthanum zirconate titanate ceramics [5], the effect of field memory was revealed using the same method.

The application of the above method to ferroelectric films has some specific features. The reasons for this are as follows. First, the measuring fields, which are weak in measurements of $\varepsilon'(E)$ in bulk ferroelectrics, are rather strong in the case of ferroelectric films. Second, the prolonged effect of a dc bias field on a film may cause its breakdown. Therefore, in studying the reverse dependences $\varepsilon^*(E_=)$ in ferroelectric films, fields varying continuously with frequency much lower than that of the measuring field are used (as, for example, in [6]) rather than constant fields.

In this paper, we report the results of investigations of the dielectric response of ferroelectric films by reversing a dc bias field ($E_=$) and applying a weak measuring field E_0 with a frequency of 1 kHz, as well as by measuring the polarization loops at infralow frequencies with the use of a modified Sawyer–Tower circuit. The data obtained allow one to compare the dielectric responses in films and bulk samples of ferroelectric materials in studies of the effect of domain structure on polarization or near-electrode phenomena.

EXPERIMENTAL

The permittivity ε' in a weak ($V \approx 0.02$ V) measuring field with bias field $E_=$ on a sample was measured in a wide temperature range by a bridge method. The polarization loops were observed at different magnitudes of applied voltage (from 10 to 60 V) and different frequencies (1, 10, 100, 1000 Hz) of measuring voltage in a modified Sawyer–Tower circuit. The polarization loops and the dependences $\varepsilon'(E_=)$ were measured in a quasistatic heating mode at temperatures fixed accurate to ±0.1 K.

Ferroelectric films were prepared in the Research Institute of Physics of Rostov State University by high-frequency magnetron sputtering of lead zirconate titanate targets of stoichiometric composition onto a stainless steel substrate in oxygen. The film thickness was 2 μm, and the area of the top aluminum electrode amounted to 1.76 mm^2.

1063-7745/04/4901-0134$26.00 © 2004 MAIK "Nauka/Interperiodica"

RESULTS AND DISCUSSION

Figure 1 shows the reverse dependences $\varepsilon'(E_=)$ for a PZT ferroelectric film measured at –100, 30, and 100°C with a measuring-signal frequency of 1000 Hz and a measuring voltage of 0.02 V. It can be seen that the maxima in the curves are diffuse for both field directions, while the maximum values of $\varepsilon'(E_=)$ are virtually equal. At the same time, at temperatures of 30 and 100°C, the point of intersection of the forward and reverse parts of the dependences is shifted with respect to zero field (Figs. 1b, 1c). This shift may indicate the presence of internal bias field E_i in the sample.

Thus, the shape of the dependence $\varepsilon'(E_=)$ for the noted sample suggests the following. (1) There is a wide distribution of domains over coercive fields. (2) The unipolarity (which is usually typical of films [1, 2, 7]) is practically absent. (3) The internal field is temperature-dependent (Fig. 2). Figure 2 shows the temperature dependences of the internal field $E_1(T)$; the coercive fields $E_{c+}(T)$ and $E_{c-}(T)$, derived from the positions of the maxima in the reverse dependence $\varepsilon'(E_=)$; and the coercive field $E_c(T)$, derived from polarization loops at a frequency of 1 Hz.

Concerning the shape of the dependence $E_i(T)$ (Fig. 2), we should note that similar behavior was reported in [8], where $E_i(T)$ was measured by the shift of the polarization loops observed for Ni-doped PZT ceramics. On the basis of the model for the formation of the internal field $E_i(T)$ in bulk perovskite-like ceramics [9], it was suggested in [8] that the appearance of the internal field is related to the slow orientation of dipole defects in ceramics. According to [8], the maximum in $E_i(T)$ results from two temperature-dependent processes: (1) domain-wall pinning and (2) defect diffusion. In our case, the formation of internal field may be due to the same processes, i.e., the interaction of the defect structure typical of PZT ceramics (O_2 vacancies, Pb vacancies, or vacancy–impurity defects) with domains in the film.

The presence of a well-developed defect structure in the film under study is evidenced by the structural analysis data [10]. In this context, the local minimum in $\varepsilon'(E_=)$ at $E_= > E_c$ revealed in this study (Fig. 1b) may indicate the switching of 180° domains. The minimum in $\varepsilon'(E_=)$ at 30°C (Fig. 1b) is most likely due to the well-known antiparallel-domain-clamping effect reported by Drougard and Young [4] for bulk ceramic samples. It is worth noting that the local minimum in the dependence $\varepsilon'(E_=)$ was also observed in [7] for PZT films obtained by the sol–gel method [11].

As can be seen from Fig. 2 (curves *2*, *3*), the values of $E_{c+}(T)$ and $E_{c-}(T)$ for the film under study increase when temperature exceeds $T \sim 50$°C (in contrast to the dependences $E_c(T)$ for bulk samples of PZT ceramics, in which, as a rule, the coercive field decreases with increasing temperature). Apparently, the increase

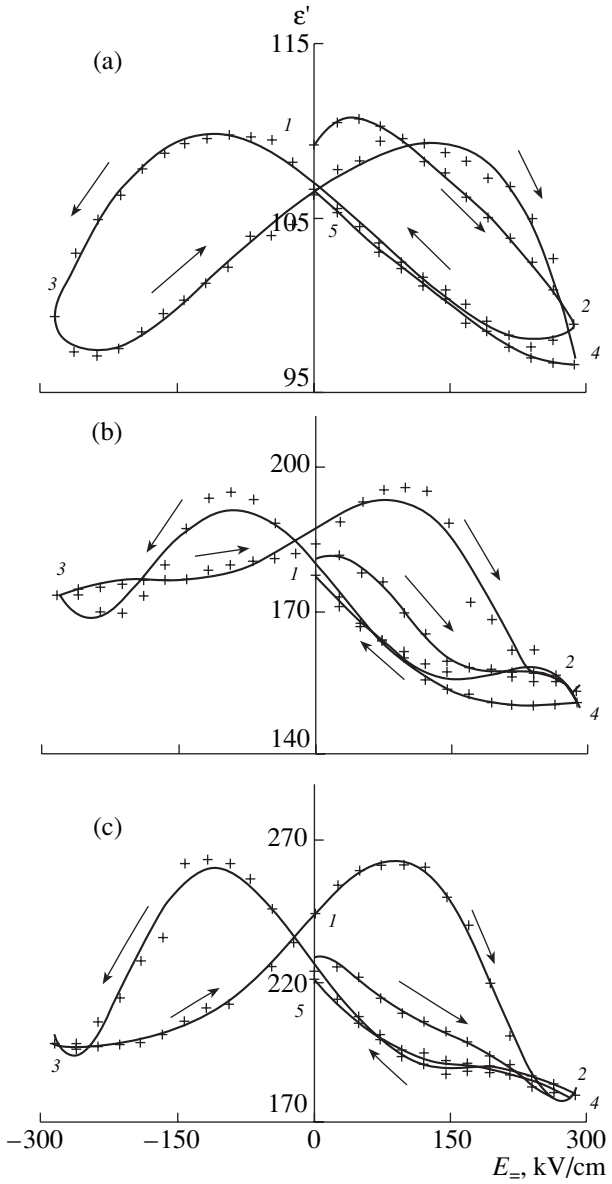

Fig. 1. Reverse dependences $\varepsilon'(E_=)$ for a PZT film at T = (a) –100, (b) 30, and (c) 100°C.

observed is related to the specific features of the mechanisms of polarization switching in ferroelectric films. In this case, there should be an significant distinction (e.g., in the coercive fields) between near-electrode crystallites (domains) and domains in the central region of the film (as was noted in [2]). It seems likely that the switching of the near-electrode (hard) domains also becomes possible when a certain temperature is exceeded (the coercive field for near-electrode domains is much higher than that for domains in the central region of the film).

In contrast to bulk materials, the number of near-electrode crystallites in a ferroelectric film is comparable to their number in the central region of a film. Therefore, analysis of the maxima in the reverse curve

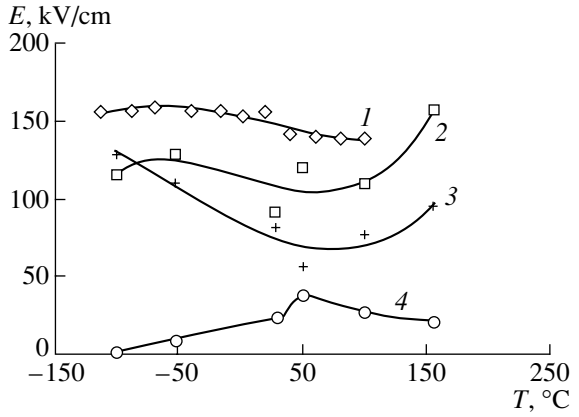

Fig. 2. Temperature dependences of (*1*) the coercive field $E_c(T)$ derived from the polarization loops at a frequency of 1 Hz; the coercive fields (*2*) $E_{c-}(T)$ and (*3*) $E_{c+}(T)$ derived from the maxima of the reverse dependence $\varepsilon'(E_=)$ for the negative and positive values of $E_=$, respectively; and (*4*) the internal field $E_i(T)$.

$\varepsilon'(E_=)$, which determine the averaged coercive field (E_{c+} and E_{c-}), shows an "increase" in this field. At temperatures exceeding the experimental temperature (i.e., when the entire sample is involved in the repolarization process), the aforementioned increase in $E_{c+}(T)$ and $E_{c-}(T)$ is likely to be replaced by a decrease. However, the dc-conductivity increases significantly at high temperatures, which may lead to a breakdown. Hence, we failed to measure such a decrease in $E_{c+}(T)$ and $E_{c-}(T)$. In the dependence $E_c(T)$ derived from the polarization loops, no increase in this parameter was observed at $T >$ 50°C ($E_c(T)$) decreases steadily with increasing temperature). This circumstance may indicate that, in ac fields with amplitudes used in our experiment, near-electrode domains are not involved in the repolarization process even at a field frequency of 1 Hz.

The results obtained show that, despite some structural imperfection, films of sufficiently high quality can be formed by high-frequency magnetron sputtering on stainless steel substrates. The characteristics of these films are similar to those of bulk materials, in which the basic mechanism of polarization and repolarization is the motion of domain boundaries.

ACKNOWLEDGMENTS

This study was supported by the Russian Foundation for Basic Research, project no. 02-02-16232, and the Leading Scientific School (NSh-15.14.2003.2).

REFERENCES

1. V. K. Yarmarkin, N. V. Zaĭtseva, S. V. Shtel'makh, and A. V. Motornyĭ, Fiz. Tverd. Tela (St. Petersburg) **37**, 324 (1995) [Phys. Solid State **37**, 176 (1995)].
2. V. P. Dudkevich and E. G. Fesenko, *Physics of Ferroelectric Films* (Rostov. Gos. Univ., Rostov-on-Don, 1979).
3. G. A. Smolenskiĭ, V. A. Bokov, V. A. Isupov, N. N. Kraĭnik, R. E. Pasynkov, A. I. Sokolov, and N. K. Yushin, *Physics of Ferroelectric Phenomena* (Nauka, Leningrad, 1985).
4. M. E. Drougard and D. R. Young, Phys. Rev. **94**, 1561 (1954).
5. A. V. Shil'nikov, A. I. Burkhanov, and E. Kh. Birks, Fiz. Tverd. Tela (Leningrad) **29** (3), 899 (1987) [Sov. Phys. Solid State **29**, 520 (1987)].
6. D. Bolten, O. Lohse, M. Grossmann, and R. Waser, Ferroelectrics **221**, 251 (1999).
7. A. V. Shil'nikov, I. V. Otsarev, A. I. Burkhanov, *et al.*, Izv. Ross. Akad. Nauk, Ser. Fiz. **64** (6), 1239 (2000).
8. U. Robels, L. Schneider-Störmann, and G. Arlt, Ferroelectrics **168**, 301 (1995).
9. G. Arlt and U. Robels, Ferroelectrics **3**, 343 (1993).
10. G. M. Konstantinov, Candidate's Dissertation in Physics and Mathematics (Rostov-on-Don, 1989).
11. K. A. Vorotilov, M. I. Yanovskaya, and O. A. Dorokhova, Integr. Ferroelectr. **3**, 33 (1993).

Translated by A. Zolot'ko

Crystallography Reports, Vol. 49, No. 1, 2004, pp. 137–142. Translated from Kristallografiya, Vol. 49, No. 1, 2004, pp. 145–150.

SURFACE, THIN FILMS

Dedicated to the 80th Birthday of L.A. Shuvalov

Domain Contribution to the Low and Infralow Frequency Dielectric Response of Ferroelectric Thin PZT Films Prepared by the Sol–Gel Method

A. V. Shil'nikov*, R. A. Laletin*, A. I. Burkhanov*, A. S. Sigov, and K. A. Vorotilov****

** Volgograd State Architectural and Civil Engineering Academy, Akademicheskaya ul. 1, Volgograd, 400074 Russia*

e-mail: postmaster@vgasa.ru

*** Moscow State Institute of Radioengineering, Electronics, and Automation, pr. Vernadskogo 78, Moscow, 117454 Russia*

Received June 5, 2003

Abstract—Dielectric properties of thin Ni/PZT/Pt films grown by the sol–gel method are studied at low and infralow frequencies over the wide ranges of temperatures and measuring-field amplitudes. Based on the data obtained, the conclusion is drawn about a considerable contribution of domain boundaries to the dielectric response of these films. A new refined classification of point defects interacting with domain boundaries is suggested. © *2004 MAIK "Nauka/Interperiodica".*

In recent decades, an ever increasing interest has been shown in ferroelectric thin films. This is associated, first and foremost, with the optimistic perspectives of their wide use for microminiaturization and their high sensitivity, low energy consumption, and fast operation. These films are also widely used in nonvolatile memory [1–9] based on the phenomenon of switching of spontaneous polarization. The character (and even possibility) of switching in thin ferroelectric films and physical nature of their dielectric response and, first of all, the role of domain boundaries in these processes are actively discussed [10–12]. In some instances (especially if one considers dielectric relaxation), the role of domain boundaries is completely ignored (no such mechanism is considered at all) because the authors *a priori* do not hold this viewpoint [2, 13, 14]. At the same time, recent studies of very thin Langmuir–Blodgett films [15] indicate the possible coexistence of the switching mechanism proper and the switching mechanism associated with the domain-boundary motion. Although it seems that the question about the role of domain boundaries in switching in thin films has already been answered, the existence of the domain-boundary contribution to the polarization and switching processes in thin ferroelectric films still gives rise to some doubts.

We should like to show that domain boundaries in thin films obtained by the sol–gel method make a considerable contribution to the dielectric response at low and infralow frequencies of applied sinusoidal electric fields with different amplitudes and, with this aim, compare the corresponding characteristics of these films with the analogous characteristics of macroscopic ferroelectric samples. As the main criterion in this comparison, we use the simplest classifications of the motion mechanisms of domain boundaries [16–18] and point defects interacting with these boundaries [19] and also consider various computer models of polarization loops created on this basis [18, 20].

SAMPLES AND METHODS OF MEASUREMENTS

The samples were thin-film PZT chips with the upper Ni electrodes with an area of $S = 0.03$ mm^2 obtained by the sol–gel methods [21–23] on Pt/Ti/SiO_2/Si substrates. A film fragment on such a substrate was incorporated into an integrated circuit. Then, the electrodes were connected with the circuit contacts. The use of thermal compression in the contact zone somewhat changed the properties of the PZT–Ni interface, which, in turn, somewhat modified the dielectric-hysteresis loops obtained in our study in comparison with the loops observed in [24]. The film thickness was 0.2 μm. The excess in lead (x) in the initial film-forming solution was 0, 5, 10, 30, and 50 mol % [21]. Below, we consider the results mainly for samples obtained from the film-forming solution with a 5 and 10 mol % excess in lead, i.e., in the final analysis, for film compositions close to stoichiometric.

Complex permittivity ε* in comparatively weak fields ($U_0 = 0.001$ V, $E_0 = 0.05$ kV/cm) was measured

1063-7745/04/4901-0137$26.00

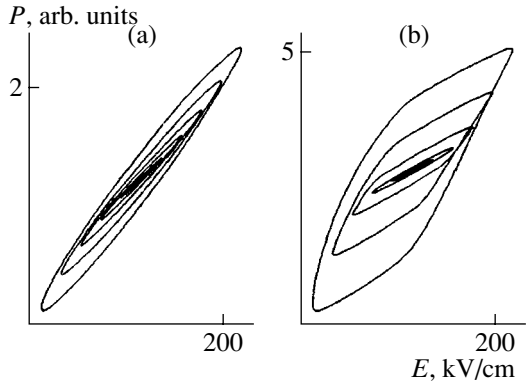

Fig. 1. Polarization loops of the sample obtained from a solution with a 5% excess in lead, all other experimental conditions being the same, at the (a) initial and (b) subsequent stages of measurements.

using the bridge scheme [25], with ε' and ε'' being measured separately in the frequency range from 10^{-1} to 10^4 Hz.

The oscillograms of polarization loops in the same frequency range were obtained using the modified Sawyer–Tower scheme with a C9-8 recording digital oscillograph controlled by an IBM-compatible computer [26]. The amplitude of the sinusoidal field in this case was set in the range from 1 kV/cm (0.02 V) to 250 kV/cm (5 V). The Evans impedance criterion [27] was fulfilled, and, therefore, a nonlinear capacitor (chip cell) of effective capacitance was replaced by a linear capacitor of variable capacitance. The temperature ranged from 100°C (373 K) to the boiling point of nitrogen. The accuracy of the temperature maintenance at the given point was not worse than 0.05 K at a measurement sensitivity of 0.001K.

RESULTS AND DISCUSSION

Figure 1 shows polarization loops for a sample with a 5% excess in lead in the initial solution at a temperature of –180°C in the field with the frequency 10 kHz and the voltage at the maximum U_0 = 5 V ($E_0 \sim$ 250 kV/cm). The first measurements of the amplitude series of polarization loops with a "fresh" cell in the field (the initial value 5 kV/cm) varying at a step of 5 kV/cm gave the polarization loops of obvious quasi-Rayleigh shape (Fig. 1a) corresponding to the following equation of domain-boundary motion [20]:

$$\eta\dot{x} + kx + F\,\mathrm{sgn}(\dot{x}) = 2P_sE\,. \qquad (1)$$

This equation takes into account the contribution of the initial value of permittivity ε_0^*.

Upon the attainment of the maximum field ($E_0 \sim$ 250 kV/cm), which is critical for some domain boundaries interacting with point defects (transformation of some strong defects into moderate ones), the volume of the repolarized part of the sample (film) under the given conditions (T = const, ν = const, E_0 = const) increased. This resulted in the transformation of the quasi-Rayleigh polarization loops into rhombus-like ones [17, 20, 28]. To obtain the complete picture of the evolution of polarization loops, we repeatedly measured these loops using the same cell in the field varying from an initial value of 5 kV/cm at a step of 5 kV/cm (Fig. 1b). It is seen from Fig. 1b that, at $E_0 \le 100$ kV/cm, the polarization loops preserved the Rayleigh shape, but, with a further increase in the field amplitude E_0, they acquired a rhombus-like shape observed in the first measurements in the fields with the amplitude $E_0 \sim 250$ kV/cm. In this case, polarization loops correspond to the same motion equation of domain boundaries (1) [20] but without allowance for the contribution of the initial permittivity ε_0^*, because the domain-boundary contribution to permittivity obeys the inequality $\varepsilon_{\text{eff}}^* \gg \varepsilon_0^*$.

This statement is confirmed by Fig. 2, which shows an example of the redistribution of the relative contribution (in percent) of the hysteresis (and, therefore, relaxation) mechanism of domain-boundary motion to the real ($\varepsilon'_{\text{eff-}g}$) and imaginary ($\varepsilon''_{\text{eff-}g}$) parts of complex permittivity ($\varepsilon_{\text{eff}}^*$). It should be noted that these experimental results can hardly be explained by the influence of the measuring circuit, interface fields, and volume charge and, moreover, that similar phenomena are rather typical of macroscopic ferroelectric samples [28].

Figure 3 shows polarization loops for a sample with a 10% excess in lead in the film-forming solution (in the final analysis, the stoichiometric composition) at a temperature of +25°C in the fields with the amplitude up to $E_0 \sim 250$ kV/cm and at frequencies ranging from 0.1 to 10 kHz. One has to pay special attention to the shape of the polarization loops obtained at 0.1 and 1 Hz. In the former case (ν = 0.1 Hz), the loops are narrow concentric ellipses characterizing a linear dielectric response with low losses, which can be explained by the reversible domain-boundary motion described by the equation [17, 20]

$$\eta\dot{x} + kx = 2P_sE. \qquad (2)$$

At $\eta\dot{x} \ll kx$, a considerable number of domain boundaries move in accordance with the elastic mechanism without any losses in accordance with the equation (3) [17] $kx = 2P_sE$.

In this case, the measuring frequency is much lower than the relaxation frequency of polarization ($\nu \ll \nu_r$). In the latter case (ν = 1 Hz), polarization loops are concentric ellipses only at the initial stage of polarization (in relatively weak fields); then, in more intense fields, they are transformed into ovals characterizing the appearance of a nonlinear dielectric response (irreversible domain-boundary motion). In this case, the area of the polarization loops (and, therefore, the losses) dra-

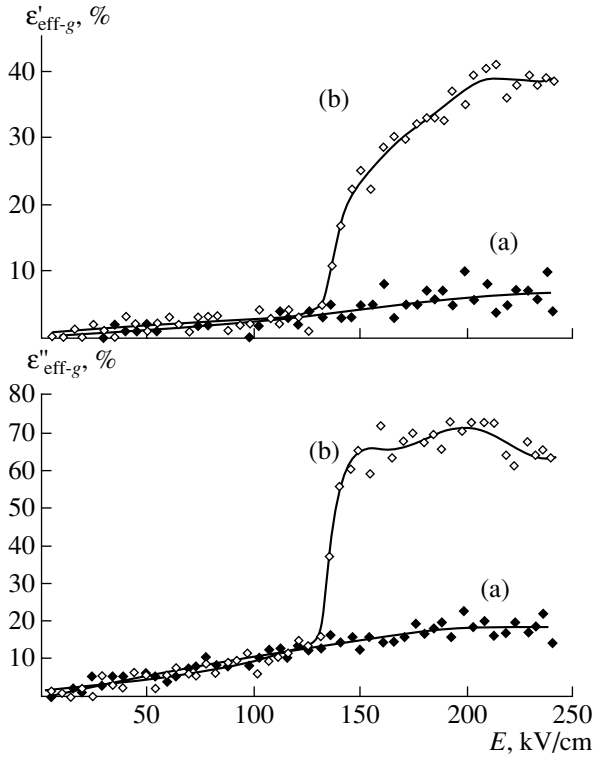

Fig. 2. Amplitude dependences of the contributions of domain-boundary motion by the hysteresis (jumpwise) mechanism to ε'_{eff} and ε''_{eff} for a sample obtained from an initial solution with a 5% excess in lead at the temperature –180°C. The polarization loops obtained (a) at the initial stage of measurements and (b) immediately after the initial stage were processed.

matically increases in comparison with their area at ν = 0.1 Hz, which indicates that the measuring frequency is close to the frequency of polarization relaxation ($\nu \sim \nu_r$). It should be emphasized that, if conductivity (volume charge) also contributes to the polarization, the losses are always proportional to the reciprocal measuring frequency ($\varepsilon''_{eff\text{-}g} \sim 1/\omega$, where $\omega = 2\pi\nu$) [29], and, therefore, such evolution of polarization loops becomes impossible. It should also be noted that the film inhomogeneity may lead to the Maxwell–Wagner relaxation [29], where the contribution to polarization (ε^*_{eff}) comes not only from domain boundaries but also from the charge migration associated, e.g., with the interface structure. However, it cannot lead to any serious changes in the evolution of polarization loops (it can only somewhat change the polarization value and ε^*_{eff}) [29].

At ν = 10 Hz (Fig. 3), we observed constricted hysteresis loops, their unipolarity, and slight displacement along the E axis. At ν = 100 Hz and higher frequencies, the polarization loops become quasi-saturated, unipolar, and are also displaced. Their dielectric response acquires pronounced nonlinearity and afteraction (polarization loops are no longer concentric). This frequency evolution of the polarization-loop shape is characteristic, e.g., of the macroscopic crystalline samples of the Rochelle salt [30].

The ν values for the polarization loops, which, in our opinion, reflect reversible and irreversible relaxation motion of domain boundaries [15, 16], were determined to construct the Arrhenius dependences of the relaxation frequency (Table 1) [31]

$$\nu_r = \nu_0 \exp(-U_a/k_B T), \quad (3)$$

where ν_0 is the frequency of the attempts of the relaxor to overcome the potential barrier U_a, U_a is the energy of polarization activation, k_B is the Boltzmann constant, and T is the absolute temperature.

One can readily see the pronounced amplitude dependence of the polarization-relaxation frequency $\nu_r(E_0)$ approximated by the expression

$$\nu_r = \nu_\infty \exp(-\alpha/E_0), \quad (4)$$

where ν_∞ is the most probable frequency of polarization relaxation at the measuring-field amplitude $E_0 \longrightarrow \infty$ and α is the activation field of polarization (Fig. 4).

We should like to emphasize (see Table 1) that the activation energy U_a and the preexponential factor ν_0 in Eq. (3) decrease with the amplitude of the measuring field E_0. In other words, the measuring field of a larger

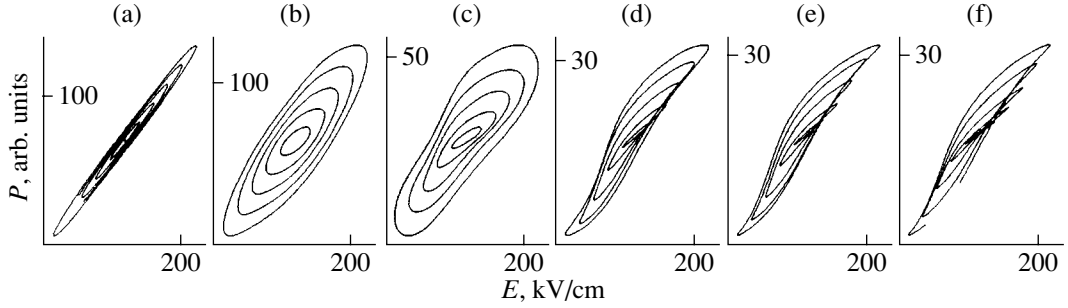

Fig. 3. Polarization loops for a sample obtained from the film-forming solution with a 10% excess in lead at several measuring-field frequencies α: (a) 0.1, (b) 1.0, (c) 10, (d) 100, (e) 1000, and (f) 10 000 Hz.

Table 1. Approximation of $\ln(\nu_r)$ as a function of the reciprocal temperature of the sample with a 10% excess in lead in a film-forming solution by Arrhenius equation (8) in fields of various amplitudes

Temperature range, °C (range of relaxation frequencies ν_r, Hz)	Amplitude of measuring field E_0 (voltage U_0), kV/cm (V)	Relaxation frequencies determined from the maxima of the dependence $\varepsilon''_{\text{eff}}(\nu)$	
		activation energy, U_a, eV	preexponential factor ν_0, Hz
$-130 < T < +25$ ($0.015 < \nu_r < 0.92$)	50 (1)	0.176 ± 0.007	590
	125 (2.5)	0.161 ± 0.009	400
	250 (5)	0.147 ± 0.006	320

amplitude would reduce the potential barrier which should be overcome by the relaxor and the number of its "attempts" to overcome this barrier in order to attain the effect taking place at lower E_0.

Table 2 lists the parameters of Eq. (5) obtained from the $\nu_r(E_0)$ curves shown in Fig. 4 at various temperatures. It shows the change in the activation fields (α) with an increase of the field E_0 and lowering of the temperature and lists the most probable relaxation frequencies (ν_∞). On the whole, these changes have the same tendency as the changes of any macroscopic ferroelectric samples in which switching occurs due to domain-boundary motion.

We believe that the above examples characterizing dielectric response of thin sol–gel films at low and infralow frequencies unambiguously indicate the domain contribution to their polarization and switching. Therefore, it is timely to introduce a new classification (refined in comparison with the classification given in [19]) of point defects interacting with grain boundaries. We classify as ultraweak the defects creating a potential barrier U at the given temperature (T = const), frequency (ν = const), and amplitude (E_0 = const) of the measuring field that should be overcome by domain boundaries thermally activated in phase with the measuring field (in this case, the equation that describes domain-boundary motion takes the form $kx = 2P_sE$). Weak defects are those which at T = const, ν = const, and E_0 = const, give rise to the barrier U that should be overcome by domain boundaries but with a phase delay with respect to the measuring field (in this case the equation of domain-boundary motion corresponds to Eq. (2)). Moderate defects are those which at the given T = const and ν = const, create the barrier U, that should be overcome by domain boundaries in a jumpwise manner as soon as the field amplitude attains a certain critical value ($E_0 = E_{cr}$); in this case, the equation of domain-boundary motion has the form either of Eq. (1) or [20]

$$kx + F\,\mathrm{sgn}(\dot{x}) = 2P_sE. \qquad (5)$$

And, finally, strong defects, which, at the fixed T = const, ν = const, and E_0 = const, rigidly fix (stop) domain boundaries vibrating under the action of an electric field like loaded membranes between the stopper line (reversible domain-wall motion obeying Eq. (2)) [31].

Now, consider in these terms the evolution of the polarization-loop shape with an increase of the frequency of the measuring (polarizing or repolarizing) field E (Fig. 3). At $\nu = 0.1$ Hz, the motion is determined mainly by ultraweak defects (and, partly, by weak and strong ones). Most of the domain boundaries move in phase with the external field (reversible elastic domain-boundary motion and irreversible relaxation domain-boundary motion). Reversible elastic domain-boundary motion contributes only to ε' ($\varepsilon'' = 0$) [17], whereas irreversible motion by the relaxation mechanism makes only the small contribution to ε'' (because of the electrocaloric effect [32]). A considerably small number of weak defects give rise to reversible relaxation motion of grain boundaries described by Eq. (2), which contributes to both ε' and ε'' (narrow concentric ellipses).

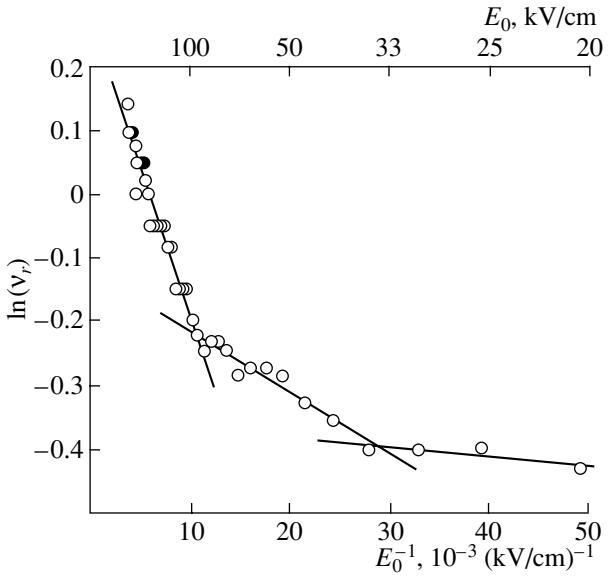

Fig. 4. Approximation of $\ln(\nu_r)$ as a function of reciprocal energy $1/E_0$ by the equation $\nu_r = \nu_\infty \exp(-\alpha/E_0)$ for a sample obtained from a film-forming solution with a 10% excess in lead at T = 25°C.

Table 2. Approximation of $\ln(\nu_r)$ as a function of reciprocal energy $1/E_0$ of the sample with a 10% excess in lead in a film-forming solution by Eq. (4)

Temperature, °C	Range of field variation, kV/cm	α, kV/cm	ν_∞, Hz
25	20–36	1.44	0.70
	36–87	9.59	0.87
	87–253	47.46	1.33
0	26–67	14.67	0.35
	67–137	47.17	0.57
	137–253	115.57	0.92
–30	15–52	3.58	0.10
	52–117	35.20	0.19
	117–253	122.13	0.39

With an increase in the measuring-field frequency (ν = 1 Hz), ultraweak defects are transformed into weak ones, and weak defects, into moderate ones. This results in a considerable increase in losses (the polarization-loop area increases, and the measuring-field frequency approaches the frequency of the polarization relaxation, $\nu \longrightarrow \nu_r$). The majority of domain boundaries in this case move by the relaxation mechanism (both reversibly and irreversibly), whereas a small number of domain boundaries move by the hysteresis mechanism (in a jumpwise manner), which leads to nonlinearity $\varepsilon^*_{\text{eff}}(E)$. At ν = 10 Hz, ultraweak defects continue transforming into weak ones; weak defects, into moderate ones; and moderate defects, into strong ones. As a result, the measuring frequency remains close to the frequency of polarization relaxation (a large number of domain boundaries move, both reversibly and irreversibly, by the relaxation mechanism), the nonlinearity $\varepsilon^*_{\text{eff}}(E)$ associated with the hysteresis mechanism of domain-boundary motion becomes more pronounced, constricted polarization loops are formed because the strong defects stop domain boundaries, and the switching part of the sample volume considerably decreases (maximum polarization $P_{\max}$ decreases). A further increase in the measuring-field frequency (100, 1000, and 10000 Hz) results in the defect transformation: weak defects become moderate and moderate defects become strong ones and, therefore, domain boundaries move mainly irreversibly by the hysteresis mechanism and reversibly by the elastic and relaxation mechanism. One also observes considerable nonlinearity of $\varepsilon^*_{\text{eff}}(E)$, quasi-saturation, aftereffects, displacement of the polarization loops along the E axis, and a decrease in the switching part of the sample volume (decrease in $P_{\max}$). It should be noted that displacement of the polarization loops does not influence the effective coercive filed $E_{C\,\text{eff}}$ [33] and, most likely, is caused by the bias field formed by the fields of interfaces.

CONCLUSIONS

Similar to macroscopic ferroelectric samples, polarization and switching in thin films obtained by the sol–gel method are caused mainly by the motion of domain boundaries. The character (mechanism) of this motion depends mainly on the interactions between grain boundaries and point defects, which are responsible for potential barriers formed on the paths of domain-boundary motion. The probability of overcoming these barriers depends on the sample temperature and the frequency and amplitude of the measuring field. A more detailed classification of point defects interacting with domain boundaries (ultraweak, weak, moderate, and strong defects) is suggested. Depending on the sample temperature and the frequency and amplitude of the measuring field, these defects can be successively transformed into one another.

ACKNOWLEDGMENTS

We are grateful to E.S. Popov and V.K. Yarmarkin for fruitful discussions. This study was supported by the Russian Foundation for Basic Research (project no. 02-02-16232), the Competition Center of the Ministry of Education of the Russian Federation (project no. E02-3.4-424), and the program *Scientific Research of Higher Schools along the Priority Directions of Science and Technology* (project no. 202.03.02.04), and the Leading Scientific School, NSh-15.14.2003.2.

REFERENCES

1. Y. J. Song, PhD Thesis (Virginia Polytechnic Inst., State Univ., Blacksburg, 1998), p. 149.
2. J. F. Scott, Ferroelectr. Rev. **1**, 1 (1998).
3. J. K. Lee, PhD Thesis (Virginia Polytechnic Inst., State Univ., Blacksburg, 1999).
4. A. Sheikholeslami and P. G. Gulak, Proc. IEEE **88** (3), 667 (2000).
5. Y. Xu and J. D. MacKenzie, Integr. Ferroelectr. **1**, 17 (1992).
6. V. V. Lemanov, A. A. Iofan, K. N. Solov'eva, *et al.*, Pis'ma Zh. Tekh. Fiz. **22** (3), 72 (1996) [Tech. Phys. Lett. **22**, 261 (1996)].
7. S. Tirumala, PhD Thesis (Virginia Polytechnic Inst., State Univ., Blacksburg, 2000).
8. S.-O. Ryu, PhD Thesis (Virginia Polytechnic Inst., State Univ., Blacksburg, 1999).
9. D. Takashima, IEICE Trans. Electron. **84-C**, 747 (2001).
10. D. Damjanovic, Rep. Prog. Phys. **61**, 1267 (1998).
11. D. V. Taylor and D. Damjanovic, Appl. Phys. Lett. **73**, 2045 (1998).
12. D. Bolten, O. Lohse, M. Grossmann, and R. Waser, Ferroelectrics **221**, 251 (1999).
13. S. J. Lee, K. Y. Kang, S. K. Han, *et al.*, J. Korean Phys. Soc. **32**, 1645 (1998).
14. V. K. Yarmarkin and S. P. Teslenko, Fiz. Tverd. Tela (St. Petersburg) **40**, 1915 (1998) [Phys. Solid State **40**, 1738 (1998)].

15. G. M. Vizdrik, Candidate's Dissertation in Physics and Mathematics (Moscow, 2003).
16. A. V. Shil'nikov, Doctoral Dissertation in Physics and Mathematics (1988).
17. A. V. Shil'nikov, N. M. Galiyarova, S. V. Gorin, *et al.*, Izv. Akad. Nauk SSSR, Ser. Fiz. **55**, 578 (1991).
18. V. N. Nesterov, Candidate's Dissertation in Physics and Mathematics (Volgograd, 1997).
19. A. V. Shil'nikov, A. P. Pozdnyakov, V. N. Nesterov, *et al.*, Fiz. Tverd. Tela (St. Petersburg) **43**, 1516 (2001) [Phys. Solid State **43**, 1576 (2001)].
20. A. V. Shil'nikov, V. N. Nesterov, and A. I. Burkhanov, Ferroelectrics **175**, 145 (1996).
21. L. I. Solov'eva, I. E. Obvintseva, M. I. Yanovskaya, *et al.*, Neorg. Mater. **32**, 866 (1996).
22. K. A. Vorotilov, M. I. Yanovskaya, and O. A. Dorokhova, Integr. Ferroelectr. **3**, 33 (1993).
23. M. I. Yanovskaya, Integr. Ferroelectr. **19**, 193 (1998).
24. A. V. Shil'nikov, I. V. Otsarev, A. I. Burkhanov, *et al.*, Izv. Ross. Akad. Nauk, Ser. Fiz. **64**, 1239 (2000).
25. ATM 150-70, in *USA Standards* (TsIONT PIK VINITI, 1979), No. 25, pp. 188–207.
26. A. V. Shil'nikov, J. Korean Phys. Soc. **32**, 305 (1998).
27. J. T. Evans, Integr. Ferroelectr. **37**, 173 (2001).
28. A. V. Shil'nikov, *Physics of Dielectrics and Semiconductors* (Volgogr. Politekh. Inst., Volgograd, 1970), No. 29, p. 95.
29. Yu. M. Poplavko, *Physics of Dielectrics* (Vishcha Shkola, Kiev, 1980).
30. A. V. Shil'nikov, A. P. Pozdnyakov, and N. M. Galiyarova, in *Proceedings of International Scientific and Practical Conference on Fundamental Problems of Piezoelectric Instrument Engineering* (Moscow, 2000), p. 95.
31. A. V. Shil'nikov, Izv. Akad. Nauk SSSR, Ser. Fiz. **51**, 1726 (1987).
32. A. M. Savin, É. S. Popov, and A. V. Shil'nikov, Fiz. Tverd. Tela (Leningrad) **28**, 2470 (1986) [Sov. Phys. Solid State **28**, 1382 (1986)].
33. A. V. Shil'nikov, R. A. Laletin, A. I. Burkhanov, *et al.*, Mikrosist. Tekh., No. 4, 16 (2002).

Translated by L. Man

Crystallography Reports, Vol. 49, No. 1, 2004, pp. 143–148. Translated from Kristallografiya, Vol. 49, No. 1, 2004, pp. 151–156.

NANOMATERIALS

Dedicated to the 80th Birthday of L.A. Shuvalov

Dispersion of Optical Anisotropy in Nanostructurized Silicon Films

L. A. Golovan'*, A. F. Konstantinova, K. B. Imangazieva***, E. Yu. Krutkova*, V. Yu. Timoshenko*, and P. K. Kashkarov***

** Faculty of Physics, Moscow State University, Vorob'evy gory, Moscow, 119992 Russia*
e-mail: leo@vega.phys.msu.su
*** Shubnikov Institute of Crystallography, Russian Academy of Sciences, Leninskiĭ pr. 59, Moscow, 119333 Russia*
e-mail: afkonst@ns.crys.ras.ru
**** Issyk-Kul State University, Kyrgyzstan*
Received August 15, 2003

Abstract—Optical characteristics of (110) oriented porous silicon films obtained by electrochemical etching are studied. Dispersion of refractive indices, dichoroism in the visible range of the spectrum, depolarization factor, and porosity of silicon films are measured. It is shown that the results obtained may be described based on the generalized Bruggeman model. Possible causes of the established discrepancies between the experimental data and the model are discussed. © *2004 MAIK "Nauka/Interperiodica".*

INTRODUCTION

The study of properties of nanostructurized semiconductor systems is one of the main directions of modern solid state physics. In particular, great interest is attracted to silicon nanostructures, including nanostructures of porous silicon obtained by electrochemical etching of crystalline silicon. Thus, porous silicon consists of silicon nanocrystals separated by pores with the size ranging from 1 to 100 nm, depending on the doping level of the wafer and the preparation conditions. Although this material has been known since 1956 [1], it only became popular in 1990 after the establishment of the fact that the efficient photoluminescence of microporous silicon consisting of 4-nm nanocrystals, which was observed in the visible range of the spectrum, can be interpreted in terms of the quantum size effect [2]. Along with remarkable electronic properties [3, 4], porous silicon also possesses a number of attractive optical properties to be studied in detail.

The dimensions of silicon nanocrystals are much less than the optical length of light waves, which allows one to consider porous silicon as a homogeneous optical medium with effective permittivity different from permittivity of crystalline silicon. Experiments show [4–6] that porous silicon with nanocrystal size ranging from 10 to 50 nm (mesoporous silicon) can be considered in the so-called effective-medium approximation within which permittivity of porous silicon is determined by permittivity and porosity of silicon and permittivity of the medium filling the pores. The real and imaginary parts of permittivity of porous silicon are often described based on the Bruggeman model [4–7].

As is well known, crystalline silicon belongs to the cubic system and can be considered as an optically isotropic medium. However, the preferable formation of pores along the ⟨100⟩ [3] directions gives rise to optical anisotropy—the so-called shape anisotropy [8].

Comparatively weak birefringence in free porous silicon films was observed at certain angles of incidence formed with the surface normal of the films prepared by electrochemical etching of (100)-oriented crystalline silicon wafers [9]. Higher birefringence values were observed in mesoporous silicon layers on crystalline-silicon substrates with low-symmetric surfaces, e.g., on (211) [10] and (110) [11, 12] wafers, with the optic axis being located in the surface plane. Moreover, birefringence of porous silicon films is very sensitive to the dielectric medium filling these pores, which allows one to use these layers in various sensor devices [11]. Further studies showed [13] that double-refracting porous-silicon layers had properties similar to those of uniaxial negative crystals and that their optic axis coincided with the ⟨001⟩ directions, whereas the difference in the refractive indices of the ordinary and extraordinary waves attained a value of 0.24 in the infrared wavelength range. The pronounced anisotropy allows one to reach phase synchronism in the generation of optic harmonics [14], which, in turn, allows one to use porous silicon as a phase-matching matrix filled with a material possessing high quadratic nonlinear

1063-7745/04/4901-0143$26.00

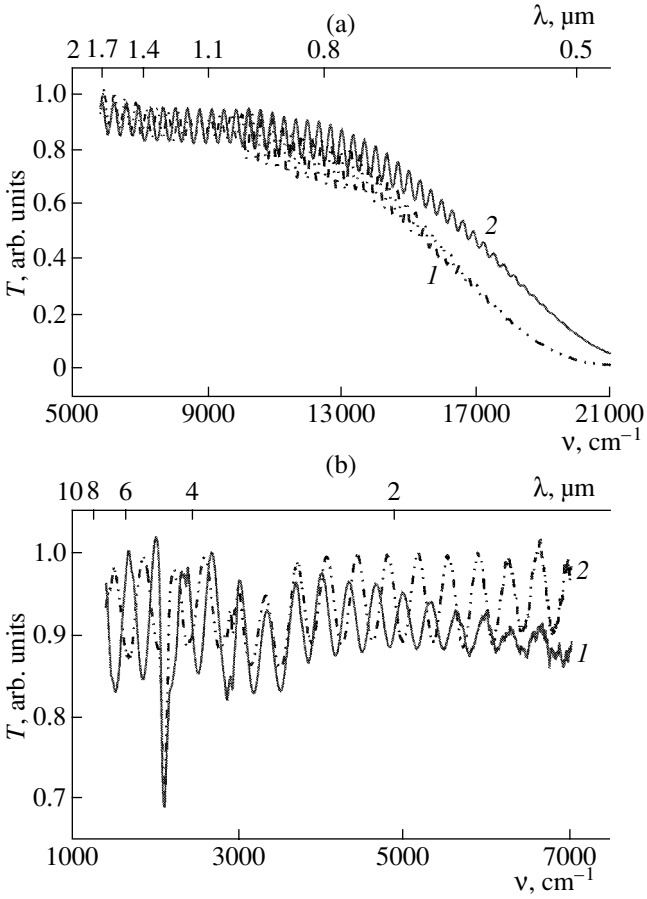

Fig. 1. Transmission spectra of a porous silicon film (d = 10 μm) in the (a) visible and near IR and (b) medium IR spectrum ranges. Curve *1* and *2* correspond to ordinary and extraordinary waves, respectively.

permittivity. The shape anisotropy of silicon nanocrystals and pores is also seen from the anisotropy of optical absorption in porous silicon layers [15].

Thus, the efficient use of anisotropic nanostructurized silicon requires the detailed study of its parameters and, first of all, their dispersion. At the same time, the knowledge of the dispersion properties of double-refracting porous silicon layers would allow one to determine the validity the effective-medium model for porous silicon.

DETERMINATION OF REFRACTIVE INDICES OF POROUS SILICON

We studied free porous-silicon films obtained by anodic electrochemical etching of (110) oriented single-crystal silicon wafers with resistivity ranging from 1.5 to 3.0 mΩ cm in fluoric acid mixed with ethanol in a 1 : 1 ratio. The density of the etching current was 50 mA/cm^2. This etching mode gives rise to the formation of mesoporous silicon. The porous silicon films were separated from the substrates because of a drastic increase in the current density. The film thickness measured under an optical microscope was 10 μm; the porosity was about 75%.

The refractive indices were determined from the transmission spectra of porous silicon films studied in the visible and near IR range on an MDR-12 monochromator and in the medium IR range (1400–7000 cm^{-1}) with the use of a Perkin-Elmer Spectrum RX I FT-IR Fourier spectrometer. The measurements were performed for two types of polarization of the normally incident light—polarization parallel to the optic axis of the sample and polarization normal to this axis.

Figure 1 shows the transmission spectra of a porous silicon film for the normal incidence of the plane-polarized light onto the sample surface. The measured values ranged from 0.5 to 14.0 μm. The spectra obtained were typical of light interference in a thin film. Different spectra clearly showed anisotropy. In the short-wave range (wave length less than 0.6 μm), no interference could be observed because of strong absorption of light in this spectral range. The IR transmission spectra showed the lines corresponding to Si–H_x bonds and distortions associated with absorption of light by water molecules.

Analysis of the spectra shown in Fig. 1 allowed us to determine the refractive indices of the ordinary and extraordinary waves. The dispersion of refractive indices did not allow us to use the simple formula

$$n = 1/2d\Delta\nu, \tag{1}$$

where n is the refractive index, d is the film thickness, and $\Delta\nu$ is the difference between the wave numbers corresponding to two neighboring maxima (minima) of the spectrum, because it yielded considerably overestimated refractive indices (see Discussion in [16]). Therefore, when determining refractive indices, one has to take into account the order of an interference maximum (minimum), which would allow one to determine the refractive index from the formula

$$\begin{aligned} n &= m\lambda/2d \text{ (for maximum)}, \\ n &= (m + 1/2)\lambda/2d \text{ (for minimum)}, \end{aligned} \tag{2}$$

where m is the order of the interference maximum (minimum) and λ is the corresponding wavelength. The minimum error in the determination of the refractive index by formula (1) is attained in the medium IR range, where dispersion has the minimum value. Once the interference order of the maximum possible wavelength is determined, one can enumerate all the interference extrema up to the visible range. Thus, the maxima with wave numbers 1669 and 1495 cm^{-1} for ordinary and extraordinary waves, respectively, have interference orders 5 and 4.

The results of such a calculation are presented in Fig. 2. It is seen that, with a decrease in the wavelength, the refractive index of silicon increases, which is associated with an increase of silicon dispersion in this range. One can also see that the difference between the

refractive indices of the ordinary and extraordinary waves increases with a decrease in the wavelength.

The refractive indices were approximated using the formula

$$n_{o,e}^2 = A_{o,e} + K_{o,e}/(\lambda^2 - B_{o,e}) + C_{o,e}\lambda^2, \quad (3)$$

where λ is the wavelength in micrometers. The coefficients were determined as $A_o = 2.249$, $K_o = 0.135$, $B_o = 0.042$, $C_o = -9.8 \times 10^{-4}$, $A_e = 1.827$, $K_e = 0.056$, $B_e = 0.034$, $C_e = -4.5 \times 10^{-4}$.

DETERMINATION OF BIREFRINGENCE AND DICHROISM OF POROUS SILICON

The measurements necessary for the determination of the optical parameters of free porous silicon films were made on a spectropolarimetric modular complex [17, 18] consisting of a stabilized light source, a diffraction high-transmission monochromator, a fiber-optical depolarizer, blocks of a rotating polarizer and a rotating analyzer, a block of a photodetector, and a sample holder. The measurements were made in the spectral range from 0.4 to 0.8 μm. The complex operation and processing of the experimental results were controlled with the use of a specially designed package of programs that enabled one to set the rotation steps of the analyzer and polarizer separately or to set their synchronous rotation in the range from 0° to 360° and to vary the wavelength and calculate the anisotropic optical characteristics of the sample.

The intensity of light transmitted by the polarizer–sample–analyzer system is written in the form [18]

$$I = K[a + b_1\cos 2\alpha + b_2\sin 2\alpha + c_1\cos 4\alpha + c_2\sin 4\alpha], \quad (4)$$

where α is the angle of sample rotation about the horizontal axis or the simultaneous rotation of the polarizer and analyzer, with the sample being in the fixed position. For a sample possessing dichroism and birefringence, the coefficients in Eq. (4) are

$$\begin{gathered} K = 0.25e^{(-2\pi d(\kappa_o + \kappa_e)/\lambda)}, a = 3\cosh\delta + \cos\Delta, \\ b_1 = 2\sinh\delta\cos 2\alpha_0, \quad b_2 = -2\sinh\delta\sin 2\alpha_0, \\ c_1 = (\cosh\delta - \cos\Delta)\cos 4\alpha_0, \\ c_2 = -(\cosh\delta - \cos\Delta)\sin 4\alpha_0, \end{gathered} \quad (5)$$

where α_0 is the angle between the transmission direction of the polarizer and the principal direction of the sample (direction of sample extinction in the crossed polarizer and analyzer), and the quantities δ and Δ have the form

$$\Delta = 2\pi d\delta n/\lambda, \quad \delta = 2\pi d\delta\kappa/\lambda. \quad (6)$$

Here, the complex refractive indices of the ordinary and extraordinary waves are written as $N_{o,e} = n_{o,e} + i\kappa_{o,e}$, $\delta n = n_o - n_e$ is birefringence, and $\delta\kappa = \kappa_o - \kappa_e$ is dichroism. Using the package of programs, one can calculate

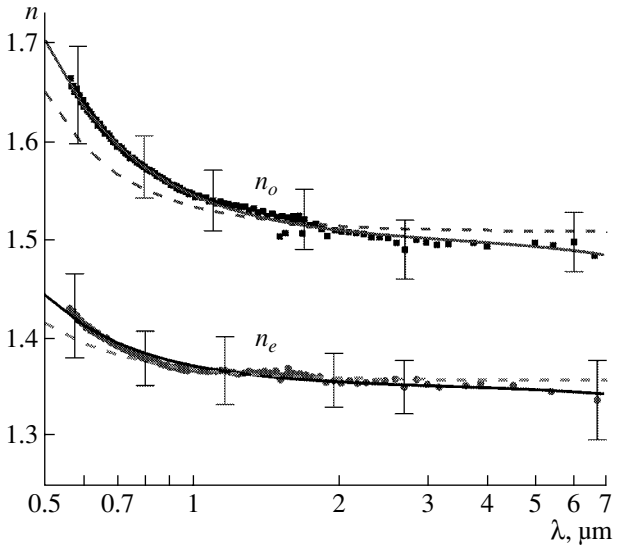

Fig. 2. Dispersion of refractive indices n_o and n_e in porous silicon. Solid lines indicate approximation by Eq. (3), and dashed lines, by Eq. (8) at porosity $p = 0.74$ and depolarization factor $L_e = 0.43$.

the Fourier coefficients a, b, and c ($b^2 = b_1^2 + b_2^2$, $c^2 = c_1^2 + c_2^2$) and determine the parameters Δ and δ,

$$\begin{gathered} \cos\Delta_0 = (a - 3c)/\sqrt{(a + c)^2 - b^2}, \\ e^{2\delta} = (a + b + c)/(a - b + c) \end{gathered} \quad (7)$$

and also birefringence δn and dichroism $\delta\kappa$. One has to take into account that $\Delta = 2\pi k + \pi l \pm \Delta_0$ ($k = 0, 1, 2, 3\ldots$, and $l = 0, \pm 1$ depending on the path difference $d\delta n$).

Figure 3 shows the $I(\alpha)$ dependences obtained at various wavelengths. It is clearly seen that a porous silicon film is doubly refracting (because the $I(\alpha)$ dependences oscillate) and possesses dichroism (because the extremum $I(\alpha)$ values are not equal to one another). Thus, at $\lambda = 0.79$ μm (curve *1*), this dependence has four maxima having the same amplitudes, which indicates that the sample has no noticeable dichroism at this wavelength. At $\lambda = 0.55$ μm (curve *2*), the maxima considerably differ, which indicates the presence of dichroism. At $\lambda = 0.52$ μm (curve *3*), two of the four maxima are suppressed, which indicates an increase in dichroism. Finally, at $\lambda = 0.5$ μm (curve *4*), $I(\alpha)$ also has four maxima.

The δn and $\delta\kappa$ values determined from the above curves are shown in Figs. 4a and 4b. Birefringence values determined from formula (3) in the range from 0.6 to 0.8 μm are consistent with the results obtained. With a decrease in the wavelength, birefringence increases monotonically and attains the value $\delta n = 0.265$ at $\lambda = 0.52$ μm, whereas, at $\lambda = 7$ μm, we have $\delta n = 0.15$. The

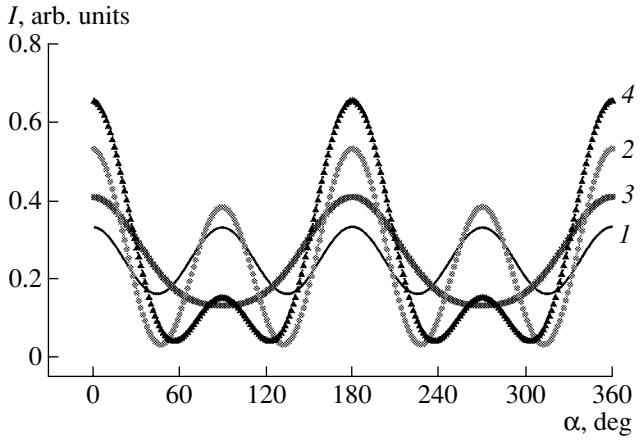

Fig. 3. Intensity I as a function of the rotation angle $I(\alpha)$ of a porous silicon film at the wavelengths λ (*1*) 0.79, (*2*) 0.55, (*3*) 0.52, and (*4*) 0.5 μm.

dependence of dichroism on the wavelength is nonmonotonic and has an extremum at $\lambda = 0.52$ μm.

DISCUSSION OF RESULTS WITHIN THE FRAMEWORK OF THE EFFECTIVE-MEDIUM MODEL

To describe optical anisotropy of porous silicon films we invoked the generalized Bruggeman model [19], which allowed us to consider an ensemble of ellipsoids of rotation with the parallel axes and the rotation axis of ellipsoids being coincident with the optic axis. The Bruggeman theory relates the effective permittivity of such a system, ε_{eff}, to the permittivity of silicon, ε_{Si}, and permittivity of the dielectric material filling its pores, ε_d (in our case, air with $\varepsilon_d = 1$):

$$p\frac{\varepsilon_d - \varepsilon_{\text{eff}}}{\varepsilon_{\text{eff}} + L(\varepsilon_d - \varepsilon_{\text{eff}})} + (1-p)\frac{\varepsilon_{\text{Si}} - \varepsilon_{\text{eff}}}{\varepsilon_{\text{eff}} + L(\varepsilon_{\text{Si}} - \varepsilon_{\text{eff}})} = 0. \quad (8)$$

Here, p is the material porosity and $L_{\parallel,\perp}$ is the depolarization factor determined by the semiaxis ratio of the ellipsoid of rotation. The $L_{\parallel,\perp}$ value depends on the direction of polarization of the electric field of a light wave. If the electric field is polarized along the ellipsoid axis, the wave is extraordinary [8, 19] and is given by the formula [20]

$$L_{\parallel} = 1/(1-x^2)[((1-x)\arcsin(\sqrt{1-x^2}))/\sqrt{1-x^2}], \quad (9)$$

where x is the ratio of the polar to equatorial semiaxis of the ellipsoid of rotation.

The depolarization factor $L_{\perp}$ for the perpendicular polarization of the ordinary wave is related to $L_{\parallel}$ by the formula

$$2L_{\perp} + L_{\parallel} = 1. \quad (10)$$

The effective permittivities $\varepsilon^o_{\text{eff}}$ and $\varepsilon^e_{\text{eff}}$ are determined from the measured refractive indices [see formula (3)] as $\varepsilon^o_{\text{eff}} = n_o^2$ and $\varepsilon^e_{\text{eff}} = n_e^2$. Substituting the latter values into Eq. (8), we arrive at the formula of the depolarization factor $L_{\parallel}$ and porosity p (in this case, the real part of the refractive index of crystalline silicon was approximated by the method suggested in [21], whereas the imaginary part was approximated using the data from [22]):

$$L_{\parallel} = \frac{(\varepsilon^o_{\text{eff}} - \varepsilon^e_{\text{eff}})\varepsilon^e_{\text{eff}}\varepsilon^o_{\text{eff}} + 0.5(\varepsilon^o_{\text{eff}} - 1)(\varepsilon_{\text{Si}} - \varepsilon^o_{\text{eff}})\varepsilon^e_{\text{eff}}}{\varepsilon^o_{\text{eff}}(\varepsilon^e_{\text{eff}} - 1)(\varepsilon_{\text{Si}} - \varepsilon^e_{\text{eff}}) + 0.5(\varepsilon^o_{\text{eff}} - 1)(\varepsilon_{\text{Si}} - \varepsilon^o_{\text{eff}})\varepsilon^e_{\text{eff}}},$$
$$p = \frac{(\varepsilon_{\text{Si}} - \varepsilon^e_{\text{eff}})(\varepsilon^e_{\text{eff}} - L_{\parallel}(\varepsilon^e_{\text{eff}} - 1))}{(\varepsilon_{\text{Si}} - 1)\varepsilon^e_{\text{eff}}}. \quad (11)$$

The parameters $L_{\parallel}$, $L_{\perp}$, and p are shown in Fig. 5 as functions of wavelength. Within the Bruggeman model, these parameters are independent of the wavelengths. As follows from our analysis, the values determined by formulas (10) and (11) really only weakly depend on the wavelength—the L value varies within 0.427–0.435, and porosity, within 0.727–0.750. It should also be noted that, as a rule, the experimental errors in porosity measured by the gravimetric method are somewhat higher; the discrepancy in the refractive indices does not exceed the experimental error. The value $L_{\parallel} \sim 0.43$ corresponds to the semiaxis ratio $x \sim 0.7$. As is seen from Fig. 5, in the range 0.7–7.0 μm, the value of $L_{\parallel}$ increases with a decrease in the wavelength. This deviation from the Bruggeman model seems to be associated with the closeness of the wavelength to the nanocrystal size. At shorter wavelengths, one has to take into account absorption, which is rather difficult because of the lack of data on the absolute values of the imaginary parts of permittivities in a porous silicon layer.

Now, proceed to analysis of dichroism dispersion. Using the parameters $L_{\parallel}$, $L_{\perp}$, and p determined above and taking into account the imaginary part of permittivity for crystalline silicon, we calculated the imaginary parts of the effective refractive indices of porous silicon from Eq. (8). The results are presented in Fig. 4b (solid line). In this case, the model used allows us to describe the behavior of $\delta\kappa$ at $\lambda > 0.55$ μm; however, with a decrease in the wavelength, the experimentally determined and calculated $\delta\kappa$ values become inconsistent.

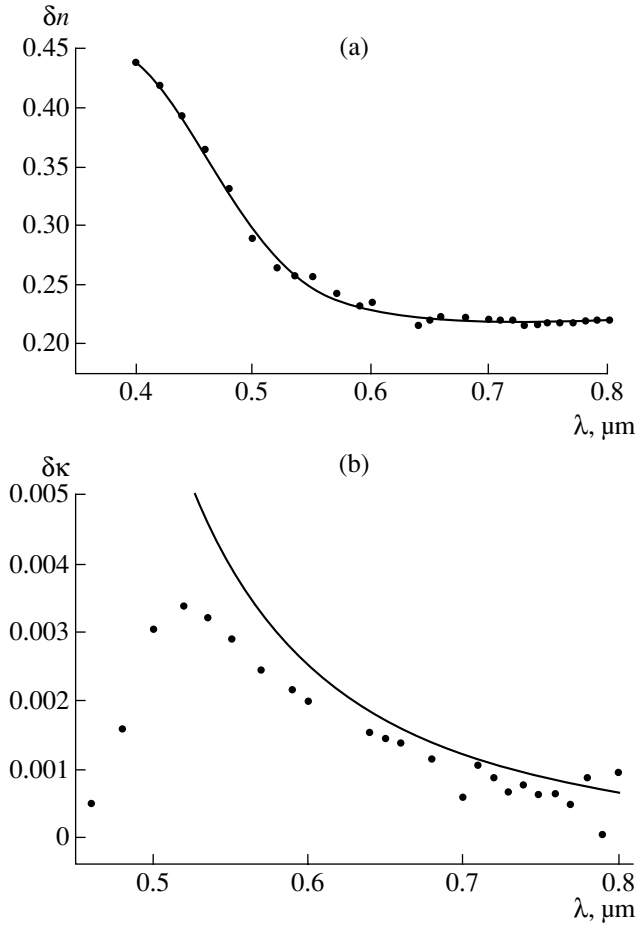

Fig. 4. Dispersion of anisotropy parameters in porous silicon films: (a) dispersion of birefringence, (●) birefringence calculated by Eq. (7), solid line indicates approximated birefringence, (b) dichroism calculated by Eq. (7), solid line indicates dichroism approximated by Eq. (8).

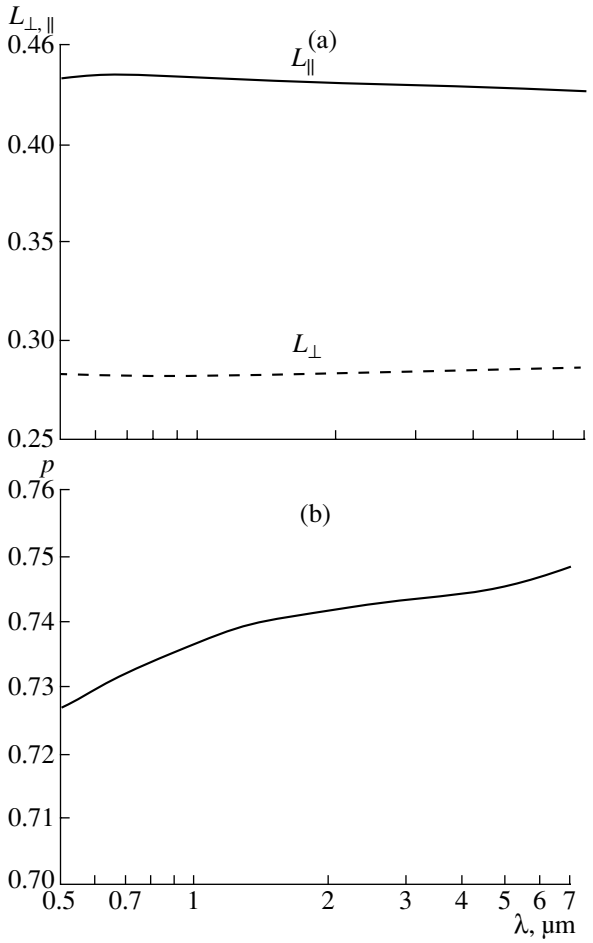

Fig. 5. (a) Depolarization factor and (b) porosity of a silicon film obtained from analysis of the experimental data.

It should be noted that the optical properties of mesoporous silicon in the visible part of the short-wave range should be studied in more detail, because, with an approach of the wavelength to the nanocrystal size, the optical properties of porous silicon can considerably change. In particular, it was recently established that the third-harmonic generation (355 nm) in mesoporous silicon is much more efficient than its generation in crystalline and microporous silicon [23].

In order to interpret the results obtained, we assumed that, with a decrease in the wavelength, scattering from silicon nanocrystals becomes more intense and is probably also anisotropic. It seems that a certain role in this spectral range is also played by the effects of light localization [24]. Thus, for silicon nanocrystals 20 nm in diameter and at a wavelength of 0.5 μm, the estimation of the free paths of photons yields a value of about 0.8 μm, which indicates the approach to the mode of light localization. To study dichroism in porous silicon films in more detail, one has to perform new experiments, including experiments on films with various porosities.

CONCLUSIONS

Thus, the optical characteristics of porous silicon films obtained by electrochemical etching of heavily doped (110) oriented silicon wafers have been studied. For the first time, the dispersion of the refractive indices was determined over the wide spectrum range. Dispersion of birefringence and dichroism in the visible spectrum range up to 0.4 μm were measured. Birefringence monotonically increases with a decrease in the wavelength, whereas the dependence of dichroism on the wavelength is nonmonotonic. The experimental data obtained were compared with the data calculated based on the generalized Bruggeman model. It was shown that dispersion of refractive indices, birefringence, and dichroism in the red and infrared spectrum ranges are satisfactorily described within the framework of this model. The deviation from the Bruggeman model at shorter wavelengths is explained by the approach of the wavelength to the size of nanocrystals.

ACKNOWLEDGMENTS

We are grateful to A.I. Efremova, G.I. Utkin, B.V. Nabatov, and E.A. Evdishchenko for fruitful discussions. This study was supported by the Russian Foundation for Basic Research (project no. 02-02-17259), the American Foundation for Civil Research and Developments (project no. RE2-2369), and the Programs of the Ministry of Science and Technologies of the Russian Federation.

REFERENCES

1. A. Uhlir, Bell Syst. Tech. J. **35**, 333 (1956).
2. L. T. Canham, Appl. Phys. Lett. **57**, 1046 (1990).
3. A. G. Cullis, L. T. Canham, and P. D. G. Calcott, J. Appl. Phys. **82**, 909 (1997).
4. D. Kovalev, H. Heckler, G. Polisski, and F. Koch, Phys. Status Solidi B **215**, 871 (1999).
5. W. Theiss, Surf. Sci. Rep. **29**, 91 (1997).
6. O. Bisi, S. Ossicini, and L. Pavesi, Surf. Sci. Rep. **38**, 1 (2000).
7. D. A. G. Bruggeman, Ann. Phys. (Leipzig) **24**, 636 (1935).
8. M. Born and E. Wolf, *Principles of Optics*, 4th ed. (Pergamon Press, Oxford, 1969; Nauka, Moscow, 1970).
9. M. E. Kompan, Y. Salonen, and I. Yu. Shabanov, Zh. Éksp. Teor. Fiz. **117**, 368 (2000) [JETP **90**, 324 (2000)].
10. O. G. Sarbeĭ, E. K. Frolova, R. D. Fedorovich, and D. B. Dan'ko, Fiz. Tverd. Tela (St. Petersburg) **42**, 1205 (2000) [Phys. Solid State **42**, 1240 (2000)].
11. D. Kovalev, G. Polisski, J. Diener, *et al.*, Appl. Phys. Lett. **78**, 916 (2001).
12. N. Künzner, D. Kovalev, J. Diener, *et al.*, Opt. Lett. **26**, 1265 (2001).
13. L. P. Kuznetsova, A. I. Efimova, L. A. Golovan', *et al.*, Fiz. Tverd. Tela (St. Petersburg) **44**, 780 (2002) [Phys. Solid State **44**, 811 (2002)].
14. L. A. Golovan, V. Yu. Timoshenko, A. B. Fedotov, *et al.*, Appl. Phys. B **73**, 31 (2001).
15. V. Yu. Timoshenko, L. A. Osminkina, L. A. Golovan, *et al.*, Phys. Rev. B **67**, 113405-1 (2003).
16. M. I. Strashnikova, Opt. Spektrosk. **93**, 142 (2002) [Opt. Spectrosc. **93**, 132 (2002)].
17. A. F. Konstantinova, B. N. Grechushnikov, B. V. Bokut', and E. G. Valyashko, *Optical Properties of Crystals* (Nauka i Tekhnika, Minsk, 1995).
18. G. I. Utkin, S. V. Alekseev, U. V. Volnov, *et al.*, Proc. SPIE, Lightmetry **42**, 178 (2000).
19. J. E. Spanier and I. P. Herman, Phys. Rev. B **61**, 10437 (2000).
20. J. A. Osborn, Phys. Rev. **67**, 351 (1945).
21. E. M. Voronkova, B. N. Grechushnikov, G. I. Distler, and I. P. Petrov, *Optical Materials for Infrared Technology* (Nauka, Moscow, 1965).
22. D. E. Aspnes and A. A. Studna, Phys. Rev. B **27**, 985 (1983).
23. L. A. Golovan, L. P. Kuznetsova, A. B. Fedotov, *et al.*, Appl. Phys. B **76**, 429 (2003).
24. V. E. Kravtsov, V. M. Agranovich, and K. I. Grigorishin, Phys. Rev. B **44**, 4931 (1991).

Translated by L. Man

Crystallography Reports, Vol. 49, No. 1, 2004, pp. 15–19. Translated from Kristallografiya, Vol. 49, No. 1, 2004, pp. 20–24.

THEORY OF CRYSTAL STRUCTURES

Dedicated to the 80th Birthday of L.A. Shuvalov

Correlation between the Lattice Parameters of Crystals with Perovskite Structure

G. A. Geguzina and V. P. Sakhnenko

Institute of Physics, Rostov State University, pr. Stachki 194, Rostov-on-Don, 344090 Russia

e-mail: denis@ip.rsu.ru

Received August 15, 2003

Abstract—The correlation $(\bar{a}_2 + \bar{a}_3) = (\bar{a}_1 + \bar{a}_4)$ has been established for the mean parameters of the reduced perovskite unit cells, $\bar{a}_1$, $\bar{a}_2$, $\bar{a}_3$, and $\bar{a}_4$, of four arbitrary compounds with the perovskite structure having the compositions (1) ABX_3, (2) $A'BX_3$, (3) $AB'X_3$, and (4) $A'B'X_3$, where A, A' and B, B' are the pairs of metal atoms with equal valences and X is an oxygen or halogen atom. The above correlation is consistent with the model of harmonic quasi-elastic atomic interactions. © *2004 MAIK "Nauka/Interperiodica".*

INTRODUCTION

The symmetric phases of crystals with the perovskite structure whose chemical composition is described by the general formula ABX_3 (where X is an oxygen or halogen atom) have a primitive cubic lattice, with the parameter of each group of crystals (with the given X) being determined by the "sizes" of the constituent atoms. Obviously, it is impossible to attain the in-pair correlation between cationic radii for the whole family of these crystals, which dictates the introduction of the notion of deformable interatomic A–X and B–X bonds [1]. The model based on this notion correlates the equilibrium unit-cell parameter with the minimum elastic energy of deformation of interatomic bonds, which allows us to calculate parameters of the cubic unit cell from the given compound composition [1–3].

The main assumption underlying the approach suggested states that it is possible to introduce an equilibrium length and rigidity for each A–X and B–X bond equal for all the compounds of the perovskite family. Note here that these parameters, characterizing the interaction of each pair of A and X or B and X atoms, are determined mainly by the coordination number with respect to X and the valence of an A or B atom, respectively, which allows one to use these parameters in the solution of similar problems for the compounds of other structure types if they possess the same coordination numbers of A and B atoms [4–6].

At room temperature, most of the compounds with the perovskite structure (described in a large number of structural data) are in the low-symmetric phase states characterized by the space groups that are the subgroups of the sp. gr. O_h^1 that describes the symmetric phase. These phases are formed as a result of one or several phase transitions accompanied by the change of the unit-cell shape. However, experiments show that the unit-cell volume only weakly depends on temperature and that the jumps in the volume accompanying the first-order phase transitions characteristic of the perovskite structures are feebly marked. The $\Delta V/V$ value is determined by the second-order effects (such as the striction accompanying phase transitions) and is proportional to the squared or higher-degree order parameter.

All these changes are the results of small variations in high energies, which determine the mean unit-cell parameter and are taken into account by the model of deformable interatomic bonds. Taking into account the aforesaid and considering the whole perovskite family, we can compare the parameters of the reduced cubic perovskite unit cells of various compounds calculated as the average parameter $\bar{a} = \sqrt[3]{V_{\text{cell}}}$, where V_{cell} is the volume corresponding to one ABX_3 formula unit of a distorted (in the general case) perovskite unit cell at room temperature.

FROM THE MODEL TO CRYSTALLOGRAPHIC REGULARITY

The search for the method of *a priori* calculation of the unit-cell parameters in structure modeling proceeds from at least three requirements. First, the method should be internally consistent. Second, it should allow one to calculate the unit-cell parameters with a sufficient accuracy. And third, the system of bond lengths of unstrained interatomic A–X and B–X bonds calculated by this method should include all the distances between

1063-7745/04/4901-0015$26.00

Table 1. Groups of four binary oxides and fluorides with the compositions of the $A^{II}B^{IV}O_3$ and $A^{I}B^{II}F_3$ types, the experimental mean parameters $\bar{a}_{exp}$ of the reduced perovskite unit cells, and their sums $s_{23} = \bar{a}_2 + \bar{a}_3$ and $s_{14} = \bar{a}_1 + \bar{a}_4$, and $\Delta = s_{23} - s_{14}$

Serial number of the group	Composition of the oxides in the group	Parameters $\bar{a}_{exp}$, s_{23}, s_{14}, and Δ(Å)				Serial number of the group	Composition of the oxides in the group	Parameters $\bar{a}_{exp}$, s_{23}, s_{14}, and Δ(Å)			
		$\bar{a}_{exp}$	s_{23}	s_{14}	Δ			$\bar{a}_{exp}$	s_{23}	s_{14}	Δ
OXIDES						1. $PbTiO_3$: $\bar{a}_1$ = 3.97; 2. $BaTiO_3$: $\bar{a}_2$ = 4.00					
$A^{II}B^{IV}O_3$						16	3. $PbHfO_3$ 4. $BaHfO_3$	4.12 4.17	8.12	8.14	−0.02
1. $CaTiO_3$: $\bar{a}_1$ = 3.822; 2. $SrTiO_3$: $\bar{a}_2$ = 3.90						17	3. $PbZrO_3$ 4. $BaZrO_3$	4.15 4.19	8.15	8.16	−0.01
1	3. $CaRuO_3$ 4. $SrRuO_3$	3.84 3.92	7.74	7.74	0	1. $PbTiO_3$: $\bar{a}_1$ = 3.97; 2. $CaTiO_3$: $\bar{a}_2$ = 3.82					
2	3. $CaSnO_3$ 4. $SrSnO_3$	3.95 4.03	7.85	7.85	0	18	3. $PbHfO_3$ 4. $CaHfO_3$	4.12 3.99	7.94	7.96	−0.02
3	3. $CaHfO_3$ 4. $SrHfO_3$	3.99 4.07	7.89	7.89	0	19	3. $PbZrO_3$ 4. $CaZrO_3$	4.15 4.01	7.97	7.98	−0.01
4	3. $CaZrO_3$ 4. $SrZrO_3$	4.01 4.10	7.91	7.92	−0.01	1. $PbTiO_3$: $\bar{a}_1$ = 3.97; 2. $SrTiO_3$: $\bar{a}_2$ = 3.90					
1. $CaTiO_3$: $\bar{a}_1$ = 3.82; 2. $BaTiO_3$: $\bar{a}_2$ = 4.00						20	3. $PbHfO_3$ 4. $SrHfO_3$	4.12 4.07	8.02	8.04	−0.02
5	3. $CaRuO_3$ 4. $BaRuO_3$	3.84 4.05	7.84	7.87	−0.03	21	3. $PbZrO_3$ 4. $SrZrO_3$	4.15 4.10	8.05	8.07	−0.02
6	3. $CaSnO_3$ 4. $BaSnO_3$	3.95 4.11	7.95	7.93	0.02	1. $PbTiO_3$: $\bar{a}_1$ = 3.97; 2. $CdTiO_3$: $\bar{a}_2$ = 3.90					
7	3. $CaHfO_3$ 4. $BaHfO_3$	3.99 4.17	7.99	7.99	0	22	3. $PbHfO_3$ 4. $CdHfO_3$	4.12 3.96	7.91	7.93	−0.02
8	3. $CaZrO_3$ 4. $SrZrO_3$	4.01 4.19	8.01	8.01	0	1. $CaTiO_3$: $\bar{a}_1$ = 3.82; 2. $CdTiO_3$: $\bar{a}_2$ = 3.79					
1. $SrTiO_3$: $\bar{a}_1$ = 3.90; 2. $BaTiO_3$: $\bar{a}_2$ = 4.00						23	3. $CaSnO_3$ 4. $CdSnO_3$	3.95 3.93	7.74	7.75	−0.01
9	3. $SrIrO_3$ 4. $BaIrO_3$	3.95 4.03	7.95	7.93	0.02	24	3. $CaHfO_3$ 4. $CdHfO_3$	3.99 3.96	7.78	7.78	0
10	3. $SrSnO_3$ 4. $BaSnO_3$	4.03 4.11	8.03	8.01	0.02	1. $SrTiO_3$: $\bar{a}_1$ = 3.90; 2. $CdTiO_3$: $\bar{a}_2$ = 3.79					
11	3. $SrHfO_3$ 4. $BaHfO_3$	4.07 4.17	8.07	8.07	0	25	3. $SrSnO_3$ 4. $CdSnO_3$	4.03 3.93	7.82	7.83	−0.01
12	3. $SrZrO_3$ 4. $BaZrO_3$	4.10 4.19	8.10	8.09	0.01	26	3. $SrHfO_3$ 4. $CdHfO_3$	4.07 3.96	7.86	7.86	0
13	3. $SrPuO_3$ 4. $BaPuO_3$	4.28 4.36	8.28	8.26	0.02	1. $BaTiO_3$: $\bar{a}_1$ = 4.00; 2. $CdTiO_3$: $\bar{a}_2$ = 3.79					
14	3. $SrCeO_3$ 4. $BaCeO_3$	4.28 4.39	8.28	8.29	−0.01	27	3. $BaSnO_3$ 4. $CdSnO_3$	4.11 3.93	7.9	7.9	0
15	3. $SrThO_3$ 4. $BaThO_3$	4.42 4.49	8.42	8.39	0.03	28	3. $BaHfO_3$ 4. $CdHfO_3$	4.17 3.96	7.96	7.96	0

Table 1. (Contd.)

Serial number of the group	Composition of the oxides in the group	Parameters $\bar{a}_{exp}$, s_{23}, s_{14}, and Δ(Å)			
		$\bar{a}_{exp}$	s_{23}	s_{14}	Δ
$A^{III}B^{III}O_3$					
1. $NdMnO_3$: $\bar{a}_1$ = 3.90; 2. $LaMnO_3$: $\bar{a}_2$ = 3.94					
29	3. $NdGaO_3$ 4. $LaGaO_3$	3.86 3.90	7.8	7.8	0
30	3. $NdFeO_3$ 4. $LaFeO_3$	3.89 3.93	7.83	7.83	0
31	3. $NdInO_3$ 4. $LaInO_3$	4.07 4.11	8.01	8.01	0
32	3. $NdScO_3$ 4. $LaScO_3$	4.01 4.05	7.95	7.95	0
1. $EuMnO_3$: $\bar{a}_1$ = 3.87; 2. $LaMnO_3$: $\bar{a}_2$ = 3.94					
33	3. $EuGaO_3$ 4. $LaGaO_3$	3.84 3.90	7.78	7.77	0.01
34	3. $EuFeO_3$ 4. $LaFeO_3$	3.87 3.93	7.81	7.80	0.01
35	3. $EuInO_3$ 4. $LaInO_3$	4.03 4.11	7.97	7.98	−0.01
36	3. $EuScO_3$ 4. $LaScO_3$	3.98 4.05	7.92	7.92	0
FLUORIDES					
1. $NaCoF_3$: $\bar{a}_1$ = 3.90; 2. $AgCoF_3$: $\bar{a}_2$ = 3.98					
37	3. $NaMgF_3$ 4. $AgMgF_3$	3.84 3.92	7.82	7.86	0
38	3. $NaZnF_3$ 4. $AgZnF_3$	3.88 3.97	7.86	7.87	−0.01
1. $NaNiF_3$: $\bar{a}_1$ = 3.85; 2. $KNiF_3$: $\bar{a}_2$ = 4.01					
39	3. $NaMgF_3$ 4. $KMgF_3$	3.84 3.97	7.85	7.82	0.03
40	3. $NaZnF_3$ 4. $SrZnF_3$	3.88 4.05	7.89	7.90	−0.01
41	3. $NaCoF_3$ 4. $KCoF_3$	3.90 4.07	7.91	7.92	−0.01
42	3. $NaCuF_3$ 4. $KCuF_3$	3.88 4.07	7.89	7.92	−0.03
1. $NaMgF_3$: $\bar{a}_1$ = 3.84; 2. $RbMgF_3$: $\bar{a}_2$ = 4.08					
43	3. $NaZnF_3$ 4. $RbZnF_3$	3.88 4.11	7.92	7.95	−0.03
44	3. $NaCoF_3$ 4. $RbCoF_3$	3.90 4.12	7.98	7.96	0.02
45	3. $NaCuF_3$ 4. $RbCuF_3$	3.88 4.13	7.96	7.97	−0.01
1. $RbCdF_3$: $\bar{a}_1$ = 4.40; 2. $CsCdF_3$: $\bar{a}_2$ = 4.47					
46	3. $RbCaF_3$ 4. $CsCaF_3$	4.46 4.52	8.93	8.92	0.01
47	3. $RbHgF_3$ 4. $CsHgF_3$	4.47 4.57	8.94	8.97	−0.03
1. $KCdF_3$: $\bar{a}_1$ = 4.34; 2. $RbCdF_3$: $\bar{a}_2$ = 4.40					
48	3. $KZnF_3$ 4. $RbZnF_3$	4.05 4.11	8.45	8.45	0
49	3. $KCoF_3$ 4. $RbCoF_3$	4.07 4.12	8.47	8.46	0.01
50	3. $KCuF_3$ 4. $RbCuF_3$	4.07 4.13	8.47	8.47	0
51	3. $KCaF_3$ 4. $RbCaF_3$	4.38 4.46	8.78	8.80	−0.02

metal atoms in the *A* or *B* positions in the crystal lattice of the compounds with the given structure and the oxygen and halogen atoms.

In perovskite and perovskite-like structures, the interatomic distances L_{AX} and L_{BX} are considerably different from the corresponding equilibrium L^0_{AX} and L^0_{BX} distances. It is assumed in the model that the equilibrium distance corresponds to the minimum elastic energy of deformation of interatomic distances. In the harmonic approximation with due regard of twelve *A*–*X* and six *B*–*X* bonds per reduced perovskite unit cell of the composition ABX_3, the deformation energy has the

Table 2. Groups of four ternary oxides with the compositions of the $A^{II}B'_{1/2}B''_{1/2}O_3$ type, experimental mean parameters $\bar{a}_{exp}$ of their reduced perovskite unit-cells, and their sums $s_{23} = \bar{a}_2 + \bar{a}_3$ and $s_{14} = \bar{a}_1 + \bar{a}_4$, and $\Delta = s_{23} - s_{14}$

Serial number of the group	Composition of the oxides in the group	Parameters $\bar{a}_{exp}$, s_{23}, s_{14}, and Δ(Å)			
		$\bar{a}_{exp}$	s_{23}	s_{14}	Δ
$A^{II}B^{V}_{1/2}B^{III}_{1/2}O_3$					
1. $PbNb_{1/2}Sc_{1/2}O_3$: $\bar{a}_1$ = 4.08; 2. $BaNb_{1/2}Sc_{1/2}O_3$: $\bar{a}_2$ = 4.11					
1	3. $PbNb_{1/2}Co_{1/2}O_3$ 4. $BaNb_{1/2}Co_{1/2}O_3$	4.03 4.06	8.14	8.14	0
2	3. $PbNb_{1/2}Fe_{1/2}O_3$ 4. $BaNb_{1/2}Fe_{1/2}O_3$	4.01 4.04	8.12	8.12	0
3	3. $PbNb_{1/2}Mn_{1/2}O_3$ 4. $BaNb_{1/2}Mn_{1/2}O_3$	4.01 4.04	8.13	8.16	–0.03
4	3. $PbNb_{1/2}Sc_{1/2}O_3$ 4. $BaNb_{1/2}Sc_{1/2}O_3$	4.08 4.11	8.19	8.19	0
5	3. $PbTa_{1/2}Sc_{1/2}O_3$ 4. $BaTa_{1/2}Sc_{1/2}O_3$	4.07 4.11	8.18	8.19	–0.01
$A^{II}B^{VI}_{1/2}B^{II}_{1/2}O_3$					
1. $SrW_{1/2}Co_{1/2}O_3$: $\bar{a}_1$ = 3.97; 2. $PbW_{1/2}Co_{1/2}O_3$: $\bar{a}_2$ = 4.00					
6	3. $SrW_{1/2}Mg_{1/2}O_3$ 4. $PbW_{1/2}Mg_{1/2}O_3$	3.95 4.00	7.95	7.97	–0.02
7	3. $SrW_{1/2}Mn_{1/2}O_3$ 4. $PbW_{1/2}Mn_{1/2}O_3$	4.00 4.05	8.00	8.02	–0.02
1. $PbW_{1/2}Mn_{1/2}O_3$: $\bar{a}_1$ = 4.05; 2. $SrW_{1/2}Co_{1/2}O_3$: $\bar{a}_2$ = 4.00					
8	3. $PbW_{1/2}Mg_{1/2}O_3$ 4. $SrW_{1/2}Mg_{1/2}O_3$	4.00 3.95	8.00	8.00	0
9	3. $PbW_{1/2}Co_{1/2}O_3$ 4. $SrW_{1/2}Co_{1/2}O_3$	4.00 3.97	8.00	8.02	–0.02
10	3. $PbW_{1/2}Cd_{1/2}O_3$ 4. $SrW_{1/2}Cd_{1/2}O_3$	4.14 4.07	8.14	8.12	–0.02
1. $SrW_{1/2}Mg_{1/2}O_3$: $\bar{a}_1$ = 3.95; 2. $BaW_{1/2}Mg_{1/2}O_3$: $\bar{a}_2$ = 4.06					
11	3. $SrMo_{1/2}Ni_{1/2}O_3$ 4. $BaMo_{1/2}Ni_{1/2}O_3$	3.93 4.02	7.99	7.97	0.02
12	3. $SrMo_{1/2}Co_{1/2}O_3$ 4. $BaMo_{1/2}Co_{1/2}O_3$	3.97 4.05	8.03	8.00	0.03

form [1]

$$\varepsilon = 6k_A\left(\frac{\bar{a}}{\sqrt{2}} - L^0_{AX}\right)^2 + 3k_B\left(\frac{\bar{a}}{2} - L^0_{BX}\right)^2, \quad (1)$$

where L^0_{AX} and L^0_{BX} are the lengths of unstrained *A*–*X* and *B*–*X* bonds. The unit-cell parameter is determined by minimizing this energy:

$$\bar{a} = \frac{4\sqrt{2}k_AL^0_{AX} + 2k_BL^0_{BX}}{4k_A + k_B}. \quad (2)$$

Now, consider four compounds of the compositions (1) ABX_3, (2) $A'BX_3$, (3) $AB'X_3$, and (4) $A'B'X_3$, where *A* and *A*' in their chemical formulas should be different mono-, di-, or trivalent atoms and *B* and *B*' should be different penta-, tetra-, and trivalent atoms. Expressions (2) written for the compounds thus selected form four equalities that can be considered as a system of equations with four unknowns, $k_AL^0_{AX}$; $k_AL^0_{A'X}$; $k_BL^0_{BX}$; and $k_BL^0_{B'X}$. Excluding these quantities from the system of equations obtained, we find that

$$(\bar{a}_2 + \bar{a}_3) = (\bar{a}_1 + \bar{a}_4). \quad (3)$$

To verify the validity of this equation, we can find a large number of groups consisting of four compounds of types (1)–(4) among the known binary and ternary oxides (about 800 representatives [3]) and fluorides (several tens of representatives) with the perovskite structure with the concrete atoms instead of *A*, *B*, *A*', and *B*'. For these groups of compounds (Table 1), the mean parameters of the reduced perovskite unit cells calculated from the independent experimental data obey Eq. (3) with an accuracy not exceeding 1% of the parameter value.

On the one hand, the formula relating the parameters of four compounds may serve as a criterion of the internal consistency of the model of deformable interatomic distances, because it is fulfilled for the experimental values of the parameters of the real compounds. On the other hand, the validity of the formula for practically any set of four compounds is the crystallographic regularity independent of the model. As far as we know, this correlation between the mean parameters (volumes) of the perovskite unit cells has not been revealed or discussed earlier.

CONCLUSIONS

The correlation between the parameters of the reduced cubic unit cells of crystals with the perovskite structure established above indicates that the atomic interactions in all the crystals considered can be described by the harmonic terms of the corresponding potential energies. This correlation can be considered as a criterion of the validity of the elastic model used in the calculation of the unit-cell volumes of crystals with

the perovskite structure. The allowance for nonlinear interactions is necessary for the interpretation and quantitative description of fine characteristics of crystals and the phenomena observed in these crystals and, in particular, the structural phase transitions. On the other hand, correlation (3) is of importance irrespectively of the assumptions underlying the model, because it contains no model parameters and can be established empirically.

It is also possible to show that rule (3) derived from the model should also be valid for ternary oxides with the perovskite structure and isovalent atomic compositions. This is confirmed by the parameters of ternary oxides calculated from the known X-ray diffraction data at room temperature. Possibly, the compounds with more complicated compositions would also obey this correlation for unit-cell parameters.

REFERENCES

1. V. P. Sakhnenko, E. G. Fesenko, A. T. Shuvaev, *et al.*, Kristallografiya **17**, 316 (1972) [Sov. Phys. Crystallogr. **17**, 268 (1972)].
2. V. P. Sakhnenko, N. V. Dergunova, and L. A. Reznichenko, *Energy and Crystal Chemistry of Solid Solutions of the Oxide Octahedral-Type Compounds and Modeling of Piezoceramic Materials* (MP Kniga, Rostov-on-Don, 1999).
3. E. G. Fesenko, *Family of Perovskites and Ferroelectricity* (Atomizdat, Moscow, 1972).
4. V. M. Talanov, Kristallografiya **24**, 706 (1979) [Sov. Phys. Crystallogr. **24**, 405 (1979)].
5. V. M. Talanov, Phys. Status Solidi B **106**, 99 (1981).
6. G. A. Geguzina, E. G. Fesenko, and E. T. Shuvayeva, Ferroelectrics **167**, 311 (1995).
7. *Landolt-Börnstein. Numerical Data and Functional Relationships in Science and Technology* (Springer, New York, 1969), New Series, Group III, Vol. 4a.

Translated by L. Man

Crystallography Reports, Vol. 49, No. 1, 2004, pp. 20–28. Translated from Kristallografiya, Vol. 49, No. 1, 2004, pp. 25–33.

THEORY OF CRYSTAL STRUCTURES

Dedicated to the 80th Birthday of L.A. Shuvalov

Tilting Structures in Perovskites

V. B. Shirokov and V. I. Torgashev

Research Institute of Physics, Rostov State University, pr. Stachki 194, Rostov-on-Don, 344090 Russia

e-mail: shirokov@ip.rsu.ru

Received May 8, 2003

Abstract—Thirty five low-symmetry tilting phases of the octahedra in which the atoms located at the initial octahedral position remain equivalent are derived for the perovskite structure at the $\mathbf{k}_{10}(X)$, $\mathbf{k}_{11}(M)$, and $\mathbf{k}_{13}(R)$ points of the Brillouin zone. For each low-symmetry phase, structural data are presented and a relationship between the atomic displacements and the order parameters is deduced. All the low-symmetry phases can be obtained by considering only one or two order parameters. © *2004 MAIK "Nauka/Interperiodica".*

INTRODUCTION

In an ideal structure of ABX_3 perovskites with space group $Pm3m = O_h^1$, the *A*, *B*, and *X* atoms occupy the *a*, *b*, and *c* positions, respectively. Each *A* cation is surrounded by 12 *X* anions located at equal distances $a/\sqrt{2}$. The octahedral environment of the *B* cations involves six *X* anions located at a distance *a*/2. As a rule, the perovskite structure is represented in the form of layers consisting of *X* octahedra. All the octahedra are shared by vertices. The commonly accepted method of revealing low-symmetry phases in the perovskite structure is a simple geometric analysis of the possible rotations of eight octahedra located in two layers [1–5]. For this analysis, Glazer [1] introduced the following notation: $a^{\pm}b^{\pm}c^{\pm}$, where the letters *a*, *b*, and *c* stand for the magnitudes of rotations about the orthogonal axes of the cubic coordinate system and the superscripts "±" specify the sense of rotation of the adjacent octahedra arranged along the corresponding axis. In the framework of this approach, Glazer [1] derived 23 low-symmetry tilting structures, many of which are described by identical symmetry groups. Refinements and further elaboration of this method are given in [2–5]. It should be noted that, in those works, the order parameters were not considered for a particular low-symmetry phase.

With the aim of describing the lowering of symmetry, the notion of the order parameter is introduced in terms of the Landau theory of phase transitions [6]. The specified order parameter completely determines the symmetry of a low-symmetry phase. The determination of the low-symmetry phases for each of the chosen (not necessarily irreducible) order parameters was described by Gufan [7]. The complete list of possible low-symmetry phases in the case when the order parameter is transformed according to one irreducible representation at unique symmetry points of the reciprocal lattice of space group $Pm3m(O_h^1)$ is given in [8]. An analysis of the order parameters that can be transformed according to several irreducible transformations (several order parameters) leads to a more formidable problem of description of the low-symmetry phases. For some combinations of order parameters, this problem was solved by Aleksandrov *et al.* [9] and Howard and Stokes [10].

The possible order parameters for describing a displacive phase transition are determined from an expansion of the mechanical representation of the relevant atomic positions. Such an expansion for all atomic positions at different points of the Brillouin zone for the perovskite structure was obtained by Cowley [11]. Since the mechanical representation for the perovskite structure has a large dimension, many authors have restricted their consideration to problems with small dimensions [12, 13]. Moreover, Howard and Stokes [10] introduced symmetry constraints. Recall that the choice of the order parameters only in part determines the mechanism of phase transitions. This means that the transition to a phase with particular symmetry can be described by another set of order parameters, especially when the phase has low symmetry. Within this approach, the order parameter does not necessarily describe the structure of the low-symmetry phase. The complete description requires the inclusion of secondary order parameters [14, 15].

In this work, we analyzed the possible low-symmetry phases for all order parameters with the mechanism of rotation of octahedra at unique symmetry points of the Brillouin zone for the perovskite structure. Among these phases, we considered only the phases for which all octahedra remain equivalent. A relationship between the atomic displacements and the order parameters was derived for the low-symmetry phases.

1063-7745/04/4901-0020$26.00 © 2004 MAIK "Nauka/Interperiodica"

ORDER PARAMETERS FOR TILTING STRUCTURES

Let us consider the rotation of octahedra whose centers occupy the positions b = (1/2, 1/2, 1/2) in the perovskite structure. As in [1], we analyze the rotation of eight octahedra arranged in two layers of four each. In order to describe these rotations, it is sufficient to solve the problem involving the unique symmetry points $\mathbf{k}_{10}(X)$, $\mathbf{k}_{11}(M)$, $\mathbf{k}_{13}(R)$, and $\mathbf{k}_{12}(\Gamma)$ (the notation is given according to [16]). The rotations of the octahedra at the b positions are described by a combination of the representations T_{2g} for the Γ point (rotation) and the permutation representation of the b position in an extended unit cell. This representation, which will be referred to as the rotation representation, consists of the following irreducible representations:

$$\mathbf{k}_{10}: \tau_2 + \tau_{10}, \mathbf{k}_{11}: \tau_5 + \tau_9, \mathbf{k}_{13}: \tau_8, \mathbf{k}_{12}: \tau_9. \quad (1)$$

Rotations of the octahedra in the perovskite structure can occur only through displacements of X anions surrounding the b position. Therefore, the order parameters for these rotations can include only those representations [among representations (1)] which are involved in the mechanical representation constructed for displacements of the X anions. The mechanical representation for the c position ($Pm3m$) can be written in the form

$$\begin{gathered}\mathbf{k}_{10}: \tau_1 + \tau_4 + \tau_6 + 2\tau_9 + \tau_{10},\\ \mathbf{k}_{11}: \tau_1 + \tau_3 + \tau_5 + \tau_6 + \tau_7 + \tau_9 + \tau_{10},\\ \mathbf{k}_{13}: \tau_4 + \tau_6 + \tau_8 + \tau_{10}, \mathbf{k}_{12}: \tau_8 + 2\tau_{10}.\end{gathered} \quad (2)$$

A comparison of representations (1) and (2) shows that the order parameters for tilting structures can correspond to the following irreducible representations:

$$\mathbf{k}_{10}: \tau_{10}(X_5'), \mathbf{k}_{11}: \tau_5(M_3) + \tau_9(M_5), \mathbf{k}_{13}: \tau_8(R_{25}), \quad (3)$$

where $\mathbf{k}_{10}: \tau_{10}(X_5')$ and $\mathbf{k}_{11}: \tau_9(M_5)$ are the six-dimensional irreducible representations and the other representations are the three-dimensional irreducible representations (notation of representations in parentheses is given according to [17]). The representations $\mathbf{k}_{11}: \tau_5(M_3)$ and $\mathbf{k}_{13}: \tau_8(R_{25})$ are traditionally included in the analysis of the octahedron rotations [9] (see also [7]).

Now, we consider an abstract eighteen-dimensional order parameter involved in set (3). The total number of all possible low-symmetry distortions with this order parameter is equal to 122. Among them, there always exists a phase with the lowest symmetry for which all 18 components of the order parameter are nonzero and are not related to each other. By symmetry, this phase can be described not only in terms of set (3) but also by a larger number of variants of the representations involved in set (2). Therefore, it is beyond reason to argue that the phase with the lowest symmetry can be obtained through the octahedron rotation, even though this phase is included in the complete list of low-symmetry phases. This situation can be explained by a specific method of examination, namely, group-theoretic analysis. On the other hand, the inclusion of the thermodynamic potential makes it possible to unambiguously separate the required phases from the complete list, even though the degree of potential necessary for describing the low-symmetry phase itself may appear to be very high [18].

As was done by Glazer [1], we examine the tilting structures, i.e., distortions at which octahedra remain equivalent. For this purpose, we choose the phases satisfying this requirement from a complete list of 122 low-symmetry phases with order parameters corresponding to irreducible representations (3). The number of these phases is 35. Their order parameters are listed in Table 1. The complete description of the low-symmetry structure involves the determination of all displacements as functions of the order parameters. In order to derive a relationship between the order parameters and the atomic displacements, it is necessary to use the symmetrical coordinates in an extended cell, which, in our problem, is doubled along each of the perovskite axes. The structural parameters for the phases presented in Table 1 are listed in Table 2. The static atomic displacements are linearly related to nonzero symmetrical coordinates in the low-symmetry phases. The linear relationship between the atomic displacements and the corresponding order parameters is determined by symmetry. Table 2 contains new order parameters, which differ from initial order parameters involved in set (3). These new order parameters are referred to as secondary order parameters. They are included in complete set (2). The dependence of the secondary order parameters on the initial order parameters is determined by the invariants liner in these new order parameters. The relationships between the new order parameters and the initial order parameters are also given in Table 2.

DISCUSSION

For each phase, we analyzed all the symmetrically equivalent distortions (domains) and chose the orientation for the most appropriate notation of the rotation according to [1] (see above). The results obtained are presented in the last column in Table 1. In the case where the symmetry and notation coincide with those described in [1], the number of the phase taken from [1] is given in parentheses in the last column. It can be seen from Table 1 that there is no one-to-one correspondence between the notation introduced in [1] and the symmetry (structure) of the low-symmetry phases. Moreover, the Glazer notation [1] cannot be used for phases **5**, **23**, **27**, **31**, and **35** (the phase numbering is given according to Table 1), because the magnitude of rotation of an adjacent octahedron along one axis proved to be identical to that of an adjacent octahedron along another axis. This fact is indicated in Table 1 by the designation a/b, where a and b are the magnitudes of rotations of the adjacent octahedra along the same axis.

Table 1. Low-symmetry tilting phases of the *b* octahedra in the perovskite structure

Phase	Order parameters	Space group	V'/V	Translations of the primitive cell **a**, **b**, and **c**	Tilting notation [1]
1	(0, 0, φ)	$I4/mcm$-D_{4h}^{18} (no. 140)	2	$\mathbf{a}_2 - \mathbf{a}_3$, $\mathbf{a}_1 + \mathbf{a}_2$, $2\mathbf{a}_3$	$a^0\,a^0\,c^-$ (no. 22)
2	(φ, φ, φ)	$R3c$-D_{3d}^{6} (no. 167)	2	$\mathbf{a}_1 + \mathbf{a}_2$, $\mathbf{a}_1 + \mathbf{a}_3$, $\mathbf{a}_2 + \mathbf{a}_3$	$a^-\,a^-\,a^-$ (no. 14)
3	(φ, −φ, 0)	$Imma$-D_{2h}^{28} (no. 74)	2	$2\mathbf{a}_3$, $\mathbf{a}_1 - \mathbf{a}_2$, $\mathbf{a}_2 + \mathbf{a}_3$	$a^0\,b^-\,b^-$ (no. 20)
4	(0, φ_1, φ_2)	$C2/m$-C_{2h}^{3} (no. 12)	2	$\mathbf{a}_1 + \mathbf{a}_2$, $2\mathbf{a}_1$, $\mathbf{a}_2 - \mathbf{a}_3$	$a^+\,b^-\,c^-$ (no. 19)
5	(φ_1 φ_2 φ_1)	$C2/c$-C_{2h}^{6} (no. 15)	2	$\mathbf{a}_1 + \mathbf{a}_3$, $\mathbf{a}_1 - \mathbf{a}_3$, $\mathbf{a}_1 + \mathbf{a}_2$	a^-, b/c, c/b
6	(0 ξ 0 0 −ξ 0)	$I4/mcm$-D_{4h}^{18} (no. 140)	4	$2\mathbf{a}_3$, $\mathbf{a}_1 + \mathbf{a}_2 + \mathbf{a}_3$, $2\mathbf{a}_2$	$a^0\,b^-\,c^-$
7	(ξ 0 ξ 0 ξ 0)	$Ia3$-T_h^7 (no. 206)	4	$2\mathbf{a}_3$, $\mathbf{a}_1 + \mathbf{a}_2 + \mathbf{a}_3$, $2\mathbf{a}_2$	$a^-\,a^-\,a^-$
8	(ξ −ξ 0 0 0 0)	$Pmna$-D_{2h}^{7} (no. 53)	2	$\mathbf{a}_3$. $\mathbf{a}_1 - \mathbf{a}_2$, $\mathbf{a}_1 + \mathbf{a}_2$	$a^0\,b^-\,b^-$
9	(0 0 0 ξ 0 0)	$Cmma$-D_{2h}^{21} (no. 67)	2	$\mathbf{a}_1 + \mathbf{a}_2$, $\mathbf{a}_1 - \mathbf{a}_2$, $\mathbf{a}_3$	$a^0\,a^0\,c^-$
10	(0 0 0 0 ξ_1 ξ_2)	$P2/c$-C_{2h}^{4} (no. 13)	2	$\mathbf{a}_2 - \mathbf{a}_3$, $\mathbf{a}_1$, $2\mathbf{a}_3$	$a^+\,b^-\,c^-$
11	(0 ξ_1 0 ξ_2 0 ξ_3)	$Ibca$-D_{2h}^{27} (no. 73)	4	$2\mathbf{a}_2$, $2\mathbf{a}_3$, $\mathbf{a}_1 + \mathbf{a}_2 + \mathbf{a}_3$	$a^-\,b^-\,c^-$
12	(0 ψ ψ)	$I4/mmm$-D_{4h}^{1} (no. 139)[7]	4	$2\mathbf{a}_1$, $2\mathbf{a}_2$, $\mathbf{a}_1 + \mathbf{a}_2 + \mathbf{a}_3$	$a^0\,b^+\,b^+$
13	(ψ 0 0)	$P4/mbm$-D_{4h}^{5} (no. 127)	2	$\mathbf{a}_1 - \mathbf{a}_2$, $\mathbf{a}_1 + \mathbf{a}_2$, $\mathbf{a}_3$	$a^0\,a^0\,c^+$ (no. 21)
14	(ψ ψ ψ)	$Im3$-T_h^5 (no. 204)	4	$2\mathbf{a}_1$, $2\mathbf{a}_2$, $\mathbf{a}_1 + \mathbf{a}_2 + \mathbf{a}_3$	$a^+\,a^+\,a^+$ (no. 3)
15	(ψ_1 ψ_2 ψ_3)	$Immm$-D_{2h}^{25} (no. 71)	4	$2\mathbf{a}_1$, $2\mathbf{a}_2$, $\mathbf{a}_1 + \mathbf{a}_2 + \mathbf{a}_3$	$a^+\,b^+\,c^+$ (no. 1)
16	(η 0 0 0 0 0)	$Pmma$-D_{2h}^{25} (no. 51)	2	$2\mathbf{a}_1$, $\mathbf{a}_2$, $\mathbf{a}_3$	$a^0\,b^0\,c^+$
17	(η η 0 0 0 0)	$Cmcm$-D_{2h}^{17} (no. 63)	2	$\mathbf{a}_1$, $\mathbf{a}_2$, $2\mathbf{a}_3$	$a^0\,b^+\,b^+$
18	(η 0 0 η 0 0)	$P4/nmm$-D_{4h}^{7} (no. 129)	4	$2\mathbf{a}_3$, $2\mathbf{a}_2$, $\mathbf{a}_1$	$a^0\,b^+\,b^+$
19	(0 0 η_1 η_2 0 0)	$P2_1/m$-C_{2h}^{2} (no. 11)	4	$\mathbf{a}_1$, $2\mathbf{a}_2$, $\mathbf{a}_3$	$a^+\,b^+\,c^+$
20	(0 0 0 ξ 0 0)(φ 0 0)	$Ccca$-D_{2h}^{22} (no. 68)	4	$\mathbf{a}_1 - \mathbf{a}_2$, $\mathbf{a}_1 + \mathbf{a}_2$, $\mathbf{a}_3$	$a^-\,b^-\,c^-$
21	(0 ξ 0 0 ξ 0)(0 φ 0)	$P4/nbc$-D_{4h}^{11} (no. 133)	8	$2\mathbf{a}_3$, $2\mathbf{a}_1$, $2\mathbf{a}_2$	$a^-\,b^-\,c^-$
22	(0 0 ξ −ξ 0 0)(φ 0 −φ)	$Pnna$-D_{2h}^{6} (no. 52)	4	$2\mathbf{a}_2$, $\mathbf{a}_1 - \mathbf{a}_3$, $2\mathbf{a}_3$	$a^-\,b^-\,c^-$
23	(0 ψ 0)(0 0 ξ −ξ 0 0)	$P2_1/c$-C_{2h}^{5} (no. 14)	2	$\mathbf{a}_1 + \mathbf{a}_3$, $\mathbf{a}_1 - \mathbf{a}_3$, $\mathbf{a}_2$	$a^+\,b/{-c}\,c/{-b}$
24	(ψ 0 −ψ)(0 ξ 0 0 −ξ 0)	$I4/m$-C_{4h}^{5} (no. 87)	4	$2\mathbf{a}_1$, $2\mathbf{a}_2$, $\mathbf{a}_1 + \mathbf{a}_2 + \mathbf{a}_3$	$a^+\,b/c\,c/b$
25	(0 ψ 0)(0 0 0 ξ 0 0)	$C2/m$-C_{2h}^{3} (no. 12)	2	$\mathbf{a}_1 + \mathbf{a}_3$, $\mathbf{a}_1 - \mathbf{a}_3$, $\mathbf{a}_2$	$a^+\,b^+\,c^-$
26	(0 0 ψ)(ξ_1 0 0 ξ_2 0 0)	$Ibam$-D_{2h}^{26} (no. 72)	4	$2\mathbf{a}_1$, $2\mathbf{a}_2$, $\mathbf{a}_1 + \mathbf{a}_2 + \mathbf{a}_3$	$a^+\,b^-\,c^-$
27	(0 η 0 0 η 0)(0 ξ 0 0 ξ 0)	$P4/ncc$-D_{4h}^{8} (no. 130)	8	$2\mathbf{a}_3$, $2\mathbf{a}_1$, $2\mathbf{a}_2$	a^-, b/c, c/b
28	(η 0 0 0 0 0)(0 0 0 ξ 0 0)	$Pcaa$- D_{2h}^{8} (no. 54)	4	$2\mathbf{a}_3$, $\mathbf{a}_2$, $2\mathbf{a}_1$	$a^+\,b^-\,c^-$
29	(η_1 0 0 0 η_2 0)(0 0 ξ 0 0 0)	$Pbcm$-D_{2h}^{11} (no. 57)	4	$\mathbf{a}_2$, $2\mathbf{a}_1$, $2\mathbf{a}_3$	$a^+\,b^+\,c^-$
30	(η_1 0 0 η_2 0 0)(0 0 ξ)	$Pmmn$-D_{2h}^{13} (no. 59)	4	$2\mathbf{a}_1$, $2\mathbf{a}_2$, $\mathbf{a}_3$	$a^+\,b^+\,c^+$
31	(0 0 η η 0 0)(0 0 ξ ξ 0 0) (0 φ 0)	$Pbcn$-D_{2h}^{14} (no. 60)	4	$\mathbf{a}_1 + \mathbf{a}_3$, $\mathbf{a}_1 - \mathbf{a}_3$, $2\mathbf{a}_2$	a^-, b/c, c/b
32	(0 0 0 η 0 0)(0 0 ξ 0 0 0) (0 φ 0)	$Cmca$-D_{2h}^{18} (no. 64)	4	$\mathbf{a}_1 + \mathbf{a}_2$, $\mathbf{a}_1 - \mathbf{a}_2$, $2\mathbf{a}_3$	$a^+\,b^-\,c^-$
33	(0 0 0 η 0 0)(0 ψ 0)(φ 0 0)	$Cmcm$-D_{2h}^{17} (no. 63)	4	$\mathbf{a}_1 + \mathbf{a}_2$, $\mathbf{a}_1 - \mathbf{a}_2$, $2\mathbf{a}_3$	$a^+\,b^+\,c^-$ (no. 17)
34	(0 η 0 0 η 0)(ψ 0 −ψ)(0 φ 0)	$P4/nmc$-D_{4h}^{15} (no. 137)	8	$2\mathbf{a}_3$, $2\mathbf{a}_1$, $2\mathbf{a}_2$	$a^+\,b^+\,c^-$
35	(0 0 η η 0 0)(0 ψ 0)(φ 0 −φ)	$Pnma$-D_{2h}^{16} (no. 62)	4	$\mathbf{a}_1 - \mathbf{a}_2$, $\mathbf{a}_1 + \mathbf{a}_2$, $2\mathbf{a}_3$	$a/b\,b/a\,c^+$

Note: Designations for the order parameters are as follows: $\mathbf{k}_{10}$: $\tau_{10}(X_5')$ = η, $\mathbf{k}_{11}$: $\tau_5(M_3)$ = ψ, $\tau_9(M_5)$ = ξ, and $\mathbf{k}_{13}$: $\tau_8(R_{25})$ = φ. Notation of representations in parentheses is given according to [17].

Table 2. Atomic displacements and their relation to the order parameters for the low-symmetry phases presented in Table 1

Phase	Displacement	*A* and *B* atoms	*X* atoms	Secondary order parameters
1	[1/2, 1/2 ,1/2]	*A*: (*b*)(0, 1/2, 1/4) *B*: (*c*)(0, 0, 0)	X_1: (*a*)(0, 0, 1/4) X_2: (*h*)(*x*, 1/2 + *x*, 0), $x = 1/4 + 1/8\varphi$	
2	[1/2, 1/2 ,1/2]	*A*: (*a*)(1/4, 1/4, 1/4) *B*: (*b*)(0, 0, 0,)	*X*: (*e*)(*x*,1/2 – *x*,1/4), $x = 3/4 + 1/4\varphi$	
3	[0, –1/2, 0]	*A*: (*e*)(0, 1/4, *z*), $z = 3/4 + \sqrt{2}/4\Phi'$ *B*: (*c*)(1/4, 1/4, 1/4)	X_1: (*e*) = (0, 1/4, *z*), $z = 1/4 + 1/4\varphi + 1/4\Phi''$ X_2: (*f*) = (*x*, 0, 0), $x = 1/4 - 1/8\,\varphi + 1/8\Phi''$	(Φ', Φ', 0) (Φ", Φ", 0) $\Phi', \Phi'' \sim \varphi^3$,
4	[0, 1/2, 0]	*A*: (*i*)(*x*, 0, *z*), $x = 1/4 + \sqrt{2}/8\Phi'_1 - 1/8\Phi'_2$, $z = \sqrt{2}/4\Phi'_2$ *B*: (*b*)(0, 1/2, 0)	X_1: (*g*)(0, *y*, 0), $y = 3/4 - 1/8\varphi_1 + 1/8\Phi''_1$ X_2: (*h*)(0, *y*, 1/2), $y = 1/4 + 1/8\varphi_2 + 1/8\Phi''_2$ X_3: (*i*) = (*x*, 0, *z*), $x = 1/4 - 1/8\varphi_1 - 1/8\varphi_2 - 1/8\Phi''_1 + 1/8\Phi''_2$, $z = 1/2 + 1/4\varphi_1 + 1/4\Phi''_1$	$(0, \Phi'_1, \Phi'_2)$ $(0, \Phi''_1, \Phi''_2)$ $\Phi'_1, \Phi''_1 \sim \varphi_1\varphi_2^2$; $\Phi'_2, \Phi''_2 \sim \varphi_1^2\varphi_2$
5	[0, 1/2, 0]	*A*: (*e*)(0, *y*, 1/4), $y = \sqrt{2}/4\Phi'$ *B*: (*b*)(0, 1/2, 0)	X_1: (*f*)(*x*, *y*, *z*), $x = 1/4 - 1/8\varphi_2 + 1/4E$, $y = 1/4 - 1/8\varphi_2 - 1/4E$, $z = 1/2 + 1/8\varphi_1 + 1/8\Phi''$ X_2: (*e*)(0, *y*, 1/4), $y = 1/4\varphi_1 - 1/4\Phi''$	$(E, \sqrt{3}E)(\Phi', 0, -\Phi')(\Phi'', 0, -\Phi'')$ $E \sim \varphi_1^2\varphi_2(\varphi_1^2 - \varphi_2^2)$; $\Phi', \Phi'' \sim \varphi_1(\varphi_1^2 - \varphi_2^2)$
6	[0, 0, 0]	A_1: (*c*)(0, 0, 0) A_2: (*d*)(0, 1/2, 0) *B*: (*e*)(1/4, 1/4, 1/4)	X_1: (*j*)(*x*, 0, 1/4), $x = 1/4 + 1/8\Xi$ X_2: (*h*)(*x*, 1/2 + *x*, 0), $x = 3/4 - \sqrt{2}/8\xi$	(0, Ξ, 0) $\Xi \sim \xi^2$
7	[0, 0, 0]	*A*: (*a*) (0, 0, 0) *B*: (*b*) (1/4, 1/4, 1/4)	*X*: (*d*)(*x* 0 1/4), $x = 1/4 + \sqrt{2}/8\xi$	
8	[0, 0, 0]	*A*: (*a*)(0, 0, 0) *B*: (*c*)(1/2, 1/2, 0)	X_1: (*b*)(1/2, 0, 0) X_2: (*g*)(1/4, *y*, 1/4), $y = 1/2 - \sqrt{2}/4\xi$	
9	[0, 0, 0]	*A*: (*c*)(0, 0, 0) *B*: (*f*)(1/4, 1/4, 1/2)	X_1: (*e*)(1/4, 1/4, 0) X_2: (*g*) (0, 1/4, *z*), $z = 1/2 + \sqrt{2}/4\xi$ X_3: (*b*)(1/4, 0, 1/2)	
10	[0, 0, 0]	*A*: (*a*)(0, 0, 0) *B*: (*b*)(1/2, 1/2, 0)	X_1: (*f*) = (1/2, *y*, 1/4), $y = 1/2 + \sqrt{2}/4\xi_2$ X_2: (*e*) = (0, *y*, 1/4), $y = 1/2 + \sqrt{2}/4\xi_1$ X_3: (*d*) = (1/2, 0, 0)	
11	[0, 0, 0,]	*A*: (*b*) (0, 0, 0) *B*: (*a*) (1/4, 1/4, 1/4)	X_1: (*c*)(*x*, 0, 1/4). $x = 1/4 + \sqrt{2}/8\xi_3$ X_2: (*e*)(0, 1/4, *z*), $z = 1/4 + \sqrt{2}/8\xi_1$ X_3: (*d*)(1/4, *y*, 0), $y = 1/4 + \sqrt{2}/8\xi_2$	
12	[–1, 0, 0]	A_1: (*c*)(0, 1/2, 0) A_2: (*a*)(0, 0, 0) A_3: (*b*)(0, 0, 1/2) *B*: (*f*) (1/4, 1/4, 1/4)	X_1: (*h*)(*x*, *x*, 0), $x = 3/4 - 1/8\psi + 1/8\Xi_2$ X_2: (*n*)(*x*, 0, *z*), $x = 3/4 + 1/8\Xi_1$, $z = 1/4 - 1/8\psi - 1/8\Xi_2$	$(\Xi_1, \Xi_2, -\Xi_2)$ $\Xi_1 \sim \psi^2$; $\Xi_2 \sim \psi^3$
13	[–1/2, –1/2, 0]	*A*: (*d*)(0, 1/2, 0) *B*: (*b*)(0, 0, 1/2)	X_1: (*a*)(0, 0, 0) X_2: (*h*)(*x*, 1/2 + *x*, 1/2), $x = 3/4 + 1/8\psi$	

Table 2. (Contd.)

Phase	Displacement	*A* and *B* atoms	*X* atoms	Secondary order parameters
14	[0, 0, 0]	A_1: (*a*)(0, 0, 0) A_2: (*b*)(0, 1/2, 1/2) *B*: (*c*) (1/4, 1/4, 1/4)	*X*: (*g*)(0, *y*, *z*), $y = 1/4 + 1/8\psi + 1/8\Xi$, $z = 1/4 - 1/8\psi + 1/8\Xi$	(0, Ξ, 0) $\Xi \sim \psi^2$
15	[0, 0, 0]	A_1: (*a*)(0, 0, 0) A_2: (*b*)(0, 1/2, 1/2) A_3: (*d*)(1/2, 0, 1/2) A_4: (*c*)(1/2, 1/2, 0) *B*: (*k*) (1/4, 1/4, 1/4)	X_1: (*n*)(*x*, *y*, 0), $x = 1/4 - 1/8\psi_2 + 1/8\Xi_2$, $y = 1/4 + 1/8\psi_3 + 1/8\Xi_3$ X_2: (*m*)(*x*, 0, *z*), $x = 1/4 + 1/8\psi_1 + 1/8\Xi_1$, $z = 1/4 - 1/8\psi_3 + 1/8\Xi_3$ X_3: (*l*)(0, *y*, *z*), $y = 1/4 - 1/8\psi_1 + 1/8\Xi_1$, $z = 1/4 + 1/8\psi_2 + 1/8\Xi_2$	(Ξ_1, Ξ_2, Ξ_3) $\Xi_1 \sim \psi_2\psi_3$; $\Xi_2 \sim \psi_1\psi_3$; $\Xi_3 \sim \psi_1\psi_2$
16	[–1/2, 0, 0]	*A*: (*e*)(0, 0, *z*), $z = \sqrt{2}/4\eta'$ *B*: (*d*)(0, 1/2, 1/2)	X_1: (*b*)(0, 1/2, 0) X_2: (*c*)(0, 0, 1/2) X_3: (*f*)(1/4, 1/2, *z*), $z = 1/2 + \sqrt{2}/4\eta''$	
17	[0, 0, –1/2]	*A*: (*c*)(0, *y*, 1/4), $y = -\sqrt{2}/4\eta'$ *B*: (*b*)(1/2, 0, 0)	X_1: (*c*)(0, *y*, 1/4), $z = 1/2 - \sqrt{2}/4\eta''$ X_2: (*d*)(1/4, 1/4, 0)	
18	[0, 0, 0]	A_1: (*a*)(0, 0, 0) A_2: (*c*)(0, 1/2, *z*), $z = \sqrt{2}/2\eta'$ *B*: (*e*)(1/4, 1/4, 1/2)	X_1: (*i*)(0, *y*, *z*), $y = 1/4 + 1/8\Xi$, $z = 1/2 + \sqrt{2}/4\eta''$ X_2: (*d*)(1/4, 1/4, 0)	(Ξ, 0, 0) $\Xi \sim \eta^2$
19	[0, 1/2, 0]	*A*: (*e*)(*x*, 1/4, *z*), $x = -\sqrt{2}/4\eta_2'$, $z = \sqrt{2}/2\eta_1'$ *B*: (*d*)(1/2, 0, 1/2)	X_1: (*b*)(1/2, 0, 0) X_2: (*e*)(*x*, 1/4, *z*), $x = 1/2 - \sqrt{2}/4\eta_2''$, $z = 1/2 + \sqrt{2}/4\eta_1''$ X_3: (*c*)(0, 0, 1/2)	
20	[–1/2, 0, 0]	*A*: (*f*)(0, *y*, 0), $y = 3/4 + \sqrt{2}/8\Phi'$ *B*: (*c*) (1/4, 0, 1/4)	X_1: (*e*)(*x*, 0, 0), $x = 1/4 + 1/8\varphi + 1/8\Phi''$ X_2: (*g*)(0, 0, *z*), $z = 1/4 - 1/8\varphi + 1/8\Phi''$ X_3: (*h*)(1/4, 1/4, *z*), $z = 3/4 - \sqrt{2}/8\xi$	(Φ', 0, 0)(Φ", 0, 0) $\Phi', \Phi'' \sim \xi^2\varphi$
21	[–1, 0, 0]	A_1: (*c*)(0, 1/2, 0) A_2: (*d*)(0, 0, 0) *B*: (*e*) (1/4, 1/4, 1/4)	X_1: (*h*)(*x*, 0, 1/4), $x = 3/4 - 1/8\varphi + 1/8\Xi$ X_2: (*i*)(*x*, 0, 3/4), $x = 3/4 + 1/8\varphi + 1/8\Xi$ X_3: (*j*)(*x*, 1/2 + *x*, 0), $x = 3/4 + \sqrt{2}/8\xi$	(Ξ, 0, 0) $\Xi \sim \xi^2$
22	[0, –1/2, 0]	*A*: (*c*)(1/4, 0, *z*), $z = -\sqrt{2}/4\Phi'$ *B*: (*b*)(0, 0, 1/2)	X_1: (*d*)(*x*, 1/4, 1/4), $x = \sqrt{2}/8\xi + 1/8\varphi + 1/8\Phi''$ X_2: (*d*)(*x*, 1/4, 1/4), $x = 1/2 + \sqrt{2}/8\xi - 1/8\varphi - 1/8\Phi''$ X_3: (*c*)(1/4, 0, *z*), $z = 1/2 + 1/4\varphi - 1/4\Phi''$	(Φ', 0, Φ')(Φ", 0, Φ") $\Phi', \Phi'' \sim \xi^2\varphi$
23	[0, 0, 0]	*A*: (*a*)(0, 0, 0) *B*: (*d*)(1/2, 0, 1/2)	X_1: (*e*)(*x*, *y*, *z*), $x = 1/2 + \sqrt{2}/4\xi$, $y = 1/4 - 1/8\psi + 1/8\Omega$, $z = 1/4 - 1/8\psi - 1/8\Omega$ X_2: (*c*)(0, 0, 1/2)	(0, Ω, 0) $\Omega \sim \psi\xi^2$
24	[0, 0, 0]	A_1: (*a*)(0, 0, 0) A_2: (*c*)(0, 1/2, 0) A_3: (*b*)(0, 0, 1/2) *B*: (*f*) (1/4, 1/4, 1/4)	X_1: (*i*)(*x*, *y*, *z*), $x = 1/4 + 1/8\Xi_2$, $y = -1/8\Omega$, $z = 1/4 - 1/8\psi + 1/8\Xi_1$ X_2: (*h*)(*x*, *y*, 0), $x = 1/4 - \sqrt{2}/8\xi + 1/8\psi + 1/8\Xi_1$, $y_h = 1/4 + \sqrt{2}/8\xi + 1/8\psi + 1/8\Xi_1$	$(\Xi_1, \Xi_2, \Xi_1)(0, \Omega, 0)$ $\Xi_1 \sim \psi^3, \psi\xi^2$; $\Xi_2 \sim \psi^2, \xi^2$; $\Omega \sim \psi\xi^2$
25	[0, 0, 0]	A_1: (*a*)(0, 0, 0) A_2: (*b*)(0, 1/2, 0) *B*: (*f*)(1/4, 1/4, 1/2)	X_1: (*h*)(0, *y*, 1/2), $y = 1/4 - 1/8\psi + 1/8\Xi$ X_2: (*e*)(1/4, 1/4, 0) X_3: (*i*)(*x*, 0, *z*), $x = 1/4 + 1/8\psi + 1/8\Xi$, $z = 1/2 + \sqrt{2}/4\xi$	(0, Ξ, 0) $\Xi \sim \psi\xi^2$

Table 2. (Contd.)

Phase	Displacement	*A* and *B* atoms	*X* atoms	Secondary order parameters
26	[0, 0, 0]	A_1: (*c*)(0, 0, 0) A_2: (*d*)(1/2, 0, 0) *B*: (*e*) (1/4, 1/4, 1/4)	X_1: (*j*)(*x*, *y*, 0), $x = 1/4 + \sqrt{2}/8\xi_2$, $y = 1/4 + \sqrt{2}/8\xi_1$ X_2: (*f*)(*x*, 0, 1/4), $x = 1/4 + 1/8\psi + 1/8\Xi$ X_3: (*g*)(0, *y*, 1/4), $y = 1/4 - 1/8\psi + 1/8\Xi$	$(\Xi, 0, 0)$ $\Xi_3 \sim \xi_1\xi_2$
27	[0, 1/2, 0]	A_1: (*a*)(0, 0, 1/4) A_2: (*c*)(0, 1/2, *z*), $z = 1/4 - \sqrt{2}/4\,\eta'$ *B*: (*d*)(1/4, 1/4, 0)	X_1: (*g*)(*x*, *y*, *z*), $x = 1/4\mathrm{E}$, $y = 1/4 + 1/8\Xi$, $z = 1/2 - \sqrt{2}/8\eta''$ X_2: (*f*)(*x*, *x*, 1/4), $x = 1/4 + \sqrt{2}/8\xi$	$(\Xi, 0, 0)(\mathrm{E}, \sqrt{3}\,\mathrm{E})$ $\Xi \sim \eta^2, \xi^2$; $\mathrm{E} \sim \eta\xi$
28	[1/2, 0, 1/2]	*A*: (*d*)(1/4, 0, *z*), $z = 1/4 + \sqrt{2}/8\eta'$ *B*: (*b*)(1/2, 1/2, 1/2)	X_1: (*e*)(1/4, 1/2, *z*), $z = 1/2 + \sqrt{2}/8\eta''$ X_2: (*a*)= (0, 0, 0) X_3: (*c*)(0, *y*, 1/4), $y = 1/2 - \sqrt{2}/4\xi$	
29	[1/2, 0, 1/2]	*A*: (*d*)(*x*, *y*, 1/4), $x = \sqrt{2}/4\eta_2'$, $y_d = 1/4 + \sqrt{2}/8\eta_1'$ *B*: (*b*)(1/2, 0, 0)	X_1: (*d*)(*x*, *y*, 1/4), $x = 1/2 + \sqrt{2}/2\xi$, $y = 1/2 + \sqrt{2}/8\eta_1''$ X_2: (*a*)(0, 0, 0) X_3: (*c*)(*x*, 1/4, 0), $y = 1/2 + \sqrt{2}/84\eta_2''$	
30	[0, 0, 0]	A_1: (*a*)(0, 0, *z*), $z = \sqrt{2}/4\eta_1' - \sqrt{2}/4\eta_2'$ A_2: (*b*)(0, 1/2, *z*), $z = -\sqrt{2}/4\,\eta_1' - \sqrt{2}/4\eta_2'$ *B*: (*d*)(1/4, 1/4, 1/2)	X_1: (*c*)(1/4, 1/4, 0) X_2: (*f*)(*x* 0 *z*), $x = 1/4 + 1/8\psi + 1/8\Xi$, $z = 1/2 + \sqrt{2}/4\eta_1''$ X_3: (*e*)(0, *y*, *z*), $x = 1/4 - 1/8\psi + 1/8\Xi$, $z = 1/2 - \sqrt{2}/4\eta_2''$	$(\Xi, 0, 0)$ $\Xi \sim \eta_1\eta_2$
31	[0, 1/2, 0]	*A*: (*c*)(0, *y*, 1/4), $y = -\sqrt{2}/4\eta'$ *B*: (*b*)(0, 1/2, 0)	X_1: (*d*)(*x*, *y*, *z*), $x = 1/4 - 1/8\varphi + 1/4\mathrm{E}$, $y = 1/4 - 1/8\varphi - 1/4\mathrm{E}$, $z_d = 1/2 + \sqrt{2}/8\xi$ X_2: (*c*)(0, *y*, 1/4), $y = 1/2 - \sqrt{2}/4\eta''$	$(\mathrm{E}, \sqrt{3}\,\mathrm{E})$ $\mathrm{E} \sim \eta\xi$
32	[0, 0, –1/2]	*A*: (*f*)(0, *y*, *z*), $y = -\sqrt{2}/8\eta'$, $z = 3/4 + \sqrt{2}/8\Phi'$ *B*: (*c*)(1/4, 1/4, 0)	X_1: (*e*)(1/4, *y*, 1/4), $y = 3/4 + \sqrt{2}/8\eta''$ X_2: (*d*)(*x*, 0, 0), $x = 1/4 + 1/8\varphi + 1/8\Phi''$ X_3: (*f*)(0, *y*, *z*), $y = 1/4 - 1/8\varphi + 1/8\Phi''$, $z = \sqrt{2}/8\xi$	$(0, 0, \Phi')(0, 0, \Phi'')$ $\Phi', \Phi'' \sim \eta\xi, \eta^2\varphi, \xi^2\varphi$
33	[0, 0, –1/2]	A_1: (*c*)(0, *y*, 1/4), $y = \sqrt{2}/8\eta' - \sqrt{2}/8\Phi'$ A_2: (*c*)(0 *y* 1/4), $y = 1/2 + \sqrt{2}/8\eta' + \sqrt{2}/8\Phi'$ *B*: (*d*)(1/4, 1/4, 0)	X_1: (*g*)(*x*, *y*, 1/4), $x = 1/4 + 1/8\varphi - 1/8\Phi_2$, $y = 1/4 + \sqrt{2}/8\eta''$ X_2: (*e*)(*x*, 0, 0), $x = 1/4 + 1/8\psi + 1/8\Xi$ X_3: (*f*)(0, *y*, *z*), $y = 1/4 - 1/8\psi + 1/8\Xi$, $z = 1/8\varphi + 1/8\Phi''$	$(\Xi, 0, 0)(0,\Phi', 0)(0, \Phi'', 0)$ $\Xi \sim \eta\xi$; $\Phi', \Phi'' \sim \eta\psi, \eta^2\varphi, \psi^2\varphi$
34	[0, 0, 0]	A_1: (*a*)(0, 0, 0) A_2: (*b*)(0, 0, 1/2) A_3: (*d*)(0, 1/2, *z*), $z = -\sqrt{2}/4\eta'$ *B*: (*e*)(1/4, 1/4, 1/4)	X_1: (*g*)(0, *y*, *z*) , $y = 1/4 - 1/8\varphi + 1/8\Xi_2$, $z = 1/4 - \sqrt{2}/8\eta'' - 1/8\psi + 1/8\Xi_1$ X_2: (*g*)(0, *y*, *z*), $y = 1/4 + 1/8\varphi + 1/8\Xi_2$, $z = 3/4 - \sqrt{2}/8\eta'' + 1/8\psi - 1/8\Xi_1$ X_3: (*f*)(*x*, *x*, 0), $x = 1/4 + 1/8\psi + 1/8\Xi_1$	(Ξ_1, Ξ_2, Ξ_1) $\Xi_1 \sim \eta\varphi$; $\Xi_2 \sim \eta^2, \psi^2$
35	[0, 1/2, 0]	*A*: (*c*)(*x*, 1/4, *z*), $x = -\sqrt{2}/4\eta'$, $z = \sqrt{2}/4\Phi'$ *B*: (*b*)(0, 0, 1/2)	X_1: (*c*)(*x*, 1/4, *z*), $x = -\sqrt{2}/4\eta''$, $z = 1/2 - 1/4\varphi + 1/4\Phi''$ X_2: (*d*)(*x*, *y*, *z*), $x = 1/4 - 1/8\psi + 1/8\Omega$, $y = 1/2 + 1/8\varphi + 1/8\Phi''$, $z = 1/4 - 1/8\psi - 1/8\Omega$	$(0, \Omega, 0)(\Phi', 0, \Phi')(\Phi'', 0, \Phi'')$ $\Omega \sim \eta^2\psi$; $\Phi', \Phi'' \sim \eta\psi, \eta^2\varphi, \psi^2\varphi$

Note: The last column contains the remaining order parameters (not presented in Table 1 and nonzero in each phase) from the complete list of expansions of the mechanical representation in terms of irreducible representations (1) for the *X* position in the perovskite structure. For the irreducible representation $\mathbf{k}_{10}$: $\tau_{10}(X_5') = \eta$, which is twice included in the mechanical representation, the order parameters are designated as η' and η''. In the last column, η denotes both η' and η''. Designations for the secondary order parameters are as follows: $\mathbf{k}_{13}$: $\tau_{10}^{1,2}(R_{15}) = \Phi', \Phi''$, $\tau_6(R_{12}') = \mathrm{E}$, $\mathbf{k}_{11}$: $\tau_1(M_1) = \Xi$, and $\tau_3(M_3) = \Omega$. Notation of representations in parentheses is given according to [17].

Table 3. Phases of tilting about the *b* position which cannot be described as displacements of oxygen atoms

Phase	Order parameters	Space group	V'/V	Translations of the primitive cell	Tilting notation according to [1]
1	(0 μ μ)	$P4/nbm$-D_{4h}^{12} (no. 134)	4	$2\mathbf{a}_1$, $2\mathbf{a}_2$, $\mathbf{a}_3$	$a^0\,b^-\,b^-$
2	(μ μ μ)	$Pn3n$-O_h^2 (no. 222)	8	$2\mathbf{a}_1$, $2\mathbf{a}_2$, $2\mathbf{a}_3$	$a^-\,a^-\,a^-$
3	(0 μ 0)	$P4/mcc$-D_{4h}^1 (no. 124)	2	$\mathbf{a}_1$, $2\mathbf{a}_2$, $\mathbf{a}_3$	$a^0\,a^0\,c^-$
4	(0 λ 0)	$P4/m$-C_{4h}^1 (no. 83)	1	$\mathbf{a}_1$, $\mathbf{a}_2$, $\mathbf{a}_3$	$a^0\,a^0\,c^+$
5	(λ λ λ)	$R\bar{3}$=C_{3i}^2 (no. 148)	1	$\mathbf{a}_1$, $\mathbf{a}_2$, $\mathbf{a}_3$	$a^+\,a^+\,a^+$
6	(λ λ 0)	$C2/m$-C_{2h}^3 (no. 12)	1	$\mathbf{a}_1$, $\mathbf{a}_2$, $\mathbf{a}_3$	$a^0\,b^+\,b^+$
7	(λ_1 λ_2 λ_3)	$P\bar{1}$-C_i^1 (no. 2)	1	$\mathbf{a}_1$, $\mathbf{a}_2$, $\mathbf{a}_3$	$a^+\,b^+\,c^+$
8	(μ μ 0)(η 0 0 –η 0 0)(λ 0 0)	$P4/n$-C_{4h}^3 (no. 85)	4	$\mathbf{a}_1$, $2\mathbf{a}_2$, $2\mathbf{a}_3$	$a^+\,b/c\,c/b$
9	(μ 0 0)(η 0 0 0 0 0)(λ 0 0)	$P2/c$-C_{2h}^4 (no. 13)	2	$\mathbf{a}_1$, $\mathbf{a}_2$, $2\mathbf{a}_3$	$a^+\,b^+\,c^-$
10	(μ_1 0 μ_2)(0 ψ 0)	$Pcna$-D_{2h}^4 (no. 50)	4	$2\mathbf{a}_1$, $\mathbf{a}_2$, $2\mathbf{a}_3$	$a^+\,b^-\,c^-$
11	(μ_1 μ_2 μ_1)(ψ 0 –ψ)	$P4/nnc$-D_{4h}^4 (no. 126)	8	$2\mathbf{a}_1$, $2\mathbf{a}_2$, $2\mathbf{a}_3$	$a^-\,b/-c\,c/-b$
12	(0 μ 0)(0 0 η η 0 0)(λ 0 –λ)	$C2/c$- C_{2h}^6 (no. 15)	2	$\mathbf{a}_1$, $2\mathbf{a}_2$, $\mathbf{a}_3$	$a^+\,b^+\,c^-$

Note: Designations for the order parameters are as follows: $\mathbf{k}_{10}$: $\tau_2(X_1')$ = μ, $\mathbf{k}_{10}$: $\tau_{10}(X_5')$ = η, $\mathbf{k}_{11}$: $\tau_5(M_3)$ = ψ, and $\mathbf{k}_{12}$ = 0: $\tau_9(\Gamma_{15}')$ = λ. Notation of representations in parentheses is given according to [17].

Table 4. Order parameters calculated for phase **35** (space group *Pnma*) from structural data obtained by different authors (the phase numbering is the same as Tables 1, 2)

Crystal	Order parameter						
	φ	ψ	η'	η''	Ξ	Φ'	Φ''
$CdTiO_3$–300 K [21]	0.369	0.384	–0.109	0.079	0.009	–0.024	0.008
$GdGaO_3$ [22]	0.386	0.396	–0.168	0.078	0.005	–0.042	0.006
$LaTiO_3$ [23]	0.326	0.332	–0.133	0.019	–0.072	–0.021	0.010
$CaTiO_3$–298 K [24]	0.283	0.267	–0.093	0.03	–0.0064	–0.020	–0.006
$SrHfO_3$–300 K [25]	–0.26	0.24	0.0453	–0.0396	0.0088	0.0113	–0.008
$SrZrO_3$–273 K [26]	–0.283	0.273	0.068	–0.038	0.004	0.011	–0.008
$PrNiO_3$ [27]	0.283	0.231	–0.083	0.015	–0.032	–0.011	–0.013
$SrRuO_3$–300 K [20]	0.182	0.213	–0.046	0.010	–0.001	–0.004	–0.022
$SrRuO_3$–573 K [19]	0.002	–0.157	–0.037	0.004	0.001	0.001	–0.190
$SrRuO_3$–673 K [19]	0.002	0.002	0.008	0.017	–0.164	0.002	–0.178
$SrRuO_3$–773 K [19]	0.005	–0.008	0.0003	0.006	–0.001	0.002	–0.157

Note: Designations for the order parameters are as follows: $\mathbf{k}_{10}$: $\tau_{10}^{1,2}(X_5')$ = η', η'', $\mathbf{k}_{11}$: $\tau_1(M_1)$ = Ξ, $\tau_5(M_3)$ = ψ, $\mathbf{k}_{13}$: $\tau_8(R_{25})$ = φ, $\tau_{10}^{1,2}(R_{15})$ = Φ', Φ''. Capital letters stand for the secondary order parameters. Notation of representations in parentheses is given according to [17].

A similar analysis of the rotations was performed on the basis of the complete set of order parameters (1) instead of set (3). In this case, we revealed 12 additional low-symmetry phases whose parameters are listed in Table 3. These phases are described by the order parameters not included in set (2). Consequently, the rotations associated with these phases cannot occur through displacements of oxygen atoms in the perovskite structure. However, these phases can also be treated as phases of tilting about the *b* position. This is confirmed by the tiltings presented in the last column of Table 3 and determined using the method proposed in [1]. Moreover, this circumstance indicates the ambiguity of the Glazer notation [1], as applied to the description of the possible low-symmetry tilting phases.

Phases **1**–**19** are described by the order parameters transformed according to one irreducible representation. An analysis of phases **26**, **29**, and **30** demonstrates that they can also be considered as phases with one order parameter. In this case, the order parameters φ, ξ, and ψ, respectively (see Table 1), should be treated as secondary order parameters. The remaining phases are described by two order parameters. It was also established that, among the three order parameters given in Table 1, any pair of parameters can be chosen for phases **31**–**35**. This implies that the order parameter consisting of any two irreducible representations for phases **31**–**35** (Table 1) is sufficient for describing the symmetry of phases. The third order parameter for these phases is the secondary order parameter.

Let us now illustrate the results obtained. For this purpose, we consider the order parameters for the phase with space group *Pnma*. The order parameters calculated according to Table 2 from structural data are listed in Table 4. As can be seen from Table 4, the largest values are obtained for the order parameters φ and ψ; it is these parameters that are commonly used as order parameters [9]. For $CdTiO_3$, $GdGaO_3$, and $LaTiO_3$ crystals, the order parameter η_1 is large compared to the secondary order parameters. Although, as was noted above, these two order parameters are sufficient for describing the symmetry of the phase, the large contribution of the order parameter η_1 can lead to qualitatively new results in the description of the properties of these crystals under external actions. It should be noted that there is a considerable scatter in the order parameters determined for $SrRuO_3$ crystals from the results obtained by Kennedy and Hunter [19]. These values of order parameters are not typical of the phase with space group *Pnma*. Most likely, this can be explained by the large error in determining the structural characteristics (compare with the order parameters calculated for $SrRuO_3$ crystals from the data reported by Chakoumakos *et al.* [20] and also with the order parameters for other crystals in Table 4).

The tilting structures in perovskites can be considered a manifestation of the cooperative Jahn–Teller effect in the following context. Local octahedral symmetry of the central atom *B* leads to splitting of the atomic levels of *d* electrons into the T_{2g} and E_g levels. In the case when the number of *d* electrons involved in the formation of a bond is no more than four, the T_{2g} state has the lowest energy [28]. Symmetry T_{2g} corresponds to symmetry of rotation about the *b* position in the perovskite structure. For a triply degenerate T_{2g} level, the interaction with atomic vibrations results in the removal of the degeneracy; i.e., the Jahn–Teller effect manifests itself in the form of a structural distortion. For energy levels of the phonon subsystem, which are described by irreducible representations (3), the interaction with *d* electrons is strongest due to the linear invariants. The data on the possible lowering of symmetry are presented in Table 1. For phases **1** and **13**, the local states of electrons in the octahedral environment can be doubly degenerate (the position has symmetry C_{4h}). For these states, the structure will undergo a further distortion; i.e., these phases are intermediate. The remaining irreducible representations, namely, $\tau_2(\mathbf{k}_{10})$ and $\tau_9(\mathbf{k}_{12})$, which are involved in representations (1), do not describe the phonon subsystem. The states associated with these energy levels can arise without a distortion of the perovskite structure. However, the above interpretation of the tilting structures in each specific case should be used with caution, because, within this approach, the role played by the *A* atom in the formation of the low-symmetry phases is disregarded. Most likely, this transformation can occur with distortions in which the *B* atoms become nonequivalent [4].

REFERENCES

1. A. M. Glazer, Acta Crystallogr., Sect. B: Struct. Crystallogr. Cryst. Chem. **28**, 3384 (1972).
2. A. M. Glazer, Acta Crystallogr., Sect. A: Cryst. Phys., Diffr., Theor. Gen. Crystallogr. **31**, 756 (1975).
3. P. M. Woodward, Acta Crystallogr., Sect. B: Struct. Sci. **53**, 32 (1997).
4. P. M. Woodward, Acta Crystallogr., Sect. B: Struct. Sci. **53**, 44 (1997).
5. N. W. Thomas, Acta Crystallogr., Sect. B: Struct. Sci. **52**, 16 (1996).
6. L. D. Landau and E. M. Lifshitz, *Course of Theoretical Physics*, Vol. 5: *Statistical Physics*, 3rd ed. (Nauka, Moscow, 1976; Pergamon Press, Oxford, 1980), Part 1.
7. Yu. M. Gufan, *Structural Phase Transitions* (Nauka, Moscow, 1982).
8. É. B. Vinberg, Yu. M. Gufan, V. P. Sakhnenko, and Yu. I. Sirotin, Kristallografiya **19**, 21 (1974) [Sov. Phys. Crystallogr. **19**, 10 (1974)].
9. K. S. Aleksandrov, A. T. Anistratov, B. V. Beznosikov, and N. V. Fedoseeva, *Phase Transitions in Crystals of ABX_3 Halide Compounds* (Nauka, Novosibirsk, 1981).
10. C. J. Howard and H. T. Stokes, Acta Crystallogr., Sect. B: Struct. Sci. **54**, 782 (1998).
11. R. A. Cowley, Phys. Rev. Sect. A **134**, 981 (1964).
12. K. S. Aleksandrov, Kristallografiya **21**, 249 (1976) [Sov. Phys. Crystallogr. **21**, 133 (1976)].

13. K. S. Aleksandrov, Ferroelectrics **14**, 801 (1976).
14. W. Cochran and A. Zia, Phys. Status Solidi **25**, 273 (1968).
15. G. M. Chechin, T. I. Ivanova, and V. P. Sakhnenko, Phys. Status Solidi B **152**, 431 (1989).
16. O. V. Kovalev, *Irreducible Representations of the Space Groups* (Akad. Nauk Ukr. SSR, Kiev, 1961; Gordon and Breach, New York, 1965).
17. L. P. Bouckaert, R. Smoluchowski, and E. Wigner, Phys. Rev. **50**, 58 (1936).
18. I. A. Sergienko, Yu. M. Gufan, and S. Urazhdin, Phys. Rev. B **65**, 144104 (2002).
19. B. J. Kennedy and B. A. Hunter, Phys. Rev. B **58**, 653 (1998).
20. B. C. Chakoumakos, S. E. Negler, S. T. Misture, and H. M. Christen, Physica B (Amsterdam) **241–243**, 358 (1998).
21. B. S. Sasaki, C. T. Prewitt, and J. D. Baas, Acta Crystallogr., Sect. C: Cryst. Struct. Commun. **43**, 1668 (1987).
22. J. C. Guitel, M. Marezio, and J. Mareschal, Mater. Res. Bull. **11**, 739 (1976).
23. M. Eitel and J. E. Greedan, J. Less-Common Met. **116**, 95 (1986).
24. X. Liu and R. C. Liebermann, Phys. Chem. Miner. **20**, 171 (1993).
25. B. J. Kennedy, C. J. Howard, and B. C. Chakoumakos, Phys. Rev. B **60**, 2972 (1999).
26. B. J. Kennedy, C. J. Howard, and B. C. Chakoumakos, Phys. Rev. B **59**, 4023 (1999).
27. P. Lacorre, J. B. Torrance, J. Pannetier, *et al.*, J. Solid State Chem. **91**, 225 (1991).
28. I. B. Bersuker, *Electronic Structure and Properties of Coordination Compounds* (Khimiya, Leningrad, 1976).

Translated by O. Borovik-Romanova

Crystallography Reports, Vol. 49, No. 1, 2004, pp. 29–39. Translated from Kristallografiya, Vol. 49, No. 1, 2004, pp. 34–44.

THEORY OF CRYSTAL STRUCTURES

Dedicated to the 80th Birthday of L.A. Shuvalov

Microscopic Calculations of Displacive (Elpasolite Family) and Order–Disorder (Potassium Selenate Family) Structural Phase Transitions

V. I. Zinenko and N. G. Zamkova

Kirenskiĭ Institute of Physics, Siberian Division of the Russian Academy of Sciences, Krasnoyarsk, 660036 Russia

e-mail: zvi@iph.krasn.ru

Received June 5, 2003

Abstract—The critical temperatures and thermodynamic characteristics for the displacive phase transition $O_h^7 \longrightarrow O_{4h}^5$ in crystals of the elpasolite family Rb_2KBF_6 (B = Sc, In, Lu) and for the successive phase transitions $D_{6h}^4 \longrightarrow D_{2h}^{16} \longrightarrow I \longrightarrow C_{2h}^5$ (I is the incommensurate phase) in crystals of the selenate potassium family have been calculated. The calculations were carried out using the effective Hamiltonian method. The Hamiltonian parameters for the elpasolite-like crystals were determined from ab initio calculations, and those for the crystals of the selenate potassium family were found using a small number of fitting parameters. © *2004 MAIK "Nauka/Interperiodica".*

INTRODUCTION

Investigation of structural phase transitions is a fundamental problem of solid-state physics. Although a large number of experimental and theoretical studies were devoted to this problem, it is still of interest.

It is generally accepted to divide structural phase transitions in crystals into two groups characterized by different mechanisms: displacive and order–disorder transitions. At displacive transitions in the low-temperature phase, atoms are slightly displaced relative to their equilibrium positions in the high-temperature phase. In the middle of the last century, Cochran and Anderson [1, 2] attributed such phase transitions to the instability of crystals with respect to some of their normal vibrational modes in the high-temperature phase (the so-called soft modes). The soft-mode frequency is characterized by a critical temperature dependence and becomes zero at the transition point. The displacements of atoms in the low-temperature phase represent "frozen" displacements of soft-mode vibrations.

Order–disorder phase transitions are caused by the ordering in the low-temperature phase of some atoms or molecules, which are disordered in high-temperature phase with respect to several equiprobable equilibrium positions. In this case, displacements of atoms with respect to the equilibrium positions cannot be considered small, and the concept of the soft mode of lattice vibrations is less useful. Ising-like models are more appropriate for describing order–disorder phase transitions. In these models, a new variable (the pseudospin) is assigned to a structural element subjected to ordering, which describes the motion of this element in the crystal potential.

Most microscopic models describing structural phase transitions use the model Hamiltonian

$$H = H_1 + H_{\text{int}}, \tag{1}$$

where $H_1 = \sum V(u_i)$ is the one-particle Hamiltonian and H_{int} is the interaction Hamiltonian. The properties of a system described by the Hamiltonian H_1 depend on the form of the single-particle potential $V(u_i)$. The model Hamiltonian can be characterized by two energy parameters: the height of the local potential barrier Δ (in the single-particle potential) and the binding energy J for atoms located in different potential wells. In this case, the type of system under study is determined by the dimensionless parameter $S = \Delta/J$. The case $S \gg 1$ corresponds to order–disorder transitions. Each atom is located near the bottom of some potential well until the temperature becomes of the same order of magnitude as Δ and jumps between wells become possible. A phase transition in such a system is related to collective well-to-well motion, whereas the motion of atoms in potential wells can be disregarded. This is the situation considered in the Ising model. On the contrary, in the case corresponding to displacive transitions ($S \ll 1$),

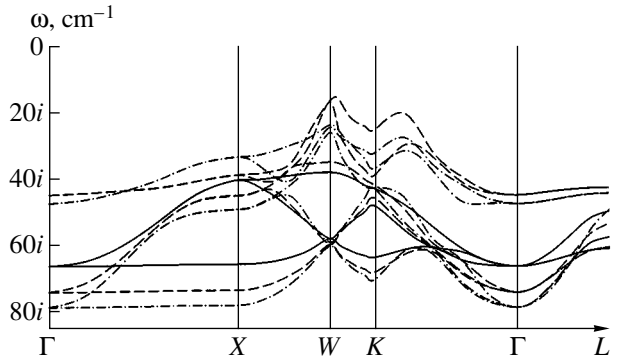

Fig. 1. Unstable part of the spectrum of $Rb_2KB^{3+}F_6$ crystals. B = Sc (solid line), In (dotted line), and Lu (dot-dashed line).

intrawell motion of atoms is dominant and their collective behavior has a phonon character.

The two above cases (single- and double-minimum potentials) are extreme ones. Other situations may occur in the case of real compounds when the single-particle potential may be, for example, multiminimum. Such a situation can be described in terms of an Ising-like model, where the pseudospin variable takes several (more than two) values, in accordance with the number of potential minima. Crystals of the selenate potassium family with the general formula $ACBX_4$ present an example of such systems. In these compounds, the ion groups BX_4 are regular tetrahedra, which have up to 12 equiprobable equilibrium positions in the high-temperature phase. In crystals of this family, successive phase transitions are realized via partially ordered phases, including incommensurate ones. This is the feature that attracts the attention of researchers. ABX_3 crystals with perovskite structure, as well as related $A_2BB^{3+}X_6$ crystals with elpasolite structure, are examples of systems with displacive transitions.

We present below the calculations of the static properties and the thermodynamics of the displacive phase transition by an example of $Rb_2KB^{3+}F_6$ (B = Sc, In, Lu) crystals and the order–disorder transition by an example of three crystals of the selenate potassium family: Rb_2ZnCl_4, K_2SeO_4, and K_2SO_4.

DISPLACIVE PHASE TRANSITIONS

Phase transitions in $A_2BB^{3+}X_6$ crystals, which belong to the elpasolite family, are due to the instability of crystal lattice in the high-symmetry cubic phase; the soft mode of normal vibrations is related in most crystals either to the rotation of the BX_6 octahedron or to the combination of the octahedron rotations and displacements of ion A. Apparently, such an instability of lattice with respect to normal vibrations is a characteristic feature of perovskite-like compounds.

The equilibrium properties, lattice dynamics, and phase transitions for a number of crystals of the elpasolite family were calculated in [3–6] in terms of the generalized Gordon–Kim model [7], with regard to the deformability and dipole polarizability of ions. We represent here more detailed results of such calculations for three isomorphous crystals $Rb_2KB^{3+}F_6$ (B = Sc, In, Lu). The structure of these crystals in the high-temperature phase is cubic with the sp. gr. O_h^7 and with one molecule in the unit cell. Under cooling, crystals undergo two successive structural phase transitions: first, to the tetragonal phase with the sp. gr. C_{4h}^5 without changing the unit-cell volume and, second, to the monoclinic phase with the sp. gr. C_{2h}^5 and two molecules per unit cell. As the structural investigations of low-temperature phases show [8], distortions of the cubic structure in the tetragonal phase are related mainly to rotations (uniform over the total crystal volume) of $B^{3+}X_6$ octahedra. Distortions in the monoclinic phase are due to nonuniform rotations of octahedra and displacements of Rb ions from equilibrium positions of the tetragonal phase.

The entire spectrum of lattice vibrations for these crystals was calculated in [5, 6]. The vibrational spectra of all three crystals contain soft modes. Figure 1 shows the unstable part of the spectra of the crystals. As can be seen, the most unstable modes belong to the vibrational branch between the points $\Gamma(\mathbf{q} = (0, 0, 0))$ and $X(\mathbf{q} = (2\pi/a_0, 0, 0))$ of the Brillouin zone. At the point Γ, the mode T_{1g} of this branch is triply degenerate. Along the directions Γ–X, Γ–Y, and Γ–Z, including the boundary points, the low-lying modes are nondegenerate. Vibrations in which fluorine ions are displaced correspond to the triply degenerate mode at $\mathbf{q} = 0$ and to the nondegenerate modes along the directions Γ–X, Γ–Y, and Γ–Z. The displacements of fluorine ions v_k^{F} in these modes are related as follows:

$$\begin{aligned}
&-v_{1y}^{\mathrm{F}} = v_{2y}^{\mathrm{F}} = v_{5z}^{\mathrm{F}} = -v_{6z}^{\mathrm{F}};\\
T_{1g}:&-v_{1x}^{\mathrm{F}} = v_{2x}^{\mathrm{F}} = -v_{3z}^{\mathrm{F}} = v_{4z}^{\mathrm{F}},\\
&-v_{3y}^{\mathrm{F}} = v_{4y}^{\mathrm{F}} = v_{5x}^{\mathrm{F}} = -v_{6x}^{\mathrm{F}};\\
X_3:&-v_{1y}^{\mathrm{F}} = v_{2y}^{\mathrm{F}} = v_{5z}^{\mathrm{F}} = -v_{6z}^{\mathrm{F}};\\
Y_3:&-v_{1x}^{\mathrm{F}} = v_{2x}^{\mathrm{F}} = -v_{3z}^{\mathrm{F}} = v_{4z}^{\mathrm{F}};\\
Z_3:&-v_{3y}^{\mathrm{F}} = v_{4y}^{\mathrm{F}} = v_{5x}^{\mathrm{F}} = -v_{6x}^{\mathrm{F}}.
\end{aligned} \qquad (2)$$

These displacements lead to the rotation of the $B^{3+}X_6$ octahedron.

Under cooling, the transition to the tetragonal phase occurs first in the crystals under consideration. This transition is related to the condensation of one component of the triply degenerate soft mode T_{1g} at the center of the Brillouin zone, which corresponds to the rotation

of the $B^{3+}X_6$ octahedron around one of the principal axes of the cubic lattice. The calculated spectrum of the frequencies of lattice vibrations in the tetragonal phase, with the coordinates of fluorine ions corresponding to their displacements along the eigenvector of the T_{1g} mode (2), also contains unstable modes. Analysis of the eigenvectors of unstable modes shows that there are no vibrational modes in the tetragonal phase, in which displacements of ions would correspond only to rotation of the $B^{3+}X_6$ octahedron. In the most unstable mode at the boundary point X of the Brillouin zone, four F^- ions and Rb^+ ions are displaced:

$$v_{1x}^{F} = -v_{2x}^{F} \approx v_{1y}^{F} = -v_{2y}^{F},$$
$$v_{5z}^{F} \approx -\frac{3}{4} v_{6z}^{F}, \quad (3)$$
$$v_{1z}^{Rb} = v_{2z}^{Rb}.$$

These displacements lead to monoclinic distortion of the tetragonal phase with doubling of the unit-cell volume, which corresponds to the second experimentally observed phase transition to the monoclinic phase ($C_{4h}^5 \longrightarrow C_{2h}^5$). The calculated spectrum of the frequencies of lattice vibrations for the monoclinic phase with the coordinates of ions, corresponding to the displacements described by (3), contains no unstable vibrational modes. Thus, the calculation of the phonon spectra for the crystals under consideration shows that the phase transitions in these crystals are related to rotations of $B^{3+}X_6$ octahedra.

In order to calculate the temperature behavior of $Rb_2KB^{3+}F_6$ crystals, we will write the effective Hamiltonian in accordance with the scheme proposed in [9], taking into account only the degrees of freedom related to unstable modes (2) (the local-mode approximation). The local mode we use can be written as

$$S_x = \frac{1}{2a_0}[v_{1y}^{F} - v_{2y}^{F} + v_{3z}^{F} - v_{4z}^{F}],$$
$$S_y = \frac{1}{2a_0}[v_{1x}^{F} - v_{2x}^{F} + v_{5z}^{F} - v_{6z}^{F}], \quad (4)$$
$$S_z = \frac{1}{2a_0}[v_{4y}^{F} - v_{3y}^{F} + v_{5x}^{F} - v_{6x}^{F}],$$

where v_k^F is the amplitude of displacement of the kth F atom from (2) and a_0 is the calculated lattice parameter for the cubic phase. The symmetry operations of the cubic phase transform the local mode (S_x, S_y, S_z) as a pseudovector. The pseudovector is placed at the sites of the fcc lattice. Now, taking into account the transformation properties of the local mode and the fcc lattice, which are subjected to the symmetry operations of the cubic phase, we can write the microscopic effective Hamiltonian. The expression for the total effective Hamiltonian is given in [3–6]. For brevity, we present here the formal expression:

Table 1. Parameters of the effective Hamiltonian (eV)

	Rb_2KScF_6	Rb_2KInF_6	Rb_2KLuF_6
One-site parameters			
A	4.10	3.09	13.82
B	2.44×10^3	1.40×10^3	1.35×10^3
C	2.63×10^3	2.25×10^3	2.21×10^3
D	-40.70×10^3	-0.73×10^3	-1.16×10^3
Interstitial parameters			
a_1	–4.33	–5.39	–7.59
a_2	–0.03	–0.05	0.10
a_3	1.87	0.63	2.71
b_1	–0.00	–1.35	–1.90
b_2	–2.17	–1.35	–1.90
Coefficients of coupling with uniform strains			
g_1	118.5	39.88	53.00
g_2	–23.6	–15.92	–21.20
Elastic constants			
C_{11}	50.0	53.6	68.6
C_{12}	12.8	11.7	18.7
C_{44}	18.2	9.5	3.4
Transition temperature			
T^{calcd} (K)	250	550	660
T^{exper} (K)	252	283	360

$$H_1 = A\{S_{i\alpha}^2\} + B\{S_{i\alpha}^4\} + C\{S_{i\alpha}^2 S_{i\beta}^2\} + D\{S_{i\alpha}^6\},$$
$$H = a_k\{S_{i\alpha}S_{i+1\beta}\} + b_k\{S_{i\alpha}S_{i+1\beta}\} + g_k\{e_n S_{i\alpha}S_{i\beta}\} + C_{nn'}\{e_n e_{n'}\}. \quad (5)$$

Here, the anharmonic terms are included only into the single-particle Hamiltonian; all the fourth-order terms (the coefficients B and C) and some of the sixth-order terms (the coefficient D) are taken into account. A is the coefficient at the harmonic terms of the single-particle Hamiltonian. The pair interactions between the local modes are taken into account within the first (coefficients a_1, a_2, a_3) and second (coefficients b_1, b_2) coordination spheres. The interaction between the local mode and uniform strains e_n (coefficients g_1 and g_2) is also taken into account. C_{nn} are the elastic constants of the crystal. It should be noted that the local mode S is nonpolar. Hence, long-range dipole–dipole interactions can be disregarded. The procedure of determining the parameters of Hamiltonian (5) is described in detail in [5, 6]. Table 1 lists the parameters of the effective Hamiltonian for all three crystals under consideration.

The thermodynamics of the phase transition with the derived effective Hamiltonian was studied by the Monte Carlo method [3–6]. The conventional Metrop-

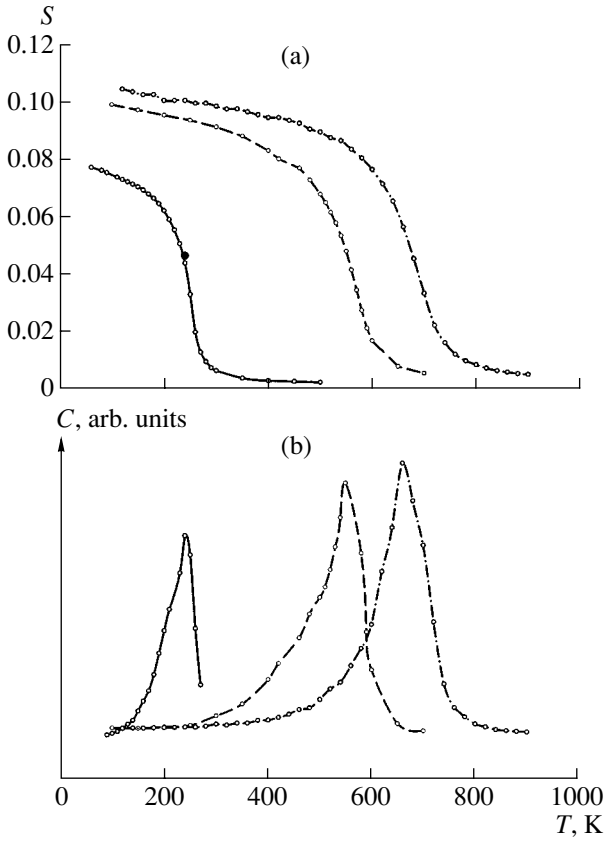

Fig. 2. Calculated temperature dependences for $Rb_2KB^{3+}F_6$ crystals: (a) order parameter in the tetragonal phase and (b) specific heat. B = Sc (solid line), In (dotted line), and Lu (dot-dashed line). The filled circle indicates the experimental value of S_z from the structural data on Rb_2KScF_6 at T = 240 K [8].

olis procedure [10] for the fcc $10 \times 10 \times 10$ lattice in size with periodic boundary conditions was used. A three-component pseudovector (S_x, S_y, S_z) was located in each lattice site, the entire lattice being in a field of uniform strains (e_1, e_2, e_3). The calculated temperature dependences of the components S_x, S_y, S_z and the specific heat are shown in Fig. 2. The phase-transition temperatures, determined from the peak positions on the temperature dependences of the specific heat (Fig. 2b), amounted to T_c = 250, 550, and 660 K for Rb_2KScF_6, Rb_2KInF_6, and Rb_2KLuF_6, respectively. At these temperatures, the second-order phase transition to the distorted phase with the pseudovector $S_z = S$, $S_x = S_y = 0$ (Fig. 2a) occurs in the crystals under study. This phase has the tetragonal symmetry, the same unit-cell volume as the cubic phase, and the sp. gr. C_{2h}^5 (which is observed experimentally in these crystals). The calculated value of the transition temperature for Rb_2KScF_6 is almost the same as the experimental value (252 K [8]), whereas the calculated transition temperatures for Rb_2KInF_6 and Rb_2KLuF_6 exceed the corresponding experimental values (283 and 360 K, respectively [8]) by nearly a factor of two. Primarily, the discrepancy may be related to the insufficient accuracy of the method of calculating the total energy of a crystal and the spectrum of lattice vibrations, which was used in this study. In the above approach, the error in calculating these values is about 5%, which exceeds the error of ab initio methods. At the same time, the phase-transition temperature is very sensitive to specific features of microscopic interactions. The parameters of the effective Hamiltonians for somewhat varied structures of Rb_2KInF_6 crystals were calculated in [5, 6], and the phase-transition temperatures were found with the use of these Hamiltonians. It was shown in [5, 6] that small changes (~4%) in the positions of ions in a crystal lattice significantly change the value of T_c.

Figure 3 shows the experimental and calculated temperature dependences of the components of the elastic-strain tensor $e_1 = e_2$, e_3 in the tetragonal phase. The quantitative agreement between the calculated and experimental values is quite satisfactory.

In our calculations of the thermodynamics of $Rb_2KB^{3+}F_6$ crystals by the Monte Carlo method, the tetragonal phase remains stable at temperatures as low as T = 0 K, whereas the second-order phase transition to the monoclinic phase C_{2h}^5 with doubling of the unit-cell volume is observed in experiments with these crystals. The results of structural analysis of the monoclinic phase [8] and the eigenvector of the mode that is most unstable in the tetragonal phase (3) show that this transition, along with the rotation of the $B^{3+}X_6$ octahedron, is related to displacements of Rb ions. This fact indicates that displacements of Rb ions play an important role in the stabilization of the monoclinic phase in these crystals. Thus, in order to describe the structural phase transition $C_{4h}^5 \longrightarrow C_{2h}^5$, one should take into account in the effective Hamiltonian, along with pure rotation of an octahedron, the vibrational modes corresponding to these degrees of freedom.

Nevertheless, these results indicate that the phase transition $O_h^7 \longrightarrow C_{4h}^5$ in $Rb_2KB^{3+}F_6$ crystals is mainly due to uniform (with respect to the lattice) rotations of the $B^{3+}X_6$ octahedron, whereas the other degrees of freedom contribute only insignificantly to both the mechanism and the thermodynamics of this phase transition.

ORDER–DISORDER PHASE TRANSITION

A family of crystals with the general formula $ACBX_4$ (the selenate potassium family) is an example of systems characterized by another type of structural phase transition: order–disorder transition. It was found experimentally [11] that the phase transitions in crystals of this family are related to ordering of tetrahedral groups BX_4 and, in most cases, the following sequence of phase transitions is observed: disordered phase $\longrightarrow$

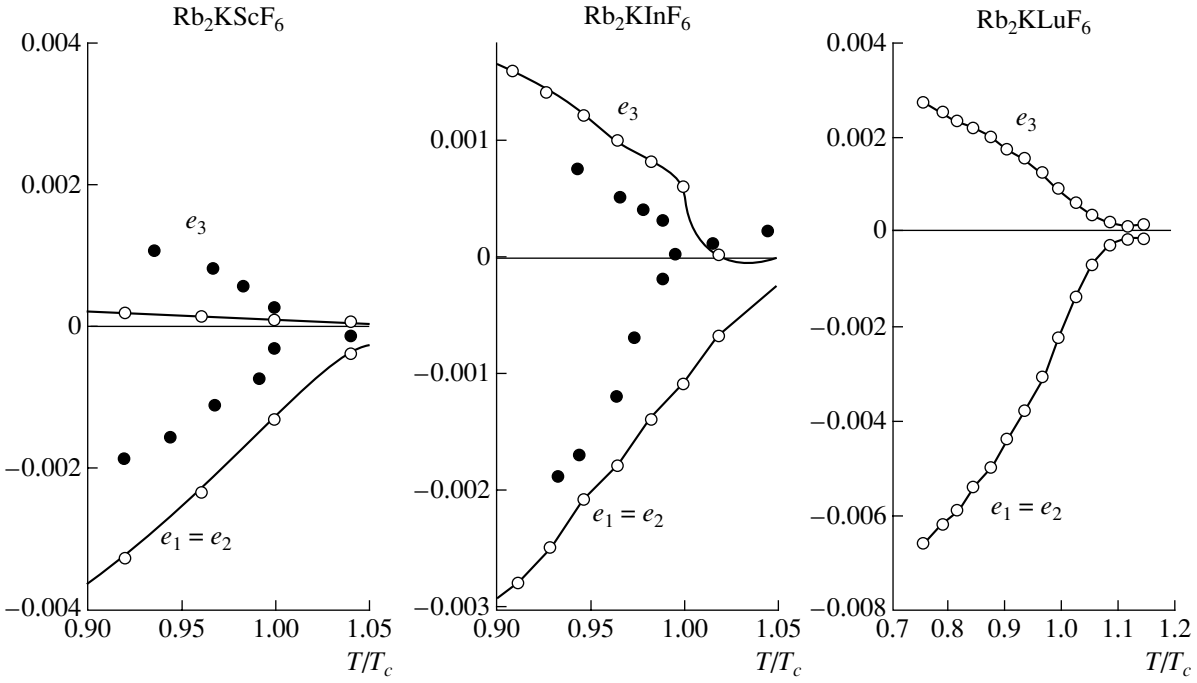

Fig. 3. Temperature dependences of the strain-tensor components for the tetragonal phase: Monte Carlo (open circles) and experimental [8] (filled circles) data.

partially ordered phase ⟶ incommensurate phase ⟶ completely ordered phase. The high-temperature phase has the structure of the α-K_2SO_4 type with the sp. gr. D_{6h}^4. The unit cell is hexagonal and contains two molecules. This structure may exist if BX_4 tetrahedra are orientationally disordered. This was observed in some crystals at temperatures much higher than room temperature. Under cooling to T_{c1}, a partial ordering of BX_4 groups occurs and the hexagonal phase D_{6h}^4 transforms into another structural phase, most often into the orthorhombic phase of the β-K_2SO_4 type with four molecules in the unit cell, described by the sp. gr. D_{2h}^{16}. As the crystal is cooled further to T_{c2}, tetrahedral groups become completely ordered. The low-temperature phase may be both ferroelectric and ferroelastic, and the phase transition into this phase may occur both with and without changing the unit-cell volume. In many crystals of this family (Rb_2ZnCl_4, Rb_2LiSO_4, K_2SeO_4, and others), the phase transition into another intermediate (incommensurate) phase is observed at the temperature T_i. In addition, phase transitions between completely ordered phases may occur in a number of crystals.

Thus, this family is characterized by a rich phase diagram, which includes, among others, incommensurate phases. It is no wonder that a large number of studies, both experimental and theoretical, were devoted to this family. It is of importance that all known structures of $ACBX_4$ crystals have a general property: they are derivatives of the high-symmetry hexagonal phase D_{6h}^4, in which tetrahedral groups BX_4 are necessarily disordered with respect to several equiprobable equilibrium positions. Thus, it is reasonable to assume that phase transitions in these compounds are related to uniform or nonuniform orderings of these groups rather than to the instability of a crystal with respect to some lattice vibrational mode.

A statistical model of phase transitions in crystals of the selenate potassium family was proposed in [12]. It is assumed in terms of this model that, in the high-temperature phase D_{6h}^4, BX_4 tetrahedra are disordered with respect to four equilibrium positions and the phase transitions are related to partial or complete ordering of these groups. In addition, only orientational degrees of

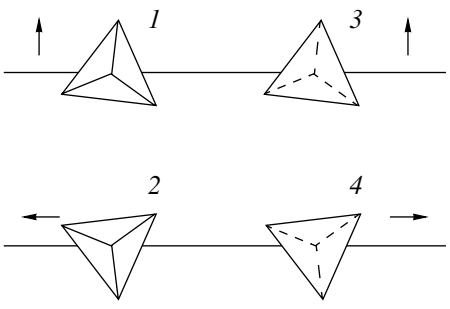

Fig. 4. Four positions of BX_4 tetrahedra in the phase D_{6h}^4.

Table 2. Effective interaction constants (K)

R	Rb_2ZnCl_4				K_2SeO_4				K_2SO_4			
	V_{11}	V_{12}	V_{13}	V_{14}	V_{11}	V_{12}	V_{13}	V_{14}	V_{11}	V_{12}	V_{13}	V_{14}
$\sqrt{a_0^2/3 + c_0^2/4}$	325	432	–746	–640	711	764	–1018	–966	794	839	–1127	–1081
a_0	435	494	–249	–188	572	604	–490	–458	623	623	–575	–576
$\sqrt{4(a_0^2/3) + c_0^2/4}$	100	53	136	89	96	83	65	52	89	83	147	141
c_0	–73	–56	90	106	–12	–4.4	53	60	32	39	103	110
$a_0\sqrt{3}$	17	16	–6.9	–7.7	17	16	–13	–14	16	15	–11	–12
$\sqrt{a_0^2 + c_0^2}$	8.8	–7.5	53	37	13	2.8	47	37	28	11	136	119
$\sqrt{7a_0^2/3 + c_0^2/4}$	114	116	84	86	81	79	53	51	90	67	93	70
$2a_0$	1.4	–0.3	–7.2	–8.9	3.9	3.6	–7.7	–7.9	–0.7	–0.9	–8.1	–8.2
$\sqrt{13(a_0^2/3) + c_0^2/4}$	–44	–23	–42	–21	–27	–20	–31	–24	–31	–27	–43	–38
$\sqrt{3a_0^2 + c_0^2}$	4.6	3.8	0.5	–0.3	3.7	3.4	–1.2	–1.5	4.4	3.9	3.2	2.8
$\sqrt{a_0^2/3 + 9c_0^2/4}$	116	92	18	–5.9	86	79	15	7.8	148	145	11	7.5
$\sqrt{16(a_0^2/3) + c_0^2/4}$	–72	–44	–57	–30	–43	–35	–41	–33	–50	–46	–61	–56
$\sqrt{4a_0^2 + c_0^2}$	1.0	0.8	–0.3	–0.5	1.4	1.4	–1.0	–1.0	0.9	0.9	0.7	0.8
$\sqrt{4a_0^2/3 + 9c_0^2/4}$	–12	2.4	–44	–30	–7.0	–3.0	–25	–21	3.7	5.6	–18	–16
$\sqrt{19(a_0^2/3) + c_0^2/4}$	–26	–39	5.2	–18	–16	–19	4.8	–7.4	–22	–15	–5.4	2.3
$a_0\sqrt{7}$	–4.4	–6.1	5.6	3.8	–2.2	–2.7	2.1	1.6	–4.0	–4.6	2.8	2.2
$\sqrt{7a_0^2/3 + 9c_0^2/4}$	–22	–30	–31	–38	–14	–18	–18	–22	–14	–13	–14	–14
$2c_0$	18	15	–32	–35	8.6	7.4	–27	–28	3.9	2.9	–61	–62

freedom of tetrahedral groups were taken into account in the model Hamiltonian:

$$H = \sum V_{ij}(\mathbf{r} - \mathbf{r}')C_i(\mathbf{r})C_j(\mathbf{r}'),$$

$$C_i(\boldsymbol{r}) = \begin{cases} 1, \text{ if the } BX_4 \text{ group} \\ \text{occupies position } i \\ 0, \text{ in the opposite case,} \end{cases} \quad (6)$$

where V_{ij} are the effective interaction constants for BX_4 groups. The effective interaction constants were calculated in [13] in terms of the electrostatic model [14]. It was assumed in [13] that BX_4 groups are regular rigid tetrahedra and their interaction includes both the direct octupole–octupole interaction and the indirect interaction via vibrations of A and C metal ions; the latter were considered as polarizable ions, and their dipole–dipole interaction was taken into account. The dipole moments of ions A and C, $\mathbf{d}_A$ and $\mathbf{d}_C$, respectively, are defined as sums of the electron and ion dipoles (the latter appear due to displacements of A and C ions from the equilibrium positions of the hexagonal phase). In this case, the polarizabilities of A and C ions, α_A and α_C, respectively, serve as fitting parameters. In addition, such an approach allows one to take into account implicitly the short-range dipole–dipole interaction, which leads to renormalization of the electronic polarizability [7]. We present below the results of calculation of the effective constants and the thermodynamics of phase transitions for the crystals Rb_2ZnCl_4, K_2SeO_4, and K_2SO_4 of the selenate potassium family.

At high temperatures, Rb_2ZnCl_4 has the structure of the β-K_2SO_4 type and undergoes a phase transition at 302 K into an incommensurate phase with the modula-

Table 3. Energies and structures of the ordered low-temperature phases

Phase	Structures of ordered phases						Energy (K)		
	1	2	3	4	5	6	Rb_2ZnCl_4	K_2SeO_4	K_2SO_4
a	↑ ↓ ↑ ↓	↓ ↑ ↓ ↑	↑ ↓ ↑ ↓	→ ← → ←	← → ← →	→ ← → ←	–702	–1225	–904
	↓ ↑ ↓ ↑	↑ ↓ ↑ ↓	↓ ↑ ↓ ↑	← → ← →	→ ← → ←	← → ← →			
b	← → ← →	↓ ↑ ↓ ↑	↑ ↓ ↑ ↓	↓ ↑ ↓ ↑	← → ← →	→ ← → ←	–410	–1083	–867
	↑ ↓ ↑ ↓	→ ← → ←	→ ← → ←	← → ← →	↑ ↓ ↑ ↓	↓ ↑ ↓ ↑			
c	↑ ↓ ↑ ↓	↓ ↑ ↓ ↑	↑ ↓ ↑ ↓	↓ ↑ ↓ ↑	↑ ↓ ↑ ↓	↓ ↑ ↓ ↑	–658	–1206	–863
	↑ ↓ ↑ ↓	↓ ↑ ↓ ↑	↑ ↓ ↑ ↓	↓ ↑ ↓ ↑	↑ ↓ ↑ ↓	↓ ↑ ↓ ↑			
d	← ← ← ←	↓ ↓ ↓ ↓	↑ ↑ ↑ ↑	↓ ↓ ↓ ↓	← ← ← ←	→ → → →	–644	–1163	–870
	← ← ← ←	↓ ↓ ↓ ↓	↑ ↑ ↑ ↑	↓ ↓ ↓ ↓	← ← ← ←	→ → → →			
e	↑ ↑ ↑ ↑	↓ ↓ ↓ ↓	↑ ↑ ↑ ↑	↓ ↓ ↓ ↓	↑ ↑ ↑ ↑	↓ ↓ ↓ ↓	–601	–1146	–829
	↑ ↑ ↑ ↑	↓ ↓ ↓ ↓	↑ ↑ ↑ ↑	↓ ↓ ↓ ↓	↑ ↑ ↑ ↑	↓ ↓ ↓ ↓			
f	→ ↑ → ↑	← ↓ ← ↓	→ ↑ → ↑	← ↓ ← ↓	→ ↑ → ↑	← ↓ ← ↓	–556	–1148	–913
	↑ → ↑ →	↓ ← ↓ ←	↑ → ↑ →	↓ ← ↓ ←	↑ → ↑ →	↓ ← ↓ ←			
g	↑ ↑ ↓ ↓	↓ ↓ ↑ ↑	↑ ↑ ↓ ↓	↓ ↓ ↑ ↑	↑ ↑ ↓ ↓	↓ ↓ ↑ ↑	–620	–1208	–899
	↓ ↓ ↑ ↑	↑ ↑ ↓ ↓	↓ ↓ ↑ ↑	↑ ↑ ↓ ↓	↓ ↓ ↑ ↑	↑ ↑ ↓ ↓			
h	↑ ↑ ↓ ↓	↓ ↓ ↑ ↑	↑ ↑ ↓ ↓	↑ ↑ ↓ ↓	↑ ↑ ↓ ↓	↑ ↑ ↓ ↓		–1150	–948
	→ → ← ←	← ← → →	→ → ← ←	→ → ← ←	→ → ← ←	→ → ← ←			
i	↑ ↑ ← ←	↓ ↓ → →	↑ ↑ ← ←	↓ ↓ → →	↑ ↑ ← ←	↓ ↓ → →		–1185	949
	→ → ↓ ↓	← ← ↑ ↑	→ → ↓ ↓	← ← ↑ ↑	→ → ↓ ↓	← ← ↑ ↑			

Note: The directions of arrows correspond to the positions of the BX_4 tetrahedron in Fig. 4. The figures in the second row indicate the number of a layer perpendicular to the hexagonal axis.

tion vector $\mathbf{q} = (1 - \delta)\mathbf{h}/3$, where $\mathbf{h}$ is the first vector of the reciprocal lattice in the hexagonal direction. As a crystal is cooled further, δ decreases, and the second-order phase transition into the commensurate ferroelectric phase with the sp. gr. C_{2v}^9 occurs at 189 K. In this phase, the pseudohexagonal axis is tripled in comparison with the D_{2h}^{16} phase and the unit cell contains 12 molecules. If the temperature decreases even more, Rb_2ZnCl_4 undergoes one more phase transition at 74 K into the monoclinic phase, whose space group has not been identified.

K_2SeO_4 and K_2SO_4 are rare representatives of this family of crystals, in which the hexagonal phase D_{6h}^4 is observed experimentally at high temperatures. The phase transition into the orthorhombic phase D_{2h}^{16} occurs in K_2SeO_4 and K_2SO_4 crystals at 860 and 745 K, respectively. As a crystal is cooled further, K_2SeO_4 undergoes the same sequence of phase transitions as Rb_2ZnCl_4, whereas K_2SO_4 either undergoes no other phase transitions in accordance with some data or, according to other data, undergoes a phase transition at 56 K [15] into a phase whose structure has not been identified (it is only suggested that this phase is neither ferroelectric nor incommensurate).

The effective interaction constants for tetrahedral groups BX_4 were calculated within the model in which these groups have four equilibrium positions in the high-temperature phase D_{6h}^4 (Fig. 4). In this case, the matrix of interaction constants has four independent components (according to the position symmetry and the crystal symmetry):

$$\|V_{ij}\| = \begin{pmatrix} V_{11} & V_{12} & V_{13} & V_{14} \\ V_{12} & V_{11} & V_{14} & V_{13} \\ V_{13} & V_{14} & V_{11} & V_{12} \\ V_{14} & V_{13} & V_{12} & V_{11} \end{pmatrix}.$$

The values of the polarizabilities α_A and α_C for Rb_2ZnCl_4 and K_2SeO_4 were chosen on the basis of the condition of lowest energy of the ferroelectric phase at low temperatures. For K_2SO_4, the corresponding values were chosen so as to satisfy the condition of existence of the D_{2h}^{16} phase in a wide temperature range [13, 16, 17].

The interaction constants calculated for all three crystals under consideration are listed in Table 2. The energies of some structures at $T = 0$ K, calculated with the use of these constants, are listed in Table 3. The

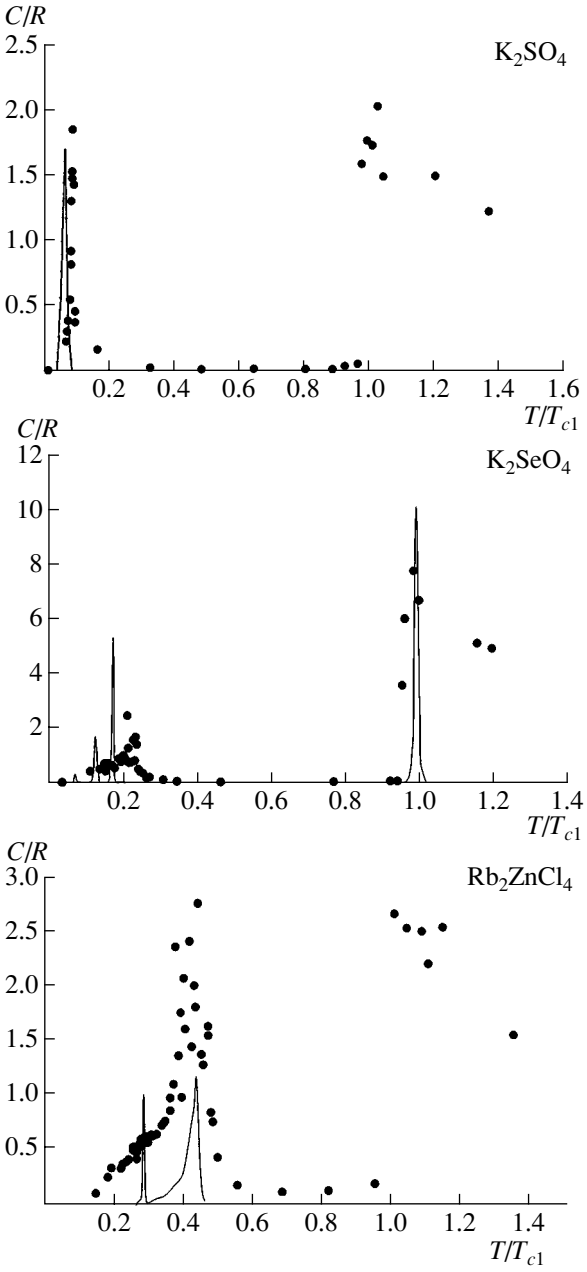

Fig. 5. Temperature dependence of the specific heat: Monte Carlo data (circles) and experimental results for Rb_2ZnCl_4 [18], K_2SeO_4 [19], and K_2SO_4 [15] (solid line). *R* is the universal gas constant.

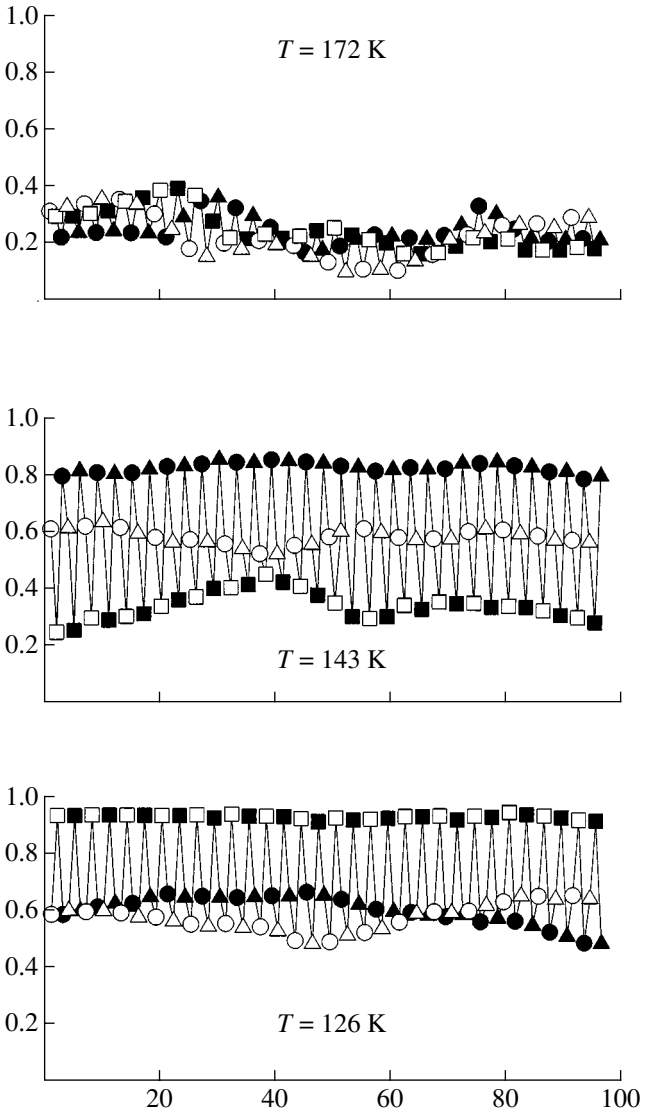

Fig. 6. Spatial dependence of the degree of layer ordering in the incommensurate phase of K_2SeO_4. The open and filled circles, triangles, and squares indicate the ↑↓↑↓, ↓↑↓↑; →←, ← →← →; and ↓↑↓↑, ↑↓↑↓ ordering, respectively.

effective constants oscillate with distance in both magnitude and sign. Therefore, there is a strong competition of interactions in these compounds. Moreover, the strongest interaction between BX_4 groups has an antiferromagnetic nature. This specific feature of interactions, in combination with the hexagonal symmetry of the disordered phase (which allows frustration), may be the reason for the existence of incommensurate phases in the above compounds.

As can be seen from Table 3, some phases have very close energies. Moreover, the phases with closest energies are characterized by different multiplications of the unit cell along the pseudohexagonal axis in Rb_2ZnCl_4 and K_2SeO_4 and the same multiplication in K_2SO_4. It is probable that such a character of interactions in these crystals leads to the appearance of an incommensurate phase at finite temperatures in some crystals (Rb_2ZnCl_4, K_2SeO_4) and to the existence of a partially ordered phase in a very wide temperature range in other crystals (K_2SO_4). Similar calculation for another representative of this family, $CsLiSO_4$ (which

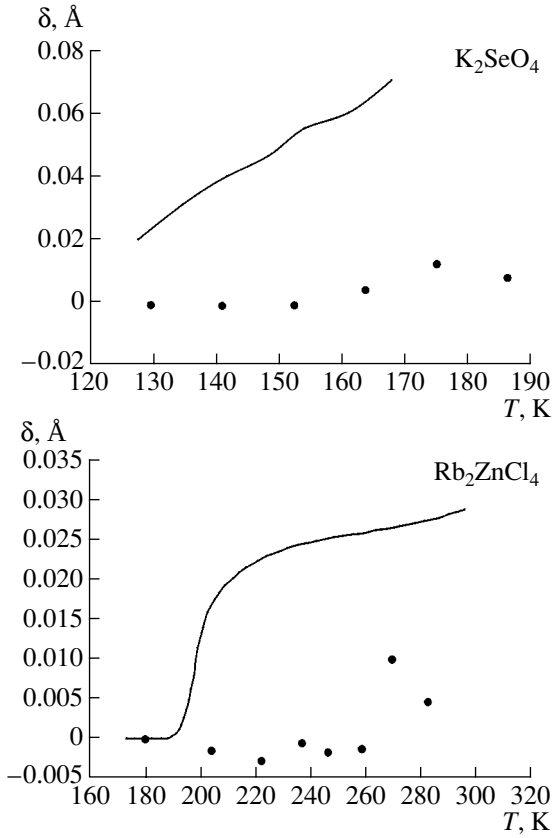

Fig. 7. Temperature dependence δ(*T*): Monte Carlo data (circles) and experimental results for Rb_2ZnCl_4 [21] and K_2SeO_4 [22] (solid line).

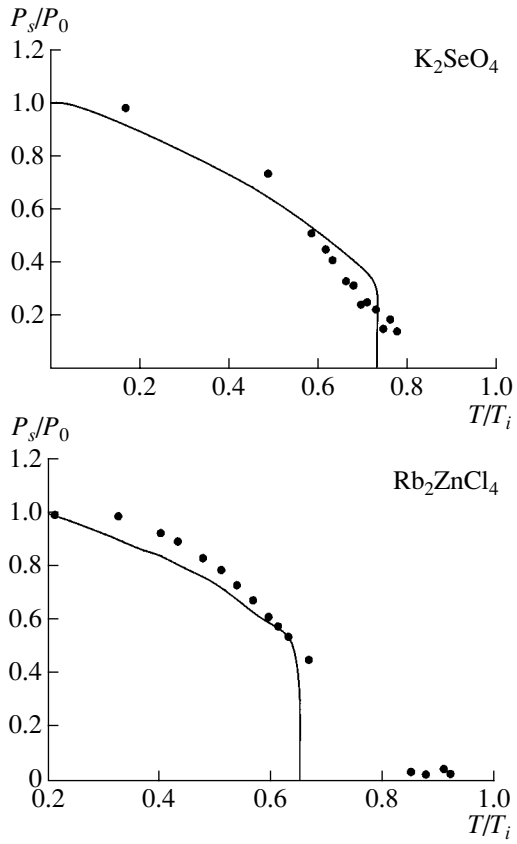

Fig. 8. Temperature dependence of the spontaneous polarization: Monte Carlo data (circles) and experimental results for Rb_2ZnCl_4 [23] and K_2SeO_4 [24] (solid line).

undergoes one phase transition $D_{2h}^{16} \longrightarrow C_{2h}^{5}$ without changing the unit-cell volume), showed that the energy of the C_{2h}^{5} phase (phase *f* in Table 3) is significantly lower than the energies of other phases [16, 17].

The temperature behavior of the crystals under consideration was studied by the Monte Carlo method. We used the conventional Monte Carlo method applicable to the Ising models [10], where it is taken into account that the pseudospin variable takes four values. The calculations were performed for the three-dimensional hexagonal lattice $16 \times 16 \times 24$. Both periodic boundary conditions and boundary conditions with "phantom spins" were used [16, 17]. We report here the results of simulation obtained only with the second type of boundary conditions. The reason is that the results of calculation for commensurate phases depend only slightly on the type of boundary conditions; at the some time, boundary conditions with phantom spins are more appropriate for incommensurate phases. As was mentioned above, the periodic boundary conditions impose their period on the system, whereas, when conditions with phantom spins are used, the system chooses the modulation period itself.

The phase-transition temperatures were determined from the peaks in the temperature dependence of the specific heat (Fig. 5) and from the inflection in the temperature dependence of the internal energy. The temperature of the transition into the partially ordered orthorhombic phase D_{2h}^{16} for Rb_2ZnCl_4 crystals (T_{c1} = 700 K) greatly exceeds the decomposition temperature of this crystal (550 K). For K_2SeO_4 and K_2SO_4 crystals, the temperatures of the high-temperature transitions were used to determine the octupole moment of the BX_4 group; therefore, $T_{c1}^{\text{calcd}} = T_{c1}^{\text{exper}}$ (860 and 745 K for K_2SO_4 and K_2SeO_4, respectively). In this phase, BX_4 tetrahedra have two equiprobable equilibrium positions, and such a structure is observed experimentally at high temperatures in all three types of crystals. Furthermore, in Rb_2ZnCl_4 and K_2SeO_4 crystals, at T_i = 302 K (T_i^{exper} = 302 K) and T_i = 177 K (T_i^{exper} = 129 K), respectively, a transition into the incommensurately modulated phase occurs.

The structure of the incommensurate phase, simulated for Rb_2ZnCl_4 and K_2SeO_4 crystals by the Monte Carlo method, is spatially modulated along the pseudohexagonal axis. The ordering of BX_4 tetrahedra

in the layers perpendicular to this axis is uniform at all temperatures; however, in the incommensurate phase, the degree of ordering of tetrahedra changes from layer to layer. As can be seen from Fig. 6, along with the long-wavelength modulation, short-wavelength modulation of layer order is also present. The period of this modulation is equal to the triple unit-cell parameter of the ferroelectric phase. Along with different orientations of tetrahedra in layers, a significant difference in the average values of these orientations from layer to layer in a triple cell is observed. Experimental studies of the modulated-phase structure in these crystals revealed no similar short-wavelength modulation [20]. The calculated long-wavelength structural modulation is in qualitative agreement with the experimentally observed one. Figure 7 shows the temperature dependence of δ. As can be seen, the measured maximum value of δ is almost three times larger than the corresponding calculated value.

At T_{c2} = 192 K (T_{c2}^{exper} = 192 K) for Rb_2ZnCl_4 and T_{c2} = 115 K (T_{c2}^{exper} = 93 K) for K_2SeO_4, a phase transition into the phase C_{2v}^9 occurs. In the low-temperature phase C_{2v}^9, these crystals are improper ferroelectrics and the spontaneous polarization P_s can be considered as the secondary order parameter. We cannot calculate the polarization in the ferroelectric phase within this model since it does not take into account displacements of ions and distortion of tetrahedra. However, one can obtain the temperature dependence of P_s. The parameter P is expressed in terms of the occupation numbers as

$$P = \frac{1}{4}[n_1^1(R_0) - n_2^1(R_0) + n_3^1(R_0) - n_4^1(R_0) + n_1^2(R_1) - n_2^2(R_1) + n_3^2(R_1) - n_4^2(R_1) + n_2^1(R_2) - n_1^1(R_2) + n_4^1(R_2) - n_3^1(R_2) + n_2^2(R_3) - n_1^2(R_3) + n_4^2(R_3) - n_3^2(R_3)],$$

where $R_0 = 0$, $R_1 = \sqrt{a_0^2/3 + c_0^2/4}$, $R_2 = a_0$, and $R_3 = \sqrt{4a_0^2/3 + c_0^2/4}$. The parameter P is proportional to the spontaneous polarization P_s. As can be seen from Fig. 8, the calculated and experimental temperature dependences of P_s are in good agreement.

Another low-temperature phase transition into the monoclinic phase is observed experimentally in the latter two crystals. This transition cannot be simulated by the Monte Carlo method since metastable states arise at low temperatures. The system is frozen in this state and cannot pass to another state even if the number of Monte Carlo steps is very large.

In K_2SO_4 crystals, the partially ordered phase D_{2h}^{16} exists in a wide temperature range and undergoes a phase transition into the completely ordered monoclinic phase C_{2h}^5 with 16 molecules in the unit cell only at 76 K. The measurements of the specific heat of K_2SO_4 [15] (Fig. 5) confirm that a low-temperature phase transition is possible in this crystal; however, the structure of the low-temperature phase has not been determined experimentally.

Thus, the model proposed, despite its evident roughness, correctly describes the sequence of phase transitions in the crystals under investigation. The calculated transition temperatures and the simulated behavior of thermodynamic quantities are in satisfactory agreement with the experimental data.

CONCLUSIONS

In this study, we reported the results of calculation of the critical temperatures and thermodynamic properties of crystals undergoing structural phase transitions of displacive and order–disorder types. The effective Hamiltonian method was used in the calculations. The effective Hamiltonian takes into account only the critical degrees of freedom of a crystal (the local mode in the case of displacive transitions and the orientation of ordering ions in the case of order–disorder transitions). The parameters of the Hamiltonian are derived from the ab initio calculations of the total energy and the vibrational spectrum of a crystal in the case of displacive transitions and using a small number of fitting parameters in the case of order–disorder transitions. The calculated phase-transition temperatures, the thermodynamic properties, and the structures of the low-symmetry phases are in satisfactory agreement with the experimental data.

ACKNOWLEDGMENTS

This study was supported by Program 9 of the Presidium of the Russian Academy of Sciences and, in part, by the Ministry of Industry, Science, and Technology of the Russian Federation, grant no. NSh-903.2003.02.

REFERENCES

1. P. Anderson, in *Physics of Dielectrics*, Ed. by G. Skanavi (Akad. Nauk SSSR, Moscow, 1960), p. 290.
2. W. Cochran, Adv. Phys. **9**, 387 (1960).
3. V. I. Zinenko, N. G. Zamkova, and S. N. Sofronova, Zh. Éksp. Teor. Fiz. **114**, 1742 (1998) [JETP **87**, 944 (1998)].
4. V. I. Zinenko and N. G. Zamkova, Fiz. Tverd. Tela (St. Petersburg) **41**, 1297 (1999) [Phys. Solid State **41**, 1185 (1999)].
5. V. I. Zinenko and N. G. Zamkova, Zh. Éksp. Teor. Fiz. **118**, 359 (2000) [JETP **91**, 314 (2000)].
6. V. I. Zinenko and N. G. Zamkova, Fiz. Tverd. Tela (St. Petersburg) **43**, 2198 (2001) [Phys. Solid State **43**, 2290 (2001)].

7. O. V. Ivanov and E. G. Maksimov, Zh. Éksp. Teor. Fiz. **108**, 1841 (1995) [JETP **81**, 1008 (1995)].
8. I. N. Flerov, M. V. Gorev, K. S. Aleksandrov, *et al.*, Mater. Sci. Eng. R **24**, 81 (1998).
9. K. M. Rabe and J. D. Jonnopoloulos, Phys. Rev. B **36**, 6631 (1987).
10. *Monte Carlo Methods in Statistical Physics*, Ed. by K. Binder (Springer, Berlin, 1979; Mir, Moscow, 1982).
11. K. S. Aleksandrov and B. V. Beznosikov, *Structural Phase Transitions in Crystals (Potassium Sulfate Family)* (Nauka, Novosibirsk, 1993).
12. D. Kh. Blat and V. I. Zinenko, Fiz. Tverd. Tela (Leningrad) **18**, 3599 (1976) [Sov. Phys. Solid State **18**, 2096 (1976)].
13. N. G. Zamkova and V. I. Zinenko, Fiz. Tverd. Tela (St. Petersburg) **34**, 2735 (1992) [Sov. Phys. Solid State **34**, 1464 (1992)].
14. A. Huller and J. W. Kane, J. Chem. Phys. **56**, 2597 (1972).
15. K. Gesi, Y. Tominaga, and H. Urabe, Ferroelectr. Lett. Sect. **44**, 71 (1982).
16. N. G. Zamkova and V. I. Zinenko, Zh. Éksp. Teor. Fiz. **107**, 1282 (1994) [JETP **80**, 713 (1994)].
17. V. I. Zinenko and N. G. Zamkova, Phys. Rev. B **57**, 211 (1998).
18. K. Nomoto, T. Atake, B. K. Chaudhuri, and H. Chihara, J. Phys. Soc. Jpn. **52**, 3475 (1983).
19. L. A. Echarri, M. J. Tello, and P. Gili, Solid State Commun. **36**, 1021 (1980).
20. M. Izumi, J. D. Axe, and G. Shirane, Phys. Rev. B **15**, 4392 (1977).
21. H. Mashiyama, S. Tanisaki, and J. Hamano, J. Phys. Soc. Jpn. **51**, 2538 (1982).
22. N. Yamada and T. Ikeda, J. Phys. Soc. Jpn. **53**, 2555 (1984).
23. K. Hamano, Y. Ikeda, T. Fujimoto, *et al.*, J. Phys. Soc. Jpn. **49**, 2278 (1980).
24. K. Aiki, K. Hukuda, and O. Matumura, J. Phys. Soc. Jpn. **26**, 1064 (1969).

Translated by Yu. Sin'kov

Crystallography Reports, Vol. 49, No. 1, 2004, pp. 4–14. Translated from Kristallografiya, Vol. 49, No. 1, 2004, pp. 8–19.

THEORY OF CRYSTAL STRUCTURES

Dedicated to the 80th Birthday of L.A. Shuvalov

Cluster Approach in First-Principle Calculations for Ferroelectrics

O. E. Kvyatkovskiĭ

Ioffe Physicotechnical Institute, Russian Academy of Sciences, Politekhnicheskaya ul. 26, St. Petersburg, 194021 Russia

e-mail: kvyatkovskii@mail.ioffe.ru

Received August 4, 2003

Abstract—It is shown that, proceeding from the first principles, it is possible to separate the contributions from short- and long-range interactions to the lattice dynamics and dielectric properties of crystalline dielectrics. The cluster calculations of local force constants and potentials for the matrix and impurity atoms in ferroelectrics with the perovskite structure were made by the Hartree–Fock MOLCAO-SCF method. The parameters of the Devonshire–Slater–Barrett single-ion model are calculated for barium titanate and potassium niobate. The influence of the quantum statistics on the Curie temperature in these ferroelectrics and the isotope effect in barium titanate are also considered. © *2004 MAIK "Nauka/Interperiodica".*

INTRODUCTION

In recent years, great attention in the theory of ferroelectrics has been given to consideration of various phenomena proceeding from the first principles [1, 2]. Material properties weakly dependent on temperature and properties at the zero temperature can be efficiently described using both analytical and *ab initio* numerical and analytical methods developed to describe the ground state of multielectron systems. These are, first of all, the density functional method [3] and the Hartree–Fock MOLCAO-SCF method and its generalizations that take into account electron correlations [4].

King-Smith and Vanderbilt [5] and Resta [6] performed the first-principle-based calculations and derived the expression for macroscopic electric polarization P induced by the change of the ground state of a crystal, which allowed one to determine the change in the electric polarization caused by homogeneous optical or acoustic deformation of the crystal lattice and the corresponding response functions (tensors of the Born effective charge and piezoelectric coefficients).

Thus far, a large number of numerical calculations based on the first principles have been made for displacive-type ferroelectrics and, first of all, for compounds with the perovskite structure. Most of these calculations are made by the methods developed for electronic structures of crystals, which are based on the theory of the density functional in the approximation of the local density [1–3]. To date, this approach has been used to calculate the equilibrium crystal structure, the matrices of force constants $\Phi_{ij}(st)$ corresponding to the transverse optical (TO) modes of lattice vibrations, the frequencies of the optical modes and some branches of the phonon spectrum, components of the tensor of the Born effective charge, piezoelectric coefficients, and some other properties of compounds with the perovskite structure [2, 7–15]. All the studies published up to 1998 were reviewed in [2].

The alternative approach to first-principle-based calculations of dielectric and ferroelectric properties of crystals and lattice dynamics was developed in [16–24]. Thus, using the exact formulation of the theory of lattice dynamics [25, 26] and the quantum-mechanical theory of the polarization electron response [20], Sham [16], Pick *et al.* [17], and Kvyatkovskiĭ [18–20] obtained the exact solution of the problem of the influence of the intercell dipole–dipole interaction on lattice dynamics and dielectric properties of crystals. They also found that the matrix of force constants $\Phi_{ij}(st, \mathbf{q} = 0)$, the tensors of the Born effective charge, $Z_{ij}(s)$, and rf (electron) permittivity, $\varepsilon_{ij}^{\infty}$, can be represented as the sum of contributions that come from short- and long-range intercell dipole–dipole interactions, $\Phi_{ij}(st) = \Phi_{ij}^{sr}(st) + X_{ij}^{dd}(s, t)$, $Z_{ij}(s) = Z_{ij}^{sr}(s) + Z_{ij}^{dd}(s)$, and $\varepsilon_{ij}^{\infty} = 1 + 4\pi\alpha^{sr} + (\varepsilon_{ij}^{\infty})^{dd}$. This representation and analysis of the experimental data allow one to clarify the nature of ferroelectricity in the $A^{IV}B^{VI}$ and other compounds without the perovskite structure with invocation of any model representations [21–23]. At the same time, any of the contributions can be determined from calculations based on the first principles. Taking into account that $X_{ij}^{dd}(s, t)$ is expressed in terms of $Z_{ij}(s)$ and $\varepsilon_{ij}^{\infty}$;

$Z_{ij}^{dd}(s)$, in terms of $Z_{ij}^{sr}(s)$ and $\varepsilon_{ij}^{\infty}$; and, finally, $(\varepsilon_{ij}^{\infty})^{dd}$, in terms of α^{sr}, it is sufficient to determine the contributions to the dielectric parameters that come from short-range interactions. In principle, this can be done using the *ab initio* calculations for appropriate multiatomic clusters that model certain fragments of a crystal [24].

On the one hand, it is necessary to calculate $\Phi_{ij}^{sr}(st)$ and $X_{ij}^{dd}(st)$ in order to construct the effective Hamiltonian for the soft polar TO mode necessary for simulating the behavior of ferroelectrics at finite temperatures [13, 27–29]. On the other hand, the results of such calculations would answer a number of important questions of the microscopic theory arising in the selection of the model lattice Hamiltonian which adequately describes a ferroelectric phase transition [30, 31]. There are two approaches to the construction of this Hamiltonian, which take into account the different roles played by short- and long-range forces in the formation of ferroelectric instability. The first approach is based on the fact that short-range forces in ionic crystals stabilize the TO modes of lattice vibrations, whereas long-range (dipole) forces decrease the stability of polar TO modes. This approach in application to displacive-type ferroelectrics was developed by Devonshire, Slater, Barrett, Cochran, *et al.* [32–35]. The second approach is based on the assumption that each atom in one of the sublattices moves in a multiple potential formed by its nearest environment. In this case, the interactions between these atoms are of a repulsive nature and are responsible for ferroelectric ordering. This model is considered in detail, e.g., in [30, 31] and, according to these studies, is a universal lattice model that describes order–disorder and displacive-type phase transitions depending on the relationship between the model parameters. This model, in which noncentral atoms of the *B* sublattice move in a multiple potential well, was first suggested by Mason and Matthias [36] for ABO_3 ferroelectrics with the perovskite structure and was repeatedly used for intepreting experimental data [37–39]. One of the arguments in favor of this model for perovskites is the fact that covalent chemical bonds in BO_6 octahedra reduce the repulsive interactions between the transition metal atom and the nearest oxygens [40]. Obviously, within the model description of the lattice dynamics, it is impossible to make the unambiguous choice between these two approaches. A similar problem also arises for impurity atoms in $Sr_{1-x}A_xTiO_3$, $K_{1-x}A_xTaO_3$, and $KTa_{1-x}Nb_xO_3$ solid solutions [14, 41, 42], which indicates the necessity of nonempirical calculation of the short-range forces arising because of the displacements of the *A*, *B* or O atoms from their equilibrium positions in the cubic perovskite lattice [24, 43, 44].

The calculations of local atomic force constants show that the central positions of all the species in the cubic phases with perovskite structure are stable, i.e., each atom moves in single-well local potential if all the other atoms are fixed at their lattice sites [24, 43, 44]. The simplest model possessing these properties, which describes the phase transition in displacive-type ferroelectrics, is the Devonshire–Slater–Barrett single-ion model [32–34, 45, 46]. The merit of this model is that it leads to a simple analytical expression for free energy whose parameters (including anharmonic coefficients) can be determined from *ab initio* cluster calculations.

1. GENERAL THEORY

Consider the free energy *F* of a displacive-type ferroelectric as a function of temperature and sublattice (homogeneous optical) displacements $\mathbf{u}(s)$. The Landau expansion for a clamped crystal can be represented in the form [45, 46]

$$\frac{F}{N} = F[\mathbf{u}(s); T] - v_0\mathbf{P}\mathbf{E}, \tag{1}$$

$$F[\mathbf{u}(s); T] = \frac{1}{2}\sum_{si,tj}\Gamma_{ij}(st; T)u_i(s)u_j(t) + F^{ah}[\mathbf{u}(s)], \tag{2}$$

where $\Gamma(T)$ is the generalized matrix of the long-wave (optical) force constants, which consists of the harmonic Φ and anharmonic $\Phi^{ah}(T)$ contributions

$$\Gamma(T) = \Phi + \Phi^{ah}(T); \quad \Phi_{ij} = \left.\frac{\partial^2 E^{\text{tot}}}{\partial u_i(s)\partial u_j(t)}\right|_{\mathbf{u}=0,\,\mathbf{E}=0}. \tag{3}$$

Polarization **P** is determined by the well-known expression [47]

$$P_i = \frac{e}{v_0}\sum_{sj} Z_{ij}(s)u_j(s) + \chi_{ij}^{\infty}E_j. \tag{4}$$

1.1. Microscopic Field and Macroscopic Polarization in Homogeneously Polarized Crystal Dielectrics

Local electric fields due to induced polarization can strongly influence the dielectric, optical, and vibrational properties of crystal dielectrics [47] and the stability of the crystal lattice in proper ferroelectrics [33, 35]. The classical theory of the local-field effects (Lorentz field theory) is based on the model of point dipoles considerably limiting the range of the theory application to real solids. The classical theory extended to the case of continuous electron-density of charge distribution in crystals faces a fundamental difficulty [48]. The point is that the classical theory of local-field effects for a system of point dipoles is based on the equality [45, 47]

$$\mathbf{P} \equiv \frac{1}{V}\int_V \mathbf{P}(\mathbf{r})dV = \frac{1}{v_0}\delta\mathbf{d}, \tag{5}$$

where *V* is the crystal volume and **P** is the electric polarization induced by the change in the dipole moment, $\delta\mathbf{d}$, of a primitive unit cell with the volume v_0.

For the continuous periodic distribution of the charge density, equality (5) in the classical theory is transformed into the following equation [48]:

$$\mathbf{P} = \frac{1}{V_0}[\delta\mathbf{d} + \delta\mathbf{d}^{\text{surf}}]; \quad \delta\mathbf{d} = \int_{V_0} \mathbf{r}\delta\rho(\mathbf{r})dV; \qquad (6)$$
$$\delta\mathbf{d}^{\text{surf}} = \oint_{S_0} \mathbf{r}(\mathbf{P}(\mathbf{r})d\mathbf{S}),$$

where $\delta\mathbf{d}^{\text{surf}}$ is the contribution of the charge transfer through the surface s_0 of the primitive unit cell. In this case, only the sum of the bulk and surface contributions in the right-hand side of Eq. (6) is invariant with respect to the selection of the unit cell. This difficulty can be overcome by invoking the quantum-mechanical theory of polarization response and the method of long waves [18–20].[1]

An expression for the force acting on the atomic nucleus in the wave of long-wave optical displacements [18, 19] is based on the fundamental Hellman–Feinman theorem [51, 52], which states that, in the adiabatic approximation, the forces acting on atomic nuclei in this case are classical electrostatic forces. Another important result is that polarization **P** induced by a wave of optical atomic displacements $u_i(s)\exp(-i\mathbf{qR})$ can be expressed in terms of the induced charge $\delta Z_e(\mathbf{q})$ and dipole moment $\delta\mathbf{d}(\mathbf{q})$ of the primitive unit cell of a crystal [20]:

$$\mathbf{P} = \mathbf{P}(\mathbf{q} \longrightarrow 0) = \frac{1}{V_0}\left[\delta\mathbf{d}(\mathbf{q}) + i\frac{\partial}{\partial\mathbf{q}}\delta Z_e(\mathbf{q})\right]_{\mathbf{q}=0}. \qquad (7)$$

This allows one to obtain the explicit solution of the problem of local-field effects proceeding from the first principles [18, 19] and also determine the corrections for the local field in $\varepsilon_{ij}^{\infty}$, $Z_{ij}(s)$, and $\Phi_{ij}(st; \mathbf{q} = 0)$. The only limitation of this approach is associated with the use of the harmonic and adiabatic approximations conventional in lattice dynamics [47].

The solution obtained depends substantially on the behavior of $\delta Z_e(q)$ at $\mathbf{q} \longrightarrow 0$ [20]. This situation, where $\delta Z_e(\mathbf{q}) \propto q$, would correspond to physically unattractive results of the classical consideration of periodic systems with a continuous charge density [48]. However, the quantum-mechanical consideration of the electron polarization response shows that $\delta Z_e(\mathbf{q}) \propto q^{\beta}$, where $\beta \geq 2$ [20], and, therefore, $\delta Z_e(\mathbf{q})$ makes no contribution to induced polarization **P** and the long-range force $\mathbf{F}^{lr}(s)$ at $q \longrightarrow 0$ [18, 19]. As a result, we arrive at [18, 19]

$$\varepsilon_{ij}^{\infty} = \delta_{ij} + 4\pi[(\mathbf{I} - 4\pi a^{\text{eff}}\mathbf{A})^{-1}a^{\text{eff}}]_{ij}$$
$$= \delta_{ij} + 4\pi a_{ij}^{\text{eff}} + [4\pi a^{\text{eff}}\mathbf{A}(\mathbf{I} - 4\pi a^{\text{eff}}\mathbf{A})^{-1}a^{\text{eff}}]_{ij}, \qquad (8)$$

$$Z_{ij}(s) = Z_{ij}^{sr}(s) + \sum_{kl}(\varepsilon_{ik}^{\infty} - \delta_{ik})A_{kl}Z_{lj}^{sr}(s), \qquad (9)$$

$$F_i^{lr}(s, \mathbf{q}) = Z_{ji}(s)eE_j(\mathbf{q})$$
$$+ \frac{4\pi e^2}{V_0}\sum_{t,kl} Z_{ki}^{sr}(s)A_{kl}Z_{lj}(t)u_j(t; \mathbf{q}), \qquad (10)$$

where $a_{ij}^{\text{eff}} = \alpha_{ij}^{sr}$ is the tensor of effective electron polarizability determined by the short-range interactions, $Z_{ij}^{sr}(s)$ is the contribution to the Born effective charge for the sublattice *s* also determined by the short-range interactions, and **A** is the tensor of dipole coefficient, which is determined as

$$Q_{ij} = \sum_{\mathbf{R}\neq 0} e^{i\mathbf{k}\cdot\mathbf{R}}\nabla_i\nabla_j\frac{1}{R}\bigg|_{q\to 0} = \frac{4\pi}{V_0}\left[-\frac{q_iq_j}{q^2} + A_{ij}\right]. \qquad (11)$$

The contribution of the intercell dipole–dipole interaction to the matrix of the force constants has the form [18, 19]

$$\Phi_{ij}^{dd}(st; \mathbf{q}) \equiv -\frac{\partial F_i^{lr}(s, \mathbf{q})}{\partial u_j(t, \mathbf{q})} = \Phi_{ij}^{M}(st; \mathbf{q}) + X_{ij}^{dd}(st; \mathbf{q}). \qquad (12)$$

The first term, $\Phi_{ij}^{M}(st; \mathbf{q})$, in the right-hand side of expression (12) related to the macroscopic field **E** is responsible for the LO–TO splitting in the phonon spectrum [1, 45, 47, 53] known from the phenomenological theory [25, 26, 53]. The second term, $X_{ij}^{dd}(st; \mathbf{q})$, is of a microscopic nature and, when $q = 0$, is determined by the expression [18, 19]

$$X_{ij}^{dd}(st) = -\kappa_0\sum_{kl} Z_{ki}^{sr}(s)G_{kl}Z_{lj}^{sr}(t)$$
$$= -\kappa_0\sum_{kl} Z_{ki}(s)B_{kl}Z_{lj}(t), \qquad (13)$$

where $\kappa_0 = 4\pi e^2/V_0$ and

$$\mathbf{G} = \mathbf{AL}; \quad \mathbf{B} = (\mathbf{L}^{\dagger})^{-1}\mathbf{A};$$
$$L_{ij} = \delta_{ij} + \sum_{k}(\varepsilon_{ik}^{\infty} - \delta_{ik})A_{kj}. \qquad (14)$$

Expressions (9)–(11) and (12)–(14) were first derived in [16, 17], proceeding from the rigorous formulation of the theory of lattice dynamics in terms of the micro-

[1] In the theory of ionic crystals, one often uses a nonempirical model based on the Thomas–Fermi–Dirac–Lenz functional [1, 47] with the continuous electron-density charge distribution, $\rho(\mathbf{r})$. However, the use of the superpositional approximation for $\rho(\mathbf{r})$ makes this model equivalent to the model of point dipoles. Being generalized, the model [49, 50] allows one to describe satisfactorily (both qualitatively and, for some properties, also quantitatively) the ground state of many ferroelectrics with the perovskite structure.

scopic electron susceptibility [25, 26]. The direct derivation of these expressions based on the solution of the exact equations for a microscopic electric field in a polarized crystal dielectric was obtained in [18, 19].

The third term in the right-hand side of expression (9), the second term in the right-hand side of expression (10), and the matrix $X_{ij}^{dd}(st)$ are, in fact, the corrections for the local field to the tensor of rf permittivity, tensor of the Born effective charge, and the matrix of force constants, respectively. As was shown in [21–23], these corrections are responsible for ferroelectric instability of the lattice of oxides and $A^{IV}B^{VI}$ compounds with the perovskite structure.

For cubic crystals ($A_{ij} = 1/3\delta_{ij}$), we have

$$\Phi_{ij}^{dd}(st; \mathbf{q} \longrightarrow 0) = \frac{4\pi e^2 Z_{ii}(s) Z_{jj}(t)}{v_0}\left[\frac{q_i q_j}{q^2 \varepsilon^{\infty}} - \frac{\delta_{ij}}{\varepsilon^{\infty} + 2}\right]. \quad (15)$$

Now, compare rigorous expression (15) with the model matrix $\tilde{\Phi}_{ij}^{dd}(st; \mathbf{q} \longrightarrow 0)$ that follows from the expression for the energy of intercell dipole–dipole interaction used in [13, 27–29],

$$\tilde{\Phi}_{ij}^{dd}(st; \mathbf{q} \longrightarrow 0) = \frac{4\pi e^2 Z_{ii}(s) Z_{jj}(t)}{v_0}\left[\frac{q_i q_j}{q^2 \varepsilon^{\infty}} - \frac{\delta_{ij}}{3\varepsilon^{\infty}}\right]. \quad (16)$$

Comparing expressions (15) and (16), we see that the matrix components nonanalytically dependent on **q**, which describe the LO–TO splitting, are the same, but the components which are regular at **q** = 0 and reduce the frequencies of polar TO modes, are different. The value of the transverse part of the model matrix used in [13, 27–29] is lower by a factor of $(\varepsilon^{\infty} + 2)/3\varepsilon^{\infty}$ than the value obtained from the rigorous expression. This signifies that, although the results considered in [13, 27–29] are nonempirical, they are obtained not from the first principles but on the basis of an approximate effective model Hamiltonian, where the absolute value of the energy of the transverse part of the intercell dipole–dipole interaction (destabilizing the cubic phase of the transverse part of the intercell dipole–dipole interaction) is considerably lower (approximately by a factor of two for ferroelectrics with the perovskite structure and a factor of three for the $A^{IV}B^{VI}$ compounds) than the absolute value of the energy obtained from expression (15) based on the first principles.

1.2. Long-Range Intercell Dipole–Dipole Interaction

To calculate the contribution of the intercell dipole–dipole interaction to the optical force constants of a crystal, which correspond to the homogeneous displacements of the sublattices, proceeding from the first principles, we use expression (13) for the $X_{ij}^{dd}(st)$ matrix. For compounds with perovskite structures described by the formula ABX_3, we have

$$k_{ii}^{dd}(s) = X_{ii}^{dd}(ss) = -\frac{4\pi e^2 Z_{ii}(s)^2}{v_0}\frac{1}{\varepsilon^{\infty} + 2}. \quad (17)$$

Then, expression (10) for the Born tensor of a cubic perovskite-type structure acquires the form

$$Z_{ij}(s) = Z_{ii}(s)\delta_{ij}; \quad Z_{ii}(s) = \frac{\varepsilon^{\infty} + 2}{3} Z_{ii}^{sr}, \quad (18)$$

where $Z_{ii}(A) = Z(A)$, $Z_{ii}(B) = Z(B)$, $Z_{xx}(X_I) = Z_{yy}(X_I) = Z_{yy}(X_{II}) = Z_{zz}(X_{II}) = Z_{xx}(X_{III}) = Z_{\perp}(X)$, and $Z_{xx}(X_{II}) = Z_{yy}(X_{III}) = Z_{zz}(X_I) = Z_{II}(X)$. For many ferroelectrics with the perovskite structure, the $Z(A)$, $Z(B)$, $Z_{\perp}(O)$, and $Z_{II}(O)$ values are known from the *ab initio* calculations [7, 54] and the solution of the inverse problem [55].

1.3. Short-Range Interaction

Consider a crystal in which only one atom is displaced from its equilibrium position, e.g., an atom from the *s*th sublattice, whereas all the remaining atoms are fixed at their equilibrium positions (lattice sites). Now, determine the matrix of local (on-site) force constants $k_{ij}^{loc}(s)$ as a matrix of coefficients before the quadratic terms of the expansion of the change in the total energy of the crystal (the local adiabatic potential of the given atoms) in powers of displacements $u_i(s)$ of this atom,

$$\Delta E(\mathbf{u}) = E(\mathbf{u}) - E(0) = 1/2\sum_{ij} k_{ij}^{loc}(s) u_i u_j + O(u^4), \quad (19)$$

where the second term in the right-hand side includes higher terms of the $\Delta E(\mathbf{u})$ expansion. Unlike optical force constants $k_{ij}(s) \equiv \Phi_{ij}(ss) = k_{ij}^{sr}(s) + k_{ii}^{dd}(s)$ corresponding to the displacement of the second sublattice as a whole, the local force constants $k_{ij}^{loc}(s)$ contain only the contributions from short-range interactions.[2] Taking into account the $\Phi_{ij}^{sr}(st)$ and $k_{ij}^{loc}(s)$ values determined, we can write

$$k_{ij}^{sr}(s) = \Phi_{ij}^{sr}(ss) = \sum_{\mathbf{R}} \Phi_{ij}^{sr}(\mathbf{R}; ss) \approx \Phi_{ij}^{sr}(\mathbf{R} = 0; ss) = k_{ij}^{loc}(s), \quad (20)$$

[2] For a lattice with one displaced atom, the contribution of the dipole–dipole interaction to the restoring force decreases with the distance R as R^{-6}, whereas the contribution of the Madelung force for atoms in the positions *A* and *B* of the cubic perovskite structure is zero.

where **R** is the vector of the Bravais lattice of the crystal. Thus, one can consider $k_{ij}^{\mathrm{loc}}(s)$ as the contribution of the short-range forces to the nondiagonal force constant $k_{ij}(s)$ of the crystal.

A crystal with one displaced atom possesses the local dipole moment $\mathbf{d}^{\mathrm{loc}}(s)$, which, in the linear approximation, can be written as

$$d_i^{\mathrm{loc}}(s) = \sum_j Z_{ij}^{\mathrm{loc}}(s)u_j(s). \quad (21)$$

The tensor of the local effective charge $Z_{ij}^{\mathrm{loc}}(s)$ for an atom from the sublattice *s* is a well defined quantity that can be found from the *ab initio* calculations. Unlike $Z_{ij}^{\mathrm{loc}}(s)$, it is impossible to describe $Z_{ij}^{sr}(s)$ by a simple expression convenient for further calculations. However, taking into account that the intercell dipole–dipole interaction is of the collective nature, i.e., takes place only at the simultaneous displacements of all the atoms of the sublattice *s*, one can assume that the effective charges have close values. Then, we can write

$$Z_{ij}^{sr}(s) \approx Z_{ij}^{\mathrm{loc}}(s). \quad (22)$$

2. CLUSTER APPROXIMATION AND METHOD FOR CALCULATING TOTAL ENERGY AND SINGLE-ELECTRON PROPERTIES

In order to determine the local adiabatic potential for an atom at a certain lattice site, one has to calculate the total energy of the crystal, **u**, as a function of the displacement of this atom from the equilibrium position at this site under the condition that all the remaining atoms occupy the equilibrium positions of the cubic perovskite lattice. The most convenient methods for nonempirical calculations of the properties of point defects in crystals are the method of supercells [14, 15] and the quasi-molecular cluster method [24, 43, 45].

Below, we use the approach described in [24, 43]. It is reduced to the following. First, one has to single out a crystal fragment containing the atom under consideration that would enable one to adequately describe the chemical bonds and the point symmetry of this atom. Then, the fragment is modeled by a quasi-molecular cluster whose geometry repeats the geometry of the crystal fragment.

For an atom at site *B* of the perovskite structure, the minimum cluster reproducing the chemical bond and the local properties (determined by this bond) is an octahedral $(BO_6)^{n-}$ cluster (cluster I) or a $[B(OH)_6]^{n-}$ cluster in which the dangling *B*–O bonds are complemented with hydrogen atoms. The next (with respect to complexity) appropriate cluster for a *B* -type atom consists of seven BO_6 octahedra and eight *A*-type atoms occupying the vertices of the primitive cubic unit cell. In order to reduce the cluster charge, the dangling *B*–O bonds are complemented with hydrogen atoms located at distances of 1 Å. As a result, we arrive at positively charged $[B'O_6A_8B_6(OH)_{30}]^{n+}$ clusters (clusters VII). For an atom at site *A*, the minimum formal cluster is $(AO_{12})^{n-}$. However, in fact, this cluster does not enable one to describe adequately the local potential of an *A*-type atom. Therefore, the minimum cluster for an atom at site *A* is a cluster containing seven *A*-type atoms (*A*' in the cluster center and six *A*-type atoms along the fourfold axes) and eight BO_6 octahedra. To decrease the cluster charge, the dangled *B*–O bonds are complemented with hydrogen atoms. As a result, we arrive at negatively charged $[A'O_{12}A_6B_8(OH)_{24}]^{n-}$ clusters (clusters VIII).

An oxygen atom in the cubic perovskite structure is characterized by two force constants, $k_{\parallel}^{\mathrm{loc}}(\mathrm{O})$ and $k_{\perp}^{\mathrm{loc}}(\mathrm{O})$, parallel and perpendicular to the *B*–O'' bond, respectively. The minimum cluster for an oxygen atom consist of two BO_6 octahedra and four *A*-type atoms located at the vertices of the cubic unit-cell face normal to the *B*–O–*B* chain; in order to reduce the cluster charge, the external dangling *B*–O bonds are complemented with hydrogen atoms. As a result, we arrive at a positively charged $[OB_2A_4(OH)_{10}]^{n+}$ cluster (cluster II).

By definition, the local potential is the difference between the total energies of the crystal in the distorted and undistorted configurations, $\Delta E(\mathbf{u}) = E(\mathbf{u}) - E(0)$, where **u** is the displacement of the central atom from the lattice site. The calculations were made in the approximation $\Delta E(\mathbf{u}) \approx \Delta E^{\mathrm{cl}}(\mathbf{u})$, where $E^{\mathrm{cl}}(\mathbf{u})$ is the total energy of the corresponding cluster and $\mathbf{d}^{\mathrm{loc}}(s) \approx \mathbf{d}^{\mathrm{cl}}(s)$. The total energy and the single-electron properties of the cluster were calculated within the framework of the restricted *ab initio* Hartree–Fock MOLCAO SCF method (RHF) using the PC GAMESS version [56] of the GAMESS (US) complex of quantum–chemical programs [57]. The influence of the correlation effects (for simple octahedral clusters) was taken into account within the framework of the Möller–Plecet perturbation theory (MP2) [57]. The calculations were performed using the extended sets of atomic basis functions described elsewhere [24, 43].

3. LOCAL ADIABATIC POTENTIALS FOR MATRIX AND IMPURITY ATOMS IN PEROVSKITES

Table 1 lists the results of *ab initio* calculations of the local force constants $k_{ii}^{\mathrm{loc}}(s)$ for *B*- and *A*-type atoms in the $BaTiO_3$, $SrTiO_3$, $CaTiO_3$, $PbTiO_3$, $KNbO_3$, and $KTaO_3$ perovskites [24, 43]. It is seen that all the rigidities $k_{ii}^{\mathrm{loc}}(s)$ have high values in comparison with the value of the atomic force constant for perovskites, $k^{\mathrm{at}}(s) = e^2/r_0 \cong 2$ eV/Å^2 (where $r_0 \simeq 2$ Å is the length of a *B*–O bond) and with the $k^{\mathrm{loc}}(s)$ value for cations in

typical ionic crystals [44], which indicates the stabilizing effect of the covalent *B*–O bonds on the stability of the central positions of these atoms in oxygen BO_6 octahedra [24, 43]. These results show that the assumption about the noncentral position of the *B*-type atoms in the cubic phase of ferroelectrics with the perovskite structure used in the interpretation of the inelastic light scattering [37], XAFS [38], and NMR [39] experiments is erroneous and that the lattice model with a noncentral ferroelectrically active ion [30, 31] is inapplicable to the above compounds. And, finally, the results obtained also show that the intercell dipole–dipole interaction in ferroelectrics with the perovskite structure is anomalously high and strongly influences the $k(B)$ and $k_{\|}(O)$ values in $BaTiO_3$, $SrTiO_3$, $CaTiO_3$, $PbTiO_3$, $KNbO_3$, and $KTaO_3$ and the k(Pb) value in $PbTiO_3$. It considerably decreases the stability of the cubic phase (or makes it unstable) at $T = 0$ K.

The *ab initio* cluster calculations of the force constants $k^{loc}(s)$ were performed for impurity Ca, Ba, Pb, and Cd atoms replacing Sr atoms in $SrTiO_3$ and for impurity Nb atoms replacing Ta atoms in $KTaO_3$ [43]. According to [43], the impurity atoms in these solid solutions move in a single-well potential with the stable central position, i.e., are "central" impurities. An especially important result was obtained for a Nb impurity in $KTaO_3$, because some authors believe that a Nb atom in this compound occupies a noncentral position [41, 42]. Thus, $Sr_{1-x}Ca_xTiO_3$, $Sr_{1-x}Ba_xTiO_3$, $Sr_{1-x}Pb_xTiO_3$, and $KTa_{1-x}Nb_xO_3$ compounds can be considered as displacive-type ferroelectrics (solid solutions of displacive type). The situation for Mg-, Zn-, and Li-doped materials is different. Calculations show [43] that the harmonic force constants $k^{loc}(s)$ for Mg, Zn, and Li impurity atoms have low negative values ($|k^{loc}| \ll k^{at}$). This signifies that the Mg and Zn impurities in $SrTiO_3$ and Li impurity in $KTaO_3$ are "noncentral" and move in a multiwell local potential along the [001] direction for Mg and Zn atoms (Fig. 1). For comparison, Fig. 1 also shows the local adiabatic potential for Ca, Ba, Pb, and Cd impurity atoms in $SrTiO_3$. The data on the structure parameters of perovskites were borrowed from [58].

4. LOCAL EFFECTIVE CHARGES AND BORN TENSOR IN PEROVSKITES

Table 2 lists the Born effective charges $\tilde{Z}_{ii}(s)$ for the $BaTiO_3$, $SrTiO_3$, $CaTiO_3$, $PbTiO_3$, $KNbO_3$, and $KTaO_3$ compounds calculated nonempirically by the above method of separating the contributions of the long- and short-range interactions described by Eqs. (17) and (19), (20) with the use of the *ab initio* cluster calculations of $Z_{ii}^{loc}(s)$. For comparison, Table 2 also lists the Born charges $Z_{ii}(s)$ calculated by the method suggested in [5, 6]. The cluster approach described above is approximate and works better, the larger the cluster used. With an increase of the cluster size, an ever increasing number of local (quasi-atomic) dipole moments induced by the field arising due to the displacement of the central atom are taken into account. As is seen from Table 2, the most pronounced error (about 100%) is contained in the results for the *B*-type atoms for a cluster consisting of only one octahedron. For the next (with respect to complexity) cluster consisting of seven octahedra, the error decreases to 40–50%. For *A*-type atoms, the error lies at a level of 20–30%, and for oxygen atoms, at a level of 20–40% for transverse components and 60–70% for longitudinal ones. For lead titanate, the errors are higher (by a factor of about 1.5) than for other materials. It should also be indicated that the allowance for electronic correlations somewhat improves the situation. Despite the insufficient accuracy, the method adequately describes the differences in the values of the Born charges for various species and materials and predicts anomalously high Z values for Ti, Nb, Ta, and Pb atoms and considerable differences between the longitudinal and transverse components for oxygen atoms. The simplicity of the method makes it useful in the search for materials with high Born effective charges which can be considered as "candidates to ferroelectrics."

5. CURIE TEMPERATURE IN THE SINGLE-ION MODEL

The simplest microscopic theory that qualitatively describes the phase transitions in displacive-type ferroelectrics can be constructed based on the single-ion (single-sublattice) model in the mean-field approximation [32–34, 45, 46]. In this model, the atoms of all the sublattices but one, e.g., the *B* sublattice, are fixed in their equilibrium positions so that each atom in the *B* sublattice behaves as an independent harmonic oscillator with a small anharmonic addition to the potential energy. Oscillators interact only via the internal electric field induced by the mean displacement of the *B* sublattice. In this model, the Hamiltonian for an atom in the position with the cubic symmetry can be represented [45, 46] as

$$H = H_0 + W_{ah}; \quad H_0 = \frac{P^2}{2M} + W_h(\mathbf{u}), \tag{23}$$

$$W_h(\mathbf{u}) = \frac{a}{2}\sum_i u_i^2 - (V_0\bar{u} + zE)u_3 + \frac{V_0}{2}\bar{u}^2;$$
$$W_{ah}(\mathbf{u}) = \frac{b_1}{4}\sum_i u_i^4 + \frac{b_2}{4}\sum_{i\neq j} u_i^2 u_j^2. \tag{24}$$

Table 1. Diagonal force constants k_{ii}^{dd}, k_{ii}^{sr}, and $k_{ii} = k_{ii}^{sr} + k_{ii}^{dd}$ for compounds with the perovskite structure

Compound	Atom	*ii*	k_{ii}^{dd}, eV/Å^2	Cluster	k_{ii}^{sr}, eV/Å^2	k_{ii}, eV/Å^2
$BaTiO_3$	Ba		–2.8	VIII	14.7	11.9
	Ti		–19.7	I	23.8 (21.0)	4.1 (1.3)
				VII	22.1	2.4
	O	∥	–12.4	II	21.2 (21.4)	8.7 (9.0)
		⊥	–1.7		9.9 (8.3)	8.2 (6.5)
$SrTiO_3$	Sr		–2.7	VIII	13.5	10.8
	Ti		–21.4	I	28.1 (24.9)	6.7 (3.5)
				VII	28.5	7.1
	O	∥	–13.5	II	28.6 (28.6)	15.1 (15.1)
		⊥	–1.8		9.0 (7.5)	7.2 (5.7)
$CaTiO_3$	Ca		–2.6	VIII	7.6	5.0
	Ti		–20.5	I	31.8 (28.3)	11.3 (7.8)
				VII	32.0	11.5
	O	∥	–13.1	II	32.5 (34.6)	22.1 (21.4)
		⊥	–1.6		7.4 (6.1)	5.8 (4.2)
$PbTiO_3$	Pb		–4.0	VIII	6.1	2.1
	Ti		–13.5	I	25.0 (22.1)	11.5 (8.6)
				VII	20.1	6.6
	O	∥	–9.2	II	25.1 (24.8)	15.8 (15.5)
		⊥	–1.7		5.8 (3.7)	4.1 (2.0)
$KNbO_3$	K		–0.6	VIII	6.2	5.6
	Nb		–33.4	I	35.7 (35.7)	2.3 (2.3)
				VII	30.6	–2.8
	O	∥	–20.3	II	23.9 (25.3)	3.6 (5.0)
		⊥	–1.1		9.2 (7.2)	8.1 (6.1)
$KTaO_3$	K		–0.6	VIII	7.0	6.4
	Ta		–29.4	I	43.7 (43.4)	14.3 (14.0)
				VII	39.0	9.6
	O	∥	–17.7	II	36.2 (36.8)	18.5 (19.2)
		⊥	–1.1		8.3 (6.8)	7.1 (5.6)

Note: The k_{ii}^{sr} values with due regard for the correlation corrections (RHF + MP2 method) are given in brackets.

The free energy in the single-ion model has the form

$$\mathcal{F}(T, \bar{u}, E) - \mathcal{F}_0(T) = \frac{1}{2}k_f(T)\bar{u}^2 + \frac{b_1\xi^4}{4}\bar{u}^4 - \xi z\bar{u}E, \quad (25)$$

where $\bar{\mathbf{u}} = (0, 0, \bar{u})$ is the mean displacement of atoms in the *B* sublattice. The generalized force constant $k_f(T)$ is determined as

$$k_f(T) = V_0(1-\xi) + \xi^2 b\overline{u^2}(T), \quad (26)$$

where

$$b = 3b_1 + 2b_2, \quad \xi = \frac{V_0}{a}, \quad \overline{u^2}(T) = \frac{\hbar}{2M\Omega}\coth\frac{\hbar\Omega}{2T}, \quad \Omega = \sqrt{\frac{a}{M}}, \quad (27)$$

and *M* is the mass of a ferroelectrically active ion.

5.1. Ab initio Calculations of Single-Ion Model Parameters

The approach considered above allows one to determine the model parameters (a, b_1, b_2, and V_0) from *ab initio* calculations. The harmonic parameters of the model for a ferroelectrically active ion from the s sublattice are given by the expressions

$$\begin{aligned} a(s) &= \Phi_{xx}(ss, \mathbf{R} - \mathbf{R}' = 0) = \Phi_{yy}(ss, \mathbf{R} - \mathbf{R}' = 0) \\ &= \Phi_{zz}(ss, \mathbf{R} - \mathbf{R}' = 0) \approx k^{sr}(s), \end{aligned} \tag{28}$$

$$\begin{aligned} V_0(s) &= -\sum_{\mathbf{R} \neq \mathbf{R}'} \Phi_{xx}(ss, \mathbf{R} - \mathbf{R}') \\ &= -\sum_{\mathbf{R} \neq \mathbf{R}'} \Phi_{yy}(ss, \mathbf{R} - \mathbf{R}') \\ &= -\sum_{\mathbf{R} \neq \mathbf{R}'} \Phi_{zz}(ss, \mathbf{R} - \mathbf{R}') \approx -k^{dd}(s), \end{aligned} \tag{29}$$

where $k^{dd}(s)$ and $k^{sr}(s)$ are defined by Eqs. (17) and (20).

The anharmonic parameters b_1 and b_2 are determined by short-range interactions because of the fast convergence of the corresponding lattice sums. Thus, the a, b_1, and b_2 parameters can be determined in *ab initio* calculations for an appropriate cluster. The $V_0(s)$ value can be determined from Eq. (17) for $k_{ii}^{dd}(s)$.

5.2. Influence of Quantum Statistics on Curie Temperature in $BaTiO_3$ and $KNbO_3$

The Curie temperature is the solution of the equation

$$k_f(T_0) = 0, \tag{30}$$

which, with due regard for Eq. (29), can be represented as

$$\begin{aligned} \xi^2 b \overline{u^2}(T_0) &= -k_h = (\xi - 1)V_0 \\ \text{or} \quad \overline{u^2}(T_0) &= (1 - \xi^{-1})\frac{a}{b}. \end{aligned} \tag{31}$$

In the high-temperature region, $T \geq \hbar\Omega/2$, one can use the expansion

$$\frac{\hbar}{2}\coth\frac{\hbar z}{2} = \frac{1}{z} + \hbar^2\frac{z}{12} - \hbar^4\frac{z^3}{720} + \ldots. \tag{32}$$

Retaining the first quantum correction, one obtains from Eqs. (30), (31), and (27) the following equation for T_0

$$\begin{aligned} T_0^2 - T_0^{\text{class}} T_0 + \frac{1}{12}(\hbar\Omega)^2 &= 0; \\ T_0^{\text{class}} &= (1 - \xi^{-1})a^2/b = (1 - \xi^{-1})E^{sr}, \end{aligned} \tag{33}$$

where T_0^{class} is the classical limit of the Curie temperature in the single-ion model, and the notation $E^{sr} = a^2/b$ is used for the energy characterizing the short-range interactions. The solution of Eq. (33) has the form

$$T_0 = \frac{1 + \sqrt{1 - \frac{1}{3}\delta^2}}{2} T_0^{\text{class}}, \quad \delta^2 = \left(\frac{\hbar\Omega}{T_0^{\text{class}}}\right)^2. \tag{34}$$

Equation (33) can be solved if the condition $T_0^{\text{class}} \geq \hbar\Omega/\sqrt{3}$ is fulfilled. One can readily see that this condition justifies leaving out all the following terms in expansion (32).

Equation (33) yields the isotope shift ΔT_0^{iso} caused by the replacement of an atom with the mass M by an isotope with the mass $M + \Delta M$

$$\Delta T_0^{\text{iso}} = \frac{\partial T_0}{\partial M}\Delta M = \frac{(\hbar\Omega)^2}{2T_0 - T_0^{\text{class}}}\frac{\Delta M}{12M}. \tag{35}$$

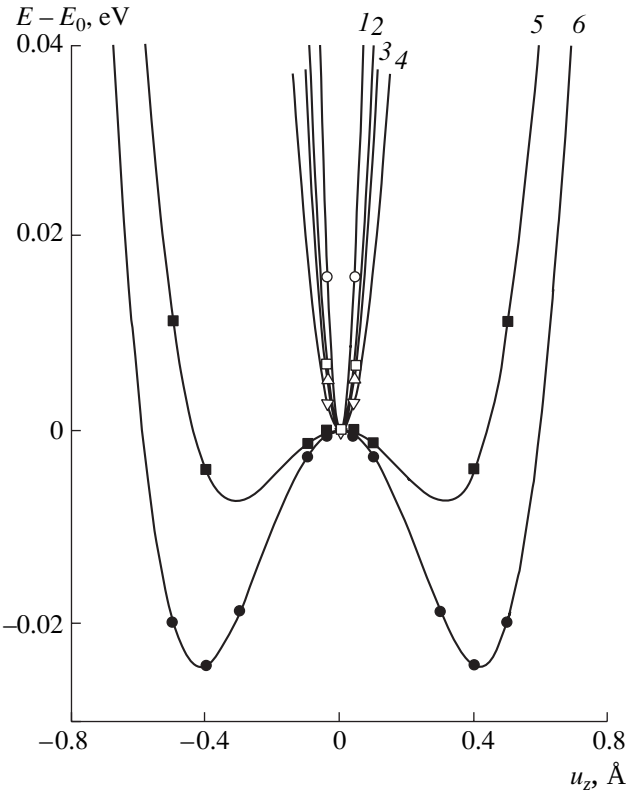

Local adiabatic potential of Ca, Ba, Pb, Cd, Mg, and Zn impurity atoms in the A position in $SrTiO_3$ (u_z is the displacement of an impurity atom from the central position at the site of the cubic perovskite lattice along the [001] direction). (*1*) Ba, (*2*) Pb, (*3*) Ca, (*4*) Cd, (*5*) Mg, and (*6*) Zn.

5.3. Results of Calculations

Table 3 presents the results of the *ab initio* cluster calculations of the harmonic force constant a for Ti and

Table 2. Effective charges $Z_{ii}^{sr}(s)$, $\tilde{Z}_{ii}(s)$, and $Z_{ii}(s)$ for compounds with the perovskite structure

Compound	Atom	Cluster	*ii*	Z_{ii}^{sr}	$\tilde{Z}_{ii} = \frac{\varepsilon^{\infty}+2}{3}Z_{ii}^{sr}$	Z_{ii}
$BaTiO_3$	Ba	VIII		1.4	3.3	2.75
	Ti	I		6.2 (5.7)	14.8 (13.8)	7.16
		VII		4.6	11.0	
	O	II	∥	–4.0	–9.7	–5.69
			⊥	–1.2	–2.9	–2.11
$SrTiO_3$	Sr	VIII		1.3	3.1	2.54
	Ti	I		6.15 (5.7)	14.7 (13.6)	7.12
		VII		4.5	10.7	
	O	II	∥	–3.9	–9.4	–5.66
			⊥	–1.2	–2.9	–2.00
$CaTiO_3$	Ca	VIII		1.3	3.4	2.58
	Ti	I		6.1 (5.7)	16.0 (14.8)	7.08
		VII		4.3	11.2	
	O	II	∥	–3.9	–10.1	–5.65
			⊥	–1.3	–3.3	–2.00
$PbTiO_3$	Pb	VIII		2.2	7.8	3.90
	Ti	I		6.2 (5.7)	21.8 (20.2)	7.06
		VII		3.5	12.3	
	O	II	∥	–2.6	–9.2	–5.83
			⊥	–1.4	–4.8	–2.56
$KNbO_3$	K	VIII		0.6	1.3	1.14
	Nb	I		8.1	18.2	9.23
		VII		6.0	13.3	
	O	II	∥	–4.95	–11.0	–7.01
			⊥	–0.92	–2.06	–1.68
$KTaO_3$	K	VIII		0.65	1.4	1.2
	Ta	I		9.3	19.7	8.1
		VII		5.5	11.6	
	O	II	∥	–4.7	–10.0	–6.3
			⊥	–0.95	–2.0	–1.5

Note: The Z_{ii} values for $KTaO_3$ are borrowed from [54] and [55]. The Z_{ii}^{sr} values calculated with due regard for the electronic correlations (RHF + MP2 method) are given in brackets.

Nb atoms in cubic $BaTiO_3$ and $KNbO_3$.[3] It is seen that these constants have positive values considerably exceeding the atomic force constant for perovskites.

The lower line of Table 3 lists the V_0 values for the Ti and Nb sublattices determined with due regard for Eqs. (29) and (17) and the data presented in Table 1. Table 3 also lists the anharmonic b_1 and b_2 parameters obtained in *ab initio* cluster calculations. Similar to the harmonic constant, these parameters, with due regard

[3] All the calculations were performed for $[Ti(OH)_6]_2$ and $[Nb(OH)_6]^{1-}$ clusters containing a single octahedron.

Table 3. Parameters of the single-ion model and the characteristics of $BaTiO_3$ (Ti is a ferroelectrically active atom) and $KNbO_3$ (Nb is a ferroelectrically active atom) obtained from *ab initio* calculations

		$BaTiO_3$		$KNbO_3$	
		RHF	RHF + MP2	RHF	RHF + MP2
a, eV/Å^2		19.1	19.4	34.31	36.85
$\hbar\Omega$, K		471	475	454	471
$\xi = \frac{V_0}{a}$		1.034	1.018	1.029	0.958
b_1, eV/Å^4		99.1	103.5	144.1	147.7
b_2, eV/Å^4		–35.6	–43.3	–72.2	–85.6
$b = 3b_1 + 2b_2$, eV/Å^4		224.2	223.7	287.9	271.8
$E^{sr} = \frac{a^2}{b}$, 10^4 K		1.89	1.95	4.745	5.798
$T_0^{\text{class}} = (1-\xi^{-1})E^{sr}$, K		621	345	1337	<0
T_0, K		590	277	1324	–
$\Delta T_0^{\text{quant}} = T_0 - T_0^{\text{class}}$, K		–31	–68	–13	–
ΔT_0^{iso}, K	$^{48}\text{Ti} \longrightarrow {}^{50}\text{Ti}$	1.4	3.8	–	–
	$^{48}\text{Ti} \longrightarrow {}^{46}\text{Ti}$	–1.4	–3.8	–	–
V_0, eV/Å^2		19.74		35.31	

for electronic correlations, vary only slightly. Comparing the calculated values of the Curie temperature with the experimental values, $T_0^{\text{exp}}(BaTiO_3)$ = 400 K and $T_0^{\text{exp}}(KNbO_3)$ = 700 K [58], we see that these data agree only qualitatively.

The above approach also allows one to consider the influence of the quantum statistics on the Curie temperature in ferroelectrics with the perovskite structure. Taking into account the experimental data on the isotope shift T_0 in $BaTiO_3$ after the $^{48}\text{Ti} \longrightarrow {}^{46}\text{Ti}$ or $^{48}\text{Ti} \longrightarrow {}^{50}\text{Ti}$ substitution [59] and the data on the influence of quantum fluctuations on T_0 in $BaTiO_3$ [60] calculated by the Monte Carlo method, these problems are of considerable interest. Table 3 lists the T_0^{class} and T_0 values for $BaTiO_3$ and $KNbO_3$ calculated by Eqs. (33) and (34) with the use of the data presented in Table 3. It is seen that the result obtained is in good agreement with the value $\Delta T_0^{\text{quant}} = -30$ K determined for $BaTiO_3$ in [60]. At the same time, the values of the isotope shift ΔT_0^{iso} calculated by Eq. (35) for $BaTiO_3$ after the $^{48}\text{Ti} \longrightarrow {}^{46}\text{Ti}$ or $^{48}\text{Ti} \longrightarrow {}^{50}\text{Ti}$ substitution from Table 3 are opposite in sign to the data obtained by Hidaka and Oka [59].

The Curie temperature T_0 in perovskites is rather sensitive to the degree of compensation of the contributions of different nature that come to the effective force constant of the sublattice of ferroelectrically active ions and, therefore, also to the accuracy of the calculations of these contributions, a and V_0. One can avoid this difficulty by considering T_0 as the only fitting parameter of the theory. Using Eq. (33), one can determine T_0^{class} and, then, also $\Delta T_0^{\text{quant}}$ and ΔT_0^{iso}. The results thus obtained are as follows. For $BaTiO_3$, T_0^{class} = 446 K (RHF method) and 447 K (RHF + MP2 method). For $KNbO_3$, T_0^{class} = 724.5 (RHF method) and 726.5 K (RHF + MP2 method). Thus, we have $T_0^{\text{quant}} \cong 47$ K for $BaTiO_3$ and 25 K for $KNbO_3$. The isotope shift ΔT_0^{iso} equals 2.2 K for the $^{48}\text{Ti} \longrightarrow {}^{50}\text{Ti}$ substitution and –2.2 K for $^{48}\text{Ti} \longrightarrow {}^{46}\text{Ti}$ substitution.

ACKNOWLEDGMENTS

The author is grateful to V.S. Vikhnin, A.P. Levanyuk, V.V. Lemanov, E.G. Maksimov, P.A. Markovin, A.K. Tagantsev, and V.A. Trepakov for numerous fruitful discussions. This study was supported by

the Russian Foundation for Basic Research, project no. 03-02-17557.

REFERENCES

1. O. E. Kvyatkovskiĭ and E. G. Maksimov, Usp. Fiz. Nauk **154** (1), 3 (1988) [Sov. Phys. Usp. **31**, 1 (1988)].
2. D. Vanderbilt, J. Korean Phys. Soc. **32**, S103 (1998).
3. V. Kon, Usp. Fiz. Nauk **172** (3), 336 (2002).
4. D. A. Popl, Usp. Fiz. Nauk **172** (3), 349 (2002).
5. R. D. King-Smith and D. Vanderbilt, Phys. Rev. B **47** (3), 1651 (1993).
6. R. Resta, Europhys. Lett. **22** (2), 133 (1993).
7. P. Ghosez, J.-P. Michenaud, and X. Gonze, Phys. Rev. B **58** (10), 6224 (1998).
8. P. Ghosez, E. Cockayne, U. V. Waghmare, *et al.*, Phys. Rev. B **60** (2), 836 (1999).
9. N. Sai and D. Vanderbilt, Phys. Rev. B **62** (21), 13942 (2000).
10. E. Cockayne and B. P. Burton, Phys. Rev. B **62** (6), 3735 (2000).
11. L. Bellaiche and D. Vanderbilt, Phys. Rev. B **61** (12), 7877 (2000).
12. B. Meyer and D. Vanderbilt, Phys. Rev. B **65**, 104111-1 (2002).
13. J. Íñiguez and D. Vanderbilt, Phys. Rev. Lett. **89** (11), 115503-1 (2002).
14. I. I. Tupitsyn, A. Deineka, V. Trepakov, *et al.*, Ferroelectrics **237**, 9 (2000).
15. R. A. Evarestov, S. Piskunov, E. A. Kotomin, *et al.*, Phys. Rev. B **67**, 064101-1 (2003).
16. L. J. Sham, Phys. Rev. **188** (3), 1431 (1969).
17. R. M. Pick, M. H. Cohen, and R. M. Martin, Phys. Rev. B **1** (2), 910 (1970).
18. O. E. Kvyatkovskiĭ, Fiz. Tverd. Tela (Leningrad) **27** (9), 2673 (1985) [Sov. Phys. Solid State **27**, 1603 (1985)].
19. O. E. Kvyatkovskiĭ, Fiz. Tverd. Tela (St. Petersburg) **35** (8), 2154 (1993) [Phys. Solid State **35**, 1071 (1993)].
20. O. E. Kvyatkovskiĭ, Izv. Ross. Akad. Nauk, Ser. Fiz. **64** (6), 1065 (2000).
21. O. E. Kvyatkovskii, Ferroelectrics **237**, 33 (2000).
22. O. E. Kvyatkovskii, J. Korean Phys. Soc. **32**, S140 (1998).
23. O. E. Kvyatkovskiĭ, Fiz. Tverd. Tela (Leningrad) **28** (4), 983 (1986) [Sov. Phys. Solid State **28**, 548 (1986)].
24. O. E. Kvyatkovskii, Ferroelectrics **153**, 201 (1994).
25. O. E. Kvyatkovskiĭ, Fiz. Tverd. Tela (St. Petersburg) **39** (4), 687 (1997) [Phys. Solid State **39**, 602 (1997)].
26. O. E. Kvyatkovskiĭ and B. F. Shchegolev, Izv. Ross. Akad. Nauk, Ser. Fiz. **64** (6), 1060 (2000).
27. W. Zhong, D. Vanderbilt, and K. M. Rabe, Phys. Rev. Lett. **73** (13), 1861 (1994).
28. W. Zhong, D. Vanderbilt, and K. M. Rabe, Phys. Rev. B **52**, 6301 (1995).
29. U. V. Waghmare and K. M. Rabe, Phys. Rev. B **55** (10), 6161 (1997).
30. B. A. Strukov and A. P. Livanyuk, *Physical Principles of Ferroelectric Phenomena in Crystals* (Nauka, Moscow, 1995), Chap. 7.
31. A. D. Bruce and R. A. Cowley, *Structural Phase Transitions* (Taylor and Francis, London, 1981), Part 2.
32. A. F. Devonshire, Philos. Mag. **40**, 1040 (1949).
33. J. C. Slater, Phys. Rev. **78** (6), 748 (1950).
34. J. H. Barrett, Phys. Rev. **86** (1), 118 (1952).
35. W. Cochran, Adv. Phys. **9** (36), 387 (1960).
36. W. P. Mason and B. T. Matthias, Phys. Rev. **74** (11), 1622 (1948).
37. T. P. Dougherty, G. P. Wiederrecht, K. A. Nelson, *et al.*, Science **258**, 770 (1992).
38. N. Sicron, B. Ravel, Y. Yacoby, *et al.*, Phys. Rev. B **50**, 13168 (1994).
39. B. Zalar, V. V. Laguta, and R. Blinc, Phys. Rev. Lett. **90** (3), 037601 (2003).
40. R. E. Cohen, Nature **358**, 136 (1992).
41. Y. Yacoby, Z. Phys. B **31**, 275 (1978).
42. O. Hanske-Petitpierre, Y. Yacoby, J. Mustre de Leon, *et al.*, Phys. Rev. B **44** (13), 6700 (1991).
43. O. E. Kvyatkovskiĭ, Fiz. Tverd. Tela (St. Petersburg) **44**, 1087 (2002) [Phys. Solid State **44**, 1135 (2002)].
44. O. E. Kvyatkovskiĭ and B. F. Shchegolev, Ferroelectrics **153**, 207 (1994).
45. V. G. Vaks, *Introduction to the Microscopic Theory of Ferroelectrics* (Nauka, Moscow, 1973).
46. O. E. Kvyatkovskiĭ, Fiz. Tverd. Tela (St. Petersburg) **43** (8), 1345 (2001) [Phys. Solid State **43**, 1401 (2001)].
47. M. Born and K. Huang, *Dynamical Theory of Crystal Lattices* (Clarendon Press, Oxford, 1954; Inostrannaya Literatura, Moscow, 1958).
48. R. M. Martin, Phys. Rev. B **9**, 1998 (1974).
49. N. G. Zamkova, V. I. Zinenko, O. V. Ivanov, *et al.*, Ferroelectrics **283**, 49 (2003).
50. O. V. Ivanov and E. G. Maksimov, Phys. Rev. Lett. **69** (1), 108 (1992).
51. H. Hellman, *Einfurung in die Quanten Theorie* (Deuticke, Leipzig, 1937), p. 285.
52. R. Feynman, Phys. Rev. **56**, 340 (1939).
53. W. Cochran and R. A. Cowley, J. Phys. Chem. Solids **23**, 447 (1962).
54. W. Zhong, R. D. King-Smith, and D. Vanderbilt, Phys. Rev. Lett. **72**, 3618 (1994).
55. J. D. Axe, Phys. Rev. **157** (2), 429 (1967).
56. A. Granovsky, http://classic.chem/msu/su/gran/gamess/index.html.
57. M. W. Schmidt, K. K. Baldridge, J. A. Boatz, *et al.*, J. Comput. Chem. **4**, 347 (1993).
58. *Landolt-Bornstein: Ferroelectric Oxides*, Ed. by K. H. Hellwege and A. M. Hellwege (Springer, Berlin, 1981), Group 3, Vol. 16a.
59. T. Hidaka and K. Oka, Phys. Rev. B **35** (16), 8502 (1987).
60. W. Zhong and D. Vanderbilt, Phys. Rev. B **53** (9), 5047 (1996).

Translated by L. Man

Crystallography Reports, Vol. 49, No. 1, 2004, pp. 40–45. Translated from Kristallografiya, Vol. 49, No. 1, 2004, pp. 45–50.

THEORY OF CRYSTAL STRUCTURES

Dedicated to the 80th Birthday of L.A. Shuvalov

Structural Hierarchy and Transformations in Crystals of the Perovskite Family

V. Sh. Shekhtman, I. S. Smirnova, V. D. Sedykh, I. M. Shmyt'ko, N. S. Afonikova, and A. V. Dubovitskiĭ

Institute of Solid-State Physics, Russian Academy of Sciences, Chernogolovka, Moscow oblast, 142432 Russia

e-mail: shekht@issp.ac.ru

Received June 5, 2003

Abstract—The specific features of structural transformations in lanthanum manganite and lithium niobate are analyzed in terms of the macrosymmetry conservation principle discussed in the papers by L.A. Shuvalov. The possible mechanisms of phase transformations are proposed reasoning from a sequence of structural transitions, including the restoration of a virtual configuration of cubic perovskite with double the lattice parameter. The basic scheme of mutual transformations of two orthorhombic modifications is described for lanthanum manganite. A similar scheme proposed for lithium niobate is used to elucidate the nature of the mechanical twinning observed upon mutual switching of orientational domains. © *2004 MAIK "Nauka/Interperiodica"*.

INTRODUCTION

The field of research concerned with analyzing symmetry properties upon diffusionless structural transformations includes different modern directions of the physical materials science. Historically, until the nature of these phenomena was elucidated, only a small number of effects associated with metal technology, such as *steel hardening*, the "*tin pest*," and others, were known in sufficient detail. The term "*martensitic transformations*" is deeply embedded in the literature owing to the numerous structural investigations of hardened steels. A generalized characteristic of structural processes is contained in the term "*cooperative transformations*." This term is taken to mean that the structure of a new phase is formed from the parent *praphase* structure through successive small oriented displacements, shifts, and rotations of the atomic fragments (planes, tetrahedra, etc.) as a whole. An important point is that, in this case, the standard mechanisms of nucleation and growth of new-phase crystals due to diffusion have failed. Such *diffusionless phase transformations* frequently occur, especially at low temperatures and under high pressures. It should be noted that the list of materials undergoing diffusionless phase transformations is not reduced to metal alloys.

Phase transitions from a paraelectric state to a ferroelectric state have been extensively investigated by diffraction methods. Although, in the course of these transitions, bulk effects and real atomic displacements, as a rule, are insignificant, the crystal symmetry can change substantially, including loss of an inversion center and a change in the type of Bravais lattice. A large number of research works performed in the last decade have demonstrated that the first representatives of high-temperature superconductors and crystals with colossal magnetoresistance have in many respects inherited structural problems formulated for related families of ferroelectric crystals. From this standpoint, the justification of structural models and inclusion of symmetry hierarchy are of particular importance. The same is especially true in regard to both the search for possible ways of transforming a given point group into a subgroup and an analysis of experimental splittings of diffraction peaks.

When solving the aforementioned experimental problems, it is expedient to use the principle of conservation of generalized symmetry (*macrosymmetry of polysynthetic twins*), which was proposed by Zheludev and Shuvalov [1].

The concept of a discrete set of *orientational domains* (*orientational states*) of a new phase has assumed a special significance in terms of structural crystallography. Let us assume that, at a certain temperature, the initial structure should undergo transformation due to specific atomic displacements in particular crystallographic directions. The symmetry properties provide a means for "multiplying" this process. As a result, there exists a series of equivalent possible ways of deformation whose number is determined by the group algebra of the parent *praphase*. Therefore, the formation of a new phase occurs through a specified set of *orientational states*. Within this approach, which is based on the principle of conservation of generalized

symmetry, the symmetry of the generalized reciprocal space for a complete set of orientational states of a *dissymmetric* phase reproduces F^2 symmetry of the initial structure.

Research into crystals of the perovskite family has revealed different aspects of the macrosymmetry conservation principle. For example, a number of interesting features manifest themselves in the sequence of several structural transformations. In particular, it is known that, upon cooling, barium titanate crystallizes from a melt in the *K* modification (cubic, *Pm*3*m*), which, in turn, undergoes the following sequence of phase transitions with a decrease in the temperature: at 393 K, $K \longrightarrow T$ (tetragonal, *P*4*mm*); at 273 K, $K \longrightarrow O$ (orthorhombic, *Bmm*2); and, at 183 K, $K \longrightarrow R$ (rhombohedral, *R*3*m*). Formally, each of the subsequent transitions could result in a jumpwise increase in the total number of orientational states due to a new transformation of the already existing domain structure with a specified multiplicity. However, such an avalanchelike multiplication of orientational states is not observed in real experiments. This means that the "memory" of the lattice of the cubic praphase is an important factor responsible for the mechanism of the structural transformation. An analysis of the data available in the literature demonstrates that, in the above sequence of phase transitions, the mutual orientation of domains and the number of orientational states in each of the new phases are governed by the transformation from the praphase, i.e., $K \longrightarrow T$, $K \longrightarrow O$, and $K \longrightarrow R$. To put it differently, within this model, each new phase transition (for example, $T \longrightarrow O$) necessitates *virtual* restoration of the praphase *K* and a new domain structure is formed in the coordinate system of the cubic phase:

$$\begin{array}{c} K \\ T_2 \Updownarrow\Leftrightarrow O. \end{array}$$

A similar approach can be used to analyze the mutual switching of domains involved in a dissymmetric phase, for example, upon polarization switching of ferroelectric domains, which are conventionally designated as T_1, T_2, T_3, T_4, …, etc. This process can be schematically represented as follows:

$$\begin{array}{c} K \\ T_2 \Updownarrow\Leftrightarrow T_3 \end{array} \text{ etc.}$$

In other words, the switching involves a (virtual) stage of returning to the coordinate axes of the crystal lattice of the cubic praphase.

It is clear that the above approach accounts only for the general features of transformations. However, as applied to particular experimental problems, this approach can provide deeper insight into the mechanism of structural transformations. Below, we will analyze specific examples of the mechanisms under consideration for a number of representatives of the large perovskite family.

STRUCTURAL TRANSFORMATIONS OF LANTHANUM MANGANITE

According to Huang *et al.* [2] and Mitchell *et al.* [3], lanthanum manganite $LaMnO_3$ has several structural modifications. Among them, the main modifications are the rhombohedral ($R\bar{3}c$), two orthorhombic (*Pnma*I, *Pnma*II), and monoclinic ($P112_1/a$) phases. Mutual transformations between the structural modifications are observed under special temperature conditions or small variations in the compositions.

It is significant that, in the framework of the known hierarchy of crystallographic groups, the point group of orthorhombic modifications (*mmm*) is not a subgroup for the rhombohedral modification (group 3*m*). At the same time, all the aforementioned groups are included in the hierarchic system of *m*3*m* cubic symmetry, which is characteristic of perovskites. Note also that the unit cell parameters of the $R\bar{3}c$ modification ($a = 5.46$ Å $\approx 3.86\sqrt{2}$, $\alpha = 60.63°$) are close to those involved in the representation of the cubic lattice through a 60° rhombohedron.

Therefore, the model of mutual transformations through an intermediate stage of restoration of the cubic configuration seems to be well substantiated. This is also confirmed by the diffraction patterns. Figure 1 shows the diffraction pattern of lanthanum manganite at room temperature.

First and foremost, it should be noted that the diffraction pattern is relatively simple and the positions of the diffraction lines are close to those in the diffraction pattern of the primitive cubic lattice. The diffraction pattern of lanthanum manganite is roughly approximated by the simplest set of the (100), (110), (111), (200), (210), (211), (220), (300), and (310) lines, as is the case with barium titanate. Within this model, the parameter *a* for a hypothetical cubic lattice is estimated from the diffraction angles as $a \approx 3.86$ Å.

Consequently, the Debye powder diffraction pattern also indicates that, in the topological model of the $R\bar{3}c \longrightarrow Pnma$ transformation, it is expedient to use the sequence of transitions $3m \longrightarrow m3m \longrightarrow mmm$, including a return to the axes of the cubic supergroup. As was shown in [4], this mechanism proved to be well justified.

Let us now consider the possible mechanisms of the structural transformation $R\bar{3}c \longrightarrow Pnma$ in greater detail. In this case, it is advisable to compare this transformation with the cube–orthorhomb transition occurring in barium titanate $BaTiO_3$. In barium titanate, the unit cell *Pm*3*m* ($a = 4.03$ Å) contains one formula unit. The shear deformation of the basis configuration composed of four cubic unit cells leads to the formation of the base-centered orthorhombic structure *Bmm*2 with the lattice parameters $a = 5.66$ Å, $b = 3.99$ Å, and $c = 5.68$ Å and two formula units.

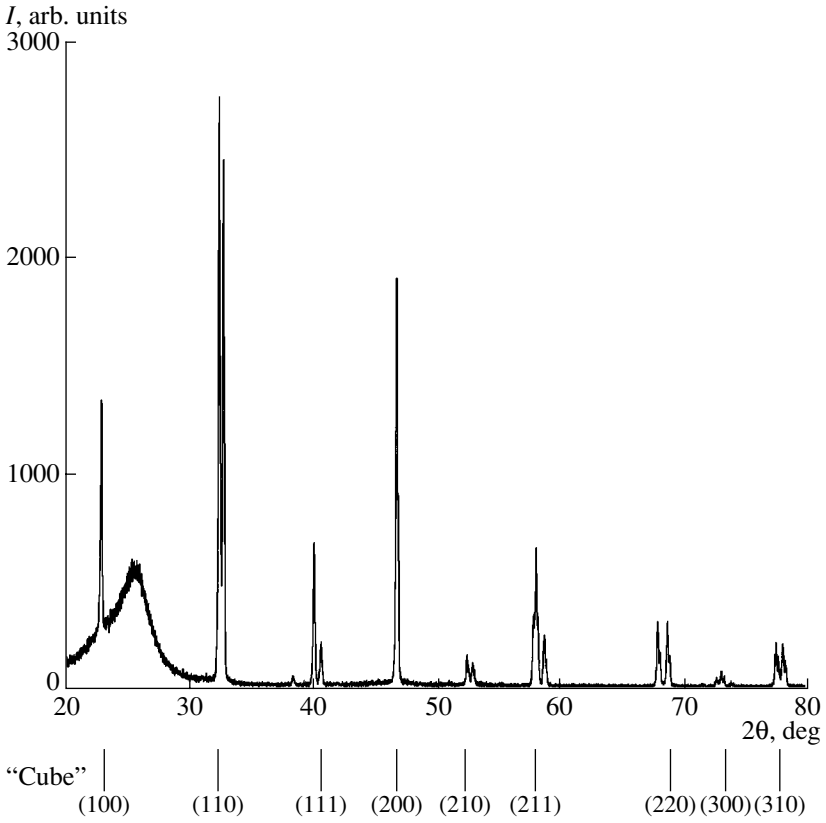

Fig. 1. Diffraction pattern of lanthanum manganite at room temperature.

In the case of lanthanum manganite, the resultant structure is described as a primitive orthorhombic lattice: *Pnma*I (a = 5.514 Å, b = 7.795 Å, and c = 5.531 Å) or *Pnma*II (a = 5.715 Å, b = 7.715 Å, and c = 5.536 Å). In either variant, the unit cell contains four formula units. Therefore, it is necessary to modify the mechanisms proposed for perovskites. A parent fragment consisting of eight cubic unit cells of the praphase (Fig. 2) can be used as a basis configuration subjected to uniform shear through a small angle. It is known [5] that a similar configuration is typical of Sr_2FeMoO_6 crystals and other representatives of the perovskite family with magnetoresistive properties.

This situation can be clearly illustrated by the schematic diagram depicted in Fig. 3. It can be seen from the diagram that a tilting of the sides of the large unit cell *ABCD* through a small angle φ results in a transformation of the initial square lattice into a rectangular lattice with the unit cell *EFGH*. Upon twinning shear, the initial structure *Pm*3*m* transforms into the primitive orthorhombic lattice *Pnma*II with specified increased lattice parameters a and c. Within this approach, we obtain the parameter $b_{\text{unit vector}} \sim 2a_{\text{cube}}$. The schematic diagram shown in Fig. 4 illustrates the orientational relationships of the orthorhombic unit cell with the coordinate axes of the cubic praphase.

As can be seen from the diagram depicted in Fig. 3, the lattice parameter a and the twinning angle φ for the cubic praphase can be determined from experimental data on the lattice parameters $EF = a$ and $FG = c$ for the orthorhombic lattice according to the expressions $a_{\text{cube}} = 1/2\sqrt{(a^2 + c^2)}$, $\sin(45 + \varphi) = a/a_{\text{cube}}$, and $\sin(45 - \varphi) = c/a_{\text{cube}}$. For the above parameters of the orthorhombic lattice, the tilt angle upon twinning shear is estimated (by solving the approximate trigonometric problem) as follows: $\varphi \sim -0.1°$ for *Pnma*I and $\varphi \sim +0.9°$ for *Pnma*II at a_{cube} = 3.905 Å.

It should be noted that the inequalities $a < c$ and $a > c$, which correspond to variants I and II of the orthorhombic structure, manifest themselves in opposite signs of the tilt angle upon twinning shear. This circumstance allows us to elucidate the possible mechanism of the mutual transformations *Pnma*I ⇔ *Pnma*II. From analyzing the simplest diagram given in Fig. 3, we can draw the conclusion that the real stage of this transition involves a (virtual) restoration of the praphase lattice, and, then, the lattice is tilted toward the opposite direction with respect to the coordinate axis:

$$Pnma\text{I} \overset{K}{\Updownarrow\Leftrightarrow} Pnma\text{II}.$$

Lanthanum manganite crystals, like barium titanate crystals, can undergo structural transitions with a decrease in the temperature. In preliminary experiments, the structure of polycrystalline samples was *in situ* investigated on a diffractometer equipped with a nitrogen cryostat. It was revealed that the diffraction pattern changes upon cooling of the sample. Specifically, at temperatures below $T \sim 200$ K, there appears a new diffraction line at the midpoint of the angle range between the (110) and (104) lines attributed to the rhombohedral phase. The intensity of the new line substantially increases with a decrease in the temperature. The angular position of this line at a temperature of 93.4 K corresponds to the parameter $d = 2.734$ Å. This value is in close agreement with the parameter $d(110)$ for the cubic phase with the above parameter a_{cube}. Note that the positions of the lines observed in the initial diffraction pattern remain constant. Figure 5 depicts the temperature dependences of the peak intensities. It can be assumed that, upon cooling, the onset of the phase transformation occurs at a temperature between 200 and 150 K and the transformation is not completed at 93.4 K. In this case, the sample retains the two-phase composition and an increase in the temperature from 93.4 K to room temperature leads to the recovery of the initial diffraction pattern. Repeated cycling of the samples in this temperature range leaves the initial set of lines in the diffraction pattern unchanged. In the immediate future, we will perform a series of experiments with the aim of studying the specific features of this transformation in greater detail. In this paper, we can only note that the appearance of new lines, their positions in the diffraction patterns, and the reversible two-phase composition can be associated with the aforementioned intermediate state with the coordinate axes of the cubic praphase.

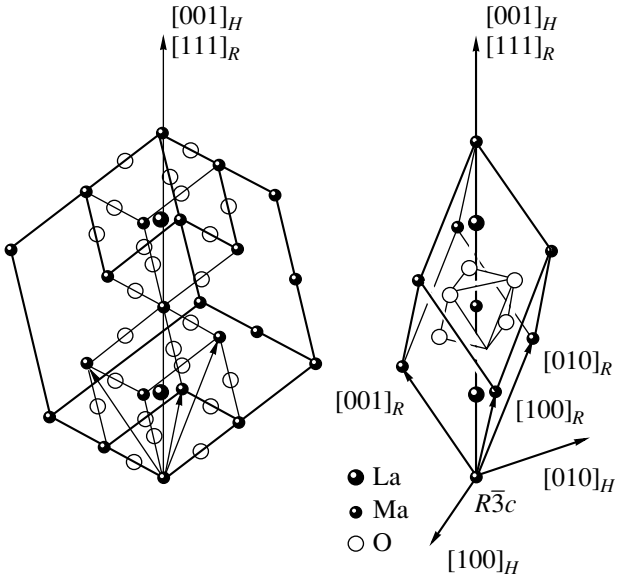

Fig. 2. Schematic diagram illustrating the orientational relationships of the rhombohedral unit cell $R\bar{3}c$ of the lanthanum manganite and the parent praphase fragment consisting of eight perovskite cubic unit cells.

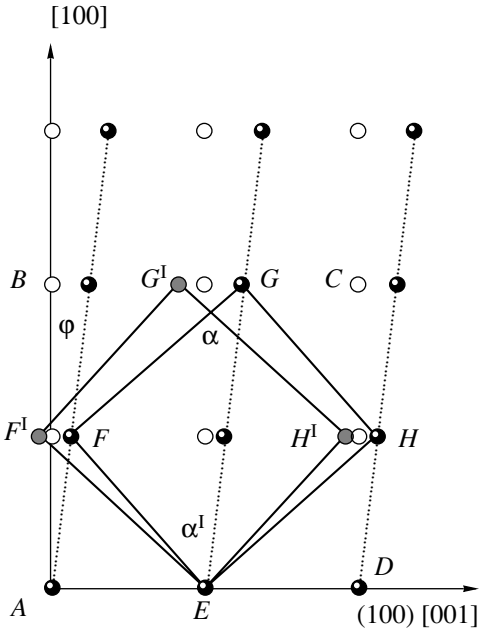

Fig. 3. A model of twinning shear for transforming the parent cubic lattice into an orthorhombic lattice with the (010) shear plane, the (100) twinning plane, and the [001] twinning direction. *ABCD* is the square face of the parent fragment, *EFGH* is the *a*/*c* face of the orthorhombic unit *Pnma*I, $E^1F^1G^1H^1$ is the *a*/*c* face of the orthorhombic unit cell *Pnma*II, and φ is the tilt angle upon twinning.

MECHANICAL TWINNING OF LITHIUM NIOBATE

An analogy with the structural transformations occurring in lanthanum manganite can be revealed from analyzing the results obtained for lithium niobate single crystals. As is known, the $LiNbO_3$ structure is described by space group $R3c$ with the unit cell parameters $a = 5.494$ Å $\sim 3.885\sqrt{2}$ and $\alpha = 55.87°$. Note that, as in the case of lanthanum manganite, the characteristic angle α of the rhombohedral unit cell is also close to 60°, which indicates the relation to the parent cubic lattice.

Barsamian *et al.* [6] investigated the plastic deformation of lithium niobate single crystals. Oriented samples in the form of parallelepipeds ($2 \times 4 \times 5$ mm^3 in size with different facetings) were subjected to uniaxial compression along the [111] direction at a constant deformation rate (from 5 to 50 μm/min) in the temperature range from 20 to 850°C. The experimental results demonstrated that, at temperatures above $t \approx 300$°C, the deformation predominantly occurs through the formation of mechanical twins. The geometric characteristics of the twin slip bands and their angular parameters with respect to the coordinate axes of single crystals were

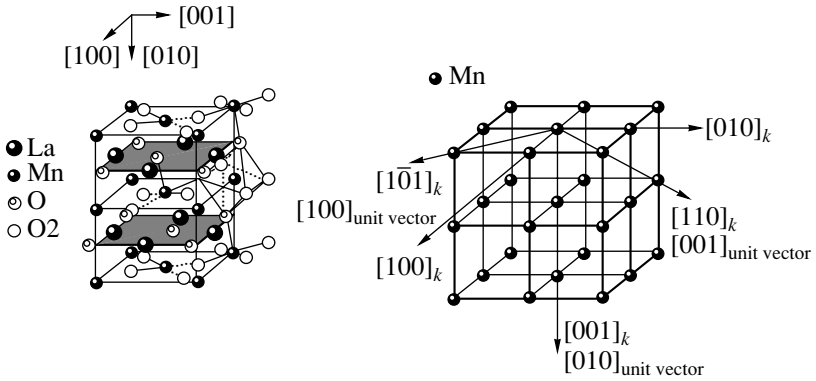

Fig. 4. Schematic diagram illustrating the orientational relationships of the orthorhombic unit cell *Pnma* with the coordinate axes of the cubic praphase.

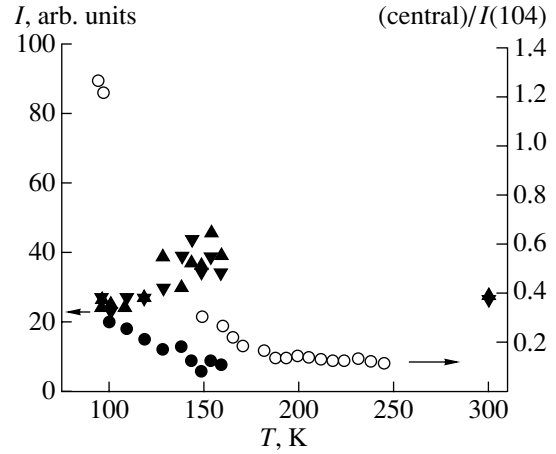

Fig. 5. Temperature dependences of the peak intensities of the (110) and (104) diffraction lines of the rhombohedral phase (triangles), the peak intensity of the new diffraction line (closed circles), and the ratio of the peak intensity of the new phase to *I*(104) (open circles).

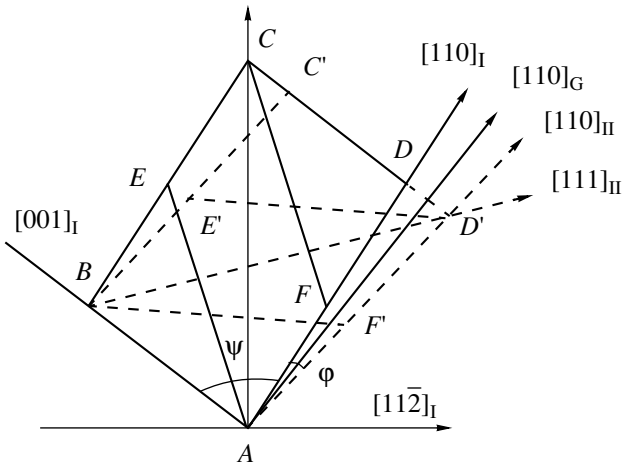

Fig. 6. Schematic diagram illustrating the switching of orientational states upon mechanical twinning of the lithium niobate crystal.

thoroughly analyzed using the results of visual observations and recording of the Laue diffraction patterns. The measurements revealed traces of three orientational states of twin interlayers on the sample faces. In this case, the twinning planes make an identical angle (~38°) with the loading axis. In [6], the authors determined the angles between the slip planes and showed that the configurations of the three observed orientations can be brought into coincidence by mutual rotation through an angle of ~120° about the [111] direction of the compressive deformation. An analysis of the Laue diffraction patterns made it possible to determine the indices of the $\{110\}/\langle 001\rangle$ twinning system in the crystals and to confirm the inference that the observed orientations of the twins are related by a threefold rotation axis.

The results obtained can be adequately interpreted in terms of cube ⇔ rhombohedron "genetic relations." However, unlike the preceding case, the case in point is not related to successive mutual transitions between crystalline modifications. In the experiments under consideration, the sole orientational state (single-domain crystal) transforms into three (equivalent) orientational states of the rhombohedral phase. To put it differently, the lithium niobate crystal is treated as a single-domain configuration formed after the phase transition from the cubic praphase. As a simple model, we can propose the dilatation mechanism of transformation, namely, an extension of the cubic unit cell along the direction (one of the four possible $\langle 111\rangle$ directions) of the body diagonal. This deformation brings about a decrease (60° ⟶ 55.87°) in the angles α ([110]/[101]/[011]); as a result, the lattice becomes rhombohedral.

Within this approach, the experimental data on the oriented uniaxial deformation along the $[111]_{rhomb}$ direction can be described by the two-stage mechanism. Formally, the oriented compression provides detwinning and the recovery of the initial characteristic angles in accordance with the (110)/[001] system

through a (virtual) restoration of the praphase lattice. Then, in a given crystal region, the lattice under the action of a force couple transforms following the (110)/[001] system, so that another possible axis, namely, $\langle 111 \rangle_{cube}$, becomes the $[111]_{rhomb}$ diagonal. In other regions, an alternative orientational state of the rhombohedral phase is formed by the same mechanism under cleavage stresses.

The mechanism of switching of orientational states is illustrated in the schematic diagram drawn in Fig. 6: the slip plane coincides with the (110) plane; the shear occurs along the [001] direction; *ABCD* is the pseudocubic cross section (*1*); *AECF* is the cross section of the rhombohedral orientational state (*1*); *ABC*'*D*' is the pseudocubic cross section (*2*); and *BE*'*D*'*F*' is the cross section of the rhombohedral orientational state (*2*). It can be seen that the experimental results indicate an analogy between mechanical twinning of the lithium niobate crystals and interdomain transformations in ferroelastics. This manifests itself in deformation mechanisms and interactions of the symmetrically justified set of orientational states.

CONCLUSIONS

Thus, the above analysis of the concrete examples considered in this work demonstrated that the inclusion of inherent features of the perovskite family in structural investigations is of fundamental importance. The same is also true for other crystalline systems. In particular, stacking faults and polytypic structures play a crucial role in both systems with the closest packing and compounds of the diamond-like family. Ordering processes are extremely important for metallic compounds. The distribution of oxygen over lattice sites and incommensurate modulation phenomena substantially affect the properties of high-temperature superconductors. It was established that manganites with magnetoresistive properties undergo a sequence of structural transitions which can be controlled by varying the temperature and composition of the material. The proposed approach is based on the inclusion of the structural hierarchy of the family with allowance made for the macrosymmetry conservation principle and the topology of the cubic praphase. Within this approach, it becomes possible to analyze the influence of structural transformations on the basic physical characteristics more consistently.

ACKNOWLEDGMENTS

We would like to thank S.S. Khasanov for his interest in this work and fruitful discussions.

This work was supported by the Russian Foundation for Basic Research, project no. 03-02-17232.

REFERENCES

1. I. S. Zheludev and L. A. Shuvalov, Kristallografiya **1**, 681 (1956) [Sov. Phys. Crystallogr. **1**, 537 (1956)]; L. A. Shuvalov, Kristallografiya **8**, 617 (1963) [Sov. Phys. Crystallogr. **8**, 495 (1963)].
2. Q. Huang, A. Santoro, J. W. Lynn, *et al.*, Phys. Rev. B **55**, 14987 (1997).
3. J. F. Mitchell, D. N. Argyriou, C. D. Potter, *et al.*, Phys. Rev. B **54**, 6172 (1996).
4. V. D. Sedykh, I. S. Smirnova, B. Sh. Bagautdinov, *et al.*, Poverkhnost, No. 12, 9 (2002).
5. H.-T. Jeng and G. Y. Guo, Phys. Rev. B **67**, 094438 (2003).
6. T. K. Barsamian, B. E. Mdivanyan, A. V. Tadevossian, *et al.*, Ferroelectrics **42**, 235 (1993).

Translated by O. Borovik-Romanova

Crystallography Reports, Vol. 49, No. 1, 2004, pp. 46–52. Translated from Kristallografiya, Vol. 49, No. 1, 2004, pp. 51–57.

THEORY OF CRYSTAL STRUCTURES

Dedicated to the 80th Birthday of L.A. Shuvalov

Change in the State of a Ferroelectric in a Strong Electromagnetic Wave

E. V. Bursian, V. V. Rychgorskiĭ, and A. I. Zaĭtsev

Herzen State Pedagogical University, Moika 48, St. Petersburg, 191186 Russia

e-mail:bursian@inbox.ru

Received July 17, 2003

Abstract—Results of investigations of changes in the state of a ferroelectric crystal, through which an intense electromagnetic-energy flux is transmitted, are analyzed. It is found that the main parameters determining the phase transition change significantly in this case. In addition, some phenomena develop which are characteristic only of open thermodynamic systems (self-assembling dissipative structures arise). These phenomena manifest themselves upon generation of the second optical harmonic in crystals where natural matching is absent. © *2004 MAIK "Nauka/Interperiodica".*

1. INTRODUCTION

The phenomenological theory of ferroelectric crystals was suggested by Ginzburg and Devonshire on the basis of the general thermodynamic theory of phase transitions developed by Landau. After a number of preliminary steps (Slater and Mason), the microscopic theory was reported approximately in 1960 by Ginzburg, Anderson, and Cochran, who introduced into consideration the model of the so-called soft mode, using the theory of lattice vibrations developed by Born [1].

Since in the nonlinear optics, as well in the optics of ferroelectrics in general, the interaction between an electromagnetic wave and the electron subsystem is dominant, the problem should be considered by selecting the electronic degrees of freedom with subsequent inclusion of the electron–phonon interaction, which leads to an instability and a phase transition in the absence of external fields. Therefore, the interband model of a ferroelectric [2–4] is optimal for analysis of changes in the state of a ferroelectric in a powerful wave.

The following circumstance should be noted, which is of much importance in view of the further consideration. In all classical studies on ferroelecticity, a ferroelectic crystal was considered as a thermodynamically closed system. The mechanical actions and the effect of electric fields and light of prelaser intensities below the typical laser intensities only insignificantly affected this condition. However, at energy-flux densities through a crystal of about 1 MW/mm^2 (laser pulses), a system cannot be considered closed even in the first approximation. Thus, the concepts of nonequilibrium thermodynamics should be used in this case. The first experimental and theoretical investigations in this area were performed in the 1960s–1970s [4–6].

The emphasis of this paper is on some recent studies on the interaction between a powerful electromagnetic wave and a ferroelectric crystal and the nonlinear optics of these objects.

2. FERROELECTRIC UNDER CONDITIONS FAR FROM THERMODYNAMIC EQUILIBRIUM

2.1. Changes in the Main Parameters of the Ferroelectric State

In a weak electromagnetic field, the electronic spectrum of a crystal (the band structure) can be considered as invariable. An external wave changes only the electron densities in bands and at local energy levels. As a result, static electric fields arise which only insignificantly affect the parameters of a ferroelectric [7]. In strong fields, the band structure of a crystal changes. In addition, a uniform state may become unstable.

A general theory of changes in the properties of a ferroelectric in a strong electromagnetic field was developed in [2–5]. The account of the electromagnetic field gives rise to a field term with the coupling constant $\lambda_{\alpha\beta}$, which takes into account the electron–field interaction in the Hamiltonian. A field is considered strong if induced transitions to the lower levels are more likely than spontaneous ones: $\tau \ll \tau_{sp}$ or $\lambda_{\alpha\beta}\tau_{sp} \gg 1$. In this case, an electron permanently passes from a lower to an upper band and vice versa due to the action of the field, thus forming a state in which it exists simultaneously in both bands. As a result, the electronic spectrum transforms. The bands shift closer to each other by ω_L (Fig. 1). According to the interband model, the instabil-

ity in the paraelectric phase increases and the critical oscillation frequency decreases. Hence, the permittivity increases and the transition temperature increases as well.

Thus, a strong external field, enhancing the effective electron–phonon interaction, changes the main parameters determining the phase transition.

Note that, in the previous studies on the effect of illumination of ferroelectrics, when only the increase in the carrier density was taken into account (the electronic spectrum was assumed to be invariable), the result was opposite: the transition temperature decreased. However, such an approach is valid only in the case of weak fields.

In strong fields, the renormalization of the interband electron–phonon interaction by an external field plays a decisive role. A strong field increases the density of correlated electron–hole pairs. Each pair has the dipole moment

$$\mathbf{d}_{12} = e\int \psi_1^* \mathbf{r} d\tau.$$

In a strong field, a coherent state of pairs is formed, which is similar to that formed in the ferroelectric phase due to the interband electron–phonon interaction. Due to the coherence, a macroscopic dipole moment arises in the electron subsystem; i.e., an additional polarization occurs in the electron subsystem, along with that arising in a ferroelectric crystal due to the interband interaction between electrons and polar transverse lattice vibrations.

Some of these effects were observed in [4, 5], where the permittivity of a crystal ε was measured in a laser field. In these experiments, the main difficulty was that the permittivity had to be measured in a short time interval, shorter than the laser-pulse duration (pulses with a duration of 5 μs were used; now these measurements can be easily reproduced with pulse durations shorter than a nanosecond). It was demonstrated in [5] how this was done and how the analysis of the complex shape of the response made it possible to reliably distinguish three components: the result of heating, the result of the change in the carrier density, and the effect of the strong field itself. The separation was possible because the corresponding relaxation times differed from each other by several orders of magnitude. Only the zero-lag component of ε, which depends nonlinearly on intensity at power fluxes exceeding 1 MW/mm^2, is related to the issue under consideration. The appearance of this component represents a new photoferroelectric effect significantly exceeding in magnitude those described above. The selection of this component led to good agreement with the above considerations.

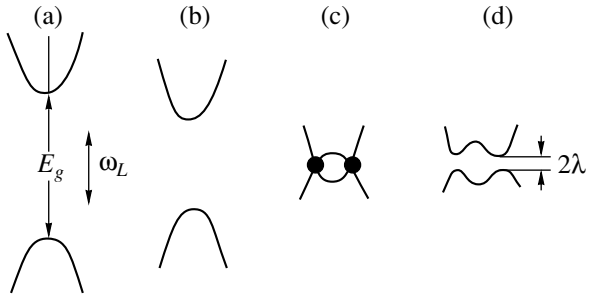

Fig. 1. (a) Initial electronic spectrum and its reconstruction in an intense light field of frequency ω_L ((b) $\omega_L < E_g$; (c, d) $\omega_L > E_g$).

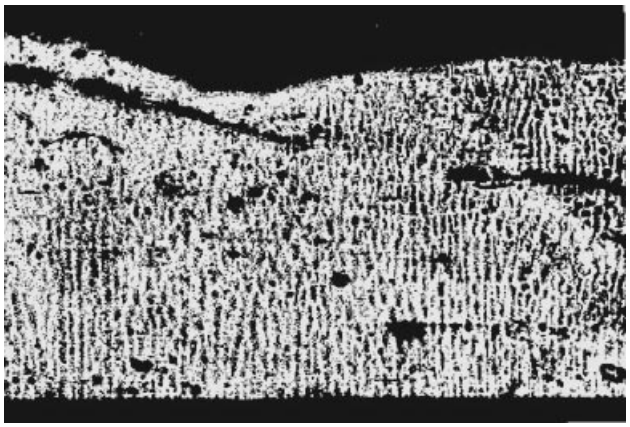

Fig. 2. Instability of a spatially homogeneous state of a ferroelectric in a powerful electromagnetic wave. The photograph shows a SbSI crystal illuminated by a laser pulse [6]. The period of the observed structure in a field with an amplitude of about 10^5 V/cm is close to 8 μm.

2.2. Decomposition into Spatially Inhomogeneous Structures

Formation of spatial structures with a period of about a few micrometers was observed in a ferroelectric in the field of a powerful electromagnetic wave (under specific experimental conditions). Figure 2 shows the corresponding photograph from [6].

It was shown by Girshberg, Trunov, and us that ferroelectric crystals indeed become unstable with respect to the decomposition of a homogeneous phase into spatially inhomogeneous structures; thus, the homogeneous state of the ferroelectric phase becomes impossible.

The theory of the effect was developed in [4]. The occurrence of a spontaneous polarization results in the nonzero order parameter Φ_0, which describes the reconstruction of the electronic spectrum. In an external field, the parameter Φ_0 and the electron density in the upper band are related by a nonlinear equation; notably, Φ_0 decreases as the electron density increases. The local decrease in Φ_0 gives rise to a potential well for electrons, which leads to a local increase in their

density. This increase gives rise to further decrease in Φ_0 and so on. A dynamic instability is developed in the system, which leads to appearance of regions with $\Phi_0 = 0$ (paraelectric phase) and high nonequilibrium-electron density. Depending on the relationship between the parameters, the size of these regions is determined by the diffusion or correlation length, and a periodic structure with a relevant period arises in the system. This process can be described by the effective negative diffusivity.

It should be noted that similar, but somewhat different, layering was also observed previously under weak illumination of photoconductive ferroelectric SbSI [7]. In the immediate vicinity of the phase transition, layering of the ferroelectric into regions of paraelectric phase and ferroelectric phase occurred. The temperature interval in which this phenomenon was observed did not exceed 1.5–2 K, and the period of the structure amounted to a few tenths of a millimeter. The above effect was attributed to the decrease in the transition temperature with increasing excited-carrier density, due to which paraelectric phase layers arose in the ferroelectric phase. In a strong electromagnetic field, the effect is qualitatively different: the proximity to the phase transition is of no importance in this case. The transition temperature increases in strong fields.

The above process can be considered as a case of ordering in an open thermodynamically strongly nonequilibrium system, since all the necessary conditions are satisfied (a high-density energy flux is passed through a crystal and the system is nonlinear and rather complex [8]). The structure formed radically differs from domain structures, which are known for ferroelectrics in states close to equilibrium.

3. FERROELECTRICS IN NONLINEAR OPTICS. NEW ASPECTS

Second-harmonic generation (SHG) is widely used for investigating the properties of ferroelectric crystals: nonlinear susceptibility, polarization states, various structures (see, for example, [9]), and so on. This method is also a promising candidate for studying structures that arise in ferroelectrics in strong fields.

3.1. Phase Matching upon Generation of Secondary Waves

Passing through a crystal, pumping waves of frequency ω generate secondary waves (for example, of frequency 2ω) at different points of the crystal. The frequency conversion is efficient only in the case of phase matching of the secondary waves (in other words, when the law of conservation of momentum for photons is satisfied). However, this situation cannot be realized in almost all cases due to the dispersion. Therefore, special measures should be taken to ensure the phase matching.

Different techniques are used to match phases: natural matching (due to the difference in the refractive indices for ordinary and extraordinary rays), matching that occurs when operating frequencies lie in the anomalous-dispersion region, the use of periodic structures (scattering from such structures leads to changes in the phase and, hence, the momentum), and so on. The method of periodic structures was first proposed by Miller [10]. This method is based on the compensation of the phase mismatch by introducing into a crystal a periodic structure with corresponding spatial frequency

$$\mathbf{q} = \mathbf{k}_{2\omega} - 2\mathbf{k}_{\omega}, \quad q = 2\pi/\Lambda, \tag{1}$$

where Λ is the space period. Such structures are formed artificially either by growing layered crystals or by using periodically spaced electrodes under voltage [11].

The required periodic structure can also be obtained by interference of light beams from external sources due to the photorefractive effect.

3.2. Matching by a Domain Structure

A weak SHG is observed in $BaTiO_3$ and $PbTiO_3$ crystals, which have no direction of natural matching. A small-domain periodic structure can to used for matching in ferroelectrics [1].

It was shown in [12] how a relatively strong SHG occurs in Fe-doped $BaTiO_3$ crystals due to a structure with 90° walls. Figure 3 shows the dependence of the second-harmonic intensity $I_{2\omega}$ on the angle φ, which was obtained by scanning with a moving detector. In all the cases, the radiation pattern contained two maxima located at angles of $(7° \pm 1°)$ in $BaTiO_3$ and $(10° \pm 1°)$ in $PbTiO_3$ to the direction of the incident radiation $\mathbf{k}_{\omega}$.

Naturally, the exact correspondence between the spatial frequency of a domain structure, which is required by relation (1), to the frequency q is unlikely. Indeed, when weak continuous radiation of frequency 2ω is scattered by these crystals (i.e., without the conversion $\omega \longrightarrow 2\omega$), a virtually continuous band can be observed on a screen which contains no maxima at angles in the range 5°–10° (sometimes, separate lines can be seen against a continuous background, but, as rule, the spatial frequency of these lines does not correspond to q). In the case of SHG from a relatively wide spectrum of q_{dom}, only the necessary harmonic is used; i.e., the *spatial-frequency selection* is performed.

3.3. Generation in the Absence of Stationary Matching Structures

3.3.1. Experimental data. However, it is well known that, even in the absence of matching structures, a weak SHG is observed in the directions not coinciding with the direction of natural matching, for example, in $LiNbO_3$ crystals. SHG is observed even in materials where the direction of natural matching is completely absent, for example, in $BaTiO_3$ or $PbTiO_3$ crystals.

Generally, this phenomenon is attributed to either the spurious scattering or the generation in a layer near the output surface with thickness equal to the coherent length. Let us consider the specific features of this radiation.

First of all, in the experiments with observation of generation in the directions ±φ (Fig. 3), beginning with some values of the pumping intensity I_ω, a generation *forward* occurs (φ = 0, "the central peak"). Two peaks are observed for $BaTiO_3$ and $PbTiO_3$ crystals due to the matching at 90° walls (see Section 3.2). In this case, the ratio between the values of $I_{2\omega}$ in the lateral peaks (or in one lateral peak) and in the center changes with increasing pumping intensity in favor of the central peak. The values of $I_{2\omega}$ in the lateral peaks increase proportionally to I_ω^2, as it should be upon SHG. However, the intensity of the central peak increases differently. At low I_ω^2, up to some threshold value *I*th, generation is absent: $I_{2\omega}$ = 0 (Fig. 4). Then, with an increase in I_ω^2, $I_{2\omega}$ begins to increase faster than I_ω^2. Further increase in $I_{2\omega}$ gives rise to an approximately linear dependence of $I_{2\omega}$ on I_ω^2.

As rule, oscillations are observed in this portion of the curve. The slope of the dependence $I_{2\omega}(I_\omega^2)$ periodically changes. The amplitude of these oscillations noticeably exceeds the spread due to measurement errors and instability of generation (Fig. 4). It is also noteworthy that, in the case of $LiNbO_3$ crystals, oscillations are more pronounced for Fe-doped crystals than for nominally pure samples. Generally, $BaTiO_3$ and $PbTiO_3$ crystals contain impurities, and oscillations are almost always observed for these crystals.

The amplitude $I_{2\omega}$ of the central peak observed for $BaTiO_3$ and $PbTiO_3$ increases not only with increasing pumping-wave intensity I_ω but also with increasing duration of the radiation action, which can be clearly seen from the dependence of $I_{2\omega}$ on pumping-pulse repetition frequency [13]. If the repetition frequency is sufficiently low, the generated second harmonic relaxes to zero after each pulse. If the pulse repetition period *T* is short, the effect of each current pulse is summarized with the effect of the previous pulse. As a result, the dependence of the SHG on the on–off time ratio of pumping pulses is observed. It was shown that the relaxation time of SHG in barium titanate is about 0.5 s.

3.3.2. Self-matching model. The SHG in the forward direction would be possible if a structure with collinear wave vector existed in a crystal, i.e., if there were layers parallel to the surface. However, no such structures (domain or some other) are observed in the crystals under consideration. It was suggested in [12–14] that such structures arise automatically under the action of intense energy fluxes.

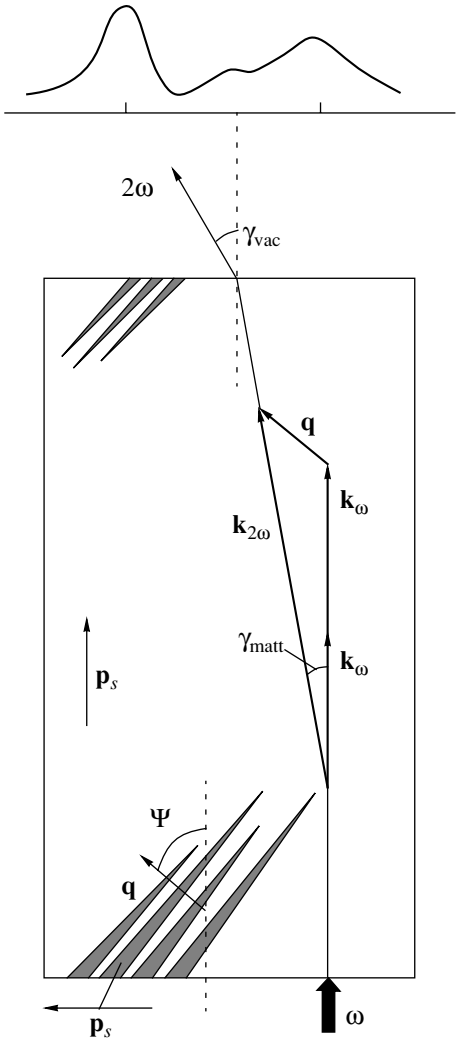

Fig. 3. Angular distribution of $I_{2\omega}$ as a result of participation of the domain structure in the matching of secondary waves under generation of the second harmonic.

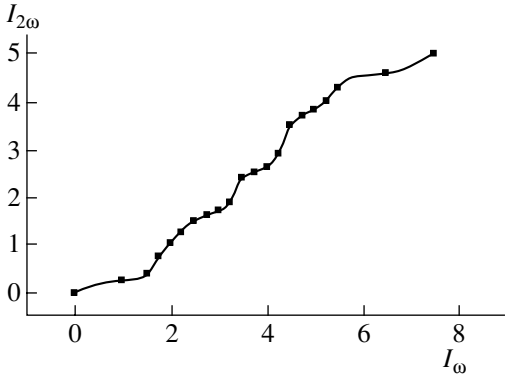

Fig. 4. Experimental dependence of the second-harmonic intensity on the squared intensity of the pumping wave in a $BaTiO_3$ crystal with high concentration of Fe impurity (the field pulsations).

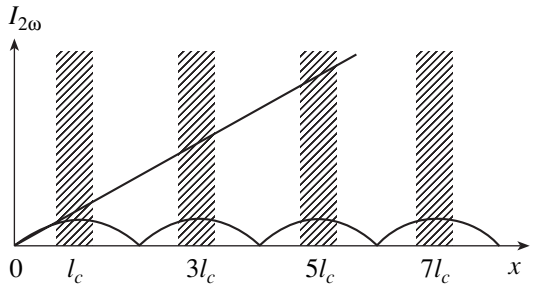

Fig. 5. Distribution of the second-harmonic intensity along an irradiated crystal and the formation of layers due to the initial instability and the dependence $\chi^{(2)}(I_{2\omega})$.

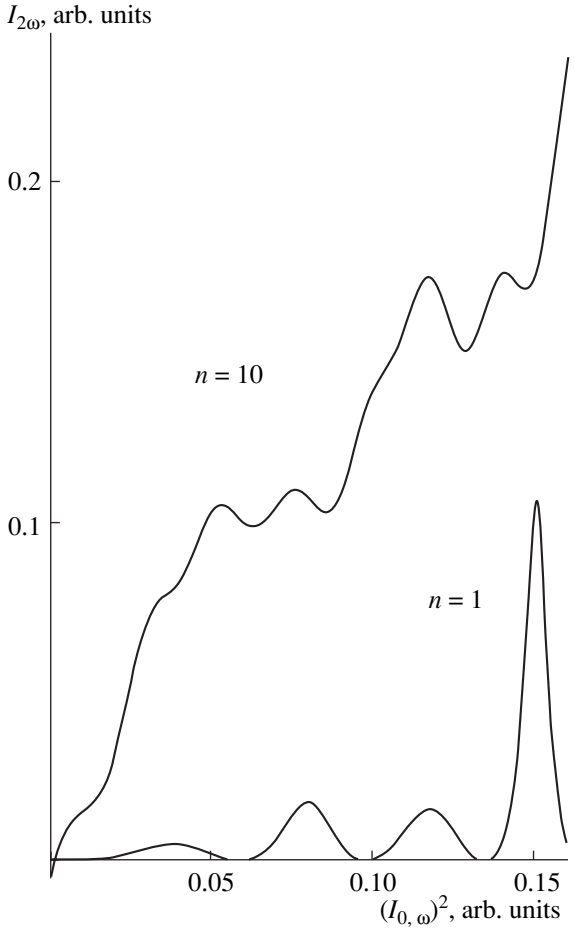

Fig. 6. Theoretical dependence $I_{2\omega}(I_\omega^2)$ in the case of irradiation by single pulses (n = 1) and by a set of ten pulses, with regard to the storage of the effect of the previous pulse during each current pulse (n = 10).

It was mentioned in Section 2.2 that a ferroelectric crystal in the field of a strong electromagnetic wave is unstable with respect to self-organization, which consists of the formation of periodic spatial structures. It is reasonable to use this circumstance in constructing a model for the case under consideration. We have to assume that the period of arising structures is set by the generation conditions. The corresponding mechanism can be derived by taking into account the fact that a ferroelectric has a maximum nonlinearity (including the optical-frequency range) near a phase transition. The magnitude of the field affects not only the refractive index but also the nonlinear optical coefficients. Let us assume $\chi^{(2)}$ to be dependent on the wave intensity $I_{2\omega}$. By analogy with the well-known photorefractive effect, where the refractive index (or $\chi^{(1)}$) depends on intensity, the change in $\chi^{(2)}$ in a powerful light wave can be called the second-order photorefractive effect.

In the absence of natural phase matching, the generated-wave strength obtained by summing all the waves 2ω excited at all points in the interval from 0 to x, is equal to

$$E_{2\omega} \sim e^{ik_{2\omega}x}\int_0^x \chi^{(2)} I_\omega e^{-iqx}dx = \chi^{(2)} I_\omega (e^{ik_{2\omega}x} - e^{i(k_{2\omega}-q)x})/iq, \quad (2)$$

where q is the wave mismatch (1) and I_ω is the pumping intensity at the crystal input. Thus, due to integration, the field of the second harmonic in a medium is a superposition of two space modes with the wave vectors $k_{2\omega}$ and $k_{2\omega} - q$. As a result, the spatial distribution $I_{2\omega}(x)$ with a period of $\Lambda = 2\pi/q$ (Fig. 5) along the wave path can be written as

$$I_{2\omega} = E_{2\omega}E_{2\omega}^* \approx \frac{4}{q^2}\sin^2\frac{qx}{2}. \quad (3)$$

Specifically such a structure is required for matching all the waves 2ω generated at different points. Thus, the conditions for formation of a structure due to the periodic acceleration of the second harmonic $I_{2\omega}$ coincide with the conditions necessary for quasi-matching. The hatched layers in Fig. 5 have a space period of $\Lambda = 2l_c$ (specifically the one required to compensate the mismatch between $k_{2\omega}$ and $2k_\omega$).

The variation in $\chi^{(2)}$ is very small, but the process is enhanced by the aforementioned instability (see the beginning of this section); thus, a weak modulation of $\chi^{(2)}$ plays only the role of a "trigger."

Thus, a strong wave of frequency 2ω makes its propagation in a ferroelectric crystal with strong nonlinearity easier by forming the relief $\chi^{(2)}(x)$ in the crystal.

However, this process requires more careful consideration. The increase in the amplitude $E_{2\omega}$ in the rising portion of the dependence $I_{2\omega}(x)$ near $x = l_c$ stops due to the phase shift. However, $\chi^{(2)}$ increases simultaneously, making $\partial E_{2\omega}/\partial x$ increase and, thus, shifting the maximum to larger x. As a result, the coherent length increases, and the maximum value of $I_{2\omega}$ increases as well.

In the simplest two-wave approximation similar to (2) (neglecting the waves with wave vectors close to $k_{2\omega} - q$ and so on), we can derive the field of the second harmonic as a superposition of two waves with the wave vectors $k_{2\omega} - Q$ and $k_{2\omega} - q$ in the form

$$E_{2\omega} = \frac{I_\omega}{2\pi\sqrt{I_s}} A(e^{i(k_{2\omega}-Q)x} - e^{i(k_{2\omega}-q)x}). \quad (4)$$

Here, $I_s = (4\pi\omega^2\Lambda\chi_0^2/(k_\omega c^2))^{-2}$. The shift of the wave vector Q accounts for the fact that now $\chi^{(2)}$ depends on $I_{2\omega}$, and the wave propagates in a medium whose nonlinearity is governed by the generated harmonic itself.

The gain of the amplitude A and the shift of the wave vector Q at relatively low pumping intensities are given by the expressions

$$A = 1 + \frac{2\alpha}{I_s}\left(\frac{I_\omega}{\pi}\right)^2, \quad Q = q\frac{\alpha}{I_s}\left(\frac{I_\omega}{\pi}\right)^2, \quad (5)$$

where $\alpha \equiv \chi_0^{(4)}/\chi_0^{(2)}$ determines the dependence of $\chi^{(2)}$ on $I_{2\omega}$. Then, from (4) we obtain

$$I_{2\omega}(x) = E_{2\omega}E_{2\omega}^* = \left(\frac{I_\omega}{\pi}\right)\frac{1}{I_s}A^2\sin^2((q-Q)x/2). \quad (6)$$

Thus, due to the dependence of $\chi^{(2)}$ on $I_{2\omega}$, the second harmonic is amplified by a factor of A^2. The space period increases simultaneously:

$$\Lambda^* = \Lambda/(1 - Q/q). \quad (7)$$

The amplification of the second harmonic is obtained due to both the increase in $\chi^{(2)}$ and the increase in the period of coherence (the parametric amplification). This circumstance makes it possible to significantly improve the conditions of SHG.

The profile of the field in a medium remains periodic, but the space period now depends on the field intensity. As a result, the dependence of generation of the field $I_{2\omega}$ at the sample end on the pumping field I_ω should exhibit pulsations which are somewhat similar to the Maker fringes but are different in origin: they arise due to the dependence of the coherent length on intensity rather than the tilt of the sample, and, hence, the alternate coincidence of the path length with the sum of either an even or odd number of fixed coherent lengths. Such pulsations could be referred to as the field pulsations. Apparently, the oscillations observed in the experimental dependences $I_{2\omega}(I_\omega)$ are related to field pulsations.

It should be noted that the increase in $I_{2\omega}(x)$ is limited. Unlike the case of artificial structures, the self-matching cannot lead to complete matching because it is due to the spatial dependence of $I_{2\omega}$ on x. If this dependence changes, the induced structure changes as well. With such a feedback, a steady increase in $I_{2\omega}(x)$ can never be attained since there would be no grounds to induce the required structure. As is well known, a feedback never leads to exact matching.

Nevertheless, let us remember that the mechanism under consideration only provokes a certain space period when a system undergoes an abrupt transition from a uniform unstable state to a more stable periodically inhomogeneous state. We may suggest that the threshold observed in the curve $I_{2\omega}(I_\omega)$ corresponds just to the instant of abrupt transition.

It is possible that the ability of a system to store the relief specified initially plays a significant role in this case, which is confirmed by the dependence of this phenomenon on the on–off time ratio for laser pulses and the found influence of impurities. After a few pulses, the second-harmonic field in a medium becomes a superposition of many space modes with different wave vectors, which deforms the spatial profile of the second-harmonic intensity. Indeed, in accordance with the calculations, flatter portions arise in the dependence $I_{2\omega}(I_\omega)$ (Fig. 6). For analysis of the correspondence between the theoretical and experimental results, we flattened the curves to eliminate the effect of the experimental factors: unevenness of faces, possible reflections from them, and so on.

As a result of storing the relief, the SHG efficiency significantly increases. Thus, account for the storage of the induced structure allows us to obtain better agreement between the theoretical and experimental data.

4. CONCLUSIONS

The efficiency of frequency conversion in arbitrary directions in the crystals under investigation, obtained in this stage, is very low (does not exceed 1%). The generated light can be easily detected and its features can be studied; however, this effect is still of no practical importance (except that it may be used in estimating scattering losses). However, we believe that some materials can be found in which matching by self-organizing structures may be useful.

The fact that *a self-organizing structure is observed* is of interest itself. In addition, the possibility of estimating high-order optical susceptibilities may be of interest.

The analysis performed shows that the study of ferroelectric phenomena in strongly nonequilibrium conditions, in particular, when a high-power flux of electromagnetic energy passes through a crystal, may become one of the most promising lines of investigation in physics of ferroelectrics in the near future. The conventional approach (the thermodynamic theory of closed systems) should be significantly expanded.

We believe that the analysis of nonlinear optical phenomena (the high-order photorefractive effects, the induced spatial self-organizing structures, and so on) will be the dominant method in studying ferroelectrics in strong electromagnetic fields.

ACKNOWLEDGMENTS

This study was supported by the Russian Foundation for Basic Research, project no. 00-02-16735, and the Ministry of Education of the Russian Federation.

REFERENCES

1. M. Lines and A. Glass, *Principles and Applications of Ferroelectrics and Related Materials* (Oxford Univ. Press, Oxford, 1977; Mir, Moscow, 1981).
2. É. V. Bursian, Ya. G. Girshberg, and N. N. Trunov, Izv. Vyssh. Uchebn. Zaved. Fiz., No. 8, 94 (1981).
3. É. V. Bursian, Ya. G. Girshberg, and N. N. Trunov, Zh. Éksp. Teor. Fiz. **82** (4), 1170 (1982) [Sov. Phys. JETP **55**, 681 (1982)].
4. É. V. Bursian and Ya. G. Girshberg, *Coherent Effects in Ferroelectrics* (Prometeĭ, Moscow, 1989).
5. É. V. Bursian, V. V. Maslov, Ya. G. Girshberg, and S. V. Baryshnikov, Fiz. Tverd. Tela (Leningrad) **25** (3), 751 (1983) [Sov. Phys. Solid State **25**, 429 (1983)].
6. S. V. Baryshnikov, É. V. Bursian, Ya. G. Girshberg, *et al.*, Fiz. Tverd. Tela (Leningrad) **26** (6), 1872 (1984) [Sov. Phys. Solid State **26**, 1135 (1984)].
7. V. M. Fridkin, *Photoferroelectrics* (Nauka, Moscow, 1976; Springer, Berlin, 1979).
8. H. Haken, *Advanced Synergetics: Instability Hierarchies of Self-Organizing Systems and Devices* (Springer, New York, 1983; Mir, Moscow, 1985).
9. N. E. Sherstyuk, V. V. Lemanov, A. S. Sigov, *et al.*, Phys. Rev. Lett. **85** (17), 3664 (2000).
10. R. C. Miller, Phys. Rev. Sect. A **134** (5), 1313 (1964).
11. Z. W. Liu, Y. Du, J. Liao, *et al.*, J. Opt. Soc. Am. B **19**, 1676 (2002).
12. É. V. Bursian and V. V. Rychgorskiĭ, Izv. Ross. Akad. Nauk, Ser. Fiz. **64** (6), 1129 (2000).
13. É. V. Bursian and V. V. Rychgorskiĭ, Fiz. Tverd. Tela (St. Petersburg) **43** (1), 108 (2001) [Phys. Solid State **43**, 110 (2001)].
14. Y. R. Shen, *The Principles of Nonlinear Optics* (Wiley, New York, 1984; Nauka, Moscow, 1989).

Translated by Yu. Sin'kov

Crystallography Reports, Vol. 49, No. 1, 2004, pp. 53–59. Translated from Kristallografiya, Vol. 49, No. 1, 2004, pp. 58–64.

STRUCTURE OF INORGANIC COMPOUNDS

Dedicated to the 80th Birthday of L.A. Shuvalov

Growth and Structure of $La_3Zr_{0.5}Ga_5Si_{0.5}O_{14}$ Crystals

A. A. Pugacheva*, B. A. Maksimov, B. V. Mill'*, Yu. V. Pisarevskiĭ**, D. F. Kondakov**, T. S. Chernaya**, I. A. Verin**, V. N. Molchanov**, and V. I. Simonov****

** Physics Faculty, Moscow State University, Vorob'evy gory, Moscow, 119992 Russia*

*** Shubnikov Institute of Crystallography, Russian Academy of Sciences, Leninskiĭ pr. 59, Moscow, 119333 Russia*

e-mail: maximov@ns.crys.ru

Received July 2, 2003

Abstract—The complete X-ray structure determination of Czochralski grown $La_3Zr_{0.5}Ga_5Si_{0.5}O_{14}$ single crystals with the $Ca_3Ga_2Ge_4O_{14}$ structure is performed (sp. gr. $P321$, $a = 8.226(1)$ Å, $c = 5.1374(6)$ Å, $Z = 1$, Mo K_{α_1} radiation, 1920 crystallographically independent reflections, $R = 0.0166$, $R_w = 0.0192$). The absolute structure is determined. It is shown that possible transition of some of La atoms (~1.2%) from the 3*e* to 6*g* position may give rise to the formation of structural defects. © *2004 MAIK "Nauka/Interperiodica".*

INTRODUCTION

Single crystals of complex oxides with the $Ca_3Ga_2Ge_4O_{14}$ structure (sp. gr. $P321$) and, in particular, of $La_3Ga_5SiO_{14}$ (langasite), $La_3Nb_{0.5}Ga_{5.5}O_{14}$, and $La_3Ta_{0.5}Ga_{5.5}O_{14}$, attract particular interest as promising piezoelectrics that can be used in high-temperature sensors and devices based on surface and bulk acoustic waves. These crystals are characterized by rather high electromechanical characteristics, temperature stability, and low acoustic losses. Large $La_3Ga_5SiO_{14}$, $La_3Nb_{0.5}Ga_{5.5}O_{14}$, and $La_3Ta_{0.5}Ga_{5.5}O_{14}$ crystals are grown by the traditional Czochralski method [1].

At present, about 140 compounds with the $Ca_3Ga_2Ge_4O_{14}$ structure are known, some of which are phases of variable composition [1–3]. Some of these compounds melt congruently; about 15 compounds are grown as single crystals by the Czochralski method; 15 more reported compounds are langasite-based solid solutions with partial or complete replacement of cations [1, 4].

The electroacoustic properties of the $La_3Ga_5SiO_{14}$, $La_3Nb_{0.5}Ga_{5.5}O_{14}$, and $La_3Ta_{0.5}Ga_{5.5}O_{14}$ crystals are studied in sufficient detail, but the analogous characteristics of other crystals obtained in various laboratories are often inconsistent. The corresponding values for solid solutions are often considerably lower than could be expected. This is explained by the insufficiently high quality of the crystals studied and the systematic measurement errors. At the same time, the study of electroacoustic properties of solid solutions allows one to control their properties by varying their compositions.

The present study is aimed at the refinement of the structural parameters of $La_3Zr_{0.5}Ga_5Si_{0.5}O_{14}$ (LZGS) crystals, determination of their absolute structure, specific features of their electron density, atomic thermal vibrations, and cation distribution over the structure positions.

GROWTH OF $La_3Zr_{0.5}Ga_5Si_{0.5}O_{14}$ CRYSTALS

Unlike $La_3ZrGa_5O_{14}$, $La_3Ga_5SiO_{14}$, and $La_3Ta_{0.5}Ga_{5.5}O_{14}$, the $La_3Nb_{0.5}Ga_{5.5}O_{14}$ compound melts incongruently, and crystals of this compound cannot be grown by the Czochralski method. However, one can expect the incorporation of a noticeable amount of Zr into the solid-solution crystals. The preliminary study of melting and crystallization of the solid solution of the 1 : 1 composition in the $La_3ZrGa_5O_{14}$–$La_3Ga_5SiO_{14}$ system demonstrated the congruent character of its melting and showed that the melting points of the solid solution and $La_3Ga_5SiO_{14}$ differ by no more than ~5°C. This allowed us to grow single crystals from the melt of the $La_3Zr_{0.5}Ga_5Si_{0.5}O_{14}$ composition by the Czochralski method; the single crystals were up to 28 mm in "diameter" and about 80 mm in length (the boule portion having a constant diameter). Crystals were grown in platinum crucibles with a diameter of 45 mm (300 g of the melt) along the ⟨0001⟩ directions, the pulling rate was 2 mm/h, and the rotation velocity ranged from 30 to 40 rpm. The crystals had no inclusions.

Electron-probe microanalysis of a single crystal of the nominal composition $La_3Zr_{0.5}Ga_5Si_{0.5}O_{14}$ (the frac-

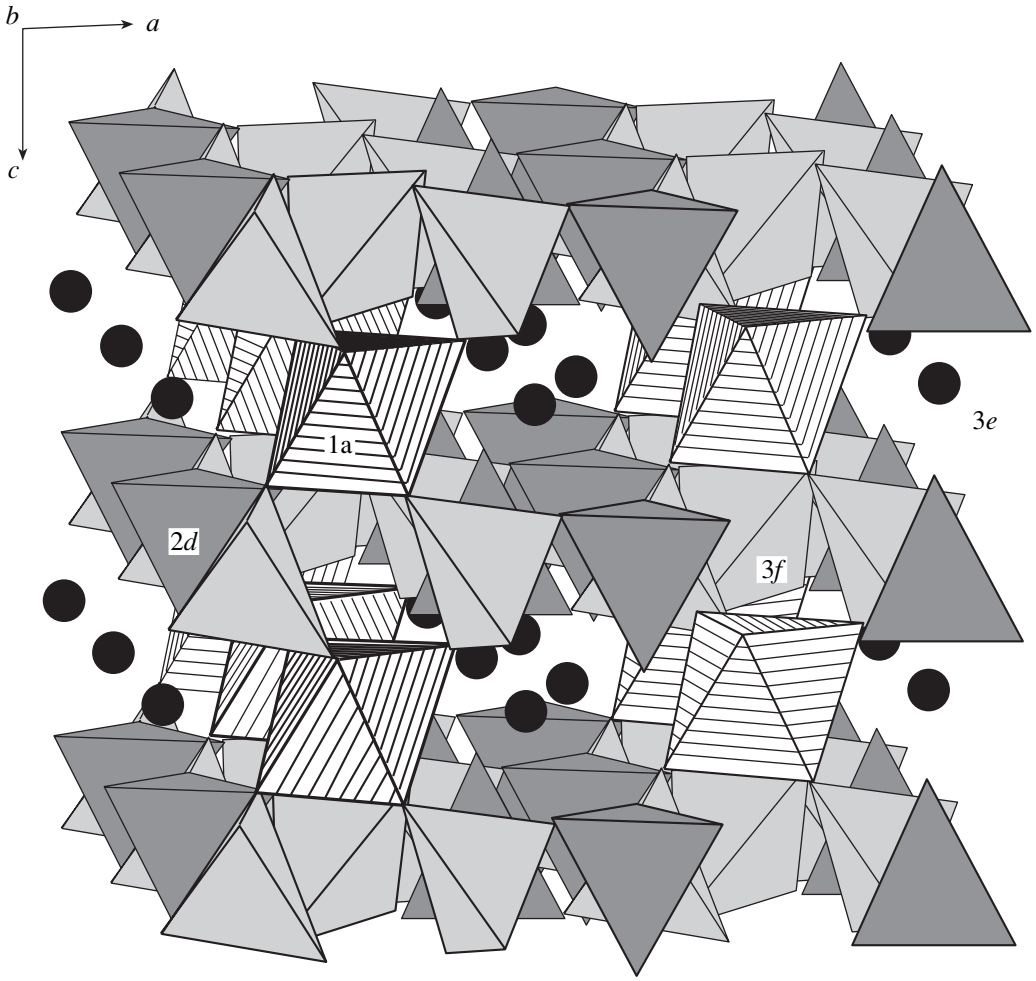

Fig. 1. $La_3Zr_{0.5}Ga_5Si_{0.5}O_{14}$ crystal structure; 3*e*, 1*a*, 3*f*, and 2*d* are the Wyckoff positions of cations.

tion of the crystallized melt amounted to 0.89) showed that the components were distributed homogeneously along the boule length, with the average composition, $La_{3.03(2)}Zr_{0.53(1)}Ga_{5.00(2)}Si_{0.44(1)}O_{13.99(1)}$, being somewhat different from the expected composition (the numerals in brackets indicate the scatter in component concentration along the boule length; the error of the chemical analysis is somewhat higher). The lattice parameters were constant along the whole boule length, a = 8.221(1) Å, c = 5.134(1) Å, and were practically the same as the values of the crystallized residual mother liquor [a = 8.222(1) Å, c = 5.134(1) Å]. The X-ray diffraction pattern of the latter had weak lines of impurity phases formed because of different compositions of the crystal and the initial melt.

CRYSTAL STRUCTURE

The crystal structure of the $Ca_3Ga_2Ge_4O_{14}$ type can be described as a mixed framework of two types of oxygen tetrahedra—small 2*d* tetrahedra (position symmetry 3), larger 3*f* tetrahedra (position symmetry 2), and 1*a* octahedra (position symmetry 32). The framework voids lying at the same *z* level as the cations in octahedra are occupied by the largest cations located in the 3*e* position (symmetry 2) (Fig. 1). The coordination polyhedron of large cations (Na^+, Ca^{2+}, Sr^{2+}, Ba^{2+}, Pb^{2+}, and Ln^{3+}) has eight oxygen vertices and can be represented as a dodecahedron with triangular faces. Depending on the chemical composition, the cationic positions can be filled either orderly or by mixed cations; most of the compounds have a disordered structure, with the corresponding positions being filled with mixed cations. Proceeding from the main crystallochemical criteria, it was natural to assume that the La^{3+} ions in $La_3Zr_{0.5}Ga_5Si_{0.5}O_{14}$ would occupy the 3*e* positions; the Zr^{4+} ions and some Ga^{3+} ions, the 1*a* position; and the remaining Ga^{3+} and Si^{4+} ions would be distributed over the 2*d* and 3*f* positions with the smaller Si^{4+} ions having the propensity to filling the 2*d* positions.

Table 1. Characteristics of experiment and crystallographic data for an LZGS sample

Composition	$La_3Zr_{0.5}Ga_5Si_{0.5}O_{14}$
Diffractometer	NONIUS CAD 4F
Radiation	MoK_α, λ = 0.7107 Å
Monochromator	Pyrolytic graphite
Scanning method	ω/2θ
Range of *hkl* variation	$-17 < h, k < 17, -10 < l < 10$
Sp. gr.	*P*321
a, Å	8.226(1)
c, Å	5.1374(6)
V, Å^3	301(1)
ρ_{calcd}, g/cm^3	5.784
Crystal radius, mm	0.14
μ_{Mo}, mm^{-1}	21.935
max sinθ/λ, Å^{-1}	1.04
Number of reflections measured	12440
Rejection criterion	$I > 1.43\sigma(I)$
R_{av}, %	3.02
Number of crystallographically independent reflections	1920
Weighting scheme	$1/(\sigma F)^2$
Flack parameter	0.02
R/R_w, %	1.66/1.92

DIFFRACTION EXPERIMENT

The lattice parameters were refined by the LS method using 25 reflections in the angular range 2θ = 27°–32° and the SET4 procedure, which allowed us to choose the angular position of each reflection from four alternative positions and, thus, increased the accuracy of the parameter determination. The measurements were made within the complete sphere of the reciprocal space. The main characteristics of the crystal, the conditions of the X-ray diffraction experiment, the refinement procedures used, and the concluding values of the R/R_w factors are indicated in Table 1.

Analysis of the complete set of experimental data showed no deviations from the sp. gr. *P*321. The intensity measurements and all the subsequent crystallographic computations were performed in the fixed (in our case, right-hand) coordinate system. The absolute structure was established by comparing two possible refined modifications which differed as an image (the initial model) and its centrosymmetric reflection.

The computations were made using the JANA 98 [5] and Prometheus [6] crystallographic program packages. In the computations, the atomic scattering curves by neutral atoms were used with due regard for the dispersion corrections [7]. The correction for secondary extinction was introduced by the Becker–Coppens formalism. The minimum values of the reliability factors *R* were obtained based on the second-type extinction model at $r = 0.683 \times 10^{-4}$ Å with the Lorentzian distribution of mosaic blocks. At the concluding stage, thermal motion of all the atoms (except for the atoms in the additional La' position) were refined in the anisotropic harmonic approximation. The coordinates of the basic atoms, the effective values of thermal parameters, and the position occupancies are indicated in Table 2; the characteristics of the ellipsoids of thermal vibrations, in Table 3; and the interatomic distances, in Table 4.

STRUCTURE REFINEMENT AND STRUCTURE CHARACTERISTICS

At the first stage of structure refinement, we used the positional parameters of the $La_3Nb_{0.5}Ga_{5.5}O_{14}$ structure as the initial coordinates [8]. In the latter compound, the 1*a* position is "mixed" and is occupied by Ga^{3+} and Nb^{5+} ions in the ratio 1 : 1, whereas in the $La_3Zr_{0.5}Ga_5Si_{0.5}O_{14}$ compound, there are two mixed positions—1*a* and 2*d*. In the initial model, we placed 0.5 Zr + 0.5 Ga in the 1*a* position, 1.5 Ga + 0.5 Si, in the 2*d* position, and in 3 Ga atoms the 3*f* position. The refinement of this model in the isotropic approximation of atomic thermal vibrations yielded the reliability factors $R/R_w = 5.11/5.76\%$. The allowance for anisotropic

Table 2. Coordinates and effective parameters of atomic thermal vibrations of basic atoms in the LZGS structure

Wyckoff position; symmetry	Occupancy	*x*/*a*	*y*/*b*	*z*/*c*	B_{eff}, Å^2
3*e*; 2	0.988 La	0.42320(1)	0	0	0.80(1)
6*g*; 1	0.012 La'	0.418(4)	0.009(4)	0.139(4)	0.80(1)
1*a*; 32	0.5 Ga_1 + 0.5 Zr	0	0	0	0.85(1)
2*d*; 3	0.75 Ga_2 + 0.25 Si	1/3	2/3	0.5310(1)	0.71(1)
3*f*; 2	Ga_3	0.7606(2)	0	0.5	0.90(1)
2*d*; 3	O_1	1/3	2/3	0.188(3)	1.08(2)
6*g*; 1	O_2	0.462(1)	0.312(1)	0.311(2)	1.50(2)
6*g*; 1	O_3	0.146(1)	−0.080(4)	0.240(2)	1.62(2)

Table 3. Dimensions and orientations of ellipsoids of thermal vibrations of basic atoms in the LZGS structure

Atom and the point symmetry of its position	Semiaxis length, Å	Orientation of the ellipsoid of thermal vibrations, angles, deg		
		<(*ia*)	<(*ib*)	<(*ic*)
La	0.089	90.00	101.53	13.35
2	0.100	90.00	147.42	103.35
	0.112	0.02	120.00	90.00
(Zr, Ga_1)	0.085	90.00	90.00	0
32	0.112	150.00	90.00	90.00
	0.112	30.00	90.00	90.00
(Ga_2, Si)	0.089	90.00	90.00	0
3	0.097	149.99	90.01	90.00
	0.097	29.99	90.01	90.00
Ga_3	0.085	90.00	51.10	46.48
2	0.100	179.98	60.00	90.00
	0.130	90.00	126.61	43.52
O_1	0.094	41.57	78.43	90.00
3	0.094	41.57	78.43	90.00
	0.151	90.00	90.00	0
O_2	0.100	138.61	89.32	59.26
1	0.128	86.69	137.03	125.55
	0.173	48.80	132.96	50.72
O_3	0.076	95.40	117.63	36.67
1	0.100	9.97	129.95	90.66
	0.180	81.65	52.37	53.33

atomic thermal vibrations for all the atoms of the initial composition reduced the R/R_w value to (1.92/2.34)%. It is seen from Table 3 that the differences in the axes of the ellipsoids of thermal vibrations are the most important for Ga_3 and O atoms. For the La and (Ga_1, Zr) atoms, the anisotropy of thermal vibrations is less important, and the thermal motion of (Ga_2, Si) atoms is almost isotropic.

In order to verify the initial formula of the crystal, we refined the occupancies q of the positions with cations. The problem was solved using step-by-step scanning [9]. We assigned a number of fixed values to the parameters q of cations (with a step of 0.02) and refined all the other parameters. The anionic positions were assumed to be fully (100%) occupied. The results of these refinement procedures were used to construct the $R_w = f(q)$ dependences. Analysis of such dependences is often used in order to refine the chemical formulas of complex minerals. It was shown [10] that this analysis allows one to fix the q value corresponding to the function minimum and consider this value as the sought solution. In LZGS crystals, the allowance for thermal vibrations of atoms in both isotropic and anisotropic approximations showed a slight deficit (1.2%) in the 3*e* position occupied with La atoms and also slight deviation of the Zr : Si ratio from unity [(0.5 Zr, 0.5 Si) in the initial chemical formula], namely, 1.13 (0.53 Zr, 0.47 Si).

The existence of mixed cationic positions in the LZGS structure requires special attention to analysis of the residual electron density ($\Delta\rho$), establishment of the chemical formula, and refinement of the distribution of cations over the crystallographic positions at all the stages of the refinement. The specific features of $\Delta\rho$

Table 4. Main interatomic distances in the LZGS structure, Å

La polyhedron	(Ga_2, Si) tetrahedron	La'–O distances
La–$O_1 \times 2$ = 2.6373(5)	Ga_2–O_1 = 1.761(2)	–O_1 = 2.47(1)
$O_2 \times 2$ = 2.478(1)	$O_2 \times 3$ = 1.789(1)	–O_1^* = 2.97(1)
$O_2^* \times 2$ = 2.902(1)	$O_1 - O_2 \times 3$ = 3.027(2)	–O_2 = 2.08(1)
$O_3 \times 2$ = 2.376(1)	$O_2 - O_2^* \times 3$ = 2.771(2)	–O_2^* = 3.00(1)
(Zr, Ga_1) octahedron	Ga_3 tetrahedron	–O_2^* = 2.56(1)
Ga_1–$O_3 \times 6$ = 2.049(1)	Ga_3–$O_2 \times 2$ = 1.887(1)	–O_2^* = 3.35(1)
O_3–$O_3^* \times 6$ = 2.833(2)	$O_3 \times 2$ = 1.834(1)	–O_3 = 2.09(1)
$O_3^{**} \times 3$ = 2.720(1)	O_2–O_2^* = 2.887(2)	–O_3^* = 2.81(1)
$O_3^{***} \times 3$ = 3.227(1)	O_3–O_3^* = 3.385(1)	
	O_2–$O_3 \times 2$ = 2.879(2)	
	O_2–$O_3 \times 2$ = 3.000(1)	

* Atoms obtained from the basic atoms using the symmetry elements of the *P*321 group.

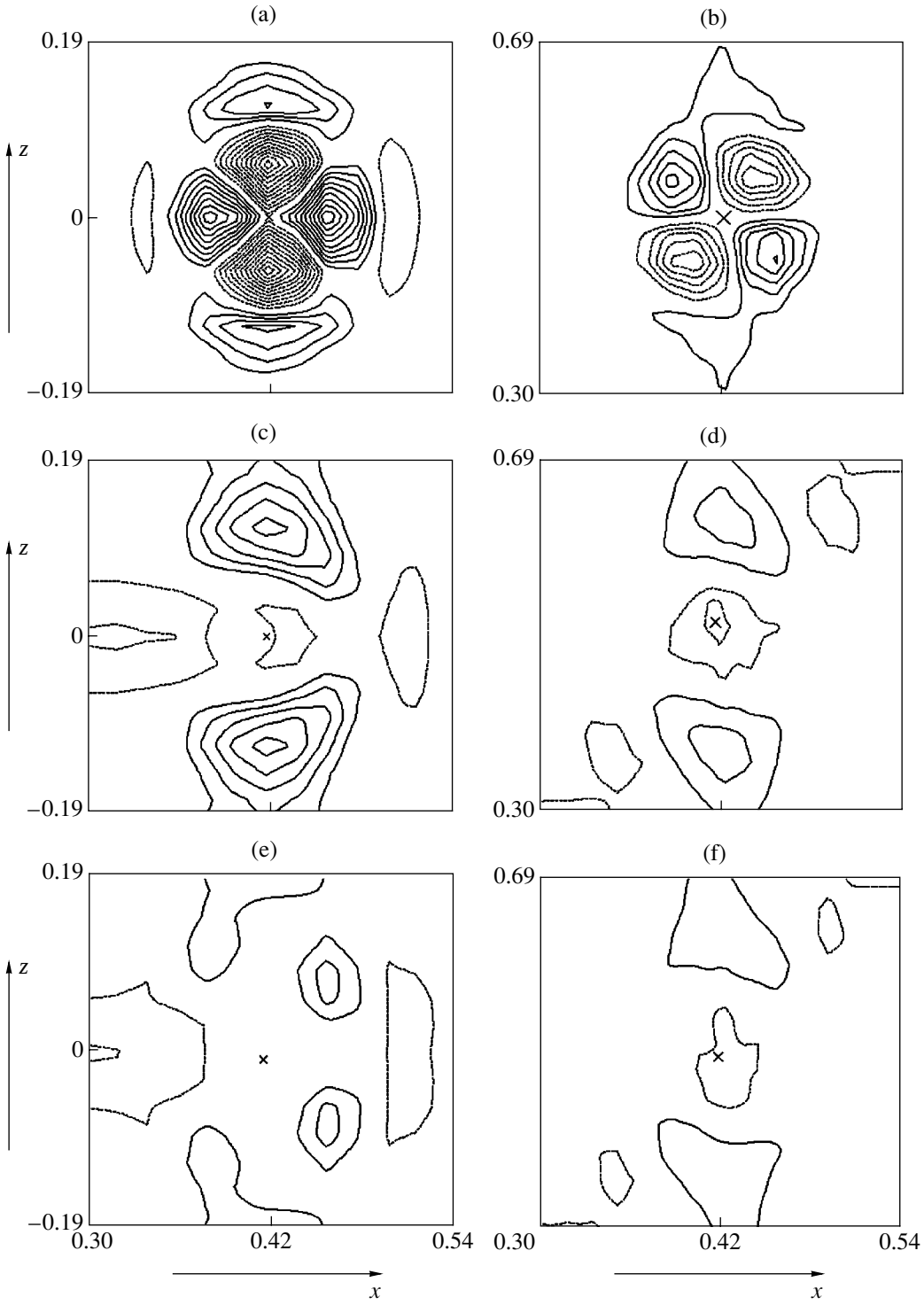

Fig. 2. (x, 0, z) and ($x - 2y = 0.760$, z) sections of $\Delta\rho(x, y, z)$ through the (a, c, e) basic La and (b, d, f) Ga_3 atoms constructed at different stages of the refinement of the LZGS structure. The cross indicates the position of the subtracted atom. The length of the section edge is 2 Å. Isolines are spaced by 1 e/Å^3 in Figs. 2c and 2b, 0.7 e/Å^3 in Figs. 2c and 2d, and 0.25 e/Å^3 in Figs. 2e and 2f.

characteristic of anisotropic thermal vibrations of atoms and possible structural disorder of cations are clearly seen in the vicinity of the positions of La and Ga_3 atoms.

With allowance for the atomic thermal vibrations in the harmonic isotropic approximation, the $\Delta\rho$ values in the vicinity of the basic La and Ga_3 atoms considerably exceeded the background values in the $x0z$ and $x - 2y =$

0.760*z* sections. Figures 2a and 2b clearly show that, in these planes, the maxima of the positive electron density and the minima of the negative electron density are located at distances of about 0.3 Å from the subtracted La and Ga_3 atoms, with the extremum values reaching 8 e/Å^3. It is natural to assume that the Δρ distributions shown in Figs. 2a and 2b can be explained by strong anisotropy of harmonic thermal vibrations of La and Ga_3 atoms in the planes perpendicular to twofold axes along which these atoms are located. The allowance for anisotropy of thermal vibrations of these atoms in the harmonic approximation results in disappearance of the residual electron-density maxima around these atoms (Figs. 2c, 2d) and a considerable decrease in R/R_w value (according to the Hamilton criterion)—from (5.11/5.76) down to (2.63/3.23)%. The allowance for the anisotropy of thermal vibrations of all the cations decreases the R/R_w value to (2.31/2.19)%, whereas the allowance for anisotropic thermal vibrations of anions reduces this ratio even more, R/R_w = (1.80/2.02)%. The dimensions and orientations of the axes of the ellipsoids of thermal vibrations indicated in Table 3 are consistent with the specific characteristics of Δρ in the vicinity of each atom with due regard for their thermal motion in the isotropic approximation.

The second characteristic feature of the Δρ distributions shown in Fig. 2 is the presence of positive maxima with values up to 3.5 e/Å^3 at distances of about 0.7 Å above and below the subtracted La atoms along the [001] direction. The values and spread of these maxima remain practically constant in the transition from the isotropic to anisotropic thermal motion of atoms. Taking into account the small deficit in La atoms in the 3*e* position observed in the refinement of the occupancies *q* of crystallographic positions, we identified one of these maxima with the additional 6*g* position with the coordinates (0.423, 0, 0.138) for La atoms. In the refinement of this structure model, we assumed that the unit cell contains three atoms per LZGS formula unit. The temperature motion of La' was taken into account in the isotropic approximation under the assumption of equal B_{iso}La' and B_{eq}La. The refined coordinates of the additional La' position are x = 0.423, y = 0.009, z = 0.143, B_{iso} = 0.83 Å^2, and q = 0.012. The allowance for the additional La' position reduced R/R_w to (1.66/1.92)% and considerably "purified" the Δρ distribution (Figs. 2d, 2f). The syntheses showed no considerable deviations from the background values (about 0.5 e/Å^3).

An important argument favoring the displacement of a small amount of La atoms from the main to additional position is the maximum with the coordinates (0, 0, 0.14) in the distribution of the Patterson function $P(uvw)$. The length (0.7 Å) and direction of this vector correspond to the length and direction of the vector between the main and additional positions of La atoms from different unit cells. This vector is translated by $P(uvw) = \int \rho(0.423; 0; 0)\rho(0.423; 0; nc \pm 0.14)dV$ to the initial cell of the P function, where c is the lattice parameter and $n \neq 0$.

At all the stages of the structure-parameter refinement, the choice of the absolute structure was checked by calculating the inverted (with respect to the initial model) twin component with a volume of 0.02 (Flack parameter). At the concluding stage, we performed the control refinement of the inverted model, which resulted in an increase in the R/R_w value to (2.72/3.28)% and confirmed the adequacy of the chosen model of the LZGS structure.

As is seen from Table 4, the closest oxygen environment of the main La position (the 3*e* position with the point symmetry 2) consists of eight oxygen atoms related by the twofold axis along the *c* axis—four oxygens below this position and four oxygens above it. The La' atoms displaced with respect to the twofold axis approach one of these four atoms, thus forming two reduced La–O distances, La'–O_2 = 2.08 and La'–O_3 = 2.09 Å. In this connection, it should be noted that, when estimating the reliability of the interatomic distances, the true thermal vibrations in some instances may be complemented with statistical displacements of atoms from the equivalent positions, which are of a probabilistic nature. These displacements in the structure are responsible for distance "tuning" to the values admissible in terms of crystal chemistry. For the reliable establishment of the character of atomic disorder and correct choice of the model in those instances, where it is necessary to establish what process takes place (thermal motion of atoms or their disordering), one must analyze in detail the electron-density distribution also at low temperatures.

In conclusion, we should like to note that the refined occupancies of crystallographic positions satisfactorily agree with the X-ray spectral data and, thus, allow us to write the formula of the solid solution studied as $La_3Zr_{0.5+\delta}Ga_5Si_{0.5-\delta}O_{14}$ at δ = 0.03(1). The displacements of a small amount of La atoms with respect to the twofold rotation axis in the LZGS structure can be caused by various factors, in particular, by some local (one or several unit cells) ordering of Zr, Ga, and Si atoms statistically occupying some crystallographic positions.

ACKNOWLEDGMENTS

This study was supported by the Russian Foundation for Basic Research, project no. 03-02-17075.

REFERENCES

1. B. V. Mill and Yu. V. Pisarevsky, in *Proceedings of IEEE/EIA International Frequence Control Symposium, Kansas City, Missouri, USA* (2000), p. 133.
2. B. V. Mill', Zh. Neorg. Khim. **47** (3), 384 (2002).
3. B. V. Mill', Zh. Neorg. Khim. **47** (5), 812 (2002).

4. B. H. T. Chai, A. N. P. Bustamante, and M. C. Chou, in *Proceedings of IEEE/EIA International Frequence Control Symposium, Kansas City, Missouri, USA* (2000), p. 163.

5. V. Petricek and M. Dusek, in *JANA'98* (Inst. of Physics, Academy of Sciences of the Czech Republic, Praha, 1998).

6. U. Zuker, K. Perenthalter, W. F. Kuhs, *et al.*, J. Appl. Crystallogr. **16** (3), 358 (1983).

7. P. B. Jamison, S. C. Abrahams, and J. L. Bernstein, J. Chem. Phys. **42**, 358 (1968).

8. V. N. Molchanov, B. A. Maksimov, A. F. Kondakov, *et al.*, Pis'ma Zh. Éksp. Teor. Fiz. **74** (4), 244 (2001) [JETP Lett. **74**, 222 (2001)].

9. E. A. Belokoneva, V. K. Garanin, G. P. Kudryavtseva, *et al.*, Dokl. Akad. Nauk SSSR **242** (2), 330 (1978) [Sov. Phys. Dokl. **23**, 626 (1978)].

10. L. A. Muradyan, S. F. Radaev, and V. I. Simonov, in *Methods of Structure Analysis* (Nauka, Moscow, 1989), p. 5.

Translated by L. Man

Crystallography Reports, Vol. 49, No. 1, 2004, pp. 60–69. Translated from Kristallografiya, Vol. 49, No. 1, 2004, pp. 65–74.

STRUCTURE OF INORGANIC COMPOUNDS

Dedicated to the 80th Birthday of L.A. Shuvalov

Phase Transitions in Compounds with the $Ca_3Ga_2Ge_4O_{14}$ Structure

B. V. Mill*, B. A. Maksimov, Yu. V. Pisarevskiĭ**, N. P. Danilova*, A. Pavlovska***, S. Werner***, and J. Schneider*****

** Faculty of Physics, Moscow State University, Vorob'evy gory, Moscow, 119992 Russia*
e-mail: mill@plms.phys.msu.ru
*** Shubnikov Institute of Crystallography, Russian Academy of Sciences, Leninskiĭ pr. 59, Moscow, 119333 Russia*
e-mail: maximov@ns.crys.ras.ru
**** Institut für Kristallographie und Angewandte Mineralogie, Universität München, Theresienstr. 41, München, D-80333 Germany*

Received June 23, 2003

Abstract—Possible structural changes described by the group–subgroup relationships in the $Ca_3Ga_2Ge_4O_{14}$-type structure (sp. gr. *P*321) are considered. The most probable phase transitions seem to be those accompanied by lowering of the symmetry to the maximal non-isomorphic subgroups *P*3 and *C*2. It is shown that only destructive phase transitions accompanied by symmetry rise up to the minimal non-isomorphic supergroups for the given structure type can take place. The change of the trigonal symmetry to monoclinic is revealed in $La_3SbZn_3Ge_2O_{14}$, whose crystal structure is refined as a derivative structure of the $Ca_3Ga_2Ge_4O_{14}$ structure type within the sp. gr. *A*2 (*C*2). At ~250°C, $La_3SbZn_3Ge_2O_{14}$ undergoes a reversible phase transition accompanied by symmetry rise, $A2 \rightleftharpoons P321$. Similar phase transitions, $P321 \rightleftharpoons A2$, are also observed in $La_3Nb_{0.5}Ga_{5.5}O_{14}$ and $La_3Ta_{0.5}Ga_{5.5}O_{14}$ under the hydrostatic pressures 12.4(3) and 11.7(3) GPa, respectively. The mechanisms of compression and phase transition are based on the anisotropic compressibility of a layer structure. With the attainment of the critical stress level in the structure, the elevated compressibility in the (*ab*) plane gives rise to a phase transition accompanied by the loss of the threefold axis. Attempts to reveal low-temperature phase transitions in a number of representatives of the langasite family have failed. © *2004 MAIK "Nauka/Interperiodica".*

INTRODUCTION

Crystals of the langasite family $La_3Ga_5SiO_{14}$ ($Ca_3Ga_2Ge_4O_{14}$ structure type, sp. gr. *P*321) are promising piezoelectric materials widely used in recent years for designing various frequency-selection devices and sensors, which have a number of advantages over those based on piezoelectric materials such as quartz and lithium niobate and lithium tantalate. Therefore, in some countries, large $La_3Ga_5SiO_{14}$ (LGS), $La_3Nb_{0.5}Ga_{5.5}O_{14}$ (LNG), and $La_3Ta_{0.5}Ga_{5.5}O_{14}$ (LTG) crystals are grown by the Czochralski technique on an industrial scale [1–3].

The first publications on these crystals showed that the representatives of the langasite family undergo no phase transitions at temperatures below T_m, which is an obvious advantage for piezoelectric applications. At the same time, some elastic and dielectric characteristics of these crystals show their anomalous temperature behavior.

In particular, it is established that the acoustic-wave velocity in some crystals of the langasite family shows an anomalous temperature dependence along some crystallographic directions, which, in turn, gives rise to such an important property of piezoelectric materials as a high temperature stability [1, 4, 5]. Usually, an increase in some elastic moduli (directly related to interatomic bonding) with temperature precedes a high-temperature phase transition (e.g., the $\alpha \rightleftharpoons \beta$ phase transition in quartz crystals).

Some crystals of the langasite family show a dramatic increase in permittivity ε_{33} with lowering of temperature, which, in turn, may indicate a possible occurrence of a low-temperature phase transition [5].

Finally, among about 140 known compounds with the $Ca_3Ga_2Ge_4O_{14}$ structure, three phases were recently established with a distorted trigonal lattice—$La_3SbZn_3Ge_2O_{14}$ (LSZG), $La_3SbZn_3Si_2O_{14}$, and $SrLa_2Ga_4Si_2O_{14}$ [6].

All the above stated brought us to the development of a special program of searching for possible phase transitions and study of their manifestation in structure

and properties of the compounds of the langasite family under high pressures and low and high temperatures. The results obtained up to date are considered below.

CRYSTAL STRUCTURE

The $Ca_3Ga_2Ge_4O_{14}$ structure (sp. gr. *P*321) can be described as a framework formed by 2*d* (symmetry 3) and 3*f* (symmetry 2) tetrahedra and 1*a* (symmetry 32) octahedra, with the cavities being occupied by large cations located in the 3*e* positions (symmetry 2) and surrounded by distorted Thomson cubes or triangular oxygen dodecahedra. The tetrahedra share vertices and form layers alternating with the layers formed by octahedra and dodecahedra along the *c* axis (Fig. 1). Inter- and intralayer bonding is provided by polyhedra sharing their edges and oxygen vertices. The smaller 2*d* tetrahedra share half of their O–O edges with dodecahedra, which results in compression of the polyhedron, whereas the larger 3*f* tetrahedra share no edges with other polyhedra. Octahedra share three edges with dodecahedra; dodecahedra share four edges with neighboring dodecahedra, one edge with an octahedron, and two more edges with 2*d* tetrahedra. In accordance with their size, small tetrahedral ions occupy the 2*d* positions; larger ions, the 3*f* positions. The Sb^{5+}, Nb^{5+}, Ta^{5+}, Mo^{6+}, and W^{6+} ions are located in the octahedral positions. The Al^{3+} and Ge^{4+} ions show a more pronounced propensity to octahedral coordination than the larger Ga^{3+}; the Ti^{4+} ions also show the propensity to octahedral coordination. Despite their layer structure, the crystals show no cleavage, which indicates strong bonding both inside and between the layers.

To date, about 20 structures of the compounds of the langasite family have been solved by single-crystal X-ray diffraction analysis. Most of these compounds have disordered structures with the mixed filling of the cationic positions. The $Ca_3NbGa_3Si_2O_{14}$ compound and its analogues and also the $Ln_3Ga_5M^{4+}O_{14}$ compounds (M = Zr and Hf) [1] are characterized by ordered structures with all the positions being occupied by only one type of cations.

Thus, the layer structure of the $Ca_3Ga_2Ge_4O_{14}$ type consists of a noncentrosymmetric framework with the cavities filled with large cations. Oxygen tetrahedra prevail over octahedra (in the ratio 5 : 1). Cation positions can either be occupied orderly or can be mixed. The crystal structure is layered. Large number of shared oxygen edges and location of a considerable number of atoms along two- and threefold axes make the structure rather rigid and stable against the action of various external factors.

POSSIBLE PHASE TRANSITIONS IN CRYSTALS OF THE LANGASITE FAMILY

We restrict our consideration to possible phase transitions associated with the group–subgroup relationship in the sp. gr. *P*321, characteristic of most of the known compounds of the langasite family.

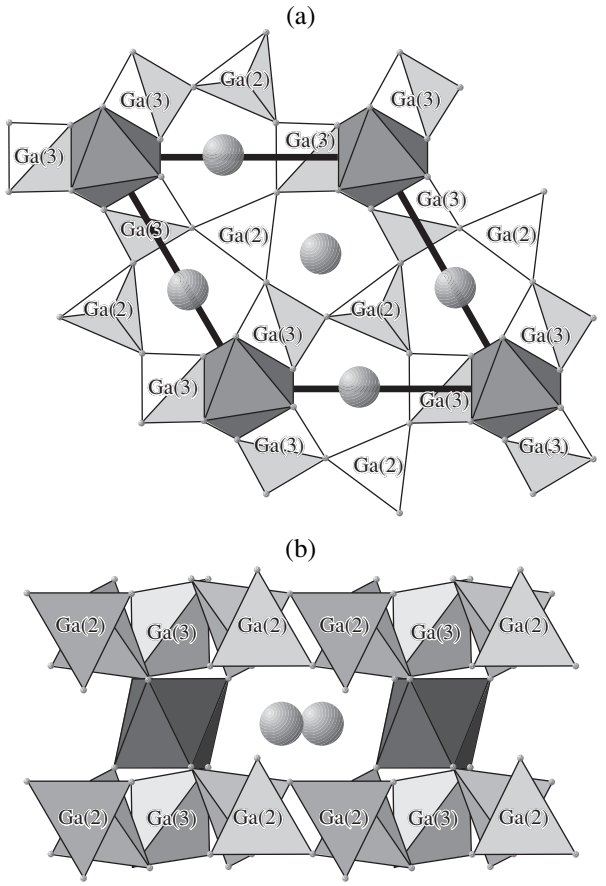

Fig. 1. Structure of a trigonal LNG crystal projected along the (a) *b* and (b) *c* axes. One can see the GaO_4 and Ga/NbO_6 polyhedra; La atoms are depicted by spheres.

The maximal non-isomorphic subgroups of the sp. gr. *P*321 with the same lattice metrics are *P*3 and *C*2 [7]. The phase transitions accompanied by the formation of these subgroups and lowering of the symmetry are characterized by the loss of the two- (*P*321 $\longrightarrow$ *P*3) or threefold (*P*321 $\longrightarrow$ *C*2) axis. If the lattice metrics is changed, the transitions accompanied by the change of the sp. gr. *P*321 to the sp. gr. $P3_121$, $P3_221$ (with tripling of the *c* parameter and appearance of screw axes), and *P*312 (triple *a* and *b* parameters) may take place. In the phase transitions in the LSZG, LNG, and LTG crystals (see below), no tripling of the *a* and *c* parameters was revealed, so these schemes of phase transitions are highly unprobable in the langasite family.

The phase transitions occurring with doubling of the *a* or *c* parameter without formation of the maximal isomorphic subgroups with low indices *P*321 are also possible. These transitions may correspond to the formation of a superstructure with disordered positions filled with ions having pronouncedly different sizes and valences. An example here is superstructural ordering

of Ga^{3+} and M^{5+} ions occupying the octahedral positions in the ratio 1 : 1 in the (*ab*) plane or along the *c* axis in $La_3M_{0.5}Ga_{5.5}O_{14}$ (*M* = Nb, Ta, and Sb). A phase transition accompanied by the formation of a superstructure should have taken place at a temperature high enough for ion migration and ordering in the structure. However, the X-ray powder diffraction patterns of these compounds showed no superstructural lines [8] and, therefore, the refinement of the LNG [9] and LTG [10] structures was performed without taking into account possible superstructural ordering. It may be assumed that, with due regard for the close ionic radii of Ga^{3+} and M^{5+}, the difference in the ion charges is insufficient for superstructural ordering. In principle, superstructural ordering with the change of the lattice parameters by a factor that is not a multiple two is possible, as well as the formation of modulated (both commensurate and incommensurate) structures.

Thus, the most probable phase transitions for the compounds of the langasite family are those which are accompanied by lowering of the symmetry, i.e., $P321 \longrightarrow P3$ and $P321 \longrightarrow C2$.

In high-temperature phase transitions accompanied by the appearance of a higher symmetry, the minimal non-isomorphic supergroups of the sp. gr. *P*321 are $P\bar{3}m1$, $P\bar{3}c1$, *P*622, $P6_322$, $P\bar{6}2m$, $P\bar{6}2c$, *P*312, and *R*32. In [11], the hexagonal pseudosymmetry of the structure is indicated. The arrangement of cations in this structure type is described by the sp. gr. $P\bar{6}2m$, which is "violated" by the coordinate *z* of the central atom of the 2*d* tetrahedron (it slightly differs from the necessary value 0.5) and arrangement of O atoms. Our analysis showed that the structure of the $Ca_3Ga_2Ge_4O_{14}$ type cannot be described by any of the above groups (including $P\bar{6}2m$) without considerable displacements of oxygen atoms such that they would destroy the polyhedra and distort the respective bonds, i.e., without the complete rearrangement or even destruction of the structure. This explains the absence of high-temperature phase transitions accompanied by the formation of a higher symmetry in the compounds of the langasite family. At the same time, isomorphous phase transitions proceeding without a change of the symmetry are possible, but they should be accompanied by jumpwise changes of the lattice parameters.

CRYSTAL STRUCTURE AND PHASE TRANSITION IN LSZG

Initially, X-ray diffraction patterns of LSZG, $La_3SbZn_3Si_2O_{14}$, and $SrLa_2Ga_4Si_2O_{14}$ were indexed in the trigonal system with the lattice parameters typical of the compounds of the langasite family [12]. The detailed analysis of these X-ray diffraction patterns showed that the lattice is slightly (presumably orthorhombically) distorted [6]. However, none of the orthorhombic space groups are subgroups of the sp. gr. *P*321. The question about the structure and true symmetry of these compounds was answered only by X-ray diffraction study of LSZG single crystals.

Small LSZG and $La_3SbZn_3Si_2O_{14}$ crystals were obtained by melting of preliminarily synthesized phases with a small excess in Sb_2O_5 in closed platinum crucibles and subsequent slow cooling of the melt.

X-ray study of an LSZG crystal (8639 reflections obtained within the complete sphere of the reciprocal space, CAD-4F diffractometer, MoK_α radiation, max $\sin\theta/\lambda = 0.97$ Å^{-1}) showed that the true symmetry is monoclinic: $a = 5.202$ Å, $b = 8.312$ Å, $c = 14.394$ Å, $\beta = 90.02°$, $Z = 2$.[1] The full-matrix anisotropic refinement lead to the polar sp. gr. *A*2 (*C*2) ($R = 5.16$ and $R_w = 4.63\%$) which is the maximal non-isomorphic subgroup of the sp. gr. *P*321. The refinement performed in the alternative sp. gr. *P*3 yielded no satisfactory results [13]. The LSZG structure is illustrated by Fig. 2. Its analysis shows that the structure only slightly differs from the $Ca_3Ga_2Ge_4O_{14}$ structure type and preserves all the main features of the latter. The loss of the threefold axis and two of the three twofold axes results in the appearance of nonequivalent positions of La and Zn atoms, of which La1, Zn1, and Sb positions are special. The remaining atoms are located in the general position, whereas the remaining twofold axis becomes polar and, thus, creates the conditions for the ferroelectric state.

Slight differences (mainly in symmetry) between the structures of the monoclinic LSZG and trigonal $Ca_3Ga_2Ge_4O_{14}$ structures allow us to assume the possible $A2 \longrightarrow P321$ high-temperature phase transition accompanied by the formation of higher symmetry. The temperature dependences of the unit-cell parameters of LSZG [14] (Fig. 3) indicate the existence of a presumably first-order phase transition near 250°C. Single crystal X-ray diffraction study showed that the symmetry of an LSZG crystal at 290°C is unchanged, but at 360°C, the symmetry becomes higher—trigonal, sp. gr. *P*321. Being cooled, the crystal returns to the initial state described by the sp. gr. *A*2. Thus, the phase transition to LSZG is reversible. The displacements observed for some O atoms in the phase transition are quite pronounced and reach ~0.9 Å. This results, e.g., in the reduction of the coordination number of one of the La atoms (La2) in the monoclinic phase from 8 to 7. In order to determine the exact value of the phase-transition temperature and the nature of this transformation, some additional investigations should be performed. Similar phase transitions should also be observed in $La_3SbZn_3Si_2O_{14}$ and $SrLa_2Ga_4Si_2O_{14}$.

[1] The crystal studied was a polysynthetic twin whose monoclinic components were related by a threefold rotation axis of the pseudohexagonal lattice.

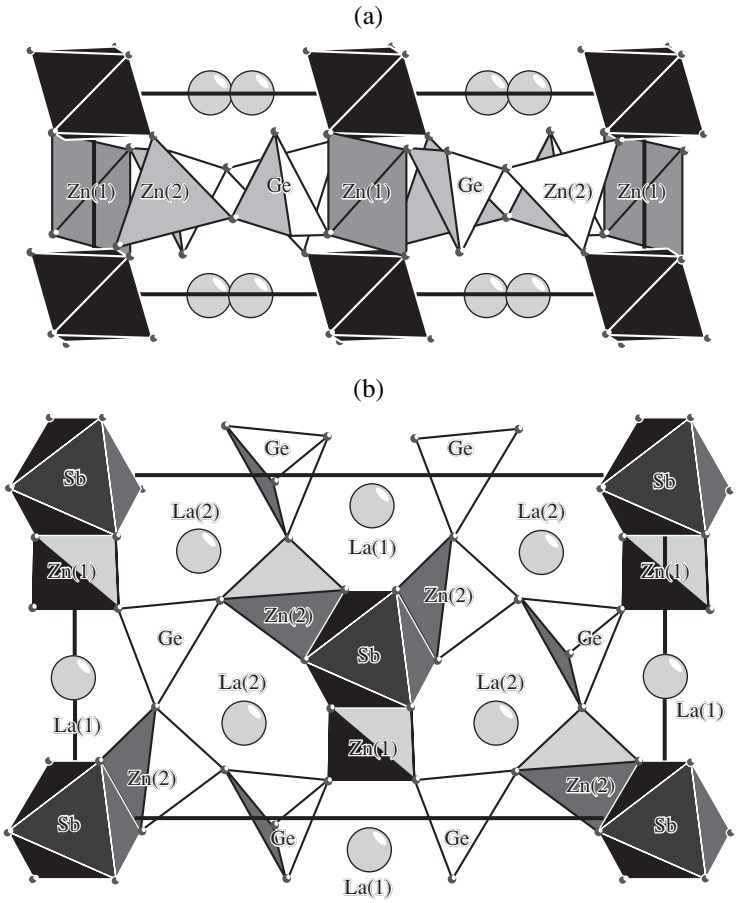

Fig. 2. Monoclinic LSZG unit cell projected along the (a) *b* and (b) *a* axes. One can see the GeO_4, ZnO_4, and SbO_6 polyhedra.

PHASE TRANSITIONS IN LNG AND LTG UNDER PRESSURE

Compressibility of LGS, LNG, and LTG crystals was studied with the aim of establishing their structural stability. The effect of pressure on solids is equivalent to their compression under a lowered temperature and may give rise to phase transitions accompanied by lowering of their symmetry.

The behavior of langasite under pressure was studied for the first time in [15]. Under the conditions of uniaxial compression at $P = 0.74$ GPa, ferrobielastic switching of the acoustic frequency of a resonator was observed, which most likely corresponded to pseudomerohedral microtwinning. The X-ray diffraction study of langasite compressibility under a hydrostatic pressure of 10.2 GPa revealed no phase transitions [16].

X-ray diffraction study of LNG and LTG under the hydrostatic compression, 22.8 and 16.7 GPa, respectively, was performed on single crystals in a high-pressure chamber with diamond anvils filled with helium [17].

The variation of the relative unit-cell parameters of LNG and LTG crystals under pressure is illustrated by Figs. 4 and 5. The kinks on these dependences indicate the phase transition under pressures of 12.4(3) GPa in LNG and 11.7(3) GPa in LTG.

The crystal structures of the high-pressure LNG and LTG phases were determined within the sp. grs. *P*3 and *C*2, the maximal non-isomorphic subgroups of the sp. gr. *P*321. The refinement performed by the structural data for a monoclinic LSZG crystal indicated that the sp. gr. *A*2 (*C*2) is preferable. Figure 6 shows the LNG structure projected along the *b* axis. The comparison of this structure with the LTG structure [17] shows more pronounced distortion of octahedra in LNG than in LTG. The scatter in the (Nb,Ga)–O distances in the octahedra [1.74(7)–2.12(6) Å] is analogous to the scatter in the Ti–O distances in the TiO_6 octahedra in the structure of the well-known nonlinear optical $KTiOPO_4$ (KTP) crystal [18]. The octahedra in the LTG structure are more regular and the (Ta,Ga)–O distances are close to 1.98(5) Å. This discrepancy can be explained by more the pronounced polarization of oxygen atoms surrounded with Nb^{5+} ions in comparison with the polarization of the oxygen atoms surrounded with Ta^{5+} ions,

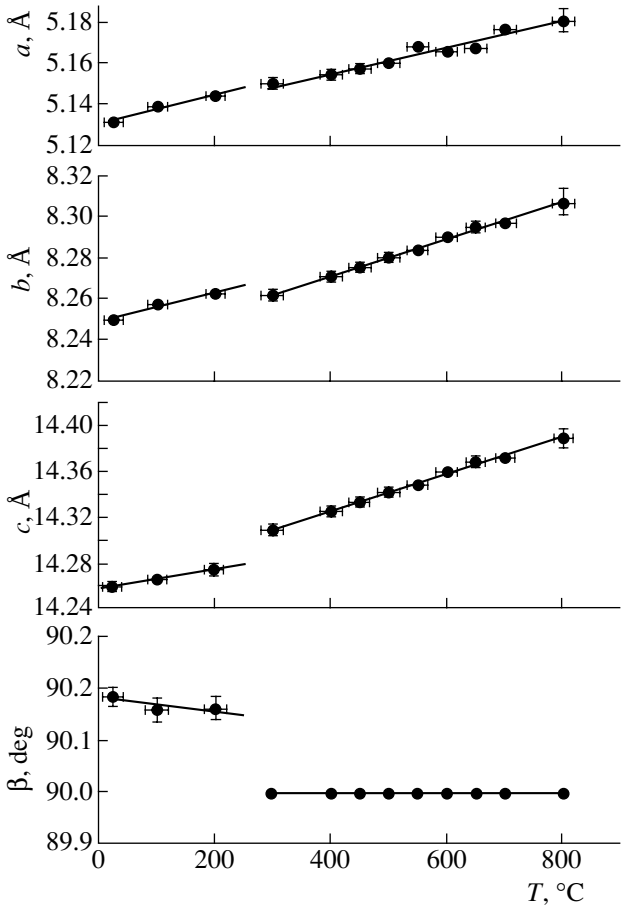

Fig. 3. Temperature variations in the unit-cell parameters of the monoclinic and trigonal (in orthorhombic setting) LSZG.

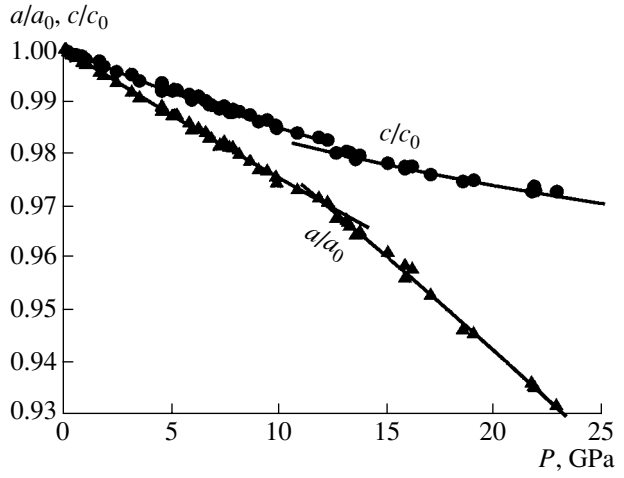

Fig. 4. The a/a_0 and c/c_0 ratios in LNG as functions of pressure.

which is characteristic of many Nb- and Ta-containing compounds. Thus, the scatter in the Nb–O and Ta–O distances in $LiNbO_3$ and $LiTaO_3$ ranges within 1.88–2.13 and 1.91–2.07 Å, respectively [19]. In a monoclinic LSZG crystal, the scatter in the Sb–I distances in octahedra ranges within 1.98–2.03 Å.

The high-pressure monoclinic LNG and LTG phases possess trigonal pseudosymmetry. The spatial arrangements of heavy atoms refined within the monoclinic sp. gr. *A*2 and the trigonal sp. gr. *P*321 coincide within the experimental error. However, the coordinates of oxygen atoms in the sp. gr. *A*2 are inconsistent with the trigonal symmetry. Within the experimental error, the lattice parameters of LNG and LTG correspond to a trigonal lattice in the entire pressure range studied; the diffraction reflections show no broadening up to a pressure of 14 GPa. Noticeable reflection broadening is observed only at higher pressures and is explained by the deviation of the angle β from 90° or by an increased difference between the *a* and *b* parameters in the monoclinic domains.

Since the action of the temperature and pressure on the crystal structure produces changes with opposite signs, the structures of the high-pressure monoclinic LNG and LTG phases and the low-temperature monoclinic LSZG modification are the same. In a similar way, the structure of the high-temperature trigonal LSZG phase is the same as the structure of the low-pressure LNG and LTG phases.

Both compounds show higher compressibility along the *a* axis than along the *c* axis in the entire pressure range studied, with the compressibility along the *c* axis for LNG and LTG being almost the same in the entire pressure range (Table 1). The compressibilities along the *a* axis are close only for low-pressure phases and differ considerably above the phase-transition pressure. Compressibility along the *a* axis in LNG after the phase transition is almost two times higher and noticeably decreases along the *c* axis. As a result, the anisotropy of compressibility becomes much more pronounced. The anisotropy of compressibility in the LTG crystal after the phase transition slightly increases, whereas compressibilities along the *a* and *c* axes decrease. The thermal expansion of the trigonal LNG, LTG, and LSZG phases is also anisotropic. In the temperature range from 300 to 850°C, thermal expansion in the (*ab*) plane is higher than in the *c* direction (Table 2).

The behavior of LNG and LTG crystals under hydrostatic compression show that these crystals may be used as pressure sensors up to a pressure of ~11 GPa at room temperature (the application range of LGS crystals seems to be rather close). With an increase in temperature, the phase-transition pressure would also increase in order to compensate thermal expansion, and the working range of pressure sensors slightly increases. At sufficiently high temperatures and pressures, the boundary of the stability region is attained, whose slope is opposite to the slope of the *P*–*T* dependence of the phase transition.

MECHANISMS OF COMPRESSION AND PHASE TRANSITION

The mechanisms of compression and phase transition in LNG and LTG phases crystallized in the trigonal sp. gr. *P*321 with a limited number of free positional parameters are rather complex. Under pressure, the unit-cell volume may decrease because of compression, distortion, and rotation of coordination polyhedra. In the $Ca_3Ga_2Ge_4O_{14}$-type structures, polyhedra share the vertices and O–O edges. Distortion and rotation of polyhedra are "damped" by valence bonds and high lattice symmetry (two- and threefold axes). The structure consists of alternating layers of tetrahedra and layers of dodecahedra and octahedra, which are practically planar and have different compressibilities. The atoms can be located in special positions with the degrees of freedom in the layer (central atoms of the 3*e* dodecahedra and 3*f* tetrahedra on twofold axes) and normally to the layer (central atoms of the 2*d* tetrahedra and the O1 atoms on threefold axes). The O2 and O3 atoms occupy the general positions and can be displaced along any direction. The octahedral atoms in the position 1*a* are fixed by the two- and threefold axes.

The data obtained indicate that compressibility of the compounds with the $Ca_3Ga_2Ge_4O_{14}$ structure in the (*ab*) plane is higher than compressibility along the *x* axis [14, 16, 17]. This can be explained by the layer structure, the large number of degrees of freedom for atoms in the layers, and the absence of considerable deviations of the layers from the plane, which leads to their corrugation. The structural data for LNG and LTG under pressures below 12 GPa show that compression results mainly in a decrease in the volume of LaO_8 dodecahedra (mainly ionic weak La–O bonds) and $[Ga,Nb(Ta)]O_6$ octahedra (ionic–covalent bonds). The GaO_4 tetrahedra, first, "try" to rotate, because rotation can occur under the action of less intense external factors than reduction of covalent Ga–O bonds. However, rotation is hindered by bonds with neighboring polyhedra, and, as a result, the tetrahedra may rotate only within certain limits. At $P > 5$ GPa, an increase in pressure gives rise to a more noticeable reduction of the Ga–O distances in tetrahedra. After the attainment of the critical stress values at 12(1) GP, an increase in stresses in the structure results in its deformation, which is seen from the redistribution of the bond lengths and disappearance of threefold axes. Upon the phase transition with lowering of symmetry, the number of degrees of freedom in the structure increases. Compressibility in the (*ab*) plane [(*bc*) plane in the monoclinic setting] in LNG increases because the barriers (threefold axes) disappear and compressibility along the *c* axis decreases (the remaining twofold axis reduces compressibility), and the resulting volume compressibility increases. Comparing Figs. 1 and 6, we see a more pronounced corrugation of "tetrahedral layers" in the monoclinic LNG phase because of the preferable compression of the structure in the (*ab*) plane.

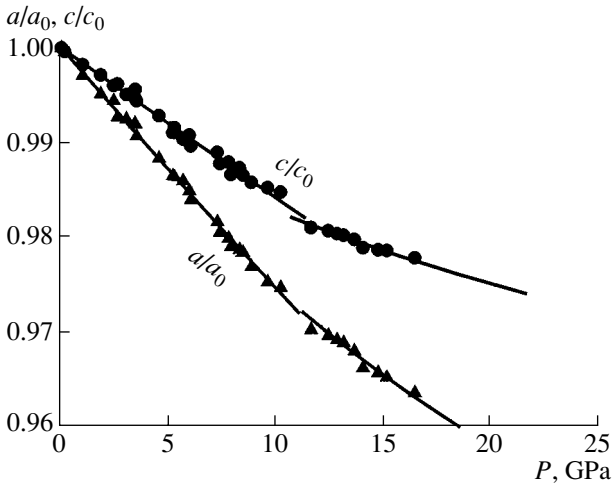

Fig. 5. a/a_0 and c/c_0 ratios in LTG as functions of pressure.

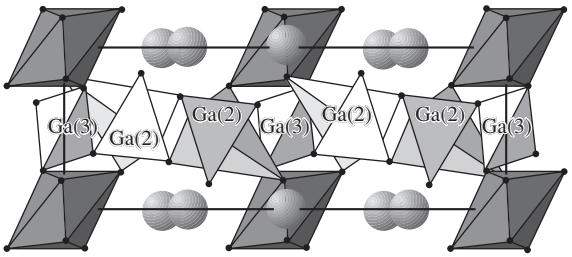

Fig. 6. Monoclinic LNG unit cell projected along the *b* axis under a pressure of 18.5(3) GPa; the GaO_4 and Ga/NbO_6 polyhedra are shown.

However, the volume and both linear compressibilities decrease in the phase transition in LTG, which is inconsistent with the phase-transition mechanism accompanied by the loss of the threefold axis.

Monoclinic distortion of the LSZG and $La_3SbZn_3Si_2O_{14}$ structures in the absence of high pressures seems to be caused by filling of the 3*f* tetrahedra with large Zn^{2+} ions (r^{iv} = 0.60 Å) rather than with small Ga^{3+} ions (r^{iv} = 0.47 Å). Possibly, a certain role is also played by the considerable scatter in the cation valences and the ordered filling of oxygen polyhedra with cations. The stresses thus formed in the structure

Table 1. Compressibilities along the *a* and *c* axes of LNG and LTG crystals under the zero pressure ($\beta_0 \times 10^4$, GPa^{-1})

Compound	Low-pressure phase (sp. gr. *P*321)		High-pressure phase (sp. gr. *A*2)	
	a axis	*c* axis	*a* axis*	*c* axis*
LNG	8.70(18)	6.24(2)	15.6(3)	4.21(3)
LTG	8.91(16)	6.57(8)	6.31(8)	3.74(7)

* In trigonal setting.

Table 2. Average thermal-expansion coefficients of the parameters of the trigonal unit cell in LSZG, LNG, and LTG crystals in the temperature range 300–850°C

α_L (10^{-6}/K)	LSZG	LNG	LTG
α_a	11.35(3)	8.038(13)	8.23(2)
α_c	7.36(2)	5.891(16)	5.97(13)
α_V	30.2(3)	22.31(23)	22.54(21)

exceed the upper level and are "removed" by the monoclinic distortion of the lattice.

The remaining monoclinic phase, $SrLa_2Ga_4Si_2O_{14}$, is formed by ions characteristic of splitting, with the octahedra and tetrahedra being orderly filled with Ga^{3+} and Si^{4+} ions. The only feature that distinguishes this structure from the other structures of the langasite family is the mixed filling of dodecahedra with Sr^{2+} and La^{3+} ions in the ratio 1 : 2 characteristic of the 3*e* position in the sp. gr. *P*321 in the transition to the sp. gr. *A*2. In some other compounds analogous with respect to the position occupancies (e.g., in $Na_2CaGe_6O_{14}$), no monoclinic lattice distortion was revealed. We assume that the disorder in the 3*e* positions (especially disorder described by the ratio 1 : 2), may reduce the pressure necessary for the transition to the monoclinic modification.

We see that the pressure giving rise to the $P321 \longrightarrow A2$ transition in the compounds with the $Ca_3Ga_2Ge_4O_{14}$ structure varies over the wide range from 10^{-4} GPa for the LSZG to 12(1) GPa for LNG and LTG. It seems that this pressure can even exceed 12 GPa.

With a further increase in pressure, the following transitions accompanied by lowering of the symmetry may take place. The attainment of the compressibility limit in the (*bc*) plane makes possible the phase transition to the triclinic sp. gr. *P*1 accompanied by the loss of the twofold axis. This triclinic space group is the maximal non-isomorphic subgroup of the sp. gr. *C*2 (*A*2). In LNG crystals, no similar phase transition is observed up to a pressure of 22.8 GPa, i.e., the value two times higher than the pressure in the $P321 \rightleftharpoons A2$ phase transition. Therefore, in this case, another scenario, explained by the strive of tetrahedral ions to increase their coordination up to 5 or 6, seems to be more probable. This should lead to the dramatic rearrangement of the tetrahedral layer and the whole structure (destructive phase transition). An example of such a structure is monoclinic $Ca_3Mn_2Ge_4O_{14}$ (sp. gr. *I*2/*c*) characterized by the same stoichiometry, layer character of the structure, and lattice metrics, which are close to those of the high-pressure LNG and LTG phases whose "tetrahedral" layers incorporate octahedra [20]. Instead of structural rearrangement, the compound can decompose into several phases. The only study dedicated to the stability of the compounds with the $Ca_3Ga_2Ge_4O_{14}$ structure under pressure is, in addition to [16, 17], the study of the high-pressure $Na_{0.9}Ca_{2.95}Si_6O_{14}$ phase decomposing at $P > 14$ GPa [21]. The further evolution of the $Ca_3Ga_2Ge_4O_{14}$-type structures with an increase in pressure can be exemplified by the LSZG structure having the monoclinic symmetry under normal pressure.

SEARCH FOR LOW-TEMPERATURE PHASE TRANSITIONS

The discovery of the monoclinic distortion of the LSZG, $La_3SbZn_3Si_2O_{14}$, and $SrLa_2Ga_4Si_2O_{14}$ lattices at room temperature and the phase transition in LSZG at ~250°C gave an impetus to the search for similar transformations in other compounds of the langasite family at low temperatures. It is well known that cooling of solids usually results in a decrease of the unit-cell parameters, i.e., is equivalent to the effect of pressure.

There are only a few low-temperature studies of crystals of the langasite family important for both fundamental and applied science. We mention here the spectroscopic studies of doped crystals at helium temperatures [22], measurements of heat conductivity, dielectric constant, acoustic-wave velocities, thermal expansion, and thermal conductivity in the LGS, LNG, and $Sr_3Ga_2Ge_4O_{14}$ crystals in the temperature range from 55(77) to 300 K [23]. We should like to emphasize that permittivity in LNG crystals in the temperature range from 4.2 to 300 K shows a dramatic increase in ε_{33} with a decrease in the temperature and the attainment of the plateau at ~30 K. A similar behavior of ε_{33} is also characteristic of the quantum paraelectric compound $Sr_{1-x}Ca_xTiO_3$ [24]. An increase in ε_{33} with lowering of the temperature was also observed for other crystals of the langasite family.

We selected as a structure-sensitive property the heat capacity and measured it for LGS, LNG, LTG, $Ca_3Ga_2Ge_4O_{14}$, $Sr_3Ga_2Ge_4O_{14}$, $Ca_3TaGa_3Si_2O_{14}$, $Sr_3TaGa_3Si_2O_{14}$, and $Na_2CaGe_6O_{14}$ single crystals and LSZG polycrystals in a VNIIFTRI microcalorimeter in the temperature range from 6 to 270 K (the data for LGS and $Ca_3Ga_2Ge_4O_{14}$ are shown in Fig. 7). The temperature curves of heat capacity of all the samples showed no anomalies (within the method sensitivity) that could indicate phase transitions. X-ray diffraction study of LNG crystals at 20 K showed no considerable changes in the structure in comparison with the structure at room temperature.

To explain the absence of low-temperature phase transitions in the above compounds, we considered the unit-cell parameter ratio *c*/*a* in a trigonal LNG crystal as a function of pressure and temperature (Fig. 8). It is seen that the temperature range studied (0–850°C) [14] corresponds to the change in the pressure by ~1.6 GPa. Compression during cooling in the temperature range 293–4.2 K is equivalent to the effect of a hydrostatic pressure of ~0.5 GPa; a pressure of 12.4 GPa corresponding to the phase transition is equivalent to cooling

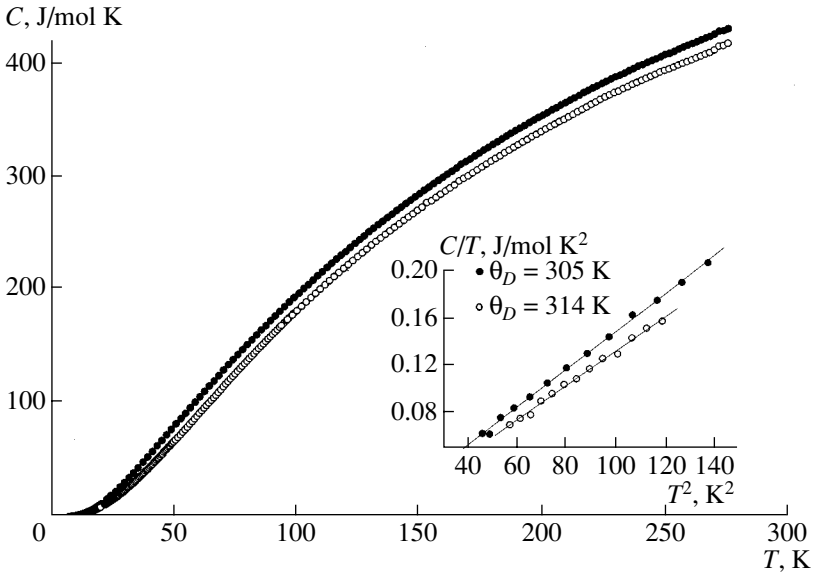

Fig. 7. Heat capacity of $La_3Ga_5SiO_{14}$ (●) and $Ca_3Ga_2Ge_4O_{14}$ (○). Inset: the Debye temperature θ_D determined from the $C/T - T^2$ dependences.

by ~6000 K. Since, depending on the stresses in the structure, the pressure under which the phase transition takes place in the compounds of the langasite family ranges from $\leq 10^{-4}$ to pressures exceeding 10 GPa, it is not astonishing that, among the nine compounds studied, there is not a single compound in which a phase transitions takes place during cooling corresponding to a compression under pressures $P \leq 0.5$ GPa. We believe that such materials should be found among the 130 remaining compounds.

POSSIBLE HIGH-TEMPERATURE PHASE TRANSITIONS

Earlier, we came to the conclusion that no phase transitions accompanied by the formation of a higher symmetry can take place in compounds of the langasite family, because a $Ca_3Ga_2Ge_4O_{14}$-type structure with the preserved unit-cell metrics cannot be described within the corresponding minimal non-isomorphic supergroups with respect to the sp. gr. *P*321. Only the isomorphous phase transitions (within the sp. gr. *P*321) may take place and they should be accompanied by the jumpwise behavior of the unit-cell parameters (although sometimes hardly observable). The dramatic changes in the unit-cell metrics corresponding to an isomorphous phase transition may take place only if some noticeable structural changes not violating the structure symmetry occur. These can be jumpwise changes of atomic coordinates, formation of new positions, splitting of positions, partial ordering of disordered positions, ordering of defects, etc.

The change of the lattice parameters with temperature can be determined by studying thermal expansion of the unit cell by X-ray diffraction (on both powders and single crystals) or dilatometry methods. The thermal-expansion data for compounds of the langasite family at temperatures higher than room temperature are rather scarce. Thermal expansion in LGS, LNG, and LTG crystals is measured in the temperature range from –100 to +150°C [25]. Thermal expansion data for LNG and LTG crystals at temperatures up to 850°C [14] are insufficiently accurate for establishment of possible weak anomalies in the unit-cell parameters. In [26], thermal expansion in LGS and $La_{2.7}Nd_{0.3}Ga_5SiO_{14}$ solid solution was measured both normally and parallel to the *c* axis at temperatures up to 1200°C. In LGS, no anomalies were revealed, but in $La_{2.7}Nd_{0.3}Ga_5SiO_{14}$, the temperature dependences of the unit-cell parameters showed a pronounced anomaly in the vicinity of 760°C, which was explained by structural changes of an

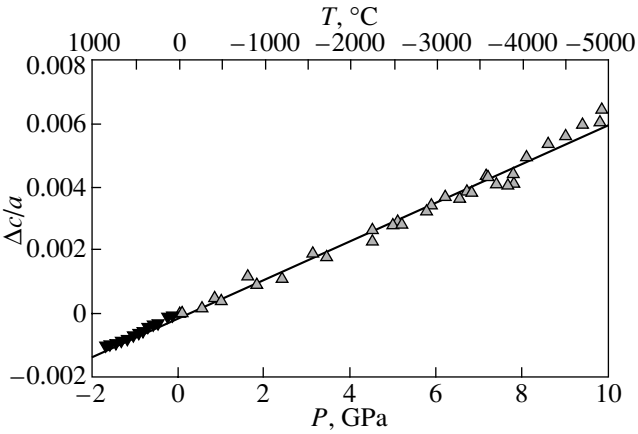

Fig. 8. *c*/*a* ratio in LNG as a function of pressure and temperature; (▲) $\Delta c/a(P)$, (▼) $\Delta c/a(T)$.

unknown nature. In order to understand whether the anomaly revealed for $La_{2.7}Nd_{0.3}Ga_5SiO_{14}$ reflects certain changes in the structure or is of a random character, some additional studies are necessary. In this respect, it seems interesting to perform precision measurements of thermal expansion in other compounds of the langasite family at temperatures up to 1000–1400°C.

The precision refinement of the $La_3Nb_{0.5}Ga_{5.5}O_{14}$ and $La_3Zr_{0.5}Ga_5Si_{0.5}O_{14}$ structures [27] showed the formation in dodecahedra of a new 6*g* position characterized by a low occupancy (~1.5%) with La atoms located along the *z* axis at a distance of ~0.7 Å from the 3*e* position. The formation of this position at elevated temperatures could manifest itself on the temperature dependences of the unit-cell parameters, but it should hardly be noticed because of the low occupancy of this position. No such position was revealed in the LGS or $Sr_3TaGa_3Si_2O_{14}$ structures.

The difficulties encountered in the attempts to grow large high-quality crystals of the langasite family were repeatedly indicated by many researchers. In many instances, these difficulties are associated with the absence of sufficiently detailed information about the homogeneity field of the crystal and insufficient control of hydrodynamic and thermal growth parameters, which leads to composition inhomogeneity over the volume, growth striations, and stresses and block formation in the crystal [28, 29]. However, these are not the only factors deteriorating the crystal quality. We should like to emphasize once again the necessity of studying the behavior of crystal lattices of compounds of the langasite family at high temperatures.

CONCLUSIONS

The anomalous behavior of some characteristics of crystals of the langasite family and the existence of three compounds with the distorted trigonal unit cell stimulate the further search for phase transitions and their manifestations in the structure and properties of the crystals.

Analysis of possible phase transitions related by the group–subgroup relationships shows that, for the $Ca_3Ga_2Ge_4O_{14}$-type structures, the most probable transitions are those which are accompanied by lowering of the symmetry from the sp. gr. *P*321 to the maximal non-isomorphic subgroups *P*3 and *C*2. The high-temperature phase transitions accompanied by the formation of a higher symmetry up to the minimal non-isomorphic supergroups for the given structure seem to be impossible.

The LSZG structure is refined within the sp. gr. *A*2 as a derivative of the $Ca_3Ga_2Ge_4O_{14}$ structure type. At ~250°C, it undergoes a reversible phase transition with the formation of a higher symmetry, $A2 \rightleftharpoons P321$. Both LNG and LTG crystals undergo analogous phase transitions $P321 \rightleftharpoons A2$ under hydrostatic compression at 12.4(3) and 11.7(3) GPa, respectively. The mechanisms of compression and phase transition are discussed in terms of the model of anisotropic compressibility of a layer structure. The elevated compressibility in the (*ab*) plane results in the phase transition with the loss of the threefold axis after the attainment of the critical stress level in the structure. A further increase in pressure can give rise to additional phase transitions accompanied by lowering of the symmetry or even structure destruction. The search for the low-temperature phase transitions in a number of compounds of the langasite family gave no positive results because of insufficient lattice compression during crystal cooling by ~300 K. Analysis of possible isomorphous phase transitions in crystals of the langasite family led to the conclusion about the necessity of precision studies of thermal expansion of these crystals at high temperatures.

ACKNOWLEDGMENTS

The authors are grateful to R.V. Galiulin and V.N. Molchanov for the fruitful discussion of the results and to M.P. Markina and N.A. Vasil'eva for their help in heat-capacity measurements. This study was supported by the Russian Foundation for Basic Research, project no. 03-02-17075.

REFERENCES

1. B. V. Mill and Yu. V. Pisarevsky, in *Proceedings of 2000 IEEE/EIA International Frequency Control Symposium, Kansas City, Missouri, USA* (2000), p. 133.
2. M. Honal, R. Fachberger, T. Holzheu, *et al.*, in *Proceedings of 2000 IEEE/EIA International Frequency Control Symposium, Kansas City, Missouri, USA* (2000), p. 113.
3. D. Puccio, N. Saldanho, D. C. Malocha, and M. Pereira da Cunha, in *Proceedings of 2002 IEEE/EIA International Frequency Control Symposium, New Orleans, Louisiana, USA* (2002), p. 324.
4. I. A. Andreev and M. F. Dubovik, Pis'ma Zh. Tekh. Fiz. **10** (4), 487 (1984) [Sov. Tech. Phys. Lett. **10**, 205 (1984)].
5. Yu. V. Pisarevsky, P. A. Senyushchenkov, P. A. Popov, and B. V. Mill, in *Proceedings of 1995 IEEE International Frequency Control Symposium, San Francisco, USA* (1995), p. 653.
6. S. Ivanov and V. Zhurov, ICDD **51**, 181/3 (2001).
7. *International Tables for Crystallography*, Ed. by T. Hahn (Reidel, Dordrecht, 1983), Vol. A, p. 497.
8. S. Ivanov and V. Zhurov, ICDD **49**, 270 (1999).
9. V. N. Molchanov, B. A. Maksimov, A. F. Kondakov, *et al.*, Pis'ma Zh. Éksp. Teor. Fiz. **74** (4), 244 (2001) [JETP Lett. **74**, 222 (2001)].
10. H. Takeda, K. Sugiyama, K. Inaba, *et al.*, Jpn. J. Appl. Phys. **36**, 919 (1997).
11. E. L. Belokoneva, S. Yu. Stefanovich, Yu. V. Pisarevskiĭ, and A. V. Mosunov, Zh. Neorg. Khim. **45** (11), 1786 (2000).
12. B. V. Mill' and T. Fukuda, Zh. Neorg. Khim. **43** (4), 545 (1998).

13. B. A. Maksimov, V. N. Molchanov, B. V. Mill, *et al.*, Kristallografiya [Crystallogr. Rep.] (in press).
14. A. Pavlovska, J. Schneider, S. Werner, *et al.*, Z. Kristallogr. **118**, 187 (2003).
15. G. D. Mansfel'd and D. D. Boy, Pis'ma Zh. Éksp. Teor. Fiz. **66** (5/6), 338 (1997) [JETP Lett. **66**, 362 (1997)].
16. S. Werner, B. Maximov, H. Schulz, *et al.*, Z. Kristallogr. **217**, 460 (2002).
17. A. Pavlovska, S. Werner, B. Maximov, and B. Mill, Acta Crystallogr., Sect. B: Struct. Sci. **58**, 939 (2002).
18. I. Torjman, R. Masse, and J. C. Guitel, Z. Kristallogr. **139** (1), 103 (1974).
19. R. Hsu, E. N. Maslen, D. du Boulay, and N. Ishizawa, Acta Crystallogr., Sect. B: Struct. Sci. **53**, 420 (1997).
20. W. Eysel, U. Lambert, C. Renkenberger, and B. Nuber, Z. Kristallogr. **B201** (3/4), 235 (1992).
21. T. Gasparik, J. B. Parise, B. A. Eilen, and J. A. Hriljak, Am. Mineral. **80**, 1269 (1995).
22. M. Yamaga, P. I. Macfarlane, B. Henderson, *et al.*, J. Phys.: Condens. Matter. **9**, 569 (1997).
23. P. A. Senyushchenkov, Candidate's Dissertation in Physics and Mathematics (Inst. of Crystallography, Russian Academy of Sciences, Moscow, 1998).
24. K. A. Müller, Jpn. J. Appl. Phys., Suppl. **24** (2), 89 (1985).
25. D. C. Malocha, E. Adler, and S. Frederick, in *Proceedings of 2000 IEEE/EIA International Frequency Control Symposium, Kansas City, Missouri, USA* (2000), p. 200.
26. E. E. Lakin, M. F. Dubovik, and I. V. Krasnopol'skiĭ, Neorg. Mater. **25** (7), 1231 (1989).
27. A. A. Pugacheva, B. A. Maksimov, B. V. Mill', *et al.*, Kristallografiya **49** (1), 94 (2004).
28. B. V. Mill, Yu. V. Pisarevsky, and E. L. Belokoneva, in *Proceedings of 1999 Joint Meet. EFTF–IEEE Frequency Control Symposium, Besançon, France* (1999), Vol. 2, p. 829.
29. B. Chai, H. Qiu, Y. Y. Ji, and J. L. Lefaucheur, in *Proceedings of 1999 Joint Meet. EFTF–IEEE Frequency Control Symposium, Besançon, France* (1999), Vol. 2, p. 821.

Translated by L. Man

Crystallography Reports, Vol. 49, No. 1, 2004, pp. 70–85. Translated from Kristallografiya, Vol. 49, No. 1, 2004, pp. 75–91.

STRUCTURE OF INORGANIC COMPOUNDS

Dedicated to the 80th Birthday of L.A. Shuvalov

Structure Type of Hexagonal Tantalum Bronzes with Variable Composition $K_6Ta_{6+Z}O_{15}F_6(F, O)_y$: $Ta^{(5-\delta)+}$ Bronzes and Ta^{5+} Compounds

A. V. Arakcheeva*, G. Chapuis, V. V. Grinevich*, and V. F. Shamraĭ***

** Baikov Institute of Metallurgy and Materials Science, Russian Academy of Sciences, Leninskiĭ pr. 59, Moscow, 119334 Russia*

e-mail: arakchee@ultra.imet.ac.ru

*** Institute of Crystallography, University of Lausanne, Lausanne, Switzerland*

Received April 3, 2003

Abstract—The structure type of hexagonal compounds with the variable composition $K_6Ta_{6+z}O_{15}F_6(F, O)_y$, where $Z \le 1$ and $y \le 3$ (sp. gr. *P6/m*, $a \sim 13.12$ Å, $c \sim 3.86$ Å) has been studied. Based on the structural data for a crystal of the Ta^{5+}-containing compound and two crystals of $Ta^{(5-\delta)+}$-containing bronzes formed at the cathode during electrolysis of salt melts containing Ta^+ cations, it was established that the bronze formation is associated with the interstitial defects of intercalated Ta cations. The scheme of reduction of Ta cations at the cathode is suggested, and the formulas of the compounds are obtained with due regard for partial Ta reduction to various integral oxidation degrees. The crystals of the colorless transparent Ta^{5+}-containing compound of the composition $K_6Ta^{5+}_{6.27}O_{15}F_{7.4}$, brown semitransparent *partly reduced* Ta^+-containing bronze of the composition $K_6Ta^{5+}_{6.33}Ta^{+}_{0.55}O_{15}F_{8.2}$, and dark gray metal-like *completely reduced* Ta^+-containing bronze of the composition $K_6Ta^{5+}_{6}Ta^{+}O_{15}F_7$ are studied experimentally. © *2004 MAIK "Nauka/Interperiodica".*

INTRODUCTION

A decrease of the maximum reduction degree of *B* elements in perovskite-like and structurally related $A_{1-\Delta}B_{1+Z}(O, F)_{3\pm y}$ compounds (where *A* is an alkali metal and *B* is a transition metal from groups V or VI) gives rise to the properties unusual for complex or fluoride oxides, such as metallic or intense color, loss of transparency, metallic luster, and metallic or semiconductor conductivity [1]. In distinction from the isostructural compounds containing one or several transition metals in the maximum degree of oxidation, these compounds are called oxide bronzes, hereafter simply referred to as bronzes. Usually, to each complex oxide there correspond several oxide bronzes with different physical (optical and electric) properties depending on the degree of reduction of transition metal [1]. As a rule, the chemical composition of bronzes includes at least one element from group VI, e.g., W, (W, Nb), (W, Ta) bronzes, and the average degree of oxidation of the *B* element becomes higher than five. The degree of reduction of the transition metal in these structures is controlled by partial filling of the alkali-metal positions [1]. We showed [2] that the positions of the alkali metal in Ta bronzes with a degree of Ta oxidation less than five are fully occupied. Since there is no information on the structural processes explaining the reduction of the tantalum oxidation degree, we decided to systematically study the structures of tantalum bronzes and compare the data obtained with the corresponding data for the isostructural Ta-containing compounds (for brevity, hereafter simply called Ta^{5+} compounds). Earlier, within this program, we studied in detail the cubic perovskite-like structure of the black bronze $KTa_{1+z}O_3$ ($z \sim 0.107$) possessing semiconductor properties [2]. Comparing the data obtained with the structural characteristics of a transparent dielectric $KTaO_3$ crystal [3], we found that a decrease in the averaged degree of tantalum oxidation in the bronze (partial reduction) results in the formation of substitutional defects (about 9% K cations per Ta–Ta dumbbell), which explains the semiconductor properties, loss of transparency, and metal-like appearance of the crystals. The establishment of these structural characteristics became possible because of the use of precision experimental and computational methods [2, 3].

The structure of the hexagonal bronze–conductor of the composition $K_6Ta_{6.5}O_{15+x}F_{6+y}$ [4] is compared with the structure of its dielectric analogue

$K_6Ta_{6.5}O_{14.5}F_{9.5}$ [5] refined in a rather crude approximation. As a result, the conclusions drawn in [4] are not complete.

The crystals of analogous hexagonal tantalum bronzes obtained in our study and having different colors and transparencies and the crystals of newly synthesized Ta^{5+} compound allowed us to perform comparative structural studies by the same methods. As a result, we obtained new data on the structure type and the effect of the degree of tantalum oxidation and their effect on the fine details of the crystal structure and the optical characteristics of these crystals. The comparative analysis of newly established structural characteristics was performed based on the data obtained and the known data [4, 5]. The results of this analysis are considered below.

EXPERIMENTAL

Synthesis. Two types of tantalum bronzes—dark-gray metal-like nontransparent crystals with metallic luster (bronze **I**) and brown semitransparent crystals (bronze **II**)—were obtained from the melted salt K_2TaOF_5–$(KF + NaF + LiF)_{eut}$ system with the use of a soluble TaO anode by electrochemical deposition at a molybdenum cathode. Electrolysis was performed at the current density $D_c = 0.15$ A/cm^2 and a temperature of 750°C. The synthesis of tantalum and Ta-containing compounds was described in detail elsewhere [3]. Both types of crystals were formed in one experiment. X-ray diffraction analysis (DRON-3M diffractometer, MoK_α radiation) of the powder prepared from the cathode product indicated that all the crystals were hexagonal tantalum bronzes, one of which was studied in detail earlier [4]. Both types of crystals had the habit of elongated hexagonal prisms or their fragments. It should be emphasized that the cathode product consisted of brown crystals of different shades and degrees of transparency. Against the background of brown crystals, there were also visually distinguishable homogeneous dark-gray metal-like nontransparent crystals. The electrolyte crystallized near the cathode also contained transparent crystals with a similar habit (**III**) whose diffraction patterns indicated the same structure type. The formation of crystals **III** without any contact with the cathode and their transparency led to the conclusion that tantalum in their composition has the same degree of oxidation (5+) as in the K_2TaOF_5 salt used in electrolysis.

It is also important to note that the formation of hexagonal bronzes at the cathode in electrolysis of the above salt melts is a poorly reproducible process even if all the controllable parameters of electrolysis, such as the melt temperature, current density, and concentration of the K_2TaOF_5 salt, are maintained constant. In addition, transparent crystals of this type were also formed during crystallization on a cathode of tetragonal (structure type of tetragonal W-bronze) and cubic (perovskite type) bronzes.

Chemical analysis. Chemical microanalysis (ARL-SEMQ analyzer (15 kV, 25 nA) equipped with EDAX (12 kV, 100 nA)) showed that the crystals grown contained K, Ta, F, and O. No traces of Na were revealed. The accuracy of the microanalysis for each type of crystal was relatively low because of the varying Ta/K ratio (Table 1). However, one can clearly see the general tendency of an increase in the tantalum content in the row "transparent crystals **III**—brown semitransparent bronze **II**—dark-gray metal-like bronze **I**" (Table 1). Within the experimental accuracy, the fluorine content (7–8 wt %) is independent of the type of crystal. The evaluation of the chemical composition based on the refined structural data (Table 1) confirms these data.

Single-crystal diffraction experiment. The structural studies were performed on selected **I**, **II**, and **III** single crystals having the shape of hexagonal prisms with the well formed {*hk*0} and {001} crystal faces. X-ray diffraction experiments on all three types of single crystals were performed on a KM4 diffractometer with a CCD detector (MoK_α radiation). The main characteristics of the experiments and the unit-cell parameters of the crystals are indicated in Table 2. The analysis of the reciprocal-space sections did not reveal any satellite reflections or reflections that would indicate a multiple increase of any lattice parameter for any of the crystals.

STRUCTURE REFINEMENT

All the structural computations were performed using the JANA2000 program system [6]. The characteristics of the refinement are indicated in Table 2. The corresponding parameters of the atomic positions are listed in the upper part of Table 3, and the interatomic distances, in Table 4.

The refinement method was described in detail in the structure determination of the analogous compound—black hexagonal bronze [4]. The atomic coordinates of the structure framework borrowed from [4] [Ta(1), K, O(1), O(2), O(3), and F(1)] were refined in the full-matrix anisotropic approximation of atomic thermal vibrations within the sp. gr. *P*6/*m*. The F(1) position of this structure type was unambiguously established earlier [4] from the balance of valence strengths at anions (calculated by the methods suggested in [7]) and was confirmed in the present study (Table 5). The successive refinement of the occupancies of the Ta(1) and K positions indicated their complete filling (within the computation accuracy).

The partly occupied Ta(2) position on the sixfold axis was established from the residual synthesis calculated from the refined positions of the framework atoms. Pronounced displacements of Ta(2) atoms along the *z* axis were refined either by splitting the atomic position along this axis or by refining the components

Table 1. Characteristics of the chemical composition of $K_6Ta_{6+z}O_{15}F_6(O, F)_y$ compounds. **I** indicates crystals of metal-like bronze; **II**, crystals of brown semitransparent bronze; and **III**, colorless transparent crystals of the Ta^{5+}-containing compound

	I	**II**	**III**
Microanalysis data			
Atomic Ta/K ratio	1.10–1.20	1.08–1.16	1.03–1.10
F content	7–8 wt % (20–23 at. %)		
Refined structural data			
Chemical formula*	$K_6Ta_{6+0.487+z1+z2+z3}O_{15}F_6(O, F)_{1.1}$	$K_6Ta_{6+0.516+z1+z2+z3}O_{15}F_6(O, F)_{2.18}$	$K_6Ta_{6+0.271}O_{15}F_{6+1.4}$
Number of atoms Ta_{int} in the $M(1)$, $M(2)$, and $M(3)$ positions	$z1 + z2 = 0.20(8)$; $z3 = 0.36(6)$; $z = z1 + z2 + z3 = 0.56(14)$	$z1 + z2 = 0.24(8)$; $z3 = 0.12(6)$; $z = z1 + z2 + z3 = 0.36(14)$	
Chemical composition with allowance for interstitial defects, Ta_{int}	$K_6Ta_{7.05}O_{15}F_6(O, F)_{1.1}$	$K_6Ta_{6.88}O_{15}F_6(O, F)_{2.18}$	$K_6Ta_{6.27}O_{15}F_{7.4}$
The most probable composition of **I** and **II**	$K_6Ta_7O_{15}F_7 = K_6Ta_6^{5+}Ta^{+}O_{15}F_7$	$K_6Ta_{6.88}O_{15}F_{8.2} = K_6Ta_{6.33}^{5+}Ta_{0.55}^{+}O_{15}F_{8.2}$	
Atomic Ta/K ratio	1.77	1.15	1.05

* The given values correspond to the refinement of the main positions of the structure with no account for intercalated Ta atoms (see Table 3).

Table 2. Main characteristics of diffraction experiments and refinement of structures **I**, **II**, and **III**

	I	**II**	**III**
X-ray experiment			
Diffractometer	KM4CCD		
Radiation	MoK_α		
Range of measurements, $\sin\theta/\lambda_{max}$	0.8	0.8	0.8
Number of measured reflections	30131	30216	29494
Number of crystallographically independent reflections with $I > 6\sigma(I)$	800	780	680
μ, cm^{-1}	31.82	31.73	30.56
Allowance for absorption	Numerical integration over the real shape of crystal		
R_{av}	0.097	0.075	0.087
Sp. gr.	*P*6/*m*	*P*6/*m*	*P*6/*m*
Unit-cell parameters *a*, *c* (Å), and *V* ($Å^3$)	13.123(1), 3.8622(4); 575.995	13.132(1), 3.8610(4); 576.606	13.110(1), 3.8625(4); 574.899
d_x, g/cm^3	5.457	5.381	5.055
Refinement characteristics*			
$R(F)$, $wR(F)$	0.0333, 0.0447	0.0318, 0.0423	0.0273, 0.0361
Weighting scheme	$w = 1/\sigma(F)^2$		
GOF	2.90	2.80	1.32
Parameter of isotropic extinction	0.0169(3)	0.0122(3)	0.0148(2)
ρ_{max}, ρ_{min}, $e/Å^3$	3.83, –1.97	3.51, –1.83	2.11, –2.14

* Values corresponding to the refinement of the main structural positions with no allowance for intercalated Ta atoms (see Table 3).

of the 6th rank tensor of anharmonic vibrations. The zero values of the *C* and *E* tensor components (because of the position symmetry) added eight parameters that should be refined independently, with the ratio of the number of reflections to the number of the parameters to be refined exceeding 15. The characteristics of the refinement quality of these two variants were practically equivalent, and the position splitting was very small (maximum Ta(2)–Ta(2) distance 0.15 Å for crystals **III**), which did not allow us to select unambigu-

Table 3. Atomic parameters in structures **I**, **II**, and **III**

Atomic positions and their characteristics	**I**	**II**	**III**
Main structural positions			
K [6*j* (*x y* 0)]:			
p; *x*, *y*	1; 0.0.6566(1), 0.9127(1)	1; 0.6568(1), 0.9131(1)	1; 0.6584(1), 0.9128(1)
U_{eq}	0.0318(5)	0.0332(5)	0.0376(5)
*U*11, *U*22	0.0468(7), 0.0209(5)	0.0465(8), 0.0236(6)	0.0562(8), 0.0241(6)
*U*33, *U*12, Å^2	0.0191(5), 0.0104(5)	0.0198(5), 0.0101(6)	0.0225(5), 0.0124(6)
Ta(1) [6*k* (*x y* 0.5)]:			
p; *x*, *y*	1; 0.36996(1), 0.84413(1)	1, 0.36989(1), 0.84412(1)	1, 0.36986(1), 0.84454(1)
U_{eq}	0.0093(2)	0.0121(2)	0.0126(2)
*U*11, *U*22	0.0099(3), 0.0064(3)	0.0129(3), 0.0099(3)	0.0129(3), 0.0103(3)
*U*33, *U*12, Å^2	0.0114(3), 0.0040(3)	0.0123(3), 0.0047(3)	0.0148(3), 0.0060(3)
O(1) [6*k* (*x y* 0.5)]:			
p; *x*, *y*	1; 0.4659(2), 0.7774(2)	1; 0.4681(2), 0.7788(2)	1; 0.4667(2), 0.7767(2)
U_{eq}	0.024(1)	0.026(1)	0.025(1)
*U*11, *U*22	0.010(1), 0.012(2)	0.018(1), 0.008(2)	0.014(1), 0.010(2)
*U*33, *U*12, Å^2	0.050(2), 0.007(1)	0.054(2), 0.009(1)	0.050(2), 0.005(1)
O(2) [3*g* (0.5 0 0.5)]:			
p; U_{eq}	1; 0.038(2)	1; 0.040(2)	1; 0.032(2)
*U*11, *U*22	0.012(2), 0.004(2)	0.015(2), 0.012(2)	0.013(2), 0.003(2)
*U*33, *U*12, Å^2	0.087(4), –0.004(2)	0.089(4), –0.001(2)	0.067(4), –0.006(2)
O(3) [6*j* (*x y* 0)]:			
p; *x*, *y*	1; 0.6465(3), 0.1513(4)	1; 0.6446(3), 0.1512(4)	1; 0.6465(3), 0.1506(4)
U_{eq}	0.044(2)	0.045(2)	0.042(2)
*U*11, *U*22	0.064(3), 0.081(3)	0.069(3), 0.073(3)	0.061(3), 0.074(2)
*U*33, *U*12, Å^2	0.000(8), 0.046(2)	0.000(9), 0.042(2)	0.000(5), 0.039(2)
F(1) [6*k* (*x y* 0.5)]:			
p; *x*, *y*	1; 0.6530(2), 0.7412(2)	1; 0.6531(2), 0.7417(2)	1; 0.6547(2); 0.7420(2)
U_{eq}	0.025(1)	0.026(1)	0.028(1)
*U*11, *U*22	0.015(1), 0.023(1)	0.011(1), 0.023(1)	0.020(1), 0.023(1)
*U*33, *U*12, Å^2	0.038(2), 0.009(1)	0.042(2), 0.006(1)	0.045(2), 0.013(1)
Ta(2)* [1*b* (0 0 0.5)]:			
p; U_{eq}	0.487(1); 0.0291(1)	0.516(1); 0.0393(1)	0.271(1); 0.066(4)
*U*11 = *U*22, *U*33	0.0104(8), 0.067(2)	0.022(1), 0.073(3)	0.016(2), 0.16(1)
*U*12, Å^2	0.0052(4)	0.0112(7)	0.008(1)
*D*1111, *D*1133	–0.0013(1), –0.015(1)	–0.0000(5), –0.017(2)	–0.0022(6), –0.020(7)
*D*3333, Å^2	–0.21(6)	–0.21(11)	4.0(9)
*F*111111, *F*111112	–0.00025(3), –0.00011(2)	0.000(1), 0.00004(6)	–0.0005(1), –0.00020(8)
*F*111122	–0.00005(2)	0.00003(5)	–0.00014(7)
*F*111133, *F*113333	–0.0010(2), –0.020(3)	–0.0014(4), –0.024(5)	–0.0031(9), –0.02(3)
*F*333333, Å^2	–0.6(2)	–0.8(4)	11(4)
F(2) [12*l* (*x y z*)]:			
p	0.092(2)	0.182(2)	0.113(2)
x, *y*, *z*	0.038(2), 0.134(1), 0.188(6)	0.036(2), 0.141(2), 0.195(4)	0.037(2), 0.111(2), 0.100(4)
U_{iso}	0.08(1)	0.093(8)	0.055(6)
Positions of intercalated Ta atoms			
M(1) [2*e* (0 0 *z*)]:			
p; *z*; U_{eq} = 0.01 Å^2	0.025(8); 0.127(2)	0.03(1); 0.122(2)	
M(2) [6*k* (*x y* 0.5)]:			
p; *x*, *y*; U_{eq} = 0.01 Å^2	0.025(8); 0.121(2), 0.046(2)	0.03(1); 0.115(2), 0.046(2)	
M(3) [6*k* (*x y* 0.5)]:			
p; *x*, *y*; U_{eq} = 0.01 Å^2	0.06(1); 0.677(2), 0.888(2)	0.02(1); 0.685(2), 0.892(2)	

* Position was refined in the anharmonic approximation of atomic thermal vibrations. The independent values of $D \times 10^4$ and $E \times 10^6$ are given.

Table 4. Interatomic distances (Å) in structures **I**, **II**, and **III**

	I	**II**	**III**
Framework [Ta(1)O_5F] octahedron			
Ta–O(1)	1.859(4) 1.989(3)	1.872(4) 1.994(3)	1.878(4) 1.977(3)
Ta–O(2)	1.899(1)	1.915(1)	1.894(1)
Ta–O(3)	1.948(1) × 2	1.944(1) × 2	1.947(1) × 2
Ta–F(1)	2.052(4)	2.055(4)	2.062(4)
Framework [KO_4F_4] polyhedron			
K–O(1)	2.950(2) × 2	2.934(2) × 2	2.958(2) × 2
K–F(1)	2.948(2) × 2 2.776(2) × 2	2.947(2) × 2 2.777(2) × 2	2.939(2) × 2 2.767(2) × 2
K–O(3)	3.19, 3.03	3.19, 3.04	3.20, 3.06
Channel [Ta(2)F_6] statistical prism			
Ta(2)–F(2)	1.98(2) × 6	2.04(2) × 6	2.00(2) × 6
Framework–channel bonds			
K–F(2)	2.82 × 0.18 2.90 × 0.18	2.92 × 0.36 2.95 × 0.36	3.01 × 0.22 3.06 × 0.22

Table 5. Balance of valence strengths at framework [$K_6Ta_6O_{15}F_6$] anions in structures **I**, **II**, and **III**

Anions		Ta(1)	K	Total charge at anions
O(1)	I	1.179 + 0.830	0.110 × 2	2.229
	II	1.139 + 0.819	0.114 × 2	2.186
	III	1.120 + 0.857	0.107 × 2	2.191
O(2)	I	1.058 × 2		2.116
	II	1.014 × 2		2.028
	III	1.073 × 2		2.146
O(3)	I	0.927 × 2	0.088 + 0.057	1.999
	II	0.937 × 2	0.086 + 0.057	2.017
	III	0.930 × 2	0.081 + 0.055	1.996
F(1)	I	0.628	0.075 × 2 + 0.120 × 2	1.018
	II	0.623	0.076 × 2 + 0.120 × 2	1.015
	III	0.611	0.077 × 2 + 0.123 × 2	1.011

ously the true variant. The data in Tables 1 and 2 are given for the variant of the anharmonic approximation of atomic displacements for all three crystals. However, we can not exclude possible splitting of the Ta(2) position, especially for crystals **III**.

The F(2) position of the anionic environment of Ta(2) atoms was determined from the residual electron densities calculated within two space groups, *P*6/*m* and $P\bar{6}$. In the sp. gr. $P\bar{6}$, the distribution of the residual electron density indicated the existence of a sixfold axis for all three crystals, which uniquely indicated the sp. gr. *P*6/*m*. Partial delocalization of the F(2) position, which manifests itself in high values of atomic thermal displacements and in the existence of regions with elevated residual electron density, was studied in detail in [4] and confirmed in this study for all three crystals. The refinement of the anisotropy of atomic displacements gave the negative *U*33 components for crystals **III**. Therefore, we returned to the isotropic coefficients for all three crystals. For crystals **III**, the requirement of electroneutrality at the known degree of Ta ion oxidation (Ta^{5+}) uniquely indicated the filling of the F(2) position solely with F ions. One cannot exclude possible partial replacement of F by O atoms in this position for crystals **I** and **II**, but this would practically not influence the refinement characteristics and, therefore, cannot unambiguously be established in the refinement.

RESIDUAL ELECTRON DENSITY

Comparing the residual electron density for crystals of bronzes **I** and **II** with those for transparent crystals **III**, we see that the latter are characterized by additional maxima *M*(1), *M*(2), and *M*(3) (Figs. 1, 2). The electron-density values at these maxima are ~2.0 e/Å^3 at M(1) for both bronzes, 2.6 and 3.3 e/Å^3 at *M*(2) for bronzes **I** and **II**, and 3.8 and 3.5 e/Å^3 at *M*(3) for bronzes **I** and **II**, respectively. The exact localization of these maxima with approximately equal coordinates for both bronzes and their absence for the transparent crystals allowed us to identify the maxima with additional (intercalated) atoms—interstitial defects.

The requirement of electroneutrality of the compounds with the reduced degree of tantalum oxidation in **I** and **II** excludes anion intercalation. Therefore, the "intercalated position" might be occupied by either K or Ta cations. According to the chemical analysis, $(Ta/K)_{obs} > 1.08$ (Table 1). For the basic atoms of the structure, this ratio has the value [Ta(1) + Ta(2)]/K = 1.8 and 1.09 for **I** and **II**, respectively. The additional K cations would decrease this ratio, but this is inconsistent with the microanalysis data. However, the assumption about possible intercalation of Ta cations in the bronze structures would explain the increase in Ta content in bronzes indicated above in comparison with the Ta content in transparent Ta^{5+} compound.

The allowance for the additional atomic positions with low occupancies with Ta_{int} atoms slightly reduces the reliability factors of the structural refinement of bronzes **I** and **II** and removes the maxima of the residual electron density from the syntheses. The refined characteristics of these positions are indicated in the lower part of Table 3.

The refinement shows that the general formula of all three crystals studied can be written as $K_6Ta_{6+z}O_{15}F_6(F, O)_y$. The values of the variable parameters and their notation are given in Table 1. The necessary corrections to these data are considered and discussed in the next section.

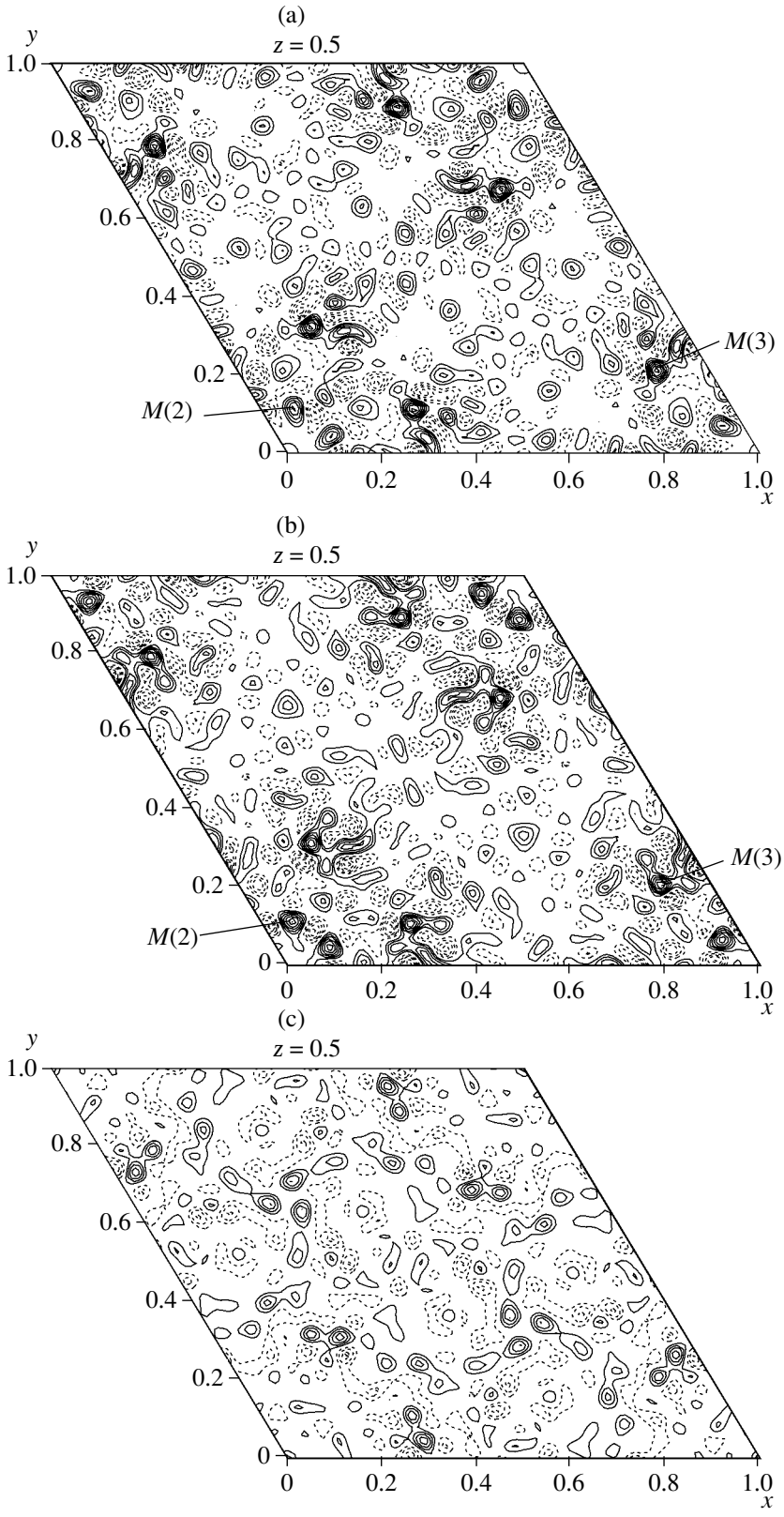

Fig. 1. (*xy* 0.5) section of the residual electron-density for $K_6Ta_{6+Z}O_{15}F_6(F, O)_y$ crystals: (a) bronze **I**, (b) bronze **II**, and (c) Ta^{5+}-containing compound. Isolines are separated by 0.5 e/Å^3. The *M*(2) and *M*(3) maxima are identified with the interstitial defects of tantalum cations.

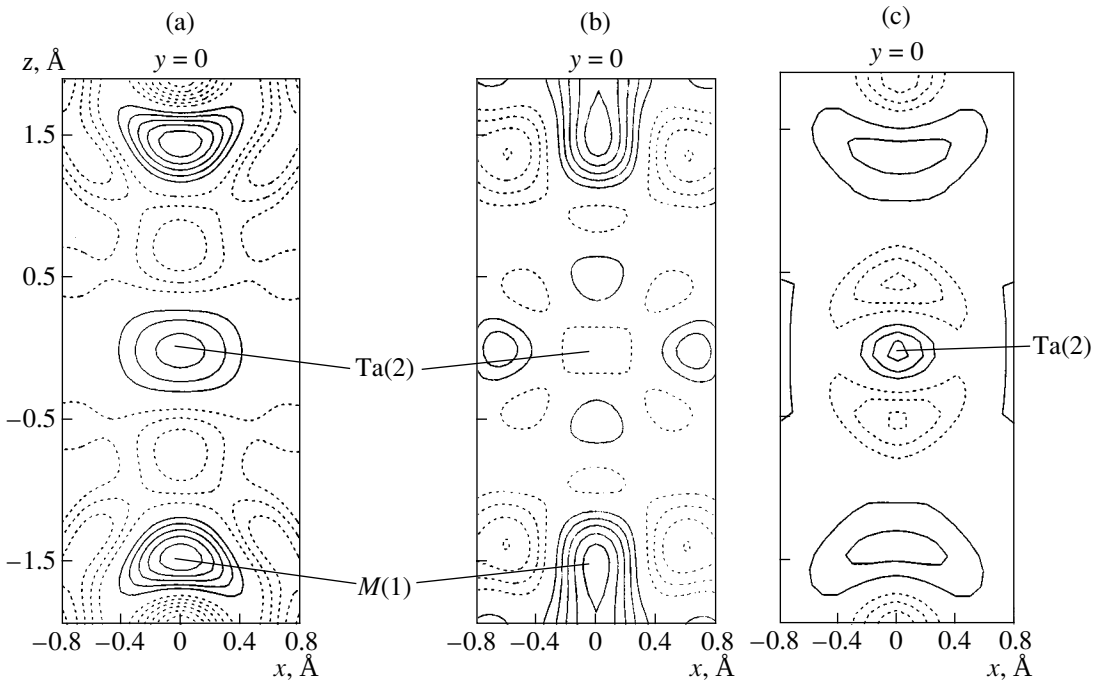

Fig. 2. ($x0z$) section of the residual electron-density for $K_6Ta_{6+z}O_{15}F_6(F, O)_y$ crystals: (a) bronze **I**, (b) bronze **II**, and (c) Ta^{5+}-containing compound. Isolines are separated by 0.25 e/Å^3. The Ta(2) position is indicated. The $M(1)$ maximum is identified with interstitial defects of tantalum cations.

DISCUSSION OF RESULTS

Characteristics of the $K_6Ta_{6+z}O_{15}F_6(F, O)_y$ structure type. Comparing the structures of the three crystals studied with the structures of two structures determined earlier [4, 5], we established the main characteristics of the structure type of hexagonal tantalum bronzes of the variable composition $K_6Ta_{6+z}O_{15}F_6(F, O)_y$ with the unit-cell parameters $a \sim 13.12$ Å and $c \sim 3.88$ Å, sp. gr. $P6/m$. Figure 3 shows this structure projected along the sixfold axis.

The [Ta(1)O_5F(1)] octahedra with the central Ta(1) atom lying in the m plane ($z = 0.5$) form an open framework with wide (about 6 Å in diameter) hexagonal channels. The framework is complemented with K atoms also located in the m plane ($z = 0$) in the channel walls and characterized by the trigonal–prismatic environment of O and F(1) atoms. The balance of valence strengths at anions (Table 5) shows that this coordination is complemented with two, more distant, O(3) atoms (at distances of ~3.0 and ~3.2 Å). The positions of all the main atoms [Ta(1), K, O(1), O(2), O(3), and F(1)] in all the crystals studied have close values of all the parameters, including the coefficients of anisotropic atomic displacements. Therefore, they all are considered as framework atoms. The chemical formula of the framework can be written as [$K_6Ta_6O_{15}F_6$]; the framework has the constant composition and structure in all the crystals studied, including those described in [4, 5].

The partially occupied Ta(2) and F(2) positions are situated in the hexagonal channels of the structure (Figs. 3, 4). The Ta(2) atom is located on the sixfold axis of the channel at the same level as the Ta(1) atom, $z = 0.5$. The atoms in this position are partly delocalized (up to splitting of the position, with the maximum amplitude along the sixfold axis being of about 1 Å [5]). The F(2) atoms surround the Ta(2) atom statistically and occupy the positions of the hexagonal prism. However, this prism cannot exist locally because of too short F(2)–F(2) contacts (~1.5 Å) in the basis. Therefore, this prism can be considered as a result of the superposition of two local trigonal prisms or two deformed octahedra (trigonal antiprisms). The atoms in the F(2) position are delocalized more pronouncedly than atoms in the Ta(2) position, which is seen from too high values of the atomic-displacement parameters and the existence of rather large area of elevated residual electron density, which was indicated in [5] and discussed in detail in [4]. Despite the fact that the coordinates of the F(2) position differ from crystal to crystal (Table 3, Fig. 4), the Ta(2)–F(2) distances have the same values, ~2.0 Å (Table 4). The chemical formula of the structural unit located in the channel can be written as [$Ta_x(F, O)_y$]. It should be noted that this unit does not necessarily contain oxygen (crystal **III**). In the crystals known, $0.27 < x < 0.52$ and $1 < y < 2.5$. Thus, the channel has a variable composition and structure.

One of the characteristic features of the structure type of hexagonal tantalum bronzes is the noticeable

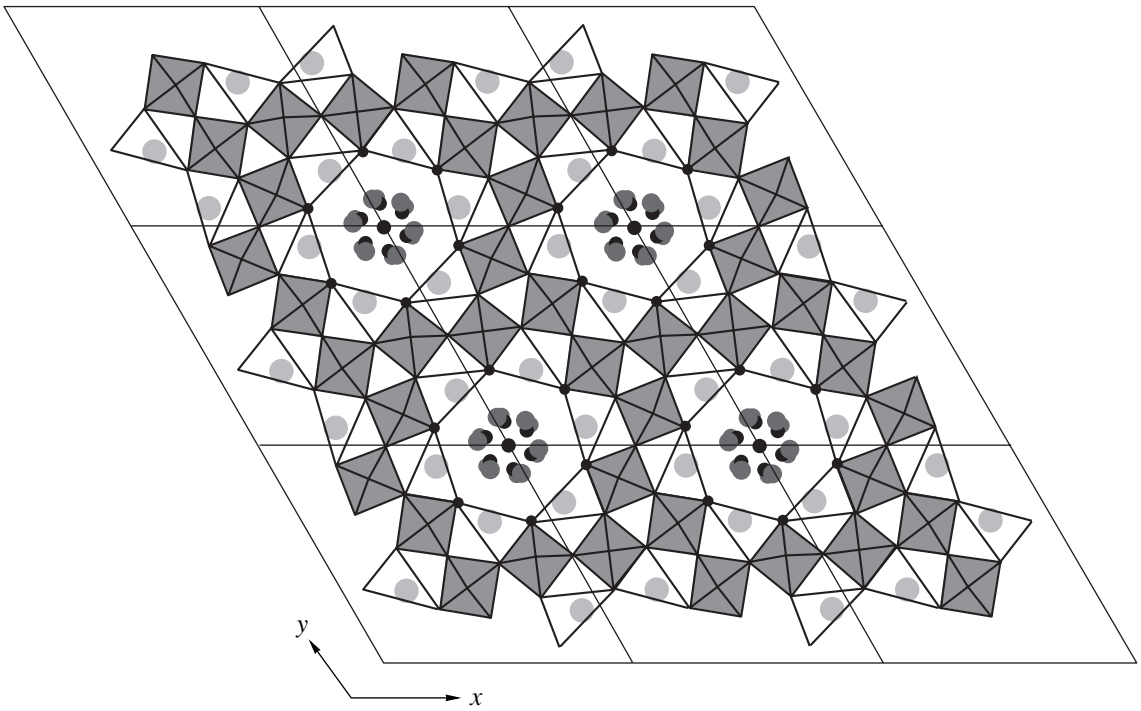

Fig. 3. $K_6Ta_{6+Z}O_{15}F_{6+y}$ structure projected along the sixfold axis. The structure framework is built by [Ta(1)O_5F(1)] octahedra and K atoms (depicted by large gray circles). The central atoms of octahedra, Ta(1), are located at a height of $z = 0.5$; the K atoms are located at a height of $z = 0$. The F(1) atoms are shown by black dots. Black circles in the centers of hexagonal channels show partly occupied Ta(2) positions. The statistical environment of Ta(2) atoms with F(2) atoms (dark gray circles) is shown as the superposition of the positions found in five crystals: **I**, **II**, and **III** (present study) and two crystals studied earlier [3, 4]. Thin lines show projections of the coordinate axes of nine unit cells.

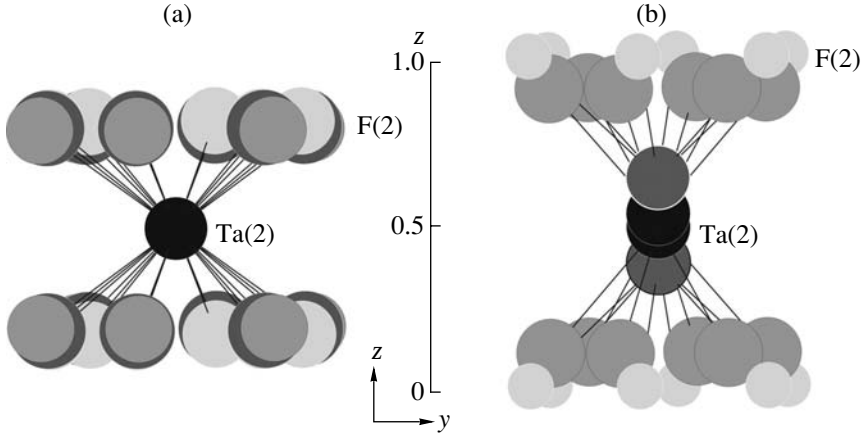

Fig. 4. Channels in the $K_6Ta_{6+Z}O_{15}F_{6+y}$ structures: (a) bronzes; F(2) positions in crystals **I** and **II** (present work) and crystal studied in [4] are shadowed differently; (b) Ta^{5+}-containing compounds; Ta(2) and F(2) positions are indicated by more intense color for crystal **III** and less intense color for a crystal studied in [5].

change in the positions of channel atoms (mobility) with respect to the framework both within one structure (partial delocalization of F(2) atoms and anharmonicity of atomic displacements or splitting of the Ta(2) position) and in the transition from one crystal to another (the change in the coordinates of the F(2) position) (Figs. 3, 4). This is associated with the fact that the Ta(2) cations located along the channel axis are not related to the framework anions (the minimum Ta(2)–F(1) distance is ~4.1 Å), whereas the channel F(2) anions and the framework cations form K–F(2) bonds statistically distributed over the channel with the low probability of their existence (0.1–0.2) determined by partial filling of the F(2) position (Table 3). Partial delocalization of F(2) and splitting of the Ta(2) position within one crystal are possible because of a possible

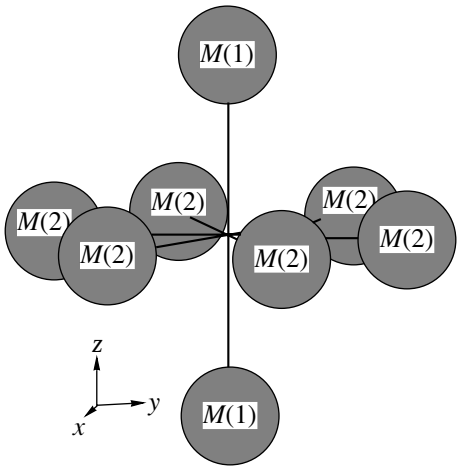

Fig. 5. Space–time cluster of interstitial defects—Ta_{int} cations—with the center in the vacant Ta(2) position in structures of bronzes (interstitial defects of the first-type).

rotation of the K–F(2)–Ta(2) rigid unit: if one end of the chain (the K atom) is fixed, the other end of the chain [Ta(2) atom, which is displaced along the channel axis] and its middle point [F(2) atom] can also change their positions as was considered in detail elsewhere [4]. The causes of the variation of the coordinates of the F(2) atom from crystal to crystal are explained by interstitial defects considered below.

Thus, the main characteristics of the structure type considered above—a framework having the constant composition and structure and the channels of the variable compositions mobile with respect to the framework—are independent of the degree of tantalum oxidation.

Differences in the structures refined. Crystals **I**, **II**, and **III** and the crystals described earlier [4, 5] have different compositions, different states of Ta-ion oxidation, and different optical properties (color and transparency). Therefore, it is interesting to consider not only the common features of the structure type but also the individual features of various crystals. The differences in their structures manifest themselves, first of all, in the statistical filling of hexagonal channels with Ta(2) and F(2) atoms (Figs. 3, 4).

The occupancies of the Ta(2) positions are 0.487(1) and 0.516(1) in bronzes **I** and **II**, respectively, whereas in crystal **III**, the occupancy of this position is almost two times lower, 0.271(1). There is no one-to-one correspondence between the occupancies of the Ta(2) and F(2) positions: to the minimum occupancy of the Ta(2) position there corresponds the intermediate occupancy of the F(2) position (Table 3). In a crystal of black bronze studied in [4], the Ta(2) position has the same coordinates as in bronzes **I** and **II**, but its occupancy is lower, 0.45(1). The coordinates (0.038 0.131 0.171) and occupancy [p = 0.13(4)] of the F(2) position in the crystal studied in [4] differ from those obtained in the present study (Fig. 4a, Table 3), but the Ta(2)–F(2) distances are the same, ~2.0 Å.

In transparent crystals studied in [5], the Ta(2) atom was located in the split position with a Ta(2)–Ta(2) distance of 1.0 Å and occupancy of 0.5. This value is approximately two times higher than in analogous transparent crystals **III**. The data obtained in this study show that this position may also be split in crystals **III**, but with a much shorter Ta(2)–Ta(2) distance, ~0.15 Å (Fig. 4b). The F(2) position was more precisely localized in the sp. gr. $P\bar{6}$ in [5], but we failed to localize this position in crystals **III**. However, despite the fact that the coordinates of this position obtained in [5] do not coincide with any of the variants in our study (Fig. 4b), the Ta(2)–F(2) distances are also equal to ~2.0 Å.

The mobility of atoms in channels (high values of the atomic thermal displacements of Ta(2) and partial delocalization of F(2) atoms) is a characteristic feature of all the crystals, although the mobility of Ta(2) atoms is considerably higher in Ta^{5+} compounds than in bronzes (Fig. 4, Table 3). These discrepancies have not been interpreted because of interstitial defects in the bronze structures.

Interstitial defects and their influence on structural characteristics. Now, proceed to the experimental data which were obtained only in the present study (no similar data were considered in [4, 5]).

Analysis of residual electron-densities revealed additional intercalated tantalum atoms (cations), Ta_{int}, in the structures of bronzes **I** and **II** [M(1), M(2), and M(3) positions in Figs. 1a, 1b and 2a, 2b] and showed their absence in the structure of compound **III** (Figs. 1c, 2c). The low occupancies of the intercalation positions ($pM(1) = pM(2) \sim 0.03$ and $pM(3) = 0.02$ and 0.06, Table 3) refined at the fixed value of the of thermal-displacement parameters (U_{eq} = 0.01 Å^2) result in low accuracy of the concentration of interstitial defects determined ($z = z1 + z2 + z3$ in Table 1, where zi is the number of Ta_{int} atoms in the $M(i)$ position per formula unit). Nevertheless, the Ta/K ratios obtained with due regard for Ta_{int} agree better with the data of chemical analysis performed without allowance for Ta_{int} atoms.

The positions of the interstitial defects Ta_{int} can be divided into two groups having different occupancies and different crystal-chemical function. The first group is formed by the M(1) and M(2) positions in the structure channels. These positions form a hexagonal bipyramidal cluster with the center coinciding with the position of the Ta(2) atom (Fig. 5). This cluster can be represented as the superposition of four Ta–Ta dumbbells whose centers are located at one point and the Ta–Ta distances range from 2.7 to 2.9 Å. One dumbbell is oriented along the sixfold axis, whereas the three other dumbbells are located in the perpendicular plane at an angle of 60° to one another. The simultaneous presence of any two dumbbells of the four with the center at the same local point is low probable because of too short

(less than 1.3 Å) interatomic distances. Therefore, the cluster configuration of the defects of the first group can be considered as a result of averaging of the statistical distribution of Ta_{int} atoms over the eight vertices of the cluster. The location of the atom at the Ta(2) position excludes the formation of a defect cluster around this local point. The crystal-chemical features of the interstitial defects of the first group can be formulated in the following way. (i) Ta_{int} atoms do not form anomalously short distances with atoms from any fully occupied position of the structure and (ii) Ta_{int} atoms form short distances with the atoms in the partially Ta(2) (~1.3 Å) and *M*(3) (~2.3 Å) positions.

The second type of interstitial defects is determined by the *M*(3) position. Similar to K atoms, this position belongs to the framework walls limiting the channel space and, therefore, can be considered as the framework position complementing the plane of location of the basic tantalum atoms, Ta(1) and Ta(2), to the configuration of a close packed layer (Fig. 6). The distances between the main Ta(1) atoms in this plane range within 3.65–3,82 Å. The *M*(3)–Ta(1) (3.09–3.77 Å) and *M*(3)–Ta(2) (3.64–3.73 Å) distances are comparable to the Ta(1)–Ta(1) distances in the plane. The centers of the statistical clusters considered above are also located in this plane. For further analysis, one should bear in mind that the positions of the first type of defects, *M*(2), are located between the vacant Ta(2) positions and the position of the interstitial defects of the second type, *M*(3) (Fig. 6). The crystal-chemical characteristic of the interstitial defects of the second type is anomalously short distances to the completely filled positions of K atoms, K–*M*(3) ~ 2.0 Å, which are equal to the sum of the ionic radii of K^+ and Ta^{5+}. We also observed anomalously short Ta–Ta_{int} distances (1.4 Å) in the crystals of the β-Ta tetragonal modification of metallic tantalum [8]. In the tantalum bronzes under consideration, the intercalated atoms in the β-Ta structure complement the plane of location of the main atoms to a close packed plane, with the average Ta–Ta distance in the plane being of about 2.8 Å (the distances range from 2.68 to 2.98 Å).

The mobility of channel atoms correlates with the concentration of defects of the second type in bronzes **I** and **II**: the thermal parameters of both Ta(2) and F(2) are much higher than those in bronze **II**, where the occupancy of the *M*(3) positions is three times lower than in bronze **I** (Table 3). This correlation can be explained in the following way. The framework–channel interaction may occur only via the formation of K–F(2) bonds. Thus, the mobility of the channel atoms depends on the strength of this interaction characterized by the corresponding bond lengths. In the Ta^{5+} compounds, the total charge of the framework of the $K_6Ta_6O_{15}F_6$ structure is zero and the lengths of the K–F(2) bonds exceeding 3.01 Å (crystal **III**, Table 4) indicate the van der Waals nature of the framework–channel interaction. Since the balance of the valence strengths at the framework anions (Table 5) calculated using the data for Ta^{5+} does not allow one to distinguish between bronzes **I** and **II**, on the one hand, and compound **III**, on the other hand, it is possible to draw the conclusion that tantalum occupying the main positions of the framework has the maximum oxidation degree (Ta^{5+}) of all three structures. In this case, the Ta cations incorporated into *M*(3) give rise to the total positive charge of the framework which should be compensated with the negative charge of the structural unit located in the channel and an increase in the ionic component of the interaction between the framework K cations and the channel F(2) anions, i.e., by shortening of the K–F(2) distances. Indeed, the bond length shorter in **I** in

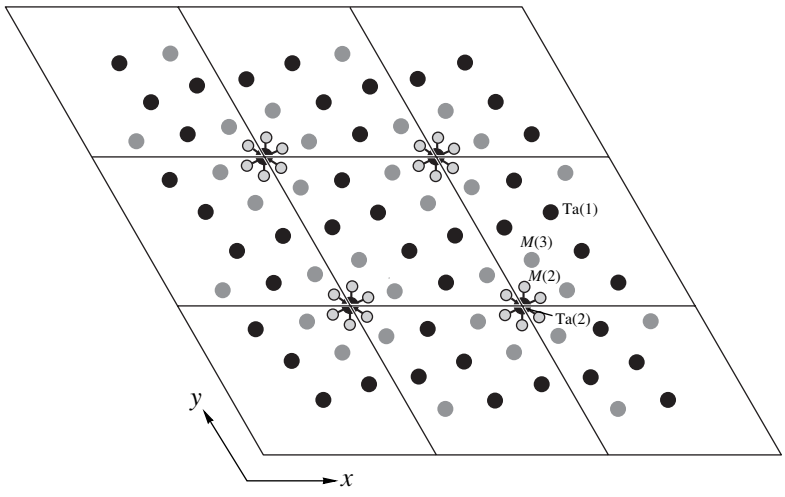

Fig. 6. Distribution of Ta_{int} cations in the (*xy*0.5) plane. Interstitial defects of the second type (*M*(3) position) are shown by dark gray circles and complement the main Ta(1) and Ta(2) positions (black circles) to a close packed layer. Interstitial defects of the first type (*M*(2) position shown by light gray circles) are located along the paths of cation migration from the Ta(1) to *M*(3) position.

comparison with the bond length formed in **II** corresponds to a higher concentration of interstitial defects in *M*(3) (Table 3). Taking into account the structural rigidity and the charge balance of the framework and, in principle, possible dynamics of channel atoms, one can assume that shortening of K–F(2) distances is explained by the displacement of F(2), which was really observed experimentally: at close K coordinates, the minimum length of the K–F(2) bond decreased from 3.01 Å in **III** to 2.82 Å in **I** and 2.92 Å in **II** because of the differences in the coordinates of the F(2) atoms (Table 3).

Thus, the change in the coordinates of the F(2) atoms observed in different crystals (Table 3) is the necessary condition for attainment of the optimum K–F(2) distances for each structure (Table 4) and is determined by the positive charge of the framework dependent, in turn, on the concentration of the second-type interstitial defects in *M*(3). On the other hand, the lower the number of these defects (i.e., the lower the occupancy of the *M*(3) position), the weaker the framework–channel interaction (i.e., the longer the K–F(2) bonds) and, therefore, the higher the mobility of atoms in the channel (i.e., the higher the values of the atomic-displacement parameters of the channel atoms). The experimental data (Table 3) confirm the above thesis: the atomic displacements of the Ta(2) atoms are minimal in **I**, somewhat more pronounced in **II**, and may reach the values resulting in splitting of this position in **III**.

Thus, the major differences between **I**, **II**, and **III** crystals—different mobilities and coordinates of Ta(2) atoms—are associated with the incorporation of positive interstitial defects Ta_{int} into the structure framework. An increase in the displacement parameter of F(2) atoms in bronzes **I** and **II** in comparison with its value in **III** can readily be understood if one takes into account the specific features of reduction of Ta^{5+} ions at the cathode considered below.

Characteristics of compounds formed due to reduction at the cathode. Reduction at the cathode may take place only at a certain potential corresponding to the attainment by some ions in the electrolyte of a certain reduced state. Therefore, all the cathode products obtained as a result of any reduction process in one experiment may contain a chemical element only in two oxidation states—one corresponding to the initial state, and the other corresponding to the reduced state. For ionic–covalent compounds, only the integral values of the oxidation degree have physical sense.

We consider the bronze formation associated with reduction of pentavalent tantalum ions at the cathode. In the general case, in addition to the initial Ta^{5+} ion, one can expect the formation of crystals containing any of the reduced Ta^{4+}, Ta^{3+}, Ta^{2+}, and Ta^{+} ions and also atomic Ta^{0}.

Taking into account that the crystals of bronzes **I** and **II** were obtained in one electrochemical experiment, we assume that all the reduced $Ta^{(5-\delta)+}$ ions in both crystals are in the same oxidation degree (the same integral parameter δ). The possible stoichiometric bronze compositions are obtained with due regard for the above characteristics of their formation at the cathode.

Scheme of formation of hexagonal tantalum bronzes at the cathode. As we have already mentioned, transparent crystals **III** not containing reduced tantalum ions were obtained simultaneously with crystals of bronzes **I** and **II**, which contain partly reduced tantalum. Under a microscope, among the crystals obtained in one batch, we also observed some crystals having the shape of hexagonal prisms with brown faces and radially colored basis—from the colorless center to the intense brown perimeter. Cleaving these crystals, we revealed that their bulk also had similar zonal structure. The middle parts of other elongated prismatic crystals had a clear boundary between the colorless center and brown periphery. These visual observations led to the conclusion that crystals of these bronzes could be formed because of reduction of tantalum ions in the already formed crystals of Ta^{5+} compounds in direct contact with the cathode. This reduction seemed to be possible because of the mobility of reducible tantalum ions in the channel. The reduction mechanism can be represented by the following sequence. Fluctuations of the melt composition in the region near the cathode give rise to nucleation and subsequent growth of crystals of the Ta^{5+} compound. The contact between the crystal and cathode results in reduction, first of all, of Ta^{5+} cations in the structure channels, because these cations are screened by anions to a lesser degree than other Ta^{5+} cations (the statistical character of anion distribution in the partly occupied F(2) position around Ta(2) cations). As a result, the channels acquire a negative charge, which is compensated because some F(2) anions migrate into the melt, whereas some Ta^{5+} cations move from the melt to the channels and also because partly reduced $Ta^{(5-\delta)+}$ cations migrate from the channels to the *M*(3) position in the framework. The cations in the *M*(3) position charge the framework and, thus, intensify the interaction between the framework and the channel via formation of K–F(2) bonds. This results in a lower mobility of F(2) anions and blocking of their migration to the melt with an increase of the framework charge, i.e., with an increase in the number of cations in *M*(3). The capture of Ta^{5+} ions from the melt, their motion along the channel, and their reduction at the cathode are limited by the unvarying number of ions. On the other hand, the velocity of Ta^{5+} migration (or the rate of electron exchange between oppositely charged tantalum cations) along the channel axes is lower, the larger the number of reduced $Ta^{(5-\delta)+}$ ions located along this axis. When all the channel cations in the crystal bulk are reduced to Ta^{5+}, the reduction process ceases and the crystal becomes *completely reduced* $Ta^{(5-\delta)+}$ bronze (depending on the conditions of electrolysis, δ may take one of integral values 1, 2, 3, or 4).

The other limiting parameter of the reduction processes is the duration of the contact between the cathode and crystal. If the reduction process is interrupted, the crystals formed can also contain unreduced Ta^{5+} cations in the structure channels. Hereafter, these crystals are called partly reduced $Ta^{(5-\delta)+}$ bronzes. Obviously, the degree of completeness of the reduction process can vary even within one crystal because of the anisotropy of conductivity (only along the hexagonal axis) and different areas of the crystal–cathode and crystal–melt contacts in different parts of the crystal. The formation of bronze crystals with different degree of the completeness of the reduction process in single experiment is explained by different influence of each of the parameters limiting reduction of randomly oriented growing crystals.

Within the framework of the above scheme of reduction, the $M(1)$ and $M(2)$ maxima of the residual electron density interpreted as interstitial defects of the first type correspond to the highest probability of encountering cations on the paths of their migration from the Ta(2) positions: $M(1)$ indicates migration of tantalum along the channel axis, and $M(2)$, migration of tantalum into the framework (into $M(3)$). Since the multiplicity of the Ta(2) position is unity and the interstitial defects arise as a result of redistribution of cations occupying this position, the total number of cations in the Ta(2), $M(1)$, $M(2)$, and $M(3)$ positions (Z in Table 1) should not exceed unity. This is confirmed (within the accuracy of standard deviations) by the results obtained for bronzes **I** ($Z = 1.05(14)$) and **II** ($Z = 0.88(14)$).

The mechanism of tantalum reduction suggested here allows one to interpret higher U_{eq} values of F(2) anions in bronzes in comparison with the analogous values in the Ta^{5+} compound and also different occupancies of the $M(1)$, $M(2)$, and $M(3)$ positions, because, in fact, various stages of the reduction process in these bronzes are fixed. The following characteristics obtained for bronze **II** indicate that the intermediate stage of the reduction process in this bronze is fixed:

—the concentration of the interstitial defects in $M(3)$ is lower (hereafter, $z3 = 0.12$ atoms per unit cell) than the concentration of atoms in the $M(2)$ and $M(1)$ positions along the migration paths ($z1 + z2 = 0.24$);

—the highest possible value of the displacement parameter of the F(2) atom ($U_{iso} = 0.093$ Å), which reflects its pronounced delocalization at the moment of cessation of crystal formation;

—the maximum number of F(2) anions (2.2) at a low number of tantalum cations ($6 + Z = 6.88$) in the unit cell.

On the contrary, the state of bronze **I** was estimated to be close to the state of complete reduction because of the following:

—a higher defect concentration in $M(3)$ ($z3 = 0.36$) than in $M(2)$ and $M(1)$ ($z1 + z2 = 0.20$);

—a lower value of the displacement parameter of F(2) ($U_{iso} = 0.08$ Å);

—the minimum number of F(2) anions (1.1) at the maximum possible number of tantalum cations ($6 + Z = 7$) in the unit cell.

Chemical formula of the compounds with the variable composition $K_6Ta_{6+Z}O_{15}F_6(F, O)_y$ (theoretical analysis). The composition of the compounds with the structure type studied can be considered at several levels:

$$\begin{aligned} &K_6Ta_{6+Z}O_{15}F_6(F, O)_y \\ &= K_6Ta_{6+x+z}O_{15}F_6(F, O)_y \\ &= [K_6Ta_6O_{15}F_6\{Ta_{z3}\}][Ta_x(F, O)_y\{Ta_{z1+z2}\}]. \end{aligned} \quad (1)$$

Square brackets show the compositions of the framework and the channel. Hereafter, the curly brackets indicate Ta_{int} atoms whose total number, $Ta_{int} - z = z1 + z2 + z3$, is represented as a sum of the atoms in the $M(1)$, $M(2)$, and $M(3)$ positions. The total variable number of tantalum atoms in the structure, $Z = x + z$, is, (x), the sum of the basic atoms in the partially occupied Ta(2) position, (x), of multiplicity 1 and the total number of Ta_{int} atoms, (z), and y is the number of atoms in partly occupied F(2) position of multiplicity 12.

Compounds of pentavalent tantalum ($\delta = 0$). The results obtained in the present study show that Ta^{5+} compounds contain no interstitial defects. Thus, relation (1) can be written in the simplified form as

$$\begin{aligned} &K_6Ta_{6+x}O_{15}F_6(F, O)_y \\ &= [K_6Ta_6O_{15}F_6][Ta_x(F, O)_y]. \end{aligned} \quad (2)$$

The framework composition $[K_6Ta_6O_{15}F_6]$ is constant and its total charge is zero. The variable composition of the compounds is explained by partial occupancy of the position in the channel [Ta(2) = xTa and F(2) = y(F, O)] and the chemical composition of its anionic component, which admits the above variations.

The ranges of x and y variation can be evaluated proceeding from the crystal-chemical limitations imposed on the F(2) position of multiplicity 12 in which the atoms form the first coordination sphere of Ta(2) with due regard for the total charge balance of cations and anions located in the channel. As has already been noted, in fact, the 12-vertex hexagonal $[Ta(2)F(2)_{12}]$ prism corresponding to the complete occupancy of the F(2) position cannot exist because of too short F(2)–F(2) contacts (~1.3 Å) in its basis. The possible statistical $[Ta(2)F(2)_6]$ polyhedra (trigonal prism and antiprism) corresponds to 50% occupancy of this position. However, these polyhedra can be formed only in every second unit cell (or even more seldom) because of too short F(2)–F(2) contacts between the polyhedra

(~1.5 Å). Therefore, the occupancy of this position is $pF(2) \le 0.25$ and $0 < y = 12 \times pF(2) \le 3$.

The condition of channel electroneutrality is written as $5x = y + y(O) = 2y(O) + y(F)$, where the total number of anions, $y = y(O) + y(F)$, is represented as the sum of the numbers of O and F ions. It follows from the above equation that $y = 5x - y(O)$. Considering two possible limiting chemical compositions of the anionic position (F or O), we obtain the following condition of electroneutrality of the channel valid for any mixed composition of the F(2) position

$$5x/2 \le y \le 5x, \qquad (3)$$

where the lower limit y corresponds to the presence in the channel solely of divalent O anions, $[Ta_xO_{2.5x}]$, whereas the upper limit, solely to the presence of monovalent F anions, $[Ta_xF_{5x}]$. This signifies that the channel can contain different number y of anions (depending on their kind) at the same occupancy $Ta(2) = x$.

The value of the local coordination number of Ta(2) atoms averaged in space and time, $(cn)_{av}$, equal to the ratio of the number of anions, y, to the number of cations, x, is obtained from Eq. (3) as $2.5 \le [(cn)_{av} = y/x = 5 - y(O)/x] \le 5$. The latter condition signifies that the maximum number of anions per Ta(2) atom cannot exceed five. Therefore, the $[Ta(2)F(2)_6]$ polyhedron is always of a statistical nature. It is logical to assume that the probability of the structure-type stabilization considered here is higher, the higher the occupancy of the vertices of this polyhedron, i.e., the closer the $(cn)_{av}$ value is to six. Obviously, the minimum possible value of $(cn)_{av}$ equal to 2.5 corresponds to filling of the anionic position with only O ions, whereas the maximum possible value, $(cn)_{av} = 5$, corresponds to filling of this position with only F ions at $y = y(F) = 5x$.

Now, evaluate the occupancies of the Ta(2) position, x, at which the value of $(cn)_{av}$ is close to the maximum possible value. It can readily be shown that

—if $0 < x \le 0.6$, the F(2) position can be filled solely with F anions irrespectively of the x value, $y = y(F) = 5x$. The O ions which reduce the $(cn)_{av}$ value can have any relative concentration ranging from zero [$y = y(F) = 5x$] to the complete filling of the F(2) position with oxygen [$y = y(O) = 5x/2$]. At the fixed concentration of O ions, the higher the x value, the less the influence of the present oxygen on the $(cn)_{av}$ of Ta(2) atoms;

—if $0.6 < x \le 1$, this structure type can be formed without oxygen anions, because $3 < 5x = y + y(O) \le 5$ and $y \le 3$. In this case, with an increase in x from 0.6 to 1.0, the possible number of F ions decreases from 5 to zero and, therefore, the maximum possible value of $(cn)_{av}$ decreases from 5 to 2.5.

The above estimation shows that the probability of the structure-type stabilization is higher in the range $0 < x \le 0.6$ and that there is no oxygen in the F(2) position; the probability decreases with an increase in x from 0.6 to 1.0. The closer x is to 0.6, the higher the probability that the F(2) position is filled not only with F ions but also with a small amount of oxygen. Thus, for the Ta^{5+} compounds, the limitations imposed on the stoichiometry in formula (2) are: $y \le 3$, $x = [y(F) + 2y(O)]/5 \le 1$, where $y(F) + y(O) = y$. The most probable compositions are $K_6Ta_{6+x}O_{15}F_{6+5x} = [K_6Ta_6O_{15}F_6][Ta_xF_{5x}]$ with the subscripts x ranging within $0 < x \le 0.6$.

It should be emphasized that the formula $K_6Ta_{6.5}O_{14.5}F_{9.5} = [K_6Ta_6O_{12.688}F_{8.312}][Ta_{0.5}O_{1.812}F_{1.188}]$ given in [5] for transparent Ta^{5+} compounds is somewhat erroneous. This can be explained by the fact that the balance of the valence strengths at framework anions, which allows one to unambiguously localize the F and O atoms (Table 5) and, thus, adequately determine the framework charge and write its formula, was not estimated in [5]. According to Eq. (3), the coefficient $pTa(2) = 0.5$ ($x = 0.5$) determined in [5] can correspond to the number of anions in the channel ranging within $1.25O \le y \le 2.5F$ but not to $y = (1.812O + 1.188\ F) = 3(F, O)$, as was indicated in [5]. Thus, the most probable formula of Ta^{5+} compound studied in [5] is $[K_6Ta_6O_{15}F_6][Ta_{0.5}F_{2.5}] = K_6Ta_{6.5}O_{15}F_{8.5}$. The refinement of structure **III**, another example of a Ta^{5+} compound, showed that the F(2) position did not contain any oxygen because $y \sim 5x$ and $[K_6Ta_6O_{15}F_6][Ta_{0.27}F_{1.4}] = K_6Ta_{6.27}O_{15}F_{7.4}$. Thus, the compositions of both Ta^{5+} compounds confirm the conclusion about the stabilization of the structure type in the absence of oxygen in the channel.

Compounds containing $Ta^{(5-\delta)+}$ ions with reduced degree of oxidation (bronzes). The variable composition of bronzes depends not only on the variations in the channel composition but also on the variable number of Ta_{int} atoms, which are absent in the Ta^{5+} compounds. The composition of the $[K_6Ta_6O_{15}F_6\{Ta_{z3}\}]$ framework has a variable component $z3$ equal to the number of Ta_{int} atoms in the $M(3)$ position, which is related to the total positive charge of the framework. Therefore, the charge of the structure channel $[Ta_x(F, O)_y\{Ta_{z1+z2}\}]$ is opposite to the charge of the framework. To estimate the variable parameters in formulas (1), we have to write the electroneutrality condition of the structure.

The positive charge of the framework due to $Ta_{int}^{(5-\delta)+}$ in the $M(3)$ position equals $(5 - \delta)z3$. The negative charge of the channel is associated with the complete or partial reduction of Ta^{5+} in the Ta(2) position and incorporation of $Ta_{int}^{(5-\delta)+}$ ions with a reduced oxidation degree into the $M(1)$ and $M(2)$ positions. Therefore, the equation of compound electroneutrality can be written as

$$y + y(O) = (5 - \delta)(Z - x') + 5x', \qquad (4)$$

where $y(O) \le y$. The left-hand side of Eq. (4) describes the total charge of the channel anions that neutralize the total charge of cations in the partly occupied positions in the right-hand side of the equation; x' is the number of unreduced Ta^{5+} ions in the Ta(2) position.

It is seen from Eq. (4) that the total varying number Z of cations is controlled, first of all, by the number y of anions and, at the given y value, depends on the degree of reduction of tantalum ions, δ, and not on the number x of reduced $Ta^{5+}x'$ ions in the position Ta(2). Taking into account that $Z \le 1$, we find from Eq. (4) that $y(O) \le 2.5$. Thus, the compositions of bronzes with the structure type considered here can be written as

$$K_6Ta_{6+x'}^{5+}Ta_{Z-x'}^{(5-\delta)+}O_{15+y(O)}F_{6+y-y(O)}, \quad (5)$$

where $\delta = 1, 2, 3, 4$, or 5, $y \le 3$ is the total variable number of (F, O) anions, including $y(O) \le 2.5$ oxygen ions, and $Z \le 1$ is the total variable number of tantalum cations, including $x' = (y + y(O) - (5 - \delta)Z)/\delta$ unreduced Ta^{5+} cations, where $0 \le x' < 1$. For completely reduced bronzes, $x' = 0$ by definition, and the corresponding bronzes have the composition $K_6Ta_6^{5+}Ta_Z^{(5-\delta)+}O_{15+y(O)}F_{6+y-y(O)}$.

All the variable parameters in the generalized composition described by formula (5) depend on the degree of reduction of tantalum ions (δ) and presence of oxygen anions in F(2). It is also interesting to consider three additional particular cases: maximum reduction of some Ta^{5+} ions up to Ta^0 ($\delta = 5$); absence of oxygen in the structure channels ($y(O) = 0$); and the combination of the first two conditions.

If reduction proceeds up to Ta^0 ($\delta = 5$), the presence of anions depends only on the unreduced Ta^{5+} ions in the Ta(2) position, $x' = y/5 + y(O)/5$. Then, formula (5) is simplified to $K_6Ta_{6+x'}^{5+}Ta_{Z-x'}^{0}O_{15+5x'-y}F_{6+2y-5x'}$. In this case, the completely reduced bronze has no anions in the channels: $K_6Ta_6^{5+}Ta_Z^0O_{15}F_6 = [K_6Ta_6^{5+}O_{15}F_6Ta_{z3}^0][Ta_{Z-z3}^0]$. This variant differs from Ta^{5+} compounds only by the presence of interstitial defects—neutral Ta_{int} atoms. The total charge of the framework is zero, which explains the high mobility of ions and atoms in the channel.

The absence of oxygen ions in the channel corresponds to the composition $K_6Ta_{6+x'}^{5+}Ta_{Z-x'}^{(5-\delta)+}O_{15}F_{6+y}$, where $\delta = 1, 2, 3, 4$, or 5; $y \le 3$, $Z \le 1$ is the total variable number of Ta cations, including $x' = (y - (5 - \delta)Z)/\delta$ unreduced Ta^{5+} cations, $0 \le x' < 1$, $Z \le y/(5 - \delta)$, if $\delta \ne 5$. With the same number of anions in the channel (y), the number of unreduced Ta^{5+} ions in the Ta(2) position (x') is less than in the presence of oxygen, which corresponds to a higher $(cn)_{av}$ of Ta and stabilizes the structure. Therefore, these compositions are more probable.

At the maximum possible tantalum reduction ($\delta = 5$) and in the absence of oxygen in the structure channels, the composition described by (5) becomes $K_6Ta_{6+0.2y}^{5+}Ta_{Z-0.2y}^{0}O_{15}F_{6+y} = [K_6Ta_6^{5+}O_{15}F_6\{Ta_{z3}^0\}] \cdot [Ta_{0.2y}^{5+}Ta_{Z-z3-0.2y}^{0}F_y]$. In terms of crystal chemistry, the compounds with such compositions are highly probable because $(cn)_{av} = 5$, i.e., is close to six for Ta^{5+} ions in the Ta(2) position and intercalation of neutral Ta atoms into the structure. Proceeding from the degree of tantalum reduction, i.e., the δ parameter, the type of compounds considered here can be related to $Ta^{(5-\delta)+}$ bronzes, with due regard for the fact that only some tantalum ions are reduced.

The occupancies of the Ta(2), F(2), and Ta_{int} positions correspond to the following compositions: $[K_6Ta_6O_{15}F_6\{Ta_{0.36(6)}\}][Ta_{0.487(1)}(F, O)_{1.10(2)}\{Ta_{0.20(8)}\}]$ for bronze **I** and $[K_6Ta_6O_{15}F_6\{Ta_{0.12(6)}\}][Ta_{0.516(1)}(F, O)_{2.18(2)}\{Ta_{0.20(8)}\}]$ for bronze **II**. With due regard for the condition $Z \le 1$, the composition of bronze **I** is $[K_6Ta_6O_{15}F_6\{Ta_{0.34}\}][Ta_{0.49}(F, O)_{1.1}\{Ta_{0.17}\}]$. The anion composition in the channels can be refined with an accuracy of the determination of possible degrees of oxidation of reduced tantalum ions by Eqs. (4) and (5).

Estimation of oxidation degree of tantalum in bronzes I and II. First of all, we should like to note that no reduction of Ta^{5+} ions to Ta^0 ($\delta = 5$) is possible in **I** and **II**, because the shortening of the K–F(2) distances in comparison with analogous distances in **III** would indicate the existence of charges of both channel and framework, i.e., the presence of cations instead of neutral atoms in the $M(3)$ position. Substitution of x, y, $z1$, $z2$, and $z3$ values obtained for **I** (Table 1) into Eq. (4) with due regard for the fact that $y(O) \le y = 1.1$ yields $\delta \ge 3$. Therefore, in order to determine the most probable degree of tantalum reduction in bronzes **I** and **II**, one has to consider two possible cases of correspondence of formula (5) to the chemical composition obtained, i.e., $\delta = 3$ and $\delta = 4$.

If $\delta = 3$, some Ta^{5+} ions are reduced to Ta^{2+}, i.e., **I** and **II** are Ta^{2+} bronzes. With due regard for the errors in the determination of the position occupancies, formula (5) can be written as $[K_6Ta_6^{5+}O_{15}F_6\}][Ta_{0.34}^{2+}\}][Ta_{0.49}^{2+}O_{1.0}\{Ta_{0.17}^{2+}\}]$ for bronze **I** and $[K_6Ta_6^{5+}O_{15}F_6\{Ta_{0.12}^{2+}\}][Ta_{x'}^{5+}Ta_{0.52-x'}^{2+}O_{3x'-0.42}F_{2.6-3x'}\{Ta_{0.24}^{2+}\}]$ for bronze **II**, where x' is the number of unreduced Ta^{5+} ions in the Ta(2) position ranging from 0.14 (no oxygen in channels) to 0.52 (mixed anionic composition of channels). The two limiting compositions of the channels in **II** are $[Ta_{0.14}^{5+}Ta_{0.38}^{2+}F_{2.18}\{Ta_{0.24}^{2+}\}]$ and $[Ta_{0.52}^{5+}O_{1.13}F_{1.05}\{Ta_{0.24}^{2+}\}]$. In this case, **I** is the completely reduced Ta^{2+} bronze containing no F anions in the channels and **II** is the partly reduced Ta^{2+} bronze containing at least 1.05 F anions in the channels.

If $\delta = 4$, some Ta^{5+} ions are reduced to Ta^{+}, i.e., **I** and **II** are Ta^{+} bronzes. Bronze **I** has the composition $[K_6Ta_6^{5+}O_{15}F_6\{Ta_{0.34}^{+}\}][Ta_{x'}^{5+}Ta_{0.49-x'}^{+}O_{4x'-0.1}F_{1.2-4x'}\{Ta_{0.17}^{+}\}]$, where, with an increase in the oxygen content in the channel from 0 to 1.1, x' varies from 0 (or, more precisely, from 0.025) to 0.3. The limiting compositions of the channels are approximately $[Ta_{0.49}^{+}F_1\{Ta_{0.17}^{+}\}]$ and $[Ta_{0.3}^{5+}Ta_{0.19}^{+}O_{1.1}\{Ta_{0.17}^{+}\}]$. Bronze **II** has the composition $[K_6Ta_6^{5+}O_{15}F_6\{Ta_{0.12}^{+}\}][Ta_{x'}^{+}Ta_{0.516-x'}^{+}O_{4x'-1.3}F_{3.48-4x'}\{Ta_{0.24}^{+}\}]$, where, with an increase in the oxygen content in the channel from 0 to 0.764, x' varies from 0.325 to 0.516. The limiting compositions of the channels are $[Ta_{0.325}^{5+}Ta_{0.191}^{+}F_{2.18}\{Ta_{0.24}^{+}\}]$ and $[Ta_{0.516}^{5+}O_{0.764}F_{1.416}\{Ta_{0.24}^{+}\}]$. In this case, **I** is the Ta^{+} bronze with an arbitrary ratio of F anions to O cations in the channels. This bronze is completely reduced if it has no oxygen in the channels. Partly reduced Ta^{+} bronze **II** contains at least 1.416 F anions in the structure channel.

Formally, both above variants of tantalum reduction are possible. However, in Ta^{2+} bronzes ($\delta = 4$), the channels of structure **I** should contain solely O anions. Since, during reduction, the anions leave the structure, the initial structure of the crystal should contain no F anions, which would correspond to the channel composition $[Ta_x^{5+}O_{2.5x}]$ with the minimum possible averaged coordination number $(cn)_{av} = 2.5$, which is hardly probable. Therefore, the variant of existence of Ta^{+} bronzes **I** and **II** seems to be more probable.

We revealed no qualitative differences between **I** and **II**. At the same time, their optical properties are obviously different—metal-like crystals **I** and smoke-brown semitransparent crystals **II**. We assume that these differences should be associated with the presence in the channels of unreduced Ta^{5+} ions—there are no such ions in completely reduced bronze **II**, but they are present in partly reduced bronze **II**. With due regard for this fact, the most probable composition of **I** is $[K_6Ta_6^{5+}O_{15}F_6\{Ta_{0.34}^{+}\}][Ta_{0.49}^{+}F_1\{Ta_{0.17}^{+}\}] = K_6Ta_6^{5+}Ta^{+}O_{15}F_7 = K_6Ta_7O_{15}F_7$. Taking into account that the absence of oxygen anions in the structure channels is favorable, it is most likely that bronze **II** has the composition $[K_6Ta_6^{5+}O_{15}F_6\{Ta_{0.12}^{+}\}][Ta_{0.325}^{5+}Ta_{0.191}^{+}F_{2.18}\{Ta_{0.24}^{+}\}] = K_6Ta_{6.33}^{5+}Ta_{0.55}^{+}O_{15}F_{8.2} = K_6Ta_{6.88}O_{15}F_{8.2}$.

Effect analogous to the effect of high pressure. We repeatedly noted [2, 4, 8, 9] that all the compounds synthesized by electrodeposition at the cathode show characteristics analogous to the effect of high pressure. The present case is no exception. The densities of bronzes **I** and **II** are $d_X = 5.46$ and 5.38 g/cm^3, respectively, i.e., are much higher than the density of Ta^{5+} compound **III**, $d_X = 5.06$ g/cm^3. Moreover, the anomalously short K–Ta_{int} distances (for Ta_{int} in the $M(3)$ position) are equal to ~2 Å, which confirms the analogy with high pressure.

CONCLUSIONS

The structures of three crystals of the (K, Ta, O, F) compounds having the same structure type of hexagonal bronzes have been studied by single crystal X-ray diffraction methods. The crystals studied possess different optical characteristics (color and degree of transparency) because of different degree of reduction of $Ta^{(5-\delta)+}$ ions. Comparison of the data obtained with the data published earlier for analogous structures of two other crystals allowed us to characterize the structure type of the crystals and establish their specific structural characteristics during partial reduction of tantalum ions.

The structure of hexagonal tantalum bronzes (sp. gr. $P6/m$, $a \sim 13.13$ Å and $c \sim 3.86$ Å) is characteristic of compounds with a variable composition $K_6Ta_{6+Z}O_{15}F_6(F, O)_y$, where $Z \leq 1$ and $y \leq 3$, which contains both tantalum oxidized to the highest degree (Ta^{5+}-containing compounds) and tantalum in two different degrees of oxidation Ta^{5+} and $Ta^{(5-\delta)+}$ ($Ta^{(5-\delta)+}$ bronzes) with δ taking the values 1, 2, 3, 4, or 5.

The Ta^{5+}-containing compounds form colorless transparent crystals. Crystals of bronzes have visually different optical characteristics. Their color varies from light to dark brown, the crystals vary from transparent to semitransparent, and the luster changes from glassy to mat finish. Against the background of this continuous spectrum of crystal characteristics, we also observed crystals of qualitatively different dark gray metal-like bronzes.

The structure of all the representatives of this structure type is built by two main structural units—$[K_6Ta_6^{5+}O_{15}F_6]$ framework with a stable structure and composition and $[Ta_x(F, O)_y]$ channels of variable composition and structure with Ta cations located along their hexagonal axes ($x \leq Z$). The channel atoms are highly mobile but form no sublattice with the symmetry and parameters different from the symmetry and parameters of the framework.

Unlike Ta^{5+}-containing compounds, the bronzes contain interstitial defects—reduced tantalum cations, $zTa_{int}^{(5-\delta)+}$, $(z + x + Z)$. All or only some reduced cations in the channel are in the same reduced state $Ta^{(5-\delta)+}$. Therefore, one should also distinguish between completely and partly reduced bronzes. Presumably, completely reduced bronzes would have metallic properties.

Unlike Ta^{5+}-containing compounds, the chemical composition of the bronzes contain interstitial defects—reduced tantalum cations, $zTa_{int}^{(5-\delta)+}$, $(z + x + Z)$. Therefore, one should also distinguish between the completely and partly reduced bronzes. Ta^{5+}-containing compounds is $K_6Ta_{6+x}O_{15}F_6(F, O)_y = [K_6Ta_6O_{15}F_6][Ta_x(F, O)_y$, where $y \le 3$ and $x \le 1$. In the square brackets, the compositions of the framework and the channel are indicated. The most probable compositions are $K_6Ta_{6+x}O_{15}F_{6+5x} = [K_6Ta_6O_{15}F_6][Ta_xF_{5x}]$ with $0 < x \le 0.6$. Both structural units in Ta^{5+} compounds have no electrostatic charge, which explains their relatively high mobility. We studied the structures of colorless transparent crystals of the Ta^{5+} compound of the composition $[K_6Ta_{6+x}O_{15}F_6][Ta_{0.27}F_{1.4}] = K_6Ta_{6.27}O_{15}F_{7.4}$.

With due regard for the specific features of the formation of compounds during reduction at the cathode in the electrolysis of the salt melt, the composition of $Ta^{(5-\delta)+}$ bronzes can be written as $K_6Ta_{6+x'}^{5+}Ta_{Z-x'}^{(5-\delta)+}O_{15+y(O)}F_{6+y-y(O)}$ with $\delta = 1, 2, 3, 4,$ or 5. Here, $y \le 3$ is the total variable number of (F, O) anions, including $y(O) \le 2.5$ oxygen ions; $Z \le 1$ is the total variable number of Ta cations including $x' = (y + y(O) - (5 - \delta)Z)/\delta$ unreduced Ta^{5+} cations, where $0 \le x' < 1$. We also studied the structure of a metal-like crystal of completely reduced Ta^{+} bronze of the composition $[K_6Ta_6^{5+}O_{15}F_6\{Ta_{0.34}^{+}\}][Ta_{0.49}^{+}F_1\{Ta_{0.17}^{+}\}] = K_6Ta_6^{5+}Ta^{+}O_{15}F_7 = K_6Ta_7O_{15}F_7$ and a brown semitransparent crystal of partly reduced Ta^{+} bronze of the composition $K_6Ta_6^{5+}O_{15}F_6\{Ta_{0.12}^{+}\}][Ta_{0.325}^{5+}Ta_{0.191}^{+}F_{2.18}\{Ta_{0.24}^{+}\}] = K_6Ta_{6.33}^{5+}Ta_{0.55}^{+}O_{15}F_{8.2} = K_6Ta_{6.88}O_{15}F_{8.2}$. Curly brackets show Ta_{int} atoms playing the role of interstitial defects.

Analysis of the structural data obtained for one Ta^{5+}-containing compound and two bronzes formed during the same electrochemical experiment allowed us to suggest the scheme of crystal reduction on the cathode in electrolysis of the salt melt. According to this scheme, the most probable composition of the $Ta^{(5-\delta)+}$ bronzes is $K_6Ta_{6+x'}^{5+}Ta_{Z-x'}^{(5-\delta)+}O_{15}F_{6+y}$, where $Z \le y/(5 - \delta)$ if $\delta \ne 5$ and $x' = (y - (5 - \delta)Z)/\delta$.

In comparison with Ta^{5+}-containing compounds obtained by reduction at the cathode, bronzes are characterized by higher density and shorter cation–cation distances. This confirms our earlier assumption that, in electrolysis, a behavior analogous to the high-pressure effect should be observed.

ACKNOWLEDGMENTS

We are grateful to G. Burri for help in chemical microanalysis and A. Schönlieber and M. Meyer (all from Lausanne University, Switzerland) for their help in the X-ray experiments. A.A. and G.Ch. are grateful to the Herbert Foundation of the University of Lausanne for financial support.

This study was supported by the Russian Foundation for Basic Research, project no. 02-03-32982.

REFERENCES

1. *Oxide Bronzes*, Ed. by V. I. Spitsyn (Nauka, Moscow, 1982).
2. A. V. Arakcheeva, G. Chapuis, V. Grinevitch, and V. Shamray, Acta Crystallogr., Sect. B: Struct. Sci. **57**, 157 (2001).
3. E. A. Zhurova, V. E. Zavodnik, and V. G. Tsirel'son, Kristallografiya **40** (5), 816 (1995) [Crystallogr. Rep. **40**, 753 (1995)].
4. A. V. Arakcheeva, V. V. Grinevich, A. V. Mitin, *et al.*, Kristallografiya **46** (2), 221 (2001) [Crystallogr. Rep. **46**, 182 (2001)].
5. M. Vlasse, Mater. Res. Bull. **14**, 101 (1979).
6. V. Petricek and M. Dusek, *Jana 2000. Structure Determination Software Programs* (Inst. of Physics, Praha, 2000).
7. I. D. Brown, J. Appl. Crystallogr. **29**, 479 (1996).
8. A. V. Arakcheeva, G. Chapuis, and V. Grinevitch, Acta Crystallogr., Sect. B: Struct. Sci. **58**, 1 (2002).
9. A. V. Arakcheeva, V. V. Grinevich, G. Chapuis, and V. F. Shamraĭ, Kristallografiya **47** (2), 272 (2002) [Crystallogr. Rep. **47**, 237 (2002)].

Translated by L. Man

Crystallography Reports, Vol. 49, No. 1, 2004, pp. 86–93. Translated from Kristallografiya, Vol. 49, No. 1, 2004, pp. 92–100.

STRUCTURE OF INORGANIC COMPOUNDS

Dedicated to the 80th Birthday of L.A. Shuvalov

Crystal Structure and Phase Transitions in the New Crystals of $[(CH_3)_2NH_2]_2CuCl_4[(CH_3)_2NH_2]Cl$

L. F. Kirpichnikova*, A. Pietraszko, W. Bednarski***, S. Waplak***, and A. U. Sheleg******

** Shubnikov Institute of Crystallography, Russian Academy of Sciences, Leninskiĭ pr. 59, Moscow, 117333 Russia*
e-mail: luba@ns.crys.ras.ru

*** Trzebiatowski Institute of Low-Temperature and Structural Research, Polish Academy of Sciences, P.O. Box 1410, Wroclaw, 2 50-950 Poland*
e-mail: adam@int.pan.wroc.pl

**** Institute of Molecular Physics, Polish Academy of Sciences, Smoluhowskiego 17, Poznan, 60-179 Poland*
e-mail: wwb@imfpan.poznan.pl and waplak@imfpan.poznan.pl

***** Institute of Solid State and Semiconductor Physics, National Academy of Sciences of Belarus, ul. P. Brovki 17, Minsk, 220072 Belarus*
e-mail: sheleg@ifttp.bas-net.by

Received July 18, 2003

Abstract—Crystals grown from a solution of dimethylammonium and copper chlorides are studied using electron paramagnetic resonance (EPR) and X-ray diffraction. The dielectric properties of the crystals grown are measured. It is established that the crystals have the composition $[(CH_3)_2NH_2]_2CuCl_4[(CH_3)_2NH_2]Cl$ and, in phase **I** at room temperature, are described by the orthorhombic space group $Pna2_1$ with the unit cell parameters $a = 11.338$ Å, $b = 9.981$ Å, and $c = 15.675$ Å. At temperatures of 279 K and 253 K, the crystals undergo jumpwise phase transitions into the incommensurate modulated ferroelectric phase **II** and commensurate modulated phase **III**, respectively. *© 2004 MAIK "Nauka/Interperiodica".*

INTRODUCTION

Crystals containing dimethylammonium $[(DMA)^+]$ molecular cations, $[CH_3)_2NH_2]^+$, are of interest due to their ferroic activity, which is associated with the ordering of hydrogen bonds and related changes in the dynamics of $(DMA)^+$ ions. For example, crystals of $(CH_3)_2NH_2\ Al(SO_4)_2 \cdot 6H_2O$ and $(CH_3)_2NH_2Ga(SO_4)_2 \cdot 6H_2O$ exhibit ferroelectric properties in the temperature ranges 152–75 K and 136–106 K, respectively [1, 2]. In addition, they possess ferroelastic properties above the Curie point. Crystals of $(CH_3)_2NH_2H_2PO_4$ undergo a ferroelectric phase transition at 259.15 K [3].

The authors of [4, 5] revealed that $[(CH_3)_2NH_2]_2CuCl_4$ crystals exhibit ferroelectric properties in the temperature range 279.65–253.05 K and that the incommensurate phase exists in the range 296–279.5 K. In our recent work [6], we investigated the temperature dependences of the unit cell parameters and thermal expansion coefficients along the crystallographic axes in the $[(CH_3)_2NH_2]_2CuCl_4$ crystals. In the $[(CH_3)_2NH_2]_2CoCl_4$ crystals [7], ferroelectric properties were observed in the temperature range 227–260 K. Studies of the crystals containing a bivalent metal,

Table 1. Coordinates ($\times 10^4$) and equivalent thermal parameters U_{eq} (Å$^2 \times 10^3$) of the non-hydrogen atoms

Atom	*x*	*y*	*z*	U_{eq}
Cu(1)	4704(1)	141(1)	2401(1)	40(1)
Cl(1)	6422(1)	–964(1)	2403(1)	56(1)
Cl(2)	4129(1)	–389(1)	1080(1)	68(1)
Cl(3)	4121(1)	–379(1)	3729(1)	69(1)
Cl(4)	4133(1)	2298(1)	2396(1)	73(1)
C(11)	6297(1)	–4705(1)	2476(2)	110(1)
C(12)	4327(1)	–3800(1)	2482(2)	121(1)
N(1*A*)	5428(2)	–3751(2)	2838(1)	60(1)
N(1*B*)	5388(2)	–3880(2)	1963(2)	82(1)
C(21)	1949(1)	3104(1)	4024(1)	72(1)
C(22)	2980(1)	1959(2)	5188(1)	83(1)
N(2*A*)	3091(1)	2719(1)	4473(1)	51(1)
N(2*B*)	3063(2)	2341(2)	4264(1)	97(1)
C(31)	–1967(2)	2950(2)	–377(1)	106(1)
C(32)	–3087(1)	2002(2)	857(1)	108(1)
N(3*A*)	–1846(1)	2422(1)	452(1)	30(1)
N(3*B*)	–2625(2)	3109(2)	503(1)	65(1)
Cl(5)	5025(2)	4976(1)	4924(2)	157(1)

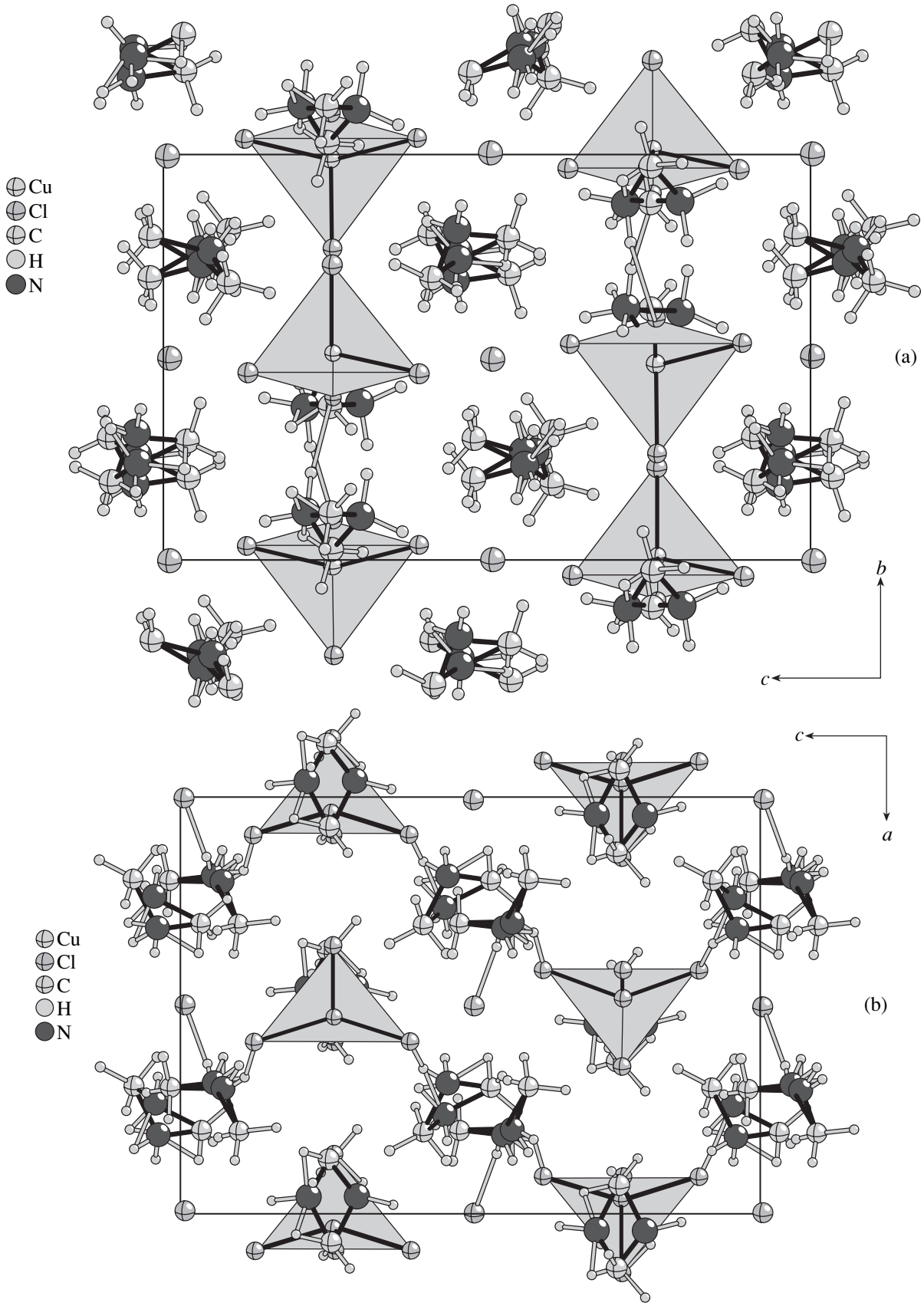

Fig. 1. Projections of the crystal structure of $[(CH_3)_2NH_2]_2CuCl_4[(CH_3)_2NH_2]Cl$ onto the planes (a) (100), (b) (010), and (c) (001) at 293 K.

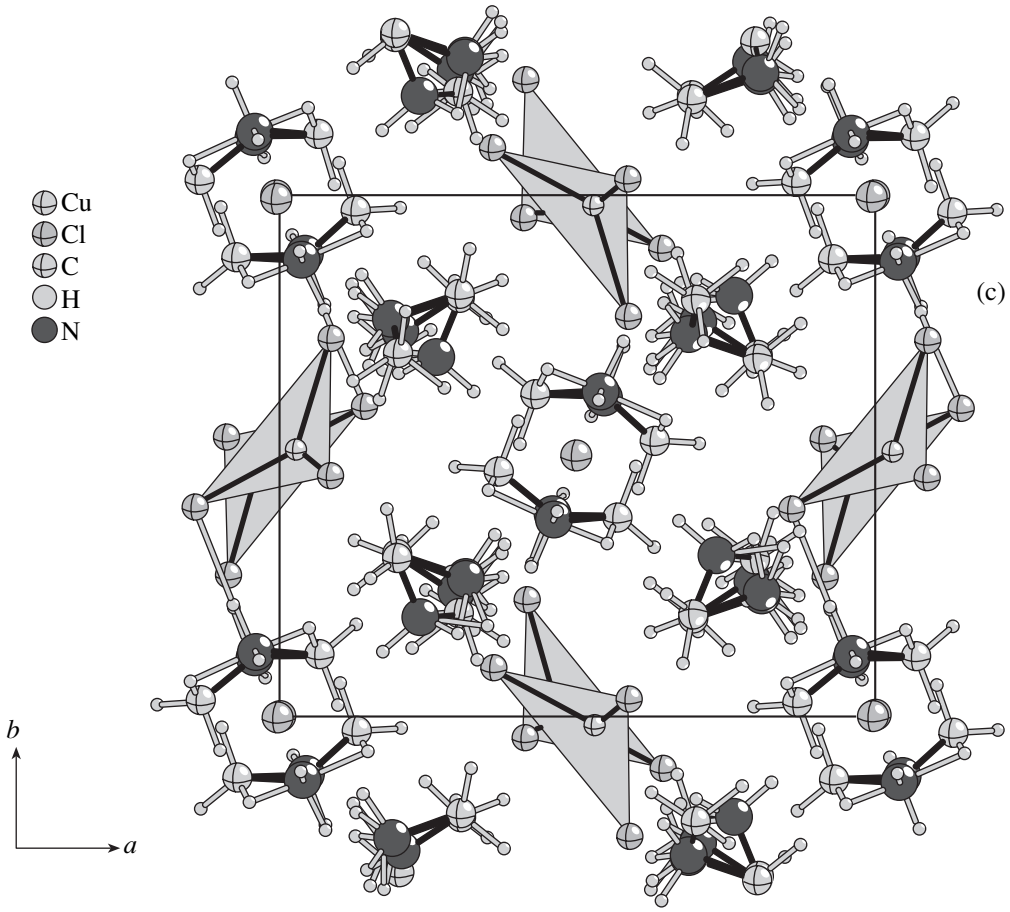

Fig. 1. (Contd.)

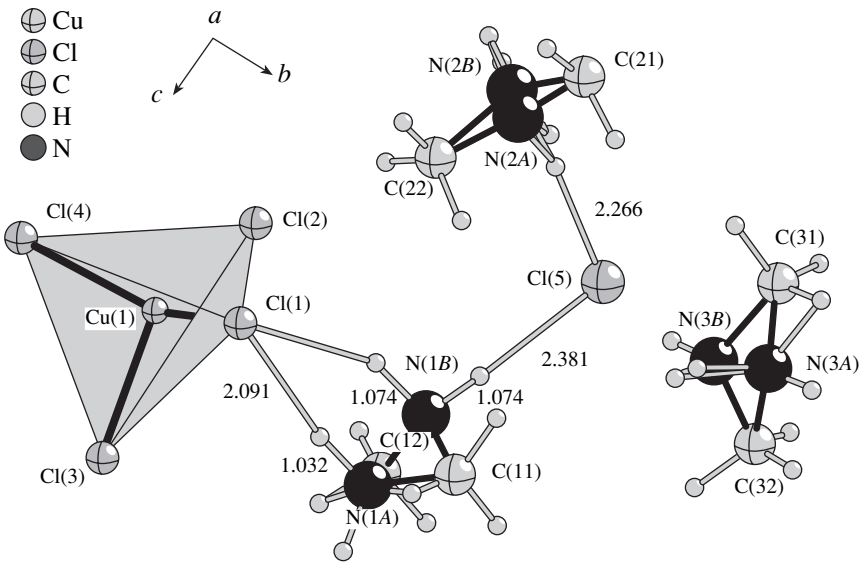

Fig. 2. A structural fragment and the formation of hydrogen bonds in the crystal of $[(CH_3)_2NH_2]_2CuCl_4[(CH_3)_2NH_2]Cl$ at 293 K.

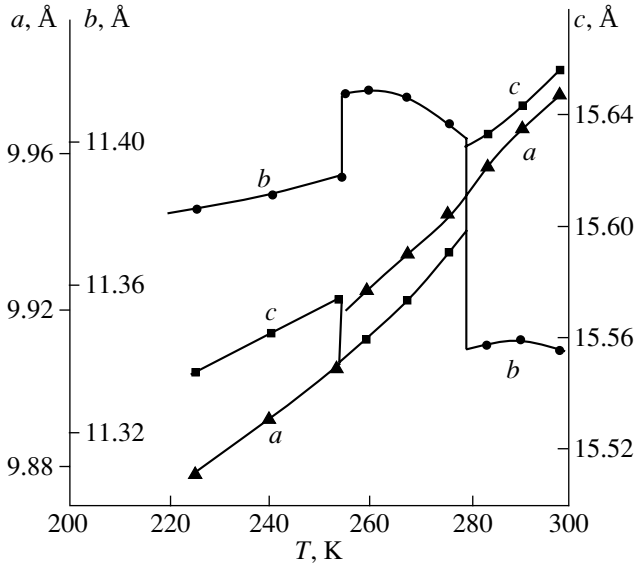

Fig. 3. Temperature dependences of the unit cell parameters.

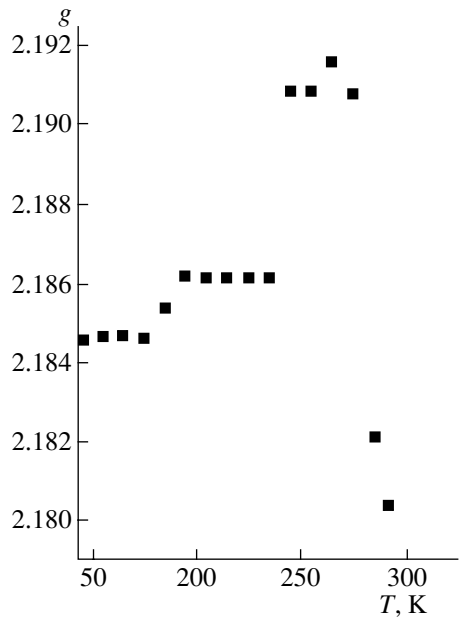

Fig. 4. Temperature dependence of the g factor measured using electron paramagnetic resonance.

chlorine anion, and dimethylammonium cation are of great interest, since data on the structure of these compounds and mechanisms of phase transitions in them are not available and data on their dielectric properties are very scarce.

The purpose of this work was to grow crystals of copper chloride with organic dimethylammonium cations and to study their structure and properties.

EXPERIMENTAL

Single crystals were grown at room temperature through isothermal evaporation of saturated aqueous solutions containing dimethylammonium chloride $[(CH_3)_2NH_2]Cl$ and copper chloride. The crystals obtained were transparent, yellow, and hygroscopic. For measurements, samples were cut out along the crystallographic axes in such a way that the crystallo-

Table 2. Coordinates ($\times 10^4$) and isotropic thermal parameters U_{iso} ($Å^2 \times 10^3$) of the hydrogen atoms

Atom	x	y	z	U_{iso}	Atom	x	y	z	U_{iso}
H(14)	6097(11)	–5597(13)	2661(8)	109	H(31*A*)	–1696(12)	3193(15)	842(9)	22
H(24)	2541(9)	2521(10)	5483(6)	65	H(21*B*)	3481(16)	1986(18)	3969(10)	40
H(13)	4193(9)	–4520(9)	2619(7)	70	H(22*B*)	2292(15)	1827(19)	4316(11)	40
H(22)	1868(10)	3098(12)	3570(7)	73	H(21*A*)	3732(11)	3489(13)	4447(8)	9
H(23)	3498(11)	1373(12)	5290(7)	82	H(22*A*)	3270(16)	2522(18)	4808(11)	40
H(21)	1424(9)	3662(10)	4509(6)	57	H(32*A*)	–1557(15)	2020(16)	267(10)	30
H(11)	6634(12)	–4595(14)	2846(7)	100	H(11*A*)	–3225(17)	1039(19)	570(12)	53
H(12)	3987(11)	–3221(12)	2706(7)	103	H(12*A*)	3967(13)	1423(15)	4451(9)	23
H(31)	–3091(9)	1715(10)	658(7)	60	H(11*B*)	4410(2)	3790(2)	3523(15)	88
H(33)	–1261(9)	3271(11)	–582(7)	66	H(12*B*)	3440(2)	–610(2)	3406(13)	70
H(34)	–2197(11)	2398(12)	–814(8)	85	H(31*B*)	5323(18)	–4260(2)	3415(13)	63
H(32)	–2780(9)	1447(10)	1266(7)	64	H(32*B*)	4770(2)	–210(2)	1450(2)	91

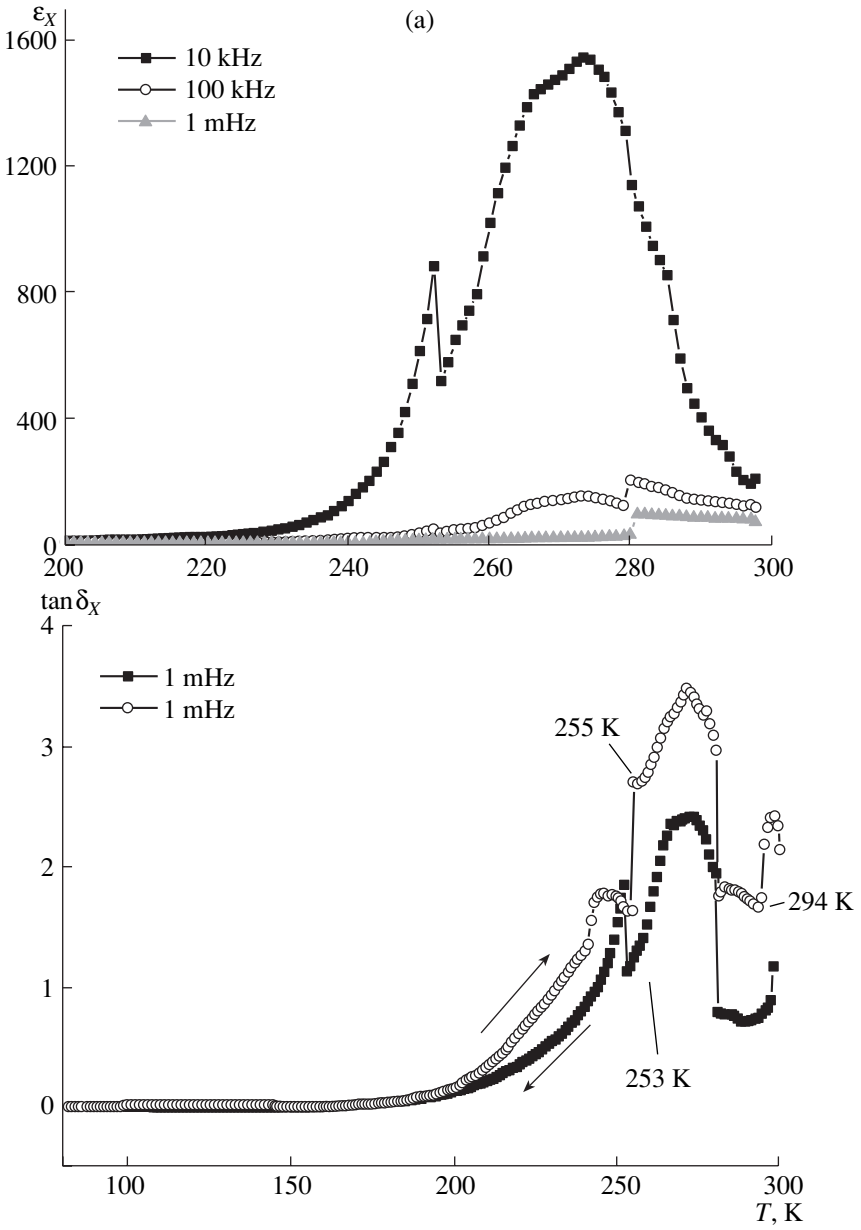

Fig. 5. Temperature dependences of the permittivity and tangent of dielectric loss of the (a) *X* section, (b) *Y* section, and (c) *Z* section.

physical axes *X*, *Y*, and *Z* were directed perpendicular to the crystallographic axes *a*, *b*, and *c*, respectively. Gold leaf was used as electrodes.

The X-ray diffraction experiments were performed on a KM4-CCD four-circle X-ray diffractometer (KUMA DIFFRACTION Company) (MoK_α radiation, λ = 0.71073 Å) [3]. The structure was solved and refined with the SHELX97 program package. The ^{1}H NMR studies were performed on a CW Radiopan spectrometer (ν = 9.4 GHz). The dielectric measurements were performed using an HP 4284A LCR precision measuring device in the frequency range from 20 Hz to 1 MHz at temperatures ranging from 80 to 300 K. An ITC4 Oxford system was used for temperature control and stabilization. The accuracy in stabilizing the temperature was 0.5 K.

RESULTS AND DISCUSSION

The X-ray diffraction study revealed that, at 293 K, the crystals grown are orthorhombic, space group $Pna2_1$, a = 11.338(2) Å, b = 9.981(2) Å, c = 15.675(3) Å, Z = 4, V = 1773.9 Å^3, and d_{calcd} = 1.397 g/cm^3. The compound has a complex chemical formula which can be written as $[(CH_3)_2NH_2]_3CuCl_4Cl$ or $[(CH_3)_2NH_2]_2CuCl_4[(CH_3)_2NH_2]Cl$. The coordinates and thermal parameters of the non-hydrogen atoms are

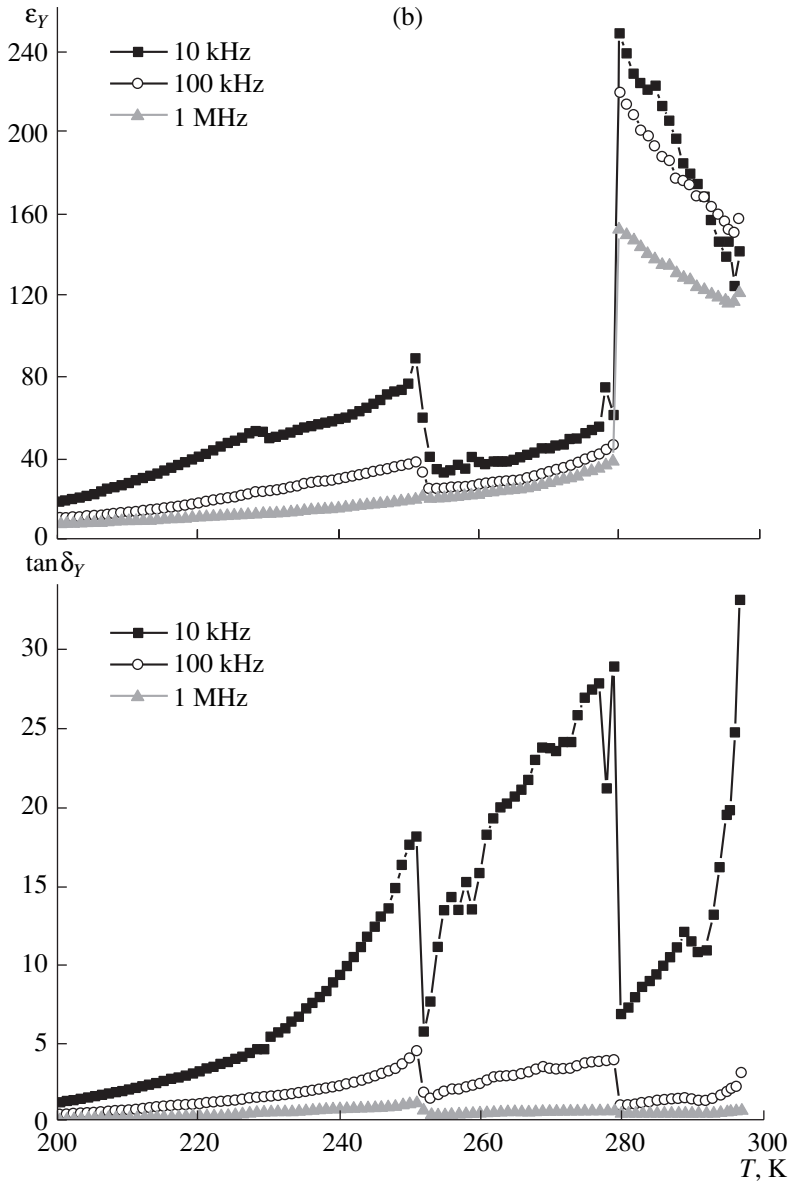

Fig. 5. (Contd.)

listed in Table 1. The coordinates of the hydrogen atoms and the geometric characteristics of the hydrogen bonds are given in Tables 2 and 3, respectively. The structure of the crystals (Fig. 1) is built of $CuCl_4$ tetrahedra, three structurally nonequivalent dimethylammonium groups, and individual chloride ions. The structure consists of two alternating layers parallel to the (001) plane. One of the layers contains $(DMA)^+$ ions and $CuCl_4^{2-}$ tetrahedra, and the other layer contains $(DMA)^+$ and $Cl(5)^-$ ions. The Cl(5) atoms are bound to nitrogen atoms of dimethylammonium groups via two hydrogen bonds (Fig. 2).

The temperature dependences of the unit cell parameters are shown in Fig. 3. As the temperature decreases, the *a*, *b*, and *c* parameters gradually decrease but, at 279 K, undergo abrupt and significant changes: the *b* parameter increases, and the *c* parameter decreases. At the same time, the unit cell size along the *a* axis triples and an incommensurate modulated structure is formed. With a further decrease in the temperature, the *b* parameter gradually increases and the *a* and *c* parameters decrease. At 253 K, the *b* and *a* parameters jumpwise decrease, the *c* parameter increases, and the incommensurate phase disappears.

Figure 4 shows the temperature dependence of the *g* factor measured by the EPR method. It is clearly seen that the *g* factor abruptly increases at 279 K and jumpwise decreases at 253 K. Note that the presence of copper makes these crystals interesting for EPR measure-

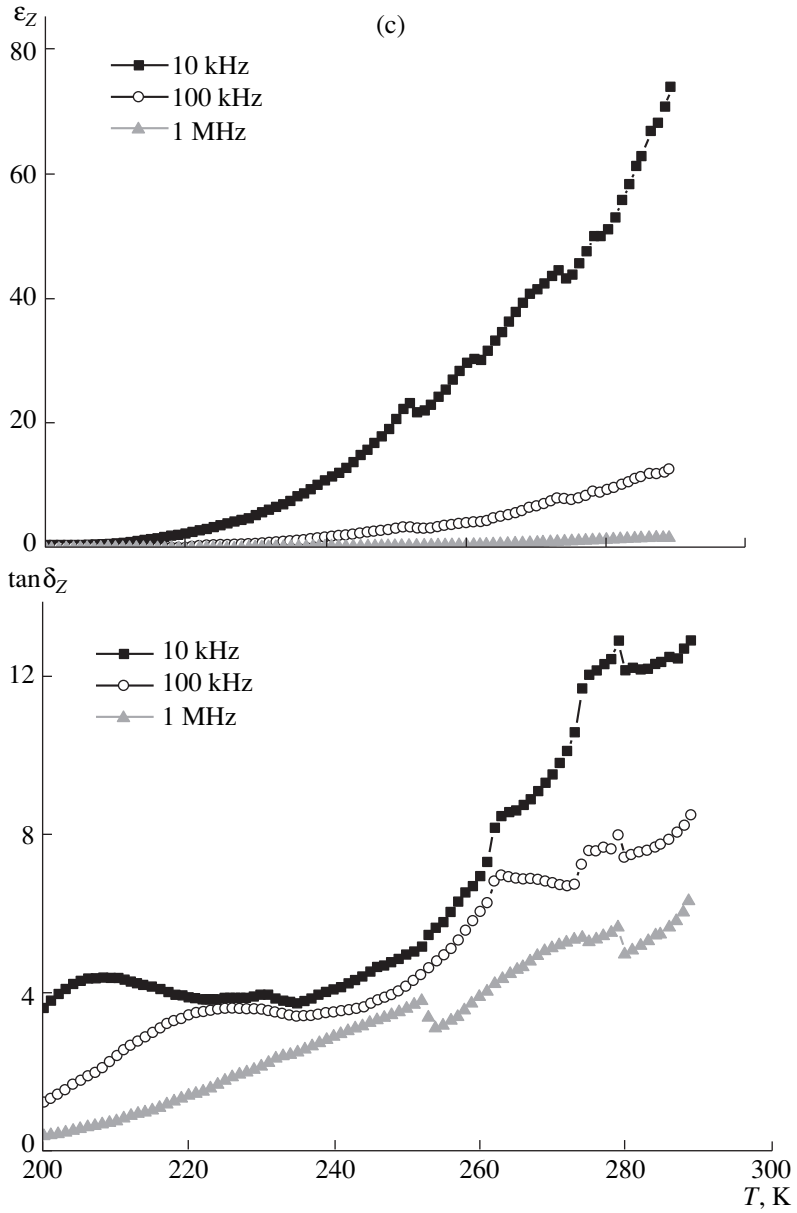

Fig. 5. (Contd.)

ments. The g factor can be represented by the relationship [8]:

$$g = g_e(1 + 8\lambda/\Delta),$$

where g_e is the factor of the free electron and Δ is the spacing between the ground and first excited orbital levels of the copper ion, which is in inverse proportion to the R distance between the Cu^{2+} and Cl ligands, i.e., $\Delta \sim 1/R^5$. It is obvious that, at 279 and 253 K, the distances between the copper atom and the nearest neighbors change.

The dielectric characteristics measured at different frequencies are presented in Fig. 5. A decrease in the temperature leads to a gradual increase in the permittivities ε_X and ε_Y of the samples of the X and Y sections (Figs. 5a, 5b). At 279 K, the permittivity ε_X significantly increases, whereas the permittivity ε_Y abruptly decreases, which is indicative of the improper first-order phase transition. The sample of the Z section (Fig. 5c) exhibits only slight anomalies in the temperature dependences of the permittivity ε_Z at different frequencies. The dielectric loss $\tan\delta$ also changes abruptly in the vicinity of the phase transitions. At 253 K, jumpwise changes in the dielectric characteristics with a temperature hysteresis of about 2 K are

Table 3. Geometric characteristics of the hydrogen bonds

D–H...*A*	(*D*–H), Å	(H…*A*), Å	(*D*…*A*), Å	<(*D*H*A*), deg
N(3*A*)–H(31*A*)…Cl(2)	0.997(14)	2.412(15)	3.3106(15)	149.6(11)
N(3*A*)–H(31*A*)…Cl(4)	0.997(14)	2.656(14)	3.2544(16)	118.7(10)
N(2*B*)–H(21*B*)…Cl(3)	0.751(18)	2.498(18)	3.0841(19)	136.2(17)
N(2*B*)–H(21*B*)…Cl(4)	0.751(18)	2.593(17)	3.170(2)	135.1(16)
N(2*B*)–H(22*B*)…Cl(5)	1.017(18)	3.279(18)	4.276(3)	166.9(13)
N(2*A*)–H(21*A*)…Cl(5)	1.058(13)	2.215(13)	3.222(2)	158.1(10)
N(3*A*)–H(32*A*)…Cl(5)	0.594(16)	2.733(17)	3.303(2)	162.0(19)
N(1*A*)–H(31*B*)…Cl(5)	1.04(2)	2.51(2)	3.539(3)	168.8(17)

observed. These changes indicate a first-order phase transition.

CONCLUSIONS

The results of our studies demonstrated that the crystals obtained have a complex composition. At room temperature, the crystal structure of phase **I** is built of three nonequivalent dimethylammonium groups, $CuCl_4$ tetrahedra, and chloride ions, which are linked via an extended hydrogen bond system into a three-dimensional framework.

A decrease in the temperature to the liquid-nitrogen point leads to two improper first-order phase transitions. The first transition is attended by the formation of the ferroelectric incommensurate modulated phase **II**. Upon this transition, the unit cell size along the *a* axis triples. After the second transition into phase **III**, the incommensurate phase disappears. The dielectric measurements revealed jumpwise changes in the permittivity and dielectric loss due to the first-order phase transitions. The shape of the curves indicates that important relaxation processes take place in the temperature range studied. They are apparently related to the dynamics of dimethylammonium ions. The EPR measurements at the paramagnetic $Cu^{2+}(3d^9)$ centers showed that the phase transitions are accompanied by jumpwise changes in the lattice parameters, which suggest changes in the distances between the copper atom and the ligands (Cu^{2+}–Cl).

ACKNOWLEDGMENTS

This study was supported by the Russian Foundation for Basic Research, project no. 03-02-16190.

REFERENCES

1. L. F. Kirpichnikova, L. A. Shuvalov, N. R. Ivanov, *et al.*, Ferroelectrics **96**, 313 (1989).
2. L. F. Kirpichnikova, A. Pietraszko, M. Polomska, *et al.*, Kristallografiya **41** (4), 722 (1996) [Crystallogr. Rep. **41**, 685 (1996)].
3. A. Pietraszko, D. Kucharczyk, and A. Pawlowski, J. Mol. Struct. **508**, 139 (1999).
4. Z. A. Bobrova, V. M. Varikash, and A. I. Baranov, Kristallografiya **32** (1), 255 (1987) [Sov. Phys. Crystallogr. **32**, 148 (1987)].
5. O. G. Vlokh, V. B. Kapustyanyk, I. I. Polovinko, *et al.*, Izv. Akad. Nauk SSSR, Ser. Fiz. **54** (6), 1143 (1990).
6. F. U. Sheleg, E. M. Zub, A. Ya. Yachkovskiĭ, and L. F. Kirpichnikova, Kristallografiya **47** (4), 634 (2002) [Crystallogr. Rep. **47**, 577 (2002)].
7. V. E. Vasil'ev, V. M. Rudyak, Z. A. Bobrova, *et al.*, Fiz. Tverd. Tela (Leningrad) **29** (5), 1539 (1987) [Sov. Phys. Solid State **29**, 882 (1987)].
8. A. Abragam and B. Bleaney, *Electron Paramagnetic Resonance of Transition Ions* (Clarendon Press, Oxford, 1970; Mir, Moscow, 1972).

Translated by I. Polyakova

Crystallography Reports, Vol. 49, No. 1, 2004, pp. 94–99. Translated from Kristallografiya, Vol. 49, No. 1, 2004, pp. 101–106.

REAL STRUCTURE OF CRYSTALS

Dedicated to the 80th Birthday of L.A. Shuvalov

Relation between the Real Structure and Optical Inhomogeneity of Lithium Niobate Single Crystals

N. Yu. Franko, B. B. Ped'ko, and I. I. Sorokina

Tver State University, Sadovyi per. 35, Tver, 170002 Russia

e-mail: Natalya.Franko@tversu.ru

Abstract—A real structure of lithium niobate single crystals has been studied by the etching method. A relationship between the real structure and the optical inhomogeneity (revealed by the polarization-optical method) was established. © *2004 MAIK "Nauka/Interperiodica".*

The set of optical properties of lithium niobate (LN) single crystals is known to be related to their real structure. The term "real structure of a crystal" implies the crystal composition and macro- and microdefects (the presence of impurities and the defect and domain structure). A distinguishing feature of niobate crystals is the violation of stoichiometry in the course of their growth. This violation results in the formation of various lattice defects, which significantly affect the properties of these compounds. Therefore, the ferroelectric, optical, electrooptical, and nonlinear properties of LN crystals should be considered in relation to their composition and real structure.

Optical homogeneity of LN crystals is the characteristic that is most sensitive to their structural imperfection. LN crystals belong to the symmetry class 3*m*. They are uniaxial ferroelectrics and exhibit no birefringence along the polar *z* axis. However, a complex pattern of optical inhomogeneities can be observed by the polarization-optical method [1, 2]. The manifestation of these inhomogeneities is related to the variation in the birefringence in separate regions of crystals (light propagates along the *z* axis). Such a birefringence appears owing to the electrooptical and elastooptical effects caused by local internal electric fields and stresses [3]. The main objective of this study was to investigate the general features of the relationship between the optical inhomogeneity and the defect structure. In this context, we studied in detail the real structure (revealed by the etching method) of LN crystals of different composition and compared the patterns obtained with the polarization-optical data.

The samples under study were LN crystals grown by the Czochralski method at the Bogoroditsk Plant of Techno-Chemical Products (identical pure samples) and at the Institute of Solid-State and Semiconductor Physics of the Belarussian Academy of Sciences (pure samples and impurity samples grown from stoichiometric melt). The samples were treated and prepared for study at the Institute of Solid-State and Semiconductor Physics. During the sample growth, the rotation axis (and, correspondingly, the pulling direction) corresponded to the polar *z* axis. The boules obtained were cut into plane-parallel plates (normal to the *z* axis) and then polished to optical quality. We studied nominally pure and doped lithium niobate crystals grown from both stoichiometric and congruent melts. Metal oxide impurities were added to the charge before starting the crystal growth. Their concentrations (indicated below) corresponded to the impurity content in the melt. We studied a wide variety of crystal samples cut from both the same boule and different boules. The presented experimental data are typical of all the crystals studied (both pure and Fe-, Zn-, Mn-, Mg-, and Cu-doped crystals, with the impurity concentration in the range 0.1–1 at %). It should be noted that the appearance and shape of the structures revealed by the etching method have some features related to the crystal composition.

Previously, we found that optically inhomogeneous regions of a crystal correspond to regions with a higher concentration of defects, whereas optically homogeneous regions correspond to regions with low defect concentration [4]. When changing the temperature, the optical inhomogeneity of LN crystals manifests itself with higher contrast in the range 20–80°C; further increase in the temperature leads to a decrease and disappearance of the inhomogeneity. Therefore, it was necessary to find the etchant composition and the etching technique most suitable for the temperature range in which the optical inhomogeneity is fairly pronounced. The etching method allows one to estimate the degree of imperfection of LN single crystals not only qualitatively but also quantitatively. This method offers high-resolution etching patterns [5] and enables one to deter-

1063-7745/04/4901-0094$26.00 © 2004 MAIK "Nauka/Interperiodica"

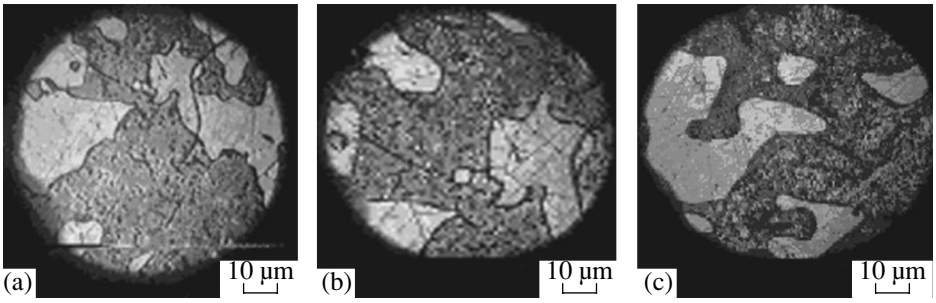

Fig. 1. Domain structure revealed by the etching method on the *z*-cut surface of an $LiNbO_3$ single crystal: (a, b) pure (mode I) and (c) iron-doped (mode III) lithium niobate. Here (and in Figs. 5–13), the photographs were taken in reflected light.

mine the main types of crystal defects from these patterns.

The abilities of various alkalis, acids, salts, and their combinations to etch LN crystals were studied in [6]. The most effective etchant for LN crystals is known to be the mixture of hydrofluoric and nitric acids at a ratio of 1 : 2 and temperature of about 110°C. In this case, it is possible to obtain a well-defined domain LN structure and etching patterns. The etching of crystals in fused potassium hydroxide at 360°C makes it possible to reveal the domain structure at 150°C. The etching temperature can be reduced by adding 35% solution of sodium hydroxide [7].

In order to reveal the real structure of the surface of pure LN crystals, various etchants were used. In the first case (mode I), we used a primarily 40% NaOH solution at room temperature and then a mixture of nitric and hydrofluoric acids at a 2 : 1 ratio at 50°C with the addition of KBr for 30 min. Such an etching mode allowed us to reveal the LN structure at a lower temperature. In the second case (mode II), we used an alkaline etchant composed of 3% KOH solution with the addition of 30% hydrogen peroxide at a ratio of 1 : 2. The etching time was 7–10 min. In the third case (mode III), we used a mixture of nitric and hydrofluoric acids at a ratio of 1 : 2 with the addition of iron trichloride. The etching was carried out at 30°C for 40 min. It is worth noting that the optimal composition of the etchant and the etching mode were chosen depending on the presence of dopants and the Li/Nb ratio. We obtained high-contrast etching patterns at temperatures much lower in comparison with the conventional method; these patterns allowed us to study both the domain and defect structures of crystals [4, 8, 9]. In order to increase the contrast and visualization, we studied the etching patterns using a NEOPHOT-30 microscope.

Etching of the polar cuts of LN single crystals (both the pure and metal-doped ones) revealed small individual antiparallel domains with irregular closed boundaries on the surface of the main domain (Fig. 1). These domains range in size from 10 to 400 μm. The domains within which etching patterns are visualized are positive; the smoother ones are negative [2]. On the surface of negative domains, one can observe marks of damage caused by mechanical polishing of samples. The regions with such a domain structure correspond to the optical inhomogeneity in the form of three-dimensional figures with dark and light areas (Fig. 2).

Using etchant I, we revealed etching patterns within the main domain in the form of regular triangles and hexagons (or in forms close to these geometric figures). The surface of etching figures in the matrix of a positive domain was smooth, whereas numerous etch pits were observed in the case of a negative domain. This fact indicates that the etch pits are microdomains up to 5–20 μm in size (Fig. 3) [10]. The comparison of the results of polarization-optical and etching studies showed that these domains correspond to the optical inhomogeneity in the form of light spots (Fig. 4).

On the surface of *z*-cut plates of pure LN, we found inclined (with respect to the polar *z* axis) charged domain walls (Fig. 5). As was noted in [8, 11, 12], these walls give rise to the electric-field components normal to the *z* axis. These patterns were obtained using alkaline etchant (III).

It is noteworthy that the structure with domains of regular geometric shape (having the symmetry of the basic material) is only observed when the domain size is smaller than a few millimeters (see above). At the same time, the shape of larger domains is not defined (Fig. 6).

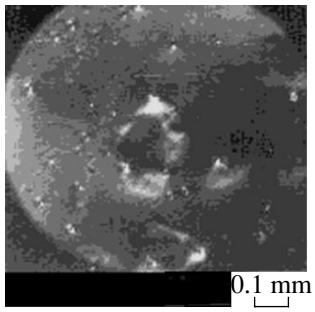

Fig. 2. Structure in the form of three-dimensional figures (the center of the photograph) revealed by the polarization-optical method on the *z*-cut surface of a lithium niobate crystal.

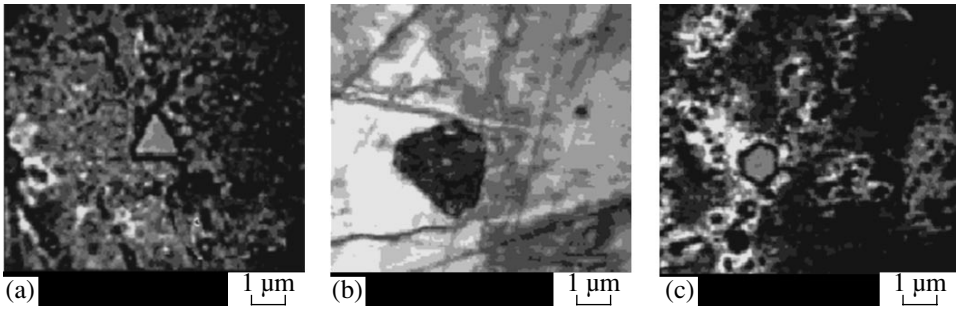

Fig. 3. Etching patterns revealed on the *z*-cut surface of a Zn-doped lithium niobate crystal in the form of regular (a) triangles and (b, c) hexagons (mode I). The photographs were obtained in (a, c) transmitted and (b) reflected light.

Interestingly, the microdomains of regular shape (Fig. 7) are located along the lines of low-angle misorientation. The distribution of microdomains within the larger domains is similar to the classic distribution of electric-field lines near protrusions on charged plates. Figure 7b shows (on the right-hand side) irregular trihedral etching pits, which were interpreted as related to dislocations emerging to the surface at an angle to the polar axis. Figure 8 shows ring-shaped domains revealed on the *z*-cut surface of a pure LN crystal using acid etchant (III).

In addition, round-shaped etching patterns that correspond to complexes of point defects were found (Fig. 9) on the surface of an LN plate. These geometric figures are mildly sloping and have no well-defined faces or vertices. Similar etching patterns were observed for a number of crystalline compounds and identified as substructures [4]. One can assume that these etching patterns are associated with the presence of dopants in LN. The comparison of the etching data with the results of polarization-optical study suggests that such etching patterns are observed in optically homogeneous regions of LN crystals.

Figure 10 shows domains (about 10 μm in size) located in the regions where the crystal was mechanically damaged. In addition to the domains, dislocations forming peculiar chains on the crystal surface are also observed (Fig. 11). Since high internal stresses around the dislocations result in a local increase of the crystal energy, it is sometimes possible to reveal the ends of the dislocation lines on the crystal surface using acid etchants. In this case, well-defined etch pits arise at the dislocation ends; the shape of these pits yields information on the inclination of dislocations with respect to the crystal surface.

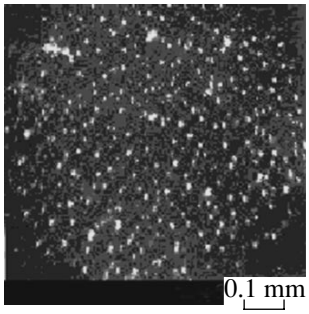

Fig. 4. Structure in the form of bright spots revealed on the *z*-cut surface of a Zn-doped lithium niobate crystal by the polarization-optical method.

Figure 12 shows nonsymmetrical etch pits, which indicate that the dislocations emerge at an angle to the (001) surface. Similar nets of dislocations were observed in Ge [13], GaAs, and some other compounds [4]. The attachment of domains to dislocations suggests a relationship between the domain structure under consideration and the dislocation structure. We also obtained an interesting pattern of a cleavage of an $LiNbO_3$ + 0.1 at. % V crystal (*z* cut). As can be seen from Fig. 13, the characteristic structure of the cleavage is associated with the growth layers of the crystal. In our opinion, the violation of the growth layers is caused by a chain of dislocations.

In order to compare the results of the etching and the polarization-optical studies, we investigated various regions of the crystal (both containing optical inhomogeneities and sufficiently homogeneous). Optically inhomogeneous regions correspond to either polydomain areas (in which domains are attached to dislocations) or areas with a higher concentration of microdomains. The crystal regions that contained no domains but, nevertheless, exhibited a weak extremal dependence of the optical inhomogeneity on temperature corresponded to the etch structure indicating the presence of a dislocation net (including dislocations emerging at an angle to the crystal surface). In optically homogeneous regions, only etching patterns in the form of irregularly shaped pits were observed (we attribute the formation of these patterns to vacancy complexes and other complexes of defects).

Thus, the optical inhomogeneity of LN crystals is associated with their real structure, i.e., with the local irregularities of the crystal structure. These irregularities are dislocations, complexes of charged defects, and charged domain walls, which, as a rule, are also located at defects of various kinds [8, 9]. The reason for the

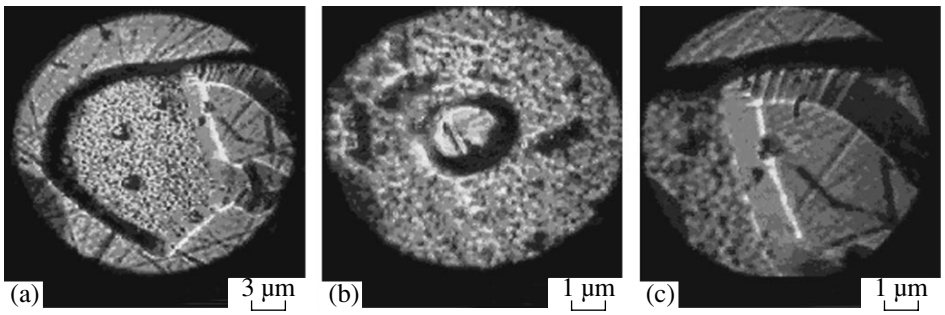

Fig. 5. Structures revealed on the *z*-cut surface of a lithium niobate crystal by the etching method (mode III).

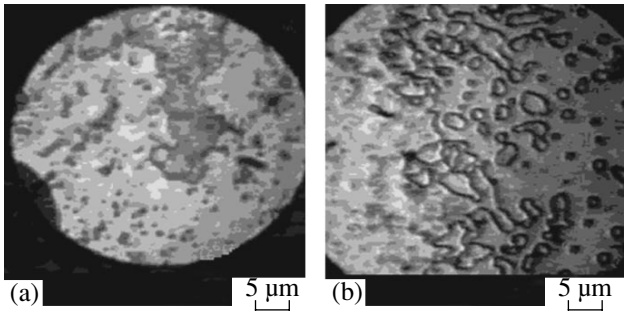

Fig. 6. Domain structure revealed by the etching method in different areas on the *z*-cut surface of an $LiNbO_3$ single crystal (mode II).

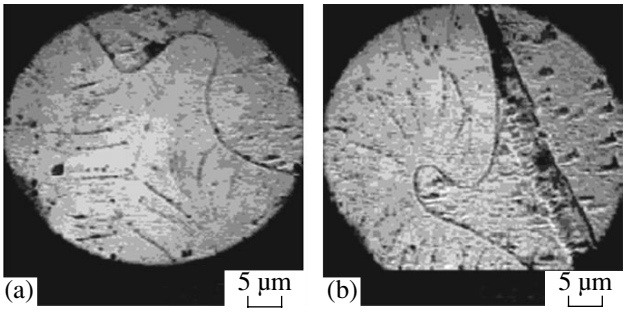

Fig. 7. Structure revealed by the etching method on the *z*-cut surface of an $LiNbO_3$ single crystal (mode II).

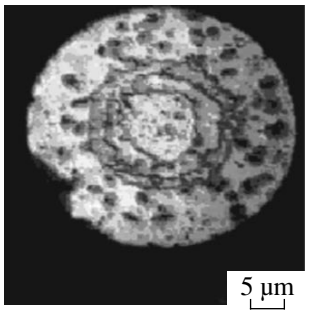

Fig. 8. Ring-shaped domains revealed by the etching method (mode II) on the *z*-cut surface of an $LiNbO_3$ single crystal.

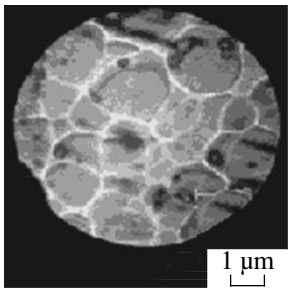

Fig. 9. Round-shaped etching patterns revealed on the *z*-cut surface of pure lithium niobate (mode II).

optical inhomogeneity is the local electrooptic effect, i.e., the electric fields generated at these defects, which have components normal to the polar axis. The disappearance of the optical inhomogeneity at temperatures higher than 150°C is due to the thermal activation of charge carriers and the screening of these fields. This is evidenced by the dependences of the thermal behavior of the optical inhomogeneity on the composition of the crystal and its prehistory and treatment [3].

At the same time, it should be admitted that similar mechanisms should also manifest themselves in other materials, including those isomorphic to LN. However, such a behavior of the optical inhomogeneity is either

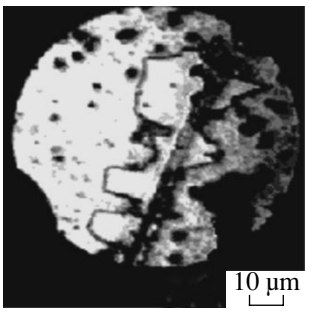

Fig. 10. Domain structure revealed by the etching method in the region of mechanical damage (scratches) on the *z*-cut surface of an $LiNbO_3$ single crystal (mode II).

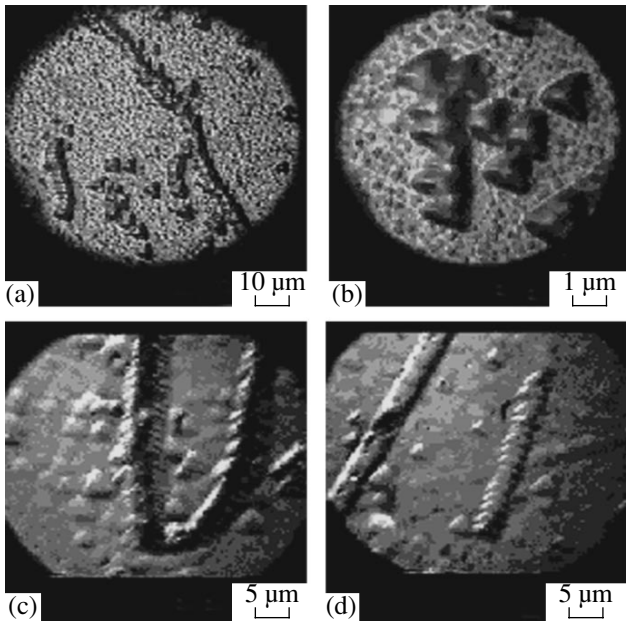

Fig. 11. Dislocations revealed by the etching method (mode III) on the *z*-cut surface of (a, b) pure $LiNbO_3$ and (c, d) $LiNbO_3$ + 0.1 at. % Fe.

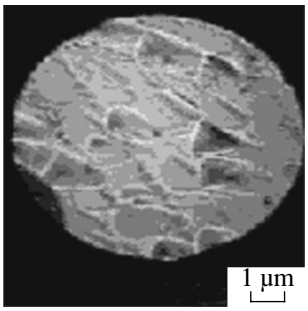

Fig. 12. Etching patterns revealed on the *z*-cut surface of pure lithium niobate (mode II).

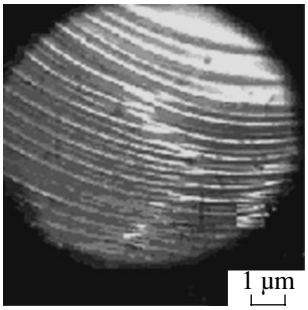

Fig. 13. The structure revealed on the cleavage of an $LiNbO_3$ crystal doped with 0.1 at. % V (*z* cut).

not observed at all or only weakly pronounced (lithium tantalate). We believe that the structure of LN crystals plays an important role in the occurrence of the growth-induced optical inhomogeneity.

The induced optical inhomogeneity was studied in [14, 15] by nuclear magnetic resonance (NMR) using ^{93}Nb nuclei. A spread of the parameters of the electric-field gradient tensor was found at the sites where ^{93}Nb nuclei were located. This spread, only weakly related to the presence of impurities, reflects the intrinsic properties of the LN structure and indicates the disorder in the localization of Nb^{5+} ions and surrounding oxygen ions. The random distortion of oxygen octahedra containing Nb ions gives rise to a component of the unit dipole moments of the lattice that is normal to the *c* axis. The value and direction of this component changes randomly in passing from one unit cell to another. Upon averaging (summing over the total crystal volume), this component vanishes. In order to experimentally verify the models of the defect structure of LN single crystals, the ^7Li NMR study of extra samples was performed. The latter were samples with different compositions ($R_{Li/Nb}$ = 0.94–1.15 in melt), samples with congruent composition, and samples doped with Fe (0.003–0.6 mol %). It was found that the behavior and parameters of the experimentally observed NMR spectra can only be explained under the assumption that the electric-field gradient is dynamically disordered at ^7Li [16] nuclei, which indicates active mobility of ^7Li nuclei in a LiO_6 octahedron.

In view of the aforesaid, we can assume that a coordinated displacement of niobium and lithium ions in the bulk of oxygen octahedra occurs near the charged defects (i.e., at the sites where the electric fields $E_{x,y}$ responsible for the growth-induced optical inhomogeneity are localized). Such a displacement will be observed in local regions adjacent to defects of the crystal structure. Obviously, the displacement direction is different in different regions and, in turn, can give rise to the electric-field components normal to the polar axis. Thus, the occurrence of optical inhomogeneity due to the electrooptic effect can, to a large extent, be controlled by the coordinated displacement of niobium ions located near defects of the crystal structure along the directions normal to the *z* axis. In our opinion, this approach explains the difference in the behavior of the optical inhomogeneity in LN and materials isomorphic to this compound.

ACKNOWLEDGMENTS

This study was supported by NWO, project no. 16-04-1999, and by the Russian Foundation for Basic Research, project no. 01-02-16511.

REFERENCES

1. V. P. Yarunichev and G. S. Berezovskaya, Vestsi Akad. Navuk Belarusi, Ser. Fiz.–Mat. Navuk **5**, 126 (1979).
2. E. I. Bratishchenko, B. B. Ped'ko, V. M. Rudyak, and V. P. Yarunichev, Izv. Akad. Nauk SSSR, Ser. Fiz. **48** (6), 1213 (1984).

3. A. A. Blistanov, E. V. Makarevskaya, V. V. Geras'kin, *et al.*, Fiz. Tverd. Tela (Leningrad) **20** (9), 2575 (1978) [Sov. Phys. Solid State **20**, 1489 (1978)].
4. B. B. Ped'ko, É. V. Lebedev, N. Yu. Franko, and I. I. Sorokina, in *Abstracts of International Conference on Growth and Physics of Crystals* (Mosk. Inst. Stali Splavov, Moscow, 1998), p. 243.
5. Yu. P. Pshenichnov, *Observation of Fine Crystal Microstructure: A Handbook* (Metallurgiya, Moscow, 1974).
6. K. Nassau, H. J. Levinstein, and G. M. Lioacono, J. Phys. Chem. Solids **27**, 983 (1966).
7. I. I. Sorokina and B. B. Ped'ko, USSR Inventor's Certificate No. 1583479 (July 7, 1988).
8. N. Yu. Franko, B. B. Ped'ko, I. I. Sorokina, and N. A. Khokhonina, in *Proceedings of 4th International Conference on Crystals: Growth, Properties, Real Structure, and Application* (VNIISIMS, Aleksandrov, 1999), Vol. 1, p. 517.
9. N. Yu. Franko, B. B. Ped'ko, I. I. Sorokina, and N. A. Khokhonina, Izv. Ross. Akad. Nauk, Ser. Fiz. **64** (64), 1140 (2000).
10. K. Nassau, H. G. Levinstein, and G. M. Lioacono, Appl. Phys. Lett. **6** (11), 228 (1965).
11. V. Ya. Shur, E. L. Rumyantsev, E. V. Nikolaeva, and E. I. Shishkin, Appl. Phys. Lett. **77** (22), 3636 (2000).
12. A. A. Blistanov, *Crystals of Quantum and Nonlinear Optics* (Mosk. Inst. Stali Splavov, Moscow, 2000).
13. V. M. Kosevich and L. S. Palatnik, *Electon-Microscopic Images of Dislocations and Stacking Faults* (Nauka, Moscow, 1976).
14. A. V. Yatsenko and N. A. Sergeev, Fiz. Tverd. Tela (Leningrad) **27** (4), 1239 (1985) [Sov. Phys. Solid State **27**, 748 (1985)].
15. S. C. Abrahams, J. M. Reddy, and S. L. Bernstein, J. Phys. Chem. Solids **27** (6), 997 (1996).
16. A. V. Yatsenko and N. A. Sergeev, Ukr. Fiz. Zh. **30**, 118 (1985).

Translated by A. Zolot'ko